Nanophotonics and Metamaterials based Tunable Optical Devices for Filtering and Harvesting Solar Radiation

A thesis submitted

in partial fulfilment of the requirements

for the Degree of

Doctor of Philosophy

by

Ashish Kumar Chowdhary

Department of Electronics and Electrical Engineering
Indian Institute of Technology Guwahati
Guwahati - 781039, Assam, India

February 2022

Dedicated to my teachers

and

most beloved parents

Certificate

This is to certify that the thesis entitled "**Nanophotonics and Metamaterials based Tunable Optical Devices for Filtering and Harvesting Solar Radiation**", submitted by **Ashish Kumar Chowdhary** (176302003), a research scholar in the *Department of Electronics and Electrical Engineering, Indian Institute of Technology Guwahati*, for the award of the degree of **Doctor of Philosophy**, is a record of an original research work carried out by him under my supervision and guidance. The thesis has fulfilled all requirements as per the regulations of the institute and in our opinion has reached the standard needed for submission. The results embodied in this thesis have not been submitted to any other University or Institute for the award of any degree or diploma.

Date: Feb. 9, 2022
Place: Guwahati

Dr. Debabrata Sikdar
Assistant Professor
Dept. of Electronics and Electrical Engineering,
Indian Institute of Technology Guwahati,
Guwahati, Assam, India - 781 039

Declaration

I certify that

- The work enclosed in this thesis is original and has been done by me under the guidance of my supervisor.
- This work has not been submitted to other Institute for any degree or diploma.
- I have followed the standard guidelines provided by the institute in preparing the thesis.
- I have conformed to the norms and guidelines given in the Ethical Code of Conduct of the Institute.
- Whenever I have used materials (data, theoretical analysis, figures, and text) from other sources, I have given due credit to them by citing them in the text of the thesis and giving them details in the references. Further, I have taken permission from the copyright owners of the sources, whenever necessary.

Date: Feb. 9, 2022

Place: Guwahati

Ashish Kumar Chowdhary

MS (Eng.) + Ph.D., Dual Degree Student

Dept. of Electronics and Electrical Engineering,

Indian Institute of Technology Guwahati,

Guwahati, Assam, India - 781 039

Acknowledgements

As I look back and walk down the memory lane, I could recollect endless reminiscence associated with this divine IIT Guwahati campus. At this juncture, while writing my PhD thesis, I have many wonderful people to thank who directly or indirectly helped me to sail through the ups and downs of this four year long journey.

First and foremost, I would like to express my sincere gratitude to my thesis supervisor Dr. Debabrata Sikdar, for his guidance and constant support through the entire course of my research work. His kindness, dedication, hard work, and attention to detail have been a great inspiration to me. He always motivated me to think, learn, and unlearn that helped me grow as a researcher. I sincerely thank him for the pain he undertook in scrutinizing every manuscript I presented to him and offering constructive critical comments.

I am indebted to my doctoral committee members for sparing their precious time out of their busy schedule to evaluate my progress and enrich this thesis work with their invaluable suggestions and feedbacks. I am grateful to Prof. Rakhesh Singh Kshetrimayum for his valuable lessons and guidance as a doctoral committee chairperson. My sincere gratitude to Dr. Gagan Kumar for the constructive suggestions during my progress review and collaborative work towards the end of my PhD journey. No word of thanks can sum up the gratitude that I owe to Dr. Mahima Arrawatia for her mentorship and constant support as a supervisor-in-charge when Dr. Sikdar was on long term academic leave.

I would like to thank our academic collaborators: Iyer Research Group (Center for Nanotechnology and Department of Chemistry, IIT Guwahati), Dr. D. Pamu (Department of Physics, IIT Guwahati) and industry collaborators: Dr. Rathish Arumugam (Saint-Gobain India Pvt. Ltd) and Dr. Ashutosh Kumar Singh (Centre for Nano and

Soft Matter Sciences, Bengaluru). At IIT Guwahati, I would like to acknowledge Central Instruments Facility for SEM and XRD instrument facilities, Center for Nanotechnology for UV-VIS spectroscopy, and Department of Physics for allowing me to use Profilometer. I am thankful to the Head of the Department, other faculty and staff members for their kind help at various stages of my academic career. My special thanks to present Head of the Department, Prof. Roy P. Paily for providing me high-end computing facility at crucial time that helped me to complete my research work within time.

I have no words to express my thanks to my seniors, specially Dr. Jitendra Prajapati for his support and guidance in the initial phase of my PhD, Dr. Darpan Mishra and Mr. Manoranjan Minz for fruitful discussions and suggestions related to our photonics field. Thanks go out to my colleges and friends Ms. Dhriti Maurya, Mr. Praveen Saraswat, Mr. Tanmay Bhowmik, and Mr. Jegyasu Gupta. I would like to mention my juniors Anurag and Aakash for their M. Tech thesis work with me. They have always been around to provide useful suggestions, companionship, and created a fun-filled research environment. My work in this place, far away from home, definitely would have been painful without their love and care that helped me to enjoy my life at IIT Guwahati.

Last but not the least, my deepest gratitude goes to my family especially my Parents: Shri Shiw Narayan Chowdhary and Smt. Anita Chowdhary, brother: Manish Chowdhary, and sister-in-law: Itu Choudhary, for supporting me throughout this journey and bearing all the pain that may have ensued due to my prolonged distraction. I am also very grateful to them for letting me free from all the responsibilities throughout my studies. The opportunities that they have given me and their immense sacrifices are the reasons where I am and what I have accomplished so far.

(Ashish Kumar Chowdhary)

Abstract

Due to continuous growth in global population and rapid industrial development over the years, the energy demand for cooling and heating through air conditioning systems has been increasing dramatically, contributing to a steep rise in fossil fuel consumption and consequently, leading to global warming. To counter this global challenge, designs of eco-friendly smart windows, capable of selective filtering of solar spectral radiation, could significantly reduce the energy consumption by heating and cooling systems, not only for residential buildings but also for state-of-the-art passenger vehicles. Having said that, robust and industry-standard designs of such windows, tunable for all-weather conditions, have been a challenge to date. Further, keeping in view the need for sustainable development, curbing down carbon emissions is the need of the hour. In this regard, utilization of waste heat from various solar and non-solar sources is of paramount importance to promote green energy. Hence, to address the above problems, this thesis investigates nanophotonics and metamaterials based on tunable optical devices for smart window design and solar energy harvesting. The research focuses on providing comprehensive theoretical models and design guidelines for realizing futuristic industry-standard smart windows, broadband metamaterial absorbers, radiative coolers, and solar absorbers—based on analytical and numerical methods in the realms of classical electrodynamic theory.

The scope of this thesis work lies over a wide spectral range, covering ultraviolet, visible, and infrared radiations. Different nanoscale passive and tunable designs based

on multilayer, grating, cross or ring patterns, and nanoparticles have been explored for designing transmission- and absorption-mode spectrally-selective filters for smart windows and solar energy harvesting. First, a design of novel plasmonic 'meta-glass' as infrared-blocking nanophotonic windows is introduced to block infrared radiation efficiently while maintaining good outdoor visibility. Then nanoparticles-based ultraviolet and infrared blocking meta-glasses are presented. After that, a design of metal–insulator–metal multilayer thin-films based passive windows is showcased, customized to operate in different climate conditions. A design of nanophotonic windows is also presented as specific color filters. However, these passive windows once fabricated cannot be tuned to weather-specific needs. Therefore, we further investigated metal–insulator–metal multilayer thin-films based electrotunable windows to dynamically control the intensity of transmitted solar radiation, depending on the weather conditions. Then, electrotunable color filters are discussed for application as electrochromic windows. Keeping in mind the current state-of-the-art nanofabrication technology, we explored alternative designs of passive and electrotunable windows, which would allow the use of a thicker metal nanofilm that would be easier to fabricate. In this regard, we proposed designs of static and electrotunable 'smart' windows based on insulator–metal–insulator multilayer thin-films, followed by a comparative study between those.

Next, we investigated different absorption-mode broadband metamaterial absorbers for harvesting heat from the solar radiation. At first, a plasmonics based broadband metamaterial absorber is introduced in the 400–1100 nm spectral window that could be used to improve the efficiency of silicon solar cells. Then, a one-dimensional grating-based wide-angle and ultrabroadband metamaterial absorber is presented in the 400–2500 nm spectral range for solar energy harvesting. A two-dimensional grating based ultrabroadband polarization-insensitive 'perfect' metamaterial absorber over a wider spectral regime of 300–4500 nm is investigated then designed, which may have consid-

erable implications in thermophotovoltaics applications. For waste heat management, a multilayer thin-films based design of a selective solar absorber is presented to harness solar energy as heat and convert it into thermal energy. These nanophotonic designs could be integrated with a thermoelectric generator to convert trapped thermal energy into usable electrical energy for low power applications, such as charging a cellphone, lighting light-emitting diodes, self-operating solar cell panels, and windmills, to name a few. Finally, the design of a passive radiative cooler is presented, which can pump excess heat to cold exterior space *via* thermal radiation.

Most of the designs presented in this thesis are polarization-independent and angle-insensitive indicating that our designs could be an excellent choice for filtering and harvesting solar energy throughout the daytime. The theoretical results agree well with those of full-wave simulations. Prospective fabrication techniques and fabrication-imperfection tolerance studies are discussed in detail, considering the practical challenges pertaining to the realization of various designs. The nanophotonics and metamaterials based smart windows, absorbers, and radiative coolers may find application in modern buildings, greenhouses, and vehicles, just to name a few.

Contents

List of Figures

List of Tables

List of Acronyms

UV	Ultraviolet
VIS	Visible
IR	Infrared
SWIR	Short-wave Infrared
MWIR	Mid-wave Infrared
LWIR	Long-wave Infrared
FIR	Far-wave Infrared
THz	Terahertz
EM	Electromagnetic
MD	Metallo-dielectric
SPPs	Surface Plasmon Polaritons
LSPs	Localized Surface Plasmons
FDTD	Finite Difference Time Domain
FEM	Finite Element Method
TMM	Transfer Matrix Method
TLM	Transmission Line Method
FPI	Fabry–Perot Interferometer
EMT	Effective Medium Theory
EO	Electro-Optic

MLMD	Multilayered Metallo-dielectric
PRC	Passive Radiative Cooler
SSA	Selective Solar Absorber
CVD	Chemical Vapour Deposition
ITO	Indium Tin Oxide
AZO	Aluminium-doped Zinc Oxide
ALON	Aluminium Oxynitride
STPV	Solar Thermophotovoltaics
TEG	Thermo-electric Generator
CFDA	Central Finite Difference Approximation
AM	Air Mass
ENZ	Epsilon-Near-Zero
MIM	Metal–Insulator–Metal
IMI	Insulator–Metal–Insulator
MW	Megawatt

List of Symbols

E	Electric field
H	Magnetic field
D	Electric displacement
ρ	Electric charge density
J	Electric current density
μ	Permeability
ϵ	Permittivity
P	Polarization response of the medium
ρ_{s}	Surface charge density
J_{s}	Surface current density
$\mathbf{n}$	surface normal
m	Mass of electron
q or e	Charge of electron
ω	Optical frequency of incident radiation
ω_{p}	Plasma frequency
ω_{L}	Plasma frequency associated with intraband transition
Δ_{ϵ}	Oscillator strength
ϵ_{∞}	High-frequency permittivity
γ	Collision frequency
Γ_{L}	Damping coefficient
v_{F}	Fermi velocity

k	Propagation wavevector
Λ	Optical path length difference
n	Refractive index
t	Transmission coefficient
r	Reflection coefficient
A	Absorbance
R	Reflectance
R	Transmittance
θ_{i}	Angle of incidence
θ_{r}	Angle of reflectance
θ_{t}	Angle of transmittance
Y	Admittance
$\mathbf{P}$	Characteristics matrix
λ	Wavelength
Z	Impedance
ϕ	Phase shift
F	Finesse
f	Fill fraction
$\mathbf{S}$	Poynting vector
V	Bias voltage
c	Speed of light
$\mathbf{K}$	Boltzman's constant
h	Plank's constant
T	Temperature
T_{amb}	Ambient temperature
T_{abs}	Operational temperature

S	Scattering parameter
P_{rad}	Thermal radiation from the object
P_{atm}	Thermal radiation of the atmosphere
P_{solar}	Incident solar irradiation
P_{con}	Parasitic heat gain
P_{cool}	Net cooling power
A_{prc}	Surface area of the cooler
I_{BB}	Wavelength-dependent spectral radiance
$I_{\text{AM1.5}}$	Standardized wavelength-dependent sun's solar irradiance
ϵ_{atm}	Emissivity of the atmosphere
η	Solar-to-thermal energy conversion efficiency
Q	Solar radiative heat flux
α	Absorption coefficient
ϵ	Emission coefficient

List of Publications

Journal Publications

1. **A. K. Chowdhary**, T. Bhowmik, and D. Sikdar, "Infrared-blocking Plasmonic Meta-glasses for Energy-saving Passive Windows," *Optics Letters* 47, 2242–2245 (2022). Publisher: OSA, **Q1**, IF: 3.8 (2020). (Related to chapter 3)

2. **A. K. Chowdhary**, V. A. Reddy, and D. Sikdar, "Nanophotonics-enabled High-efficiency Selective Solar Absorbers for Waste Heat Management," *IEEE Transactions on Nanotechnology* 21, 131–136 (2022). Publisher: IEEE, **Q2**, IF: 2.6 (2020). (Related to chapter 7)

3. **A. K. Chowdhary** and D. Sikdar, "Multilayer Thin-film Based Nanophotonic Windows: Static versus Electrotunable Design," *Journal of Optics* 24, 024002 (2022). Publisher: IOP Science, **Q1**, IF: 2.5 (2020). (Related to chapter 5)

4. **A. K. Chowdhary**, V. A. Reddy, and D. Sikdar, "Selective thermal emitters for high-performance all-day radiative cooling," *Journal of Physics D: Applied Physics* 55, 085504 (2022). Publisher: IOP Science, **Q1**, IF: 3.2 (2020). (Related to chapter 7)

5. **A. K. Chowdhary** and D. Sikdar, "Design of Electrotunable All-weather Smart Windows," *Solar Energy Materials and Solar Cells* 222, 110921 (2021). Publisher: Elsevier, **Q1**, IF: 7.3 (2020). (Related to chapter 4)

6. **A. K. Chowdhary**, T. Bhowmik, J. Gupta, and D. Sikdar, "Energy-saving All-weather Window Based on Selective Filtering of Solar Spectral Radiation," *Applied Optics* 60, 1315–1325 (2021). Publisher: OSA, **Q1**, IF: 2.0 (2020). (Related to chapter 3)

7. **A. K. Chowdhary**, T. Bhowmik, and D. Sikdar, "Polarization- and Angle-insensitive Ultra-broadband Perfect Metamaterial Absorber for Thermophotovoltaics," *Journal of the Optical Society of America B* 38, 327–335 (2021). Publisher: OSA, **Q1**, IF: 2.1 (2020). (Related to chapter 6)

8. **A. K. Chowdhary** and D. Sikdar, "Low-power Design of Electrotunable Color Filters and Optical Switches," *Journal of the Optical Society of America B* 37, 3865–3873 (2020). Publisher: OSA, **Q1**, IF: 2.1 (2020). (Related to chapter 4)

Research articles not included in this thesis

9. KM Dhriti, **A. K. Chowdhary**, B. S. Chouhan, D. Sikdar, and G. Kumar, "Tunable Terahertz Absorption Modulation in Graphene Nanoribbon-assisted Dielectric Metamaterial," *Journal of Physics D: Applied Physics* 55, 285101 (2022). Publisher: IOP Science, **Q1**, IF: 3.2 (2020).

10. T. Bhowmik, **A. K. Chowdhary**, and D. Sikdar, "Grating-assisted Polarization-insensitive Dual-Mode Spatial Light Modulators using an Epsilon-Near-Zero Material," *IEEE Journal of Quantum Electronics*. Publisher: IEEE, **Q1**, IF: 2.3 (2020), Status: Just Accepted.

Conference Publications

1. **A. K. Chowdhary** and D. Sikdar, "Nanophotonic All-weather Windows for Energy-efficient Smart Buildings," *2021 Conference on Lasers and Electro-Optics (CLEO)*, 1–2 (2021). Publisher: IEEE/OSA, Location: San Jose, California, USA. (Related to chapter 4)

2. **A. K Chowdhary**, V. A. Reddy, T. Bhowmik, and D. Sikdar, "Spectrally Selective Nanophotonic Windows for Aiding Photosynthesis in Greenhouses," *2021 IEEE Photonics Conference (IPC)*, 1-2 (2021). Publisher: IEEE, Location: Vancouver, BC, Canada. (Related to chapter 3)

3. **A. K. Chowdhary**, A. Kumar, and D. Sikdar, "Cross–Ring Based Broadband Plasmonic Metamaterial Absorbers for Boosting Silicon Solar Cell Efficiency," *2021 Fifteenth International Congress on Artificial Materials for Novel Wave Phenomena (Metamaterials)*, 102-104 (2021). Publisher: IEEE, Location: New York City, USA. (Related to chapter 6)

4. **A. K. Chowdhary** and D. Sikdar, "Ultra-broadband Wide-Angle Metallo-Dielectric Metamaterial Absorber for Solar Energy Harvesting," in *2019 Workshop on Recent Advances in Photonics (WRAP)*, 1–3 (2019). Publisher: IEEE, Location: Guwahati, India. (Related to chapter 6)

5. **A. K. Chowdhary**, T. Bhowmik, J. Gupta, and D. Sikdar, "Ultraviolet and Infrared Blocking Meta-glasses for Smart Electric Vehicles," *IEEE 9th International Conference on Photonics (ICP) 2022*. Publisher: IEEE, Location: Malaysia. Status: Submitted. (Related to chapter 3)

Conference papers not included in this thesis

6. **A. K. Chowdhary**, V. A. Reddy, T. Bhowmik, and D. Sikdar, "Vanadium Dioxide Assisted Thermo-optic Metamaterial Absorbers for Optical Switching," in *2022 Workshop on Recent Advances in Photonics (WRAP)*, 1–2 (2022). Publisher: IEEE, Location: Mumbai, India.

7. T. Bhowmik, **A. K. Chowdhary**, A. Kumar, and D. Sikdar, "Guided-Mode Resonance based All-dielectric Optical Intensity Modulator," *2021 IEEE Photonics Conference (IPC)*, 1-2 (2021). Publisher: IEEE, Location: Vancouver, BC, Canada.

8. T. Bhowmik, **A. K. Chowdhary**, J. Gupta, and D. Sikdar, "Coupling-assisted Epsilon-Near-Zero Material based Energy-efficient Electro-Absorption Modulator," in *2022 Workshop on Recent Advances in Photonics (WRAP)*, 1–2 (2022). Publisher: IEEE, Location: Mumbai, India.

9. B. S. Chouhan, KM Dhriti, **A. K. Chowdhary**, D. Sikdar, and G. Kumar, "Modulating broadband terahertz in a Graphene assisted dielectric Metamaterial," *in 2022 Workshop on Recent Advances in Photonics (WRAP)*, 1–2 (2022). Publisher: IEEE, Location: Mumbai, India.

10. T. Bhowmik, A. Kumar, **A. K. Chowdhary**, and D. Sikdar, "Polarization-insensitive Electro-tunable Broadband Plasmonic Metamaterial Absorber for Amplitude Modulation," *2021 Fifteenth International Congress on Artificial Materials for Novel Wave Phenomena (Metamaterials)*, 050–052 (2021). Publisher: IEEE, Location: New York City, USA.

1

Introduction

Contents

TODAY, the global energy demand is increasing at an unprecedented rate to meet the needs of the ever-growing world human population. In the present scenario, every basic necessity of human life needs electricity, which requires burning fossil fuels such as oil, coal, or natural gas. These fossil fuels take millions of years to replenish and will not last for eternity. Their burning releases heat into the environment, increasing carbon footprints, leading to a rise in global temperature. Over the past couple of decades, climate change and the melting of ice in the polar regions are a couple of worrisome pieces of evidence of global warming. To reduce greenhouse gas emissions, there is a dire need to reduce fossil fuel consumption and move towards renewable energy sources.

1.1 Research Motivation

"A building's heating, cooling, and lighting loads are major energy-consumption segments in any building. To meet the goals of the Paris Climate Agreement, a building's energy intensity— how much energy buildings use— will have to improve by 30% in 2030. There has been increased attention to sustainable architectural designs for better light and heat management in buildings in recent years, and deploying smart windows is the first step for such structures."

—Paris Agreement to the UNFC on Climate Change, Dec. 2015

Among all the renewable energy sources, solar energy is the most abundant and likely to last for another 5 billion years! Moreover, it is well-suited for tropical countries such as India, which is blessed with a rich solar energy source and receives on an average 200 MW (megawatt) per square km of solar radiation [1]. With a total geographical area of approx. 3.3 million km square, this amounts to over 650 million MW. Although only 6.7% of the land is currently used for either housing or industry, in theory, a significantly large area can be used for solar energy harvesting [2]. As shown in

Fig. 1.1(a), the solar radiation received on the earth's surface comprises mainly visible radiation (VIS) and a part of near-infrared (IR) radiation [3]. The visible radiation provides indoor illumination and visual comfort, whereas IR radiation causes radiative heating inside the room [4].

Modern buildings have huge energy footprints. Figure 1.1(b) depicts that buildings around the globe account for nearly 40% of energy-related carbon dioxide emissions annually to maintain indoor temperature and brightness [5]. The heating and cooling systems installed in those buildings alone consume approximately half of the building's total energy needed to maintain ambient room temperature. As illustrated in Fig. 1.1(c), by selectively controlling the transmission of visible and infrared radiations, 'smart' windows could help in developing intelligent climate control systems in buildings to save energy and reduce carbon emissions. Note that in this thesis, both passive and tunable windows will be referred to as smart windows.

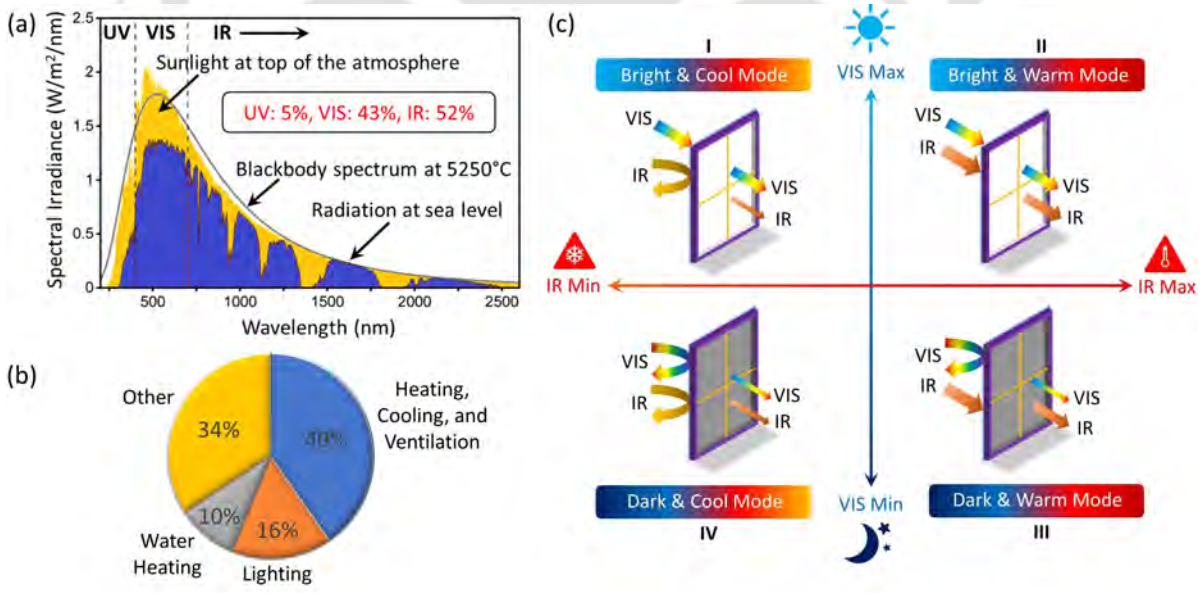

Figure 1.1: (a) Standard AM 1.5 solar irradiance spectra [3], (Data taken from National Renewable Energy Laboratory). (b) Buildings energy consumption by USA in 2008 [5]. (c) Artistic view of a smart window operating in different modes, capable of allowing or blocking the transmission of visible (VIS) or infrared (IR) radiations [6].

The present-day smart window glasses coming in double- and triple-pane glass variants, with or without low-emissivity coating, are thick, bulky, and expensive [7,8]. So, for most practical purposes, it is imperative to design a smart window using a single-pane with a low-emissivity coating, such that its figure of merit matches double- or triple-pane industry-standard commercial glasses. Creating thin and lightweight windows demands manipulating light–matter interactions at the nanoscale—enabling controlled spectral absorption, reflection, and transmission through optically engineered thin-films. In particular, spectrally selective nanophotonic thin-films based glasses have attracted substantial attention because of their potential in achieving easy scalability, improved efficiency, and low-cost design [9–11]. By selective transmission of visible and/or infrared radiation such smart glasses can find applications in windows of aircraft, windshields and sunroofs of automobiles, sunglasses, greenhouses, *etc.*, as depicted in Fig. 1.2. To give a market scenario, the electrically active transparent smart glass will be a $6.5 billion market in 2028 [12].

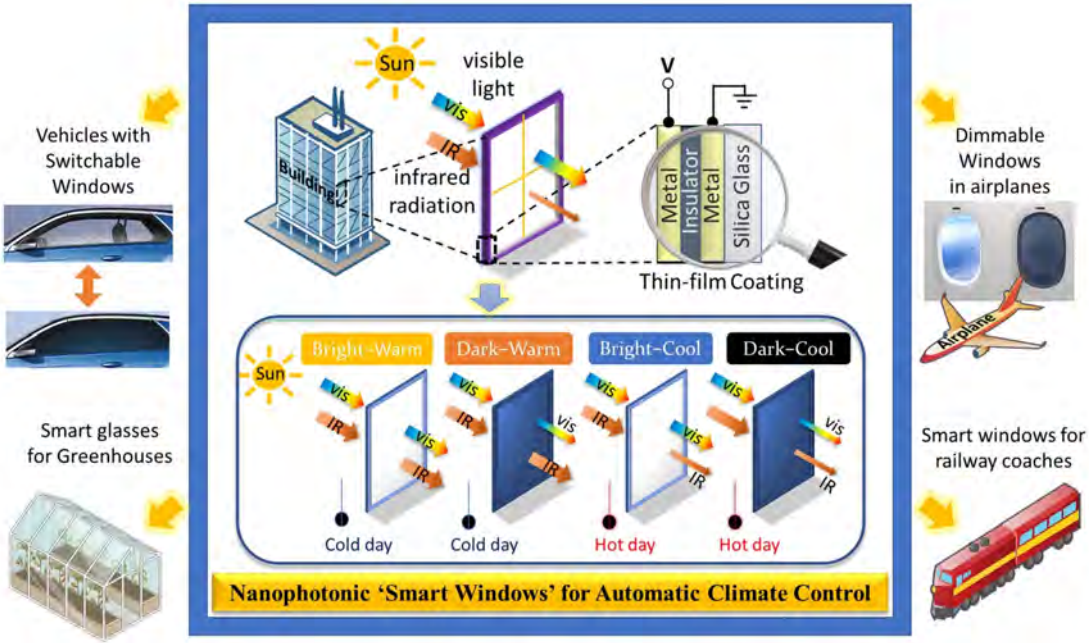

Figure 1.2: Artistic view of nanophotonic smart windows for automatic climate control: practical applications in vehicles, greenhouses, aircraft, and railway coaches.

Further, some specific applications require mounting of smart glasses on the solar cell panels to increase their absorption efficiency (by absorbing both visible and infrared radiation) or on the rooftop of cold storage buildings for radiative cooling (by reflecting both visible and infrared radiation). In this regard, solar absorbers can harness solar energy as heat and convert it into thermal energy. The absorbed energy which otherwise will be wasted, can be utilized for our day-to-day purposes like charging battery, cellphone, electric vehicles, *etc*. Another technology for waste heat management is radiative cooling. In this direction, passive radiative coolers have emerged as one of the promising alternatives to replace the conventional air conditioning systems used to cool automobiles, buildings, food depots, *etc*. [13]. Unlike traditional cooling technologies that dump the waste heat into the surroundings, passive radiative coolers cool an object on the earth by sending excessive heat directly into the extremely cold ($\sim$3 K) universe [14].

1.2 Methodology

This thesis explores different nanoscale passive and tunable designs based on multilayer, grating, cross or ring patterns, nanoparticles, and hemi-ellipsoids nanostructures. To accurately estimate the optical response of various nanostructures, analytical modeling is done using multiple theoretical methods. For the case of multilayered thin-film structures, transfer matrix method (TMM), transmission line method (TLM), and Fabry–Perot Interferometer (FPI) technique can help to find out the window characteristics accurately and quickly, eliminating the need to run computationally intensive and time-consuming numerical simulations.

The transfer matrix method calculates reflectance and transmittance by analyzing the propagation of electromagnetic waves through a multilayered structure. Here, a multilayer stack could be considered as an optical system with only one input and

output port. The optical system is assigned a transfer matrix that relates the incident and reflected waves at the input and output ports. The matrix is built by considering the multilayer stack as a cascaded system of layers and interfaces, each having its own transfer matrix. A complete transfer matrix can be obtained by multiplying the individual transfer matrices. Once the complete transfer matrix is known, by substituting the values of Fresnel reflection and transmission coefficients at different interfaces the reflectance and transmittance can be calculated.

The transmission line method is another theoretical approach to model an optical system design in the form of a circuit to determine the resonant wavelength of peak transmission or absorption. For a given multilayered structure, the input impedance is first determined at each interface, and then corresponding reflection coefficients are calculated. The accumulated round trip phase is calculated by summing up phase part of all the reflection coefficients. When the accrued round-trip phase becomes zero, maximum transmission is allowed at the resonant wavelength.

Fabry–Perot Interferometry is yet another useful technique that works on the principle of multiple-beam interference and can help us to determine the peak transmission corresponding to the resonant wavelength supported by a cavity. For instance, a metal–insulator–metal multilayer structure can be considered similar to a Fabry–Perot resonator cavity, where the two metals act as lossy mirrors which are partially transparent, and the insulator can be regarded as the cavity medium. The condition for peak transmission occurs in integral multiples of 2π.

For theoretical modeling of patterned nanostructures, effective medium theory (EMT) may be employed to describe macroscopic properties of a composite medium. The effective permittivity of a homogenized medium can be calculated using mixing formulae based on the relative fractions and permittivity of two different media. This method gives a reasonably accurate approximation and may be used to theoretically

model any patterned structure at a deep sub-wavelength scale.

To verify the theoretical findings and to obtain optical responses of systems which can not be handled analytically, computational electromagnetics can help us to solve both simple as well as complex problems. Specifically, in the case of complex patterned nanostructures, it is challenging to predict the optical response without running computationally intensive computer simulations. The finite-difference time-domain (FDTD) method and finite element method (FEM) are a couple of key methods for building the simulation model. These solvers typically solve Maxwell's equation by dividing the structure's domain into a form of a grid (or mesh). The finite element method solves partial differential equations to solve boundary value problems and gives an approximate solution. The finite difference time domain method solves the time-dependent Maxwell's equations by replacing spatial and time derivatives in the two Maxwell's curl equations by central finite difference approximation. FDTD being a time-domain solver offers several advantages over frequency domain solvers. Within the FDTD solver, the memory consumption scales only linearly with the system size. In contrast, FEM, a frequency-domain solver, the computational memory scales quadratically with system size. Therefore, the computational burden of using finer mesh is much less in the FDTD method than that of FEM. Even though the FDTD offers a faster computation than FEM, the latter produces more accurate results than the former as FEM solves the Fourier transformed Maxwell's equations. Commercially available simulation tools such as COMSOL Multiphysics®, Lumerical FDTD®, and CST Microwave Studio® will be used to carry out extensive simulations.

The selection of design parameters is usually non-trivial and requires careful choice of device dimension. Ideally, the thickness of each material needs to be minimized for reducing the overall cost and time of fabrication. In order to find the optimal thickness of each layer, a parametric sweep can be carried out, keeping all other parameters con-

stant. With the continuous advancements in state-of-the-art nanoscale fabrication facilities, the designs presented in this thesis work may be easily fabricated. RF magnetron sputtering or an e-beam evaporator may be used for thin-film deposition. Lithography could be required for grating or cross or ring structures pattering. For optical characterization, UV-VIS-NIR spectroscopy or Fourier-transform infrared spectroscopy may be used. Here, we emphasize that obtaining a smooth coating could be challenging during fabrication. Minor surface roughness may lead to some alteration in the estimated optical response of the device. Therefore, a fabrication-imperfection tolerance study may be needed to estimate the effect of variation in device dimension on the overall response of the optical system. If the variation in the spectral characteristics is marginal, one can safely assume that the proposed design is robust to fabrication imperfections.

1.3 Problem Statement Definition

1. **Design of climate-specific passive windows.** Passive windows could help in reducing global energy usage by cooling/heating and lighting systems deployed in buildings and vehicles. Therefore, it is significant to design a nanophotonic thin-film coating for passive windows. An optimal choice of materials and thicknesses of the metal and the insulator layers may provide climate-specific solutions for passive windows with desired visible and infrared transmission/blocking capability. In order to achieve the industry-standard figure of merit, designs based on noble metals as well as their relatively-inexpensive alternatives need to be analyzed.
2. **Design of all-weather electrotunable windows.** A robust and industry-standard smart windows design, tunable for all-weather conditions, has been a challenge to date. Therefore, it is crucial to investigate the design of nanophotonic electro-

tunable windows that can dynamically control the intensity of transmitted solar radiation, depending on weather conditions. A lithography-free large-area compatible design is required to provide a low-cost and fabrication-friendly solution. Further, low-power designs of electrotunable, absorption- and transmission -mode color filters can help in realizing electrochromic window glasses.

3. **Design of broadband metamaterial absorbers for solar energy harvesting.** A design of ultrabroadband absorber with near-unity absorption over the entire solar radiation regime is needed for solar energy harvesting. Also, the materials used in such an absorber should have high mechanical and thermal stability, low thermal expansion coefficient, and high melting point to withstand harsh climate conditions. As the incident radiation from the sun may fall at oblique angles and can be of any polarization, a broadband absorber design should be polarization- and angle-insensitive to a great extent.
4. **Design of solar absorbers and radiative coolers for waste heat management.** A design of spectrally-selective solar absorbers is vital in solar thermophotovoltaic and thermoelectric generator systems. However, most solar absorbers suffer from low solar-to-heat conversion efficiency and require complex nanofabrication techniques, hindering large-scale production. Hence, a nanoscale multilayer design of lithography-free and large-area compatible selective solar absorbers is essential to harness solar energy as heat and convert it into thermal energy. Further, it is crucial to investigate passive radiative coolers, which pump excess heat to cold exterior space *via* thermal radiation. However, designing a 'daytime' passive radiative cooler is challenging due to the simultaneous requirement of high reflectance in the solar spectral regime and high emissivity in the atmospheric transmittance window. Therefore, designing a passive radiative cooler is crucial for functioning under direct sunlight.

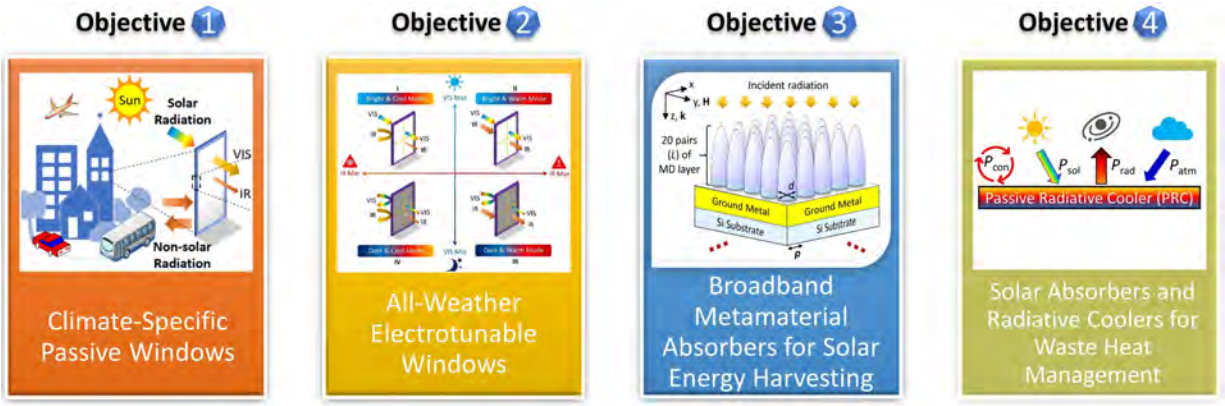

Figure 1.3: Graphical representation of problem statements.

1.4 Major Contribution of this Thesis

(i) A unique approach is adopted to design climate-specific passive windows and all-weather electrotunable windows with desired visible and infrared transmission/blocking capability.

(ii) A novel plasmonic 'meta-glass' design is proposed that could block up to ∼87% infrared radiation over 750–1800 nm spectral range while maintaining 60% average transmission in the visible regime.

(iii) An innovative approach has been adopted to design transmission-mode color filters, which could be useful for aiding photosynthesis in greenhouses. Further, low power designs of color filters have been presented for use as electrochromic windows.

(iv) A polarization- and angle-insensitive design of ultrabroadband 'perfect' metamaterial absorber is introduced. This design gives an unprecedented average absorbance of ∼99% between 300 and 4500 nm spectral range at the normal angle of incidence.

(v) A multilayer thin-films based selective solar absorber is designed that offers 87% solar-to-thermal energy conversion efficiency with a total absorbed power of 889.4

Wm^{-2} when the temperature of the solar absorber is at 100°C.

(vi) A near-perfect passive radiative cooler is designed that gives 97.3% and 97.7% average reflection over solar and atmospheric radiation region, respectively, while maintaining 80% emissivity in the atmospheric transparency window. During the daytime under direct sunlight, the net cooling power of the proposed daytime passive radiative cooler came out to be 115 Wm^{-2} with a temperature reduction up to 60 K below the ambient temperature.

(vii) A comprehensive theoretical modelling based on transfer matrix method, effective medium theory, transmission line theory, and Fabry–Perot interferometer technique is presented that can be extended to accurately predict the spectral characteristics across any system having multiple layers, for normal as well as the oblique angle of incidence.

1.5 Thesis Outline

A flow chart depicting thesis organization is shown in Fig. 1.4. The scope of this thesis work can be broadly categorized into smart window design and solar energy harvesting. The proposed smart windows are mainly based on transmission-mode spectrally-selective filter design. These window designs can be further sub-categorized into climate-specific passive windows and all-weather electrotunable windows. For passive windows, different designs based on nanorings, nanoparticles, and multilayer have been explored. The multilayer design is further sub-divided into metal–insulator–metal and insulator–metal–insulator structures. For electrotunable windows, multilayer thin-films based on metal–insulator–metal and insulator–metal–insulator structures have been studied to design all-weather 'smart' windows. The solar energy harvesting application requires absorption-mode filters. Different designs based on cross-ring, one-dimensional grating, and two-dimensional grating have

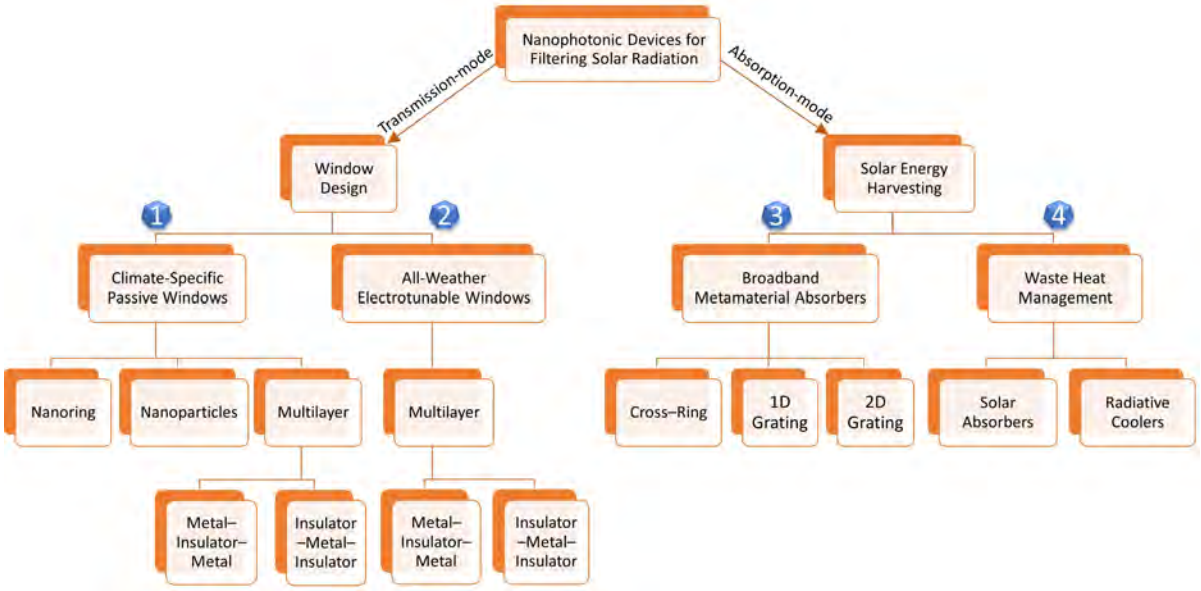

Figure 1.4: Thesis flow at a glance. Here, the numbering from 1 to 4 represent the four different problem statements proposed in this thesis work.

been proposed. Based on a multilayer structure, passive radiative coolers and solar absorbers have been proposed for waste heat management.

The thesis work has been sub-divided into eight chapters and an appendix. The thesis chapters are organized as follows:

Chapter 1 gives an overview and outline of the thesis work. This chapter includes motivation, methodology, the scope of this work, the major contribution of this thesis, and thesis organization.

Chapter 2 introduces the background of nanophotonics and metamaterials, followed by a literature review on smart windows and solar energy harvesting. Further, this chapter discusses a brief history of electromagnetic theory, Maxwell's equations, boundary conditions, relevant theoretical background and numerical techniques adopted during the research work.

Chapter 3 discusses different designs of climate-specific passive windows. First, this chapter introduces a novel plasmonic 'meta-glass' design for efficiently block-

ing infrared radiation while maintaining standard average transmission in the visible regime. After that, nanoparticles-based ultraviolet and infrared blocking meta-glasses are presented. Further, a design of metal–insulator–metal multilayer thin-films based passive glasses is shown with desired visible and infrared transmission or blocking capability optimized for different climatic conditions. This chapter concludes the discussion with a design of nanophotonic windows as specific color filters.

Chapter 4 investigates metal–insulator–metal multilayer thin-films based electrotunable windows. First, this chapter discusses the design of all-weather electrotunable windows that can dynamically control the intensity of transmitted solar radiation, depending on the weather conditions. Then low-power designs of electrotunable, absorption- and transmission-mode color filters are presented as electrochromic windows.

Chapter 5 presents insulator–metal–insulator multilayer thin-films based static and electrotunable 'smart' windows, followed by a comparative study between those. A detailed study reveals that the performance of these smart windows is unlikely to degrade during practical realization.

Chapter 6 deals with different designs of broadband metamaterial absorbers for solar energy harvesting. First, a design of plasmonics based broadband metamaterial absorber is investigated that could improve the efficiency of silicon solar cells. Next, a couple of grating based ultrabroadband metamaterial 'perfect' absorbers are presented.

Chapter 7 discusses the idea of waste heat management by designing passive radiative coolers and selective solar absorbers. Through thermal radiation, the passive radiative coolers can pump excess heat to cold exterior space. This chapter concludes by discussing selective solar absorbers that can harness solar energy as heat and convert it into thermal energy for solar thermal engineering applications.

Chapter 8 summarizes the thesis work highlighting major findings and contributions in the design of smart windows and solar energy harvesting applications. This chapter also presents potential directions for future research.

2

Literature Review and Theoretical Background

Contents

This chapter first presents a brief introduction to the emerging area of nanophotonics and metamaterials. Then it discusses the literature survey, relevant theoretical background, analytical methods, and numerical techniques needed to conduct research in the exciting domain of nanophotonics and metamaterials based smart windows and solar energy harvesters. To begin with, a literature review on smart windows and solar energy harvesting is presented. After that, a brief history of relevant electromagnetic theory is provided, followed by presenting Maxwell's equations considering a linear, homogeneous, non-magnetic, and isotropic medium. Then a discussion on the continuity equations is given that must be satisfied at boundaries between different media. Next, the propagation of plane electromagnetic waves across various media is discussed. The Lorentz–Drude model is deployed to approximate the relative permittivity of metals at optical wavelengths. Finally, various relevant theoretical methods and numerical techniques are listed which could be used to investigate optical responses from different media.

2.1 Brief Introduction to Nanophotonics and Metamaterials

Nanophotonics is that emerging multidisciplinary area of optics and engineering which could support extremely high operating speed by overcoming the challenges of typical speed limitation of semiconductor electronic circuits, besides ensuring minimal critical device dimension by breaking the conventional diffraction limit of light in dielectric photonics [15]. A comparison among semiconductor electronics, dielectric photonics, and nanophotonics is presented in Fig. 2.1. Electronic components are facing the limitation of RC delay restricting operating speed limit. Photonic components are superior to their electronic counterparts in terms of operating speed limit and operational bandwidth. However, device size poses a remarkable limitation due to diffraction limit of light for the miniaturization of large-scale photonic circuits. To

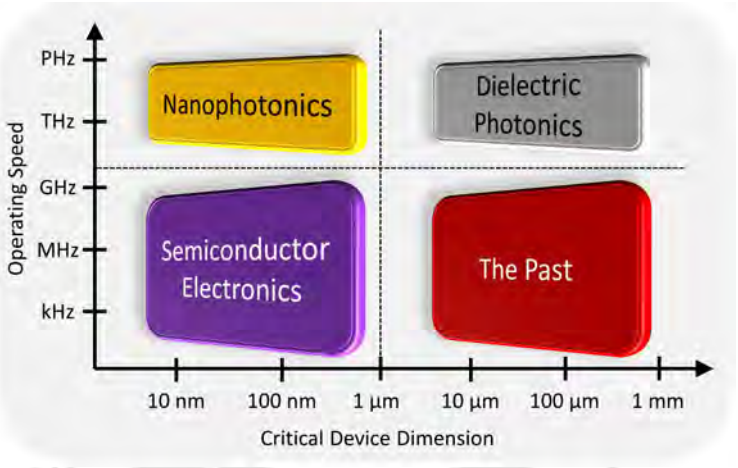

Figure 2.1: Comparison chart of semiconductor electronics, dielectric photonics, and nanophotonics with respect to operating speed limit and critical device dimension [16].

circumvent this problem, nanophotonics may be introduced.

Nanophotonics explores the light–matter interactions at the nanoscale—exhibiting new physical phenomena for developing technologies that may go well beyond what is possible with conventional photonics and electronics. Optical components such as lenses and microscopes usually cannot focus light to deep sub-wavelength scales, because of the diffraction limit. Fortunately, it is possible to confine light in nanoscale using plasmonics and metamaterials [17]. Plasmonics, a branch of nanophotonics, exploits the optical properties of metallic nanostructures to enable manipulation of light–matter interactions at the nanoscale. It deals with the interaction between electromagnetic radiation and conduction electrons at the metallo-dielectric interface [18]. Surface plasmons are coherent electromagnetic oscillations at the interface between a dielectric and a metal. These plasmons propagate along the interface until the electromagnetic energy is dissipated. Surface plasmon polaritons are electromagnetic excitations propagating at metal-air or metallo-dielectric interface. Localized surface plasmons are the non-propagating electromagnetic excitations of the conduction electrons of the metal nanostructures, as depicted in Fig. 2.2. At resonance, the absorption and scattering cross-sections of the nanostructures get enhanced by several times as compared to their

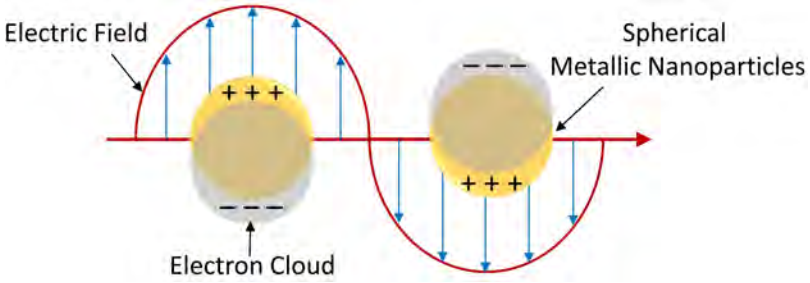

Figure 2.2: Schematic illustration of a localized surface plasmon excited in a small metallic nanoparticle [19].

geometric cross-sections. The resonance wavelength is tunable as a function of size, shape, material, and surrounding medium of the nanoparticles . This property makes these nanostructures promising candidates for many nanophotonic devices. Plasmonics has been widely proposed in fields such as tunable optical devices, nanoscale optical circuits, sensors, holography, cancer treatment, solar cells, and lasers, just to name a few [20–22].

Figure 2.3(a) shows a broad classification of materials based on intrinsic material properties. The first and second quadrants represent naturally occurring dielectrics and metals, respectively. In contrast, the third and fourth quadrants represent a special class of material called 'metamaterial'. The term metamaterial is coined from the Greek word meta, which means 'beyond' and the Latin word materia, which means 'matter' or 'material' [23]. As shown in Fig. 2.3(b), for a natural material, an atom defines its properties. On the contrary, for a metamaterial, its properties are described by an engineered unit cell or 'meta-atom' [24]. Its shape, size, and orientation can be engineered to obtain extraordinary optical properties that may not be found in nature. Recent advances in the field of metamaterials have led to the realization of absorbers, invisibility cloaking, superlenses, metasurfaces, optical switches, sensors, photodetectors, and much more [25–27]. Among them, metamaterial absorbers gained tremendous attention, particularly for thermophotovoltaics applications [28,29].

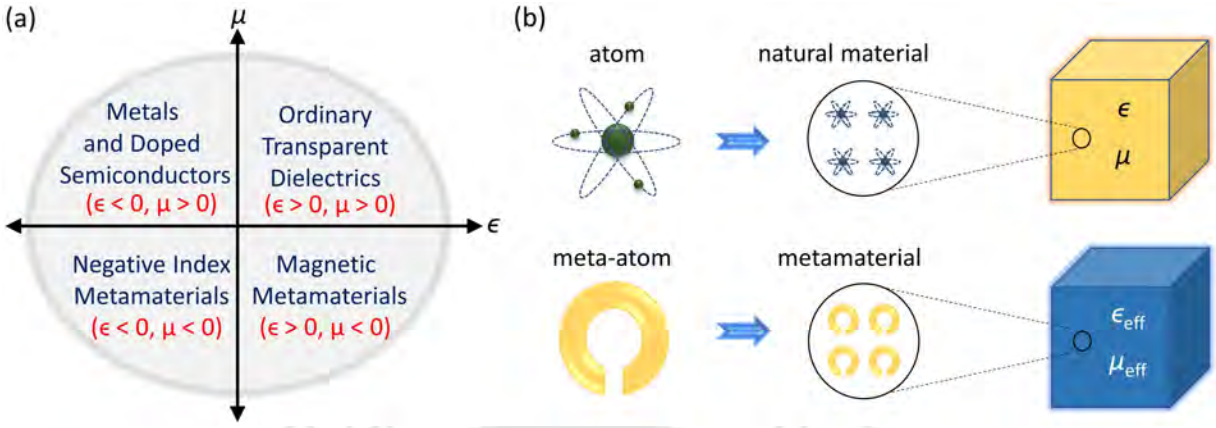

Figure 2.3: (a) Broad classification of materials based on intrinsic properties. (b) Illustrative comparison between naturally occurring materials and metamaterials. [30]

2.2 Literature Survey

Recent advancements in the field of nanophotonics and metamaterials have enabled the design and fabrication of tunable optical devices. Specifically, the design of nanophotonic windows, broadband metamaterial absorbers, spectrally-selective solar absorbers, and radiative coolers are a few areas that grabbed significant attention from engineers and scientists of multidisciplinary backgrounds due to their potential in contributing to sustainable development goals. This section reviews different techniques reported in the literature for smart window design and solar energy harvesting, followed by a summary of the research gaps identified.

2.2.1 Smart Windows

Building components such as windows, doors, ventilators, *etc.*, are considered 'less energy-efficient components' that put extra burden on the air-conditioning systems [31]. Among those components, windows emerge as the main bottleneck to check energy consumption in high-rise buildings. For example, in a double-storey house building with 30% wall coverage with windows, up to 60% of energy is lost through these windows, depending upon the geographical location and climatic condition [4].

In the United States of America (USA), air-conditioning and artificial lighting systems account for nearly 30% of the total energy demand [32]. Although traditional large-area window glazings provide visual comfort, warmth, indoor and outdoor visibility, they do not control the solar heat and light transmitted through them. Static solutions such as curtain blinds provide visual and thermal control to some extent, but they require manual interventions to adjust their position [33].

In the literature, a few passive windows with low-emissivity coatings have been demonstrated to block the solar heat and provide some energy-saving [34–36]. As shown in Fig. 2.4(a), Besteiro *et al.* theoretically showcased a design of passive window to efficiently block infrared (IR) radiation by introducing random-sized metallic nanocrystals inside a transparent glass [37]. Their passive window with silver

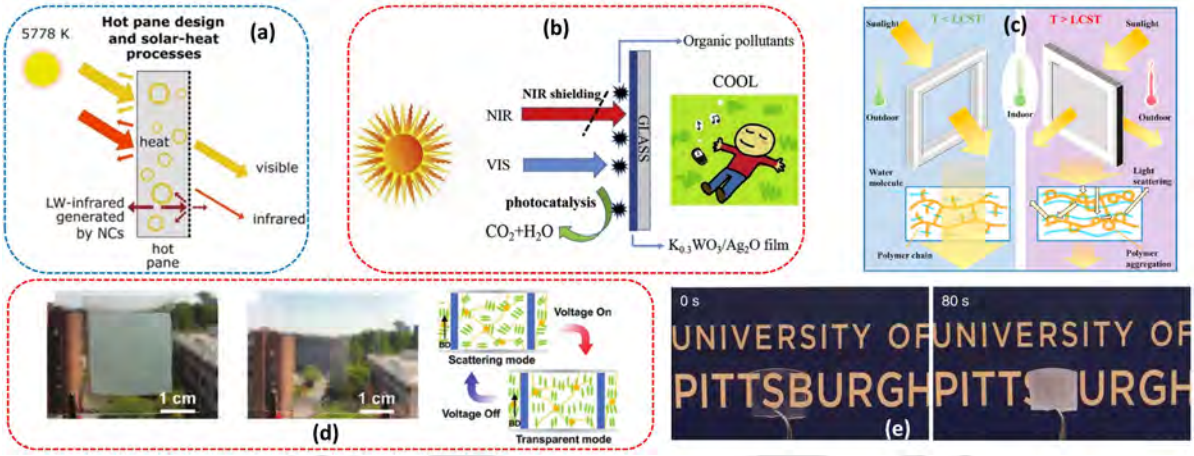

Figure 2.4: A few recently reported nanoparticles and polymer based smart windows: (a) pictorial illustration of a plasmonic nanocrystals (NCs) based metafilm in a transparent glass. Adapted with permission from: [37] Copyright © 2018 American Chemical Society. (b) Schematic view of $K_{0.3}WO_3/Ag_2O$ films based smart window. Adapted with permission from: [38] Copyright © 2019 Elsevier B.V. (c) Schematic of hydrogel particles based smart window showing transmittance modulation. Adapted with permission from: [39] Copyright © 2020 Elsevier B.V. (d) single-step dual stabilization based smart window showing light scattering state (left), transmission state (right), and corresponding schematic design. Adapted with permission from: [40] Copyright © 2019 WILEY-VCH Verlag GmbH & Co. KGaA, Weinheim. (e) Nanostructured grass-like glass showing transition between transparent (at 0 second) and haze mode (after 80 second) by putting water drops on the glass that evaporates in 80 seconds. Adapted with permission from: [41] Copyright © 2021, Optica Publishing Group.

nanoshells produced excellent IR blocking, but the complex fabrication process limits its practical value for designing a low-cost window. For designing tunable windows, various techniques such as thermochromic, photochromic, and electrochromic effects may be adopted [46–49]. Since one does not have control over the outdoor weather conditions (*e.g.* heat and light), electrochromic effect driven by applied voltage became a natural choice for designing smart windows.

Over the past decade, electrochromic smart windows based on nanocomposites [38], hydrogels [39], suspended nanoparticles [50, 51], and liquid crystals [52] have been reported, a few of them are shown in Fig. 2.4. For example, Gao *et al.* experimentally demonstrated $K_{0.3}WO_3/Ag_2O$ nanocomposite based smart window [see Fig. 2.4(b)] [38]. For the first time, their design offered thermal insulation, near-IR shielding, and visible light induced self-cleaning properties. Wei *et al.* reported temperature-responsive Ag nanorods doped poly(N-isopropyl acrylamide) hydrogel for smart windows [see Fig. 2.4(c)] [39]. Their hydrogel showed enhanced solar modulation abilities with significant temperature reduction under direct sunlight. Yoon *et al.* reported liquid crystal-based smart windows [see Fig. 2.4(d)] [40]. They practically demonstrated fast switching at low voltage with good mechanical stability. Haghanifar *et al.* fabricated silica nanograss glass with ultrahigh-transmittance and ultrahigh-haze, both over 95% at 550 nm wavelength [see Fig. 2.4(e)] [41].

In industry, electrochromic, thermochromic, and photochromic smart windows have been developed (see Table 2.1) but voltage controlled electrochromic windows gained popularity due to superior control over outdoor climate conditions (*e.g.* heat and light) [12]. Recently, Sikdar *et al.* reported voltage-controlled self-assembly/disassembly of functionalized metallic nanoparticles at liquid-liquid [42] and liquid-solid electrochemical interfaces [43–45] and realized voltage controlled mirror/window and mirror/absorber functionalities, respectively (see Table 2.1). They have demonstrated both

Table 2.1: Classification of smart glass technologies [12].

Technology	Activation	Principle	Material involved	Companies involved
Electrochromic	Voltage	Reversible change of optical transmittance in response to electrochemical charging and discharging.	1st gen: oxides (e.g. tungsten nickel oxide)	SAGE Electrochromics, Inc. / View Glass, Inc.
			2nd gen: hydrides (Mg)	View Glass, Inc. (Licensed from Lawrence Berkeley National Laboratory)
			3rd gen: amorphous metal oxides (nanocrystals in glass)	Heliotrope Technologies, Inc.
Thermochromic	Temperature	Color change due to change in temperature.	Vanadium Oxide	
			Ligand exchange transition metals	Pleotint, LLC
Photochromic	Light	Reversible change of color upon exposure to light e.g. self-tinting sunglasses.	Organic: azobencene Inorganic: silver chloride	Corning, Inc.
Thermotropic	Temperature	Visible light transmittance change in response to temperature.	Liquid Crystals	NA
Electrostatic Oriented Materials	Voltage	Materials that change their orientation in an electric field to vary transmittance.	Liquid Crystals	Glassnovations (1st gen) Scienstry (3rd gen)
			Suspended particle devices	Research frontiers Inc. and its licenses.
Electrochemical Plasmonics	Voltage	Voltage-controlled self-assembly/disassembly of functionalized nanoparticles at liquid-liquid or liquid-solid electrochemical interfaces.	Gold and silver nanoparticles, metallic/ITO electrodes	NA

theoretically and experimentally that the optical properties of these electrochemical systems can be tuned *in situ* with application of very low potential, only $\pm$ 0.5 V. However, use of liquids in their systems makes those challenging to be deployed in real-world applications.

Here we emphasize that most of these glasses are designed to block infrared radiation, which is suited only for warm climate conditions [53]. However, a typical 'smart' window is expected to control solar heat depending on the climate condition [54]. For example, low solar heat is desirable for a relatively hot climate to maintain ambient room temperature. Whereas, for cold climate conditions, a relatively high solar heating is desirable. Therefore, *a smart window that can regulate solar heat alongside visible*

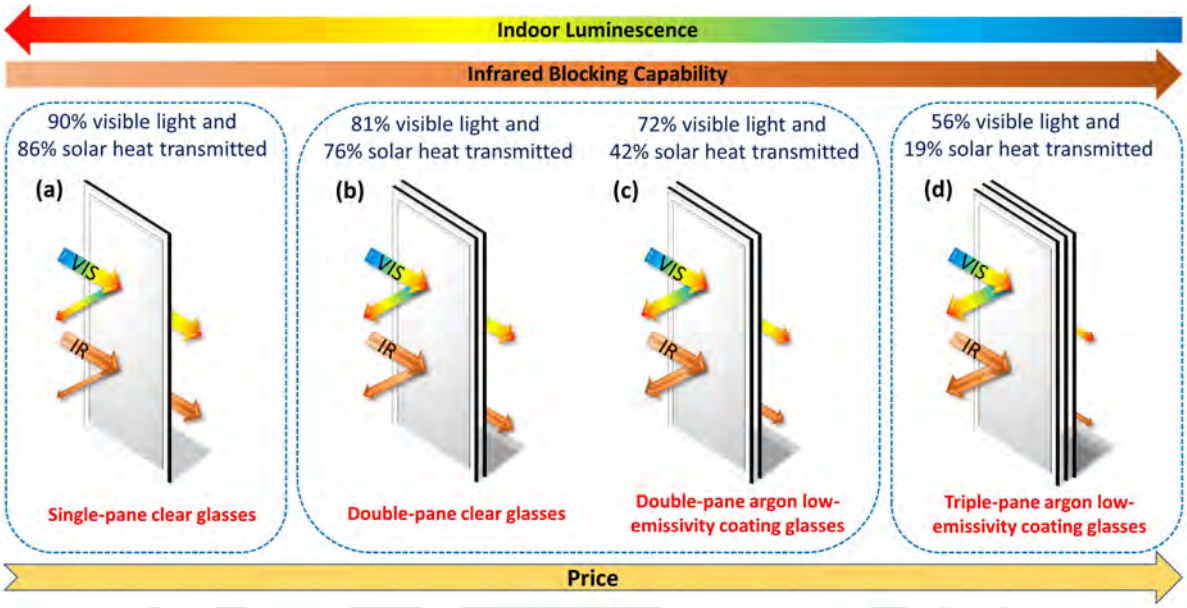

Figure 2.5: Present day commercial smart window variants: (a) single-pane clear glass, (b) double-pane clear glass, (c) double-pane argon low-emissivity coating glass, and (d) triple-pane argon low-emissivity coating glass. [7, 8].

transmission could be a better value proposition that may find application over a wider geographical location.

The present-day smart windows are coming in single-, double-, and triple-pane glass variants, with or without low-emissivity coating, with empty spaces in between filled with inert argon gas, as shown in Fig. 2.5 [7, 8]. Among them, the single-pane glasses are considered the most suitable among those for designing thin and lightweight windows. Unfortunately, most of the single-pane glasses show poor IR blocking capability. For double- and triple-pane glasses, the outer glass that blocks long wavelength infrared (LWIR) radiations is called "hot pane". Similarly, the inner glass that controls the visible and near-IR radiations is called "cold pane". Even though the double- and triple-pane glasses are quite capable of blocking IR radiation, the multi-pane glass assembly significantly increases the overall cost and make the windows thick and bulky. Specifically, triple-pane glass suffers from low visible transmittance, making the outside-view tinted and unnatural for building occupants [7].

Moreover, integrating double- and triple-pane glasses into passenger vehicles is generally impractical from the design aesthetic point of view.

Therefore, for most practical purposes, *it is imperative to design a smart window using a single-pane* with a low-emissivity coating, which can still match the IR blocking capability of double- or triple-pane commercial glasses. To achieve such goals, electrochromic window glasses are considered the best-suited candidate.

2.2.1.1 Applications of Electrochromic Smart Glasses

Electrochromic smart glasses are remarkably convenient to use, environmentally friendly, and can dramatically reduce the need for air-conditioning. They can cut peak energy use for cooling and lighting by around 20% [55]. Since they are electrically operated, they can easily be controlled by a smart-home system or a sunlight sensor, or depending on whether there are people inside the building or not. They could provide improved security and privacy at the flick of a switch. However, they are expensive to install than ordinary glasses. For instance, a single large-area smart window typically comes in at around $500–1000 [55]. Another concern is the durability of the materials as compared to current commercial windows.

2.2.2 Solar Energy Harvesting from Smart Windows

Solar energy harvesting requires absorption over the entire solar spectral range *i.e.* 300–2500 nm wavelengths. In this regard, broadband metamaterial absorbers with polarization-independent and angle-insensitive designs are usually preferred. The previous section discussed that the smart windows are designed to operate mainly in transmission filter mode. However, some specific applications require mounting smart glasses on the rooftop of buildings for facilitating radiative cooling (by reflecting both visible and infrared radiation) or on top of solar cell panels to increase their absorption efficiency (by absorbing both visible and infrared radiation). In this regard, selective solar absorber and passive radiative coolers could be used for waste solar

heat management.

2.2.2.1 Broadband Metamaterial Absorbers

Generally, lossy materials are ill-suited for most of the practical applications as they make the system inefficient. However, for the case of metamaterial absorbers, these lossy materials become useful and can significantly enhance their efficiency of absorption [21]. Over the last decade, a large scientific community is working in the field of metamaterial absorbers, as shown in Fig. 2.6. Landy *et al.* first showcased a metamaterial perfect absorber in the microwave regime utilizing a 2D metamaterial electric ring resonator [56]. Subsequently, many researchers explored different materials and structural designs to make a perfect absorber, working in the spectral window ranging from microwave to visible [22, 57–59].

Solar energy harvesting applications demand broadband absorbers with polarization-

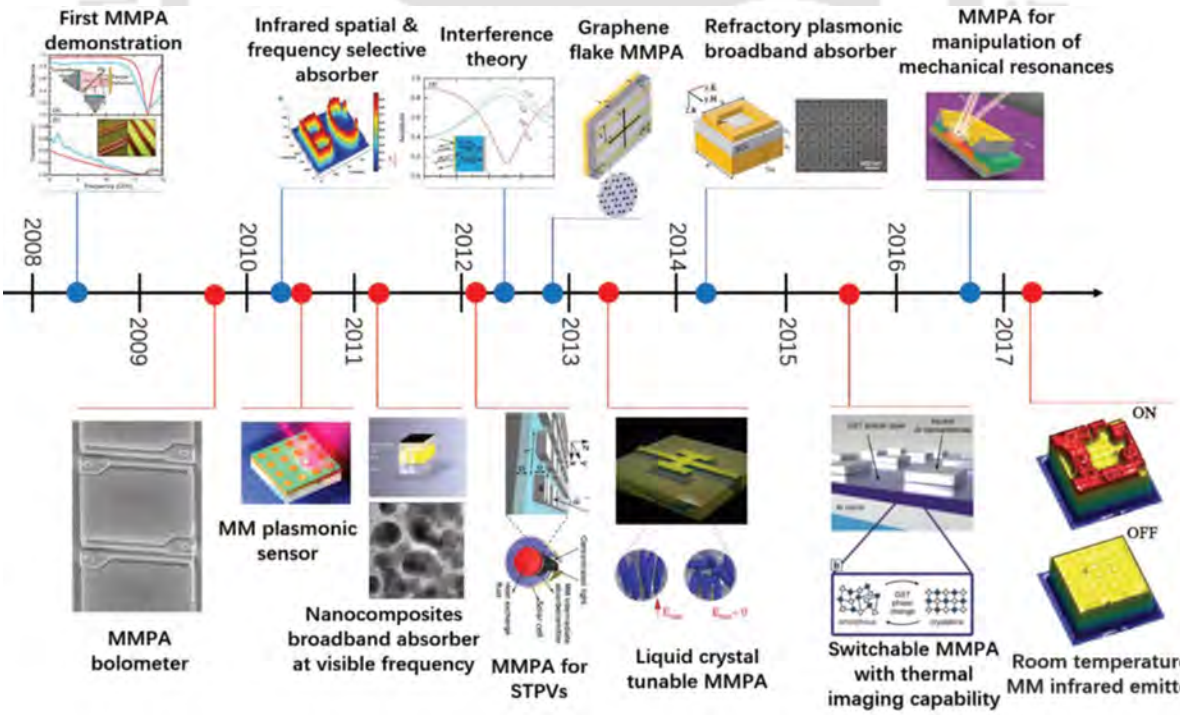

Figure 2.6: A decade history of metamaterial perfect absorbers. Here, MM: **M**eta**m**aterial, MMPA: **M**eta**m**aterial **p**erfect **a**bsorber, and STPV: **S**olar-**t**hermo **p**hoto**v**oltaics. Adapted with permission from: [25] Copyright © 2018 WILEY-VCH Verlag GmbH & Co. KGaA, Weinheim.

independent and angle-insensitive design [60]. The materials used in such an absorber should have high thermal and mechanical stability, low thermal expansion coefficient, and high melting point to withstand harsh climate conditions [61]. For this purpose, metallo-dielectric (MD) multilayered structure is usually preferred [25]. Although, metallic nanoparticles based design can also be used to achieve perfect absorption of the incident light in a thickness of hundreds of nanometers [62], unfortunately, achieving broadband absorption, especially in the visible and near-infrared regime largely remains a challenge. This is because of the intrinsically narrow bandwidth of localized surface plasmon resonances (LSPRs) or surface plasmons polaritons (SPPs) at the sub-wavelength scale, leading to narrowband absorption [63].

Figure 2.7 depicts some of the recently reported broadband absorbers over the solar regime for energy harvesting applications. For example, Liu *et al.* proposed thin-film based solar absorbers and thermal emitters with sub-wavelength size scale [see Fig. 2.7(a)] [64]. They could theoretically achieve ∼91% average absorption over 280–4000 nm wavelengths. Hoa *et al.* numerically presented broadband metamaterial absorbers based on a periodic array of metallo-dielectric multilayered conical frustums [see Fig. 2.7(b)] [65]. Their design exhibits more than 90% absorptivity over 480–1480 nm spectral range. Soydan *et al.* theoretically demonstrated transition metal carbides and nitrides based perfect light absorbers [see Fig. 2.7(c)] [66]. They could achieve 90% average absorption over the entire solar radiation regime *i.e.* 300–2500 nm wavelength range. Aalizadeh *et al.* proposed a metal–dielectric–metal based ultra-broadband absorber with an ultra-thin (5 nm) layer of Manganese (Mn) metal embedded into the dielectric layer [see Fig. 2.7(d)] [67]. They could numerically achieve 90% absorption over 480–3280 nm spectral window. Lin *et al.* theoretically designed and experimentally demonstrated graphene–SiO_2 multilayered based broadband perfect absorber [see Fig. 2.7(e)] [68]. They could achieve 85% absorption over the solar spec-

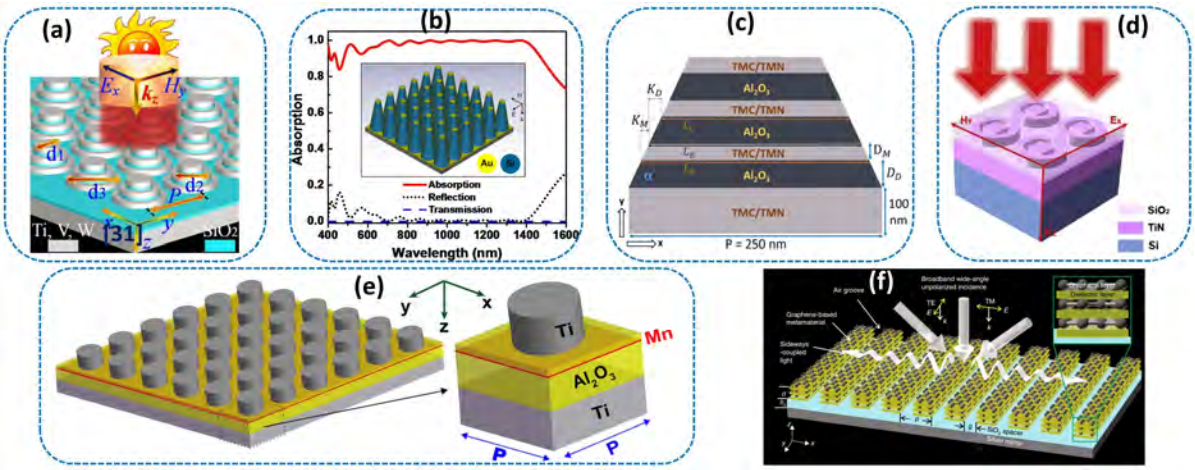

Figure 2.7: A few recently reported broadband absorbers: (a) thin-film refractory metal based solar absorbers and thermal emitters. Adapted with permission from: [64] © 2018 Elsevier B.V. (b) Spectral response for metallo-dielectric multilayered conical frustums shaped broadband absorber (tilted top view). Adapted with permission from: [65] Copyright © 2019, IEEE. (c) Trapezoidal metallo-dielectric pair based perfect light absorbers using metal carbides and nitrides. Adapted with permission from: [66] Copyright © 2019, Springer Science Business Media, LLC, part of Springer Nature. (d) Nanodisk array based metal–dielectric–metal ultrabroadband absorber. Adapted with permission from: [67] Copyright © 2019 Published by Elsevier B.V. (e) three-dimensional schematic view of graphene-based broadband metamaterial absorber. Adapted with permission from: [68] Copyright © 2019, Springer Science Business Media, LLC, part of Springer Nature. (f) Geometry of titanium nitride based broadband absorber (tilted top view). Adapted with permission from: [69] Copyright © 2019, The Author(s), under exclusive licence to Springer Nature Limited.

tral regime. Gao *et al.* numerically proposed insulator–metal–insulator–metal broadband plasmonic absorber [see Fig. 2.7(f)] [69]. They have shown 90% absorption over 200–1200 nm wavelength range.

Here, we highlight that most of the reported works based on different designs are either narrowband [70–75] or polarization-dependent [76] or angle-sensitive [77–81]. Hence, investigating different designs of *an ultra-broadband, polarization-independent, and angle-insensitive absorber* in the visible, near-IR, and short-wave IR spectral regime remains largely in demand [82–85].

2.2.2.2 Solar Absorbers

Solar-thermal energy systems are helpful in clean electricity production using solar thermoelectric generators [86], solar thermophotovoltaics [87], and concentrated solar power *via* Rankine cycle [88]. Unfortunately, their performance suffers from high thermal losses due to spontaneous blackbody radiation at high temperatures [89]. Therefore, designing a thermally-stable spectrally selective solar absorber with high solar-to-heat conversion energy efficiency is significant to prevent losses due to thermal radiation [90].

As shown in Fig. 2.8, an ideal selective solar absorber should have unity absorption in solar radiation regime *i.e.* 0.3 – 2.5 μm wavelength range and zero emissivity in mid-infrared (IR) regime *i.e.* 4 – 13 μm spectral range where blackbody radiation occurs [91]. In addition, high-temperature thermal stability is desirable for maintaining high solar-to-heat conversion efficiency at low temperatures (below 100°C) for photothermal conversion and moderately-high temperatures (between 100 and 400°C) for industrial applications [92–94]. Furthermore, solar absorbers need to be polarization-independent and angle-insensitive, since the incident solar radiation can be of arbitrary polarization and fall at arbitrary oblique angles [95].

In nature, typical examples of selective solar absorbers are pyromark, black chrome, cermet, and black carbon paint [96–98]. However, their practical usage for solar thermal applications is restricted due to high emissivity in the mid-IR wavelength range and limited tunability of their spectral selectivity. Inspired by nature, metamaterial selective solar absorbers grabbed attention owing to their highly selective absorption at particular wavelengths [99]. In literature, metamaterial solar absorbers based on photonic crystals [100], nanoparticles embedded dielectrics [101], 1D or 2D surface gratings [102], and nano-disk arrays [103] have been reported. Recently, selective solar absorbers based on multilayer thin film gained popularity due to large-area compatible

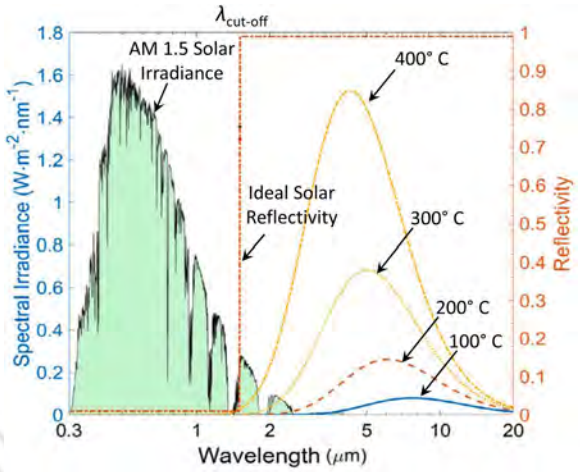

Figure 2.8: Solar spectral irradiance (AM 1.5 global tilt, spectral irradiance magnitude given on the left y-axis), radiative heat flux of blackbody thermal radiation at different temperatures (spectral irradiance magnitude given on the left y-axis), and reflectivity spectrum of ideal selective solar absorber (reflectivity given on the right y-axis). Note that $\lambda_{cut-off}$ is the optimal cut-off wavelength of an ideal selective solar absorber which should have zero reflectivity below $\lambda_{cut-off}$ to increase solar radiation absorption and unity reflectivity beyond the $\lambda_{cut-off}$ to reduce thermal emission. Adapted with permission from: [91] © 2020 Elsevier Ltd.

design and lithography-free fabrication process [91, 94, 104].

A design of multilayer selective solar absorber comprises anti-reflective coatings to enhance the visible light absorption, alternating metal or dielectric absorbing layers, and a reflective ground metal [89]. Khoza *et al.* demonstrated a ZrO_x–Zr–ZrO_x–Al_xO_y multilayer selective solar absorber [105]. They achieved solar absorption of 0.93 and thermal emissivity of 0.11 at 100°C. Dereshgi *et al.* experimentally reported Al_2O_3–Ti–Al_2O_3–W multilayer design with solar absorption of 0.90 over 0.4–1.64 μm wavelength range [106]. Tian *et al.* simulated and fabricated SiO_2–Al_2O_3–W–Al_2O_3–W multilayer selective solar absorber [91]. They achieved solar absorption of 0.87 and thermal emissivity of 0.07 at ambient room temperature. In spite of significant research in this direction, it is still challenging to design *angle- and polarization-independent selective solar absorbers with high absorption in the solar radiation regime but low emission in the mid-IR region*. Moreover, most solar absorbers suffer from low solar-to-heat conversion efficiency at moderately-high temperatures (between 100°C and 400°C). Therefore, spec-

trally selective, lithography-free solar absorbers with high thermal stability are crucial to application in solar thermal engineering.

2.2.2.3 Radiative Cooling

A particular portion of extraterrestrial radiation reaches the surface of the earth. The atmospheric absorption prevents specific types of electromagnetic radiation to pass through it. An atmospheric window can be considered like a curtain with holes in it where holes represent the spectral bands which can pass through it. As shown in Fig. 2.9, the upper portion of the atmosphere blocks 100% of the gamma rays, X-rays and most of the UV radiations [107]. However, visible and near infrared radiations can freely pass through the atmosphere.

As shown in Fig. 2.10(a), blackbody radiation's peak wavelength coincides with the atmospheric transmittance window *i.e.* 8–13 μm wavelength range, at room temperature [108]. Therefore, objects having high emissivity in the atmospheric window can dissipate heat into outer space without hindrance, as depicted in Fig. 2.10(b). Since,

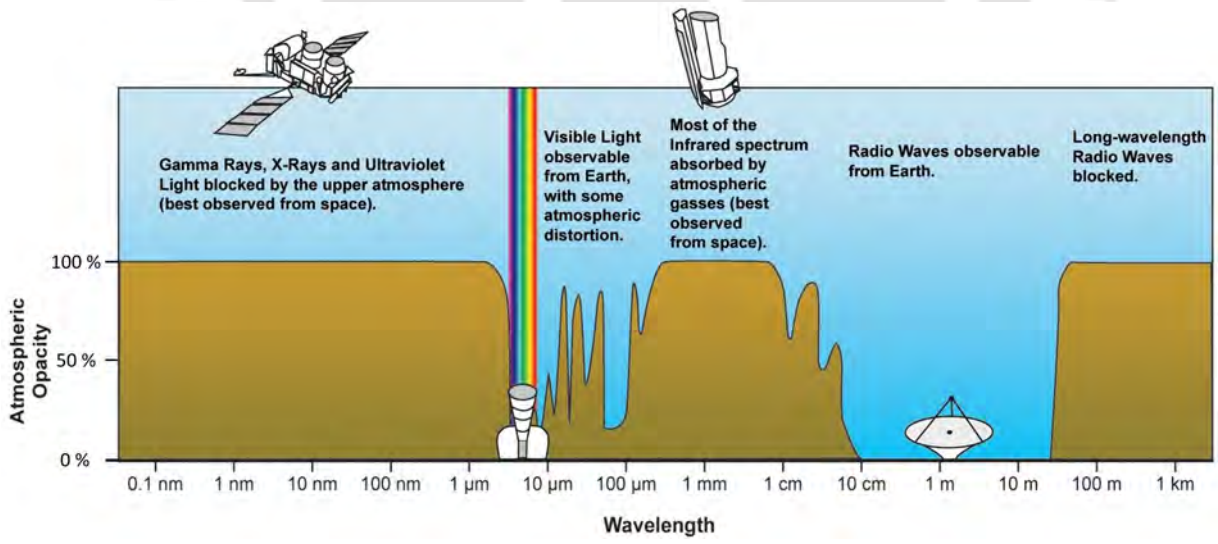

Figure 2.9: Atmospheric electromagnetic opacity: the upper portion of the atmosphere blocks gamma rays, X-rays, and UV radiation but allow visible and near infrared radiations to freely pass through the atmosphere. Note that the atmospheric transmittance window for radiative cooling purpose lies between 8 and 13 μm. Adapted from [107].

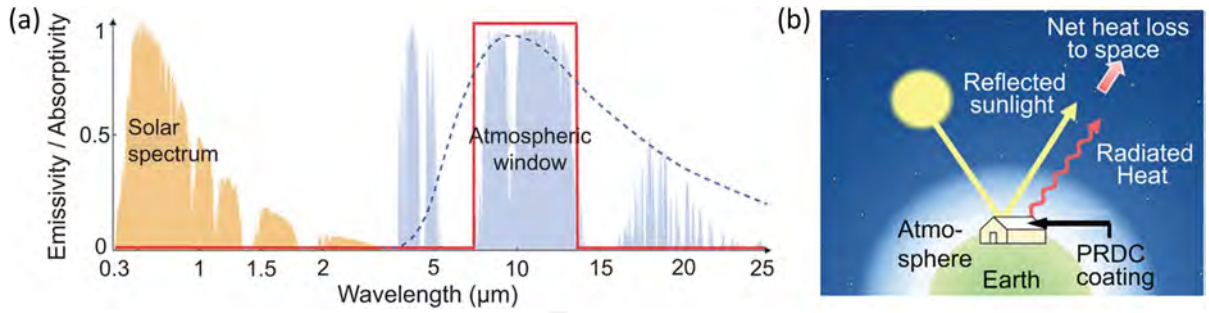

Figure 2.10: Concept of radiative cooling: (a) Night time (dashed blue line) and day time (solid red line) radiative cooling. (b) Pictorial demonstration of radiative cooling. Adapted with permission from: [113] Copyright © 2020, The Materials Research Society.

the radiations can freely pass in this spectral range, it leads to automatic radiative cooling by emitting back to outer space after absorption. The concept of radiative cooling can be utilised for various applications such as optical solar reflector, IR camouflage, energy-free all-day cooling, *etc*.

Earlier studies on radiative cooling were limited to nighttime passive radiative cooler due to the absence of solar radiation during the night [108–110]. The spectral properties of nighttime passive radiative coolers require maintaining high emissivity either at all wavelengths or only in the atmospheric transmittance window, as shown by dashed blue line in Fig. 2.10(a) [13]. However, for all-day cooling, the daytime passive radiative coolers became a more practical choice and remained in demand [111]. A daytime passive radiative cooler must have unity emissivity in the atmospheric transmittance window and unity reflectance over solar spectral regime (0.3–2.5 μm) simultaneously, as depicted using solid red line in Fig. 2.10(a) [112].

In nature, saharan silver ants in the sahara desert are a typical biological example of daytime passive radiative cooler [114]. They possess a dense array of triangular-shaped hairs that enhances solar reflectance and infrared emission in the atmospheric window. This unique feature allows silver ants to keep themselves cool to survive extreme temperatures in the desert.

In literature, daytime passive radiative coolers based on metamaterials [115], pho-

tonic crystals [116], doped polymers [110, 117], and multilayer films [118, 119] have been extensively studied. The first experimental demonstration of multilayered daytime passive radiative cooler was given by Raman *et al.* in 2014 [118]. In winter daytime, under direct sunlight, they achieved a cooling of 4.9°C lower than the ambient temperature. In 2015, Gentle and Smith first introduced and practically demonstrated sub-ambient daytime cooling of an open surface without using convection suppression [120]. It was found to be 11°C cooler than the commercial cool roof nearby. After that, different researchers used different structures and methods to design a passive radiative cooler [121]. For instance, Bao *et al.* designed a double-layered nanoparticle-based structure that gives a theoretical cooling of 5°C below the ambient temperature under direct sunlight [122]. Fu *et al.* used a porous anodic aluminum oxide membrane on an aluminum substrate to design a daytime passive radiative cooler [123]. Their group achieved a sub-ambient cooling temperature of 2.6°C during daytime by virtue of porous morphology that causes partial selective radiation. Hossain *et al.* showcased a unique conical-shaped structure, utilizing alternating layers of aluminum and germanium followed by aluminum as a reflective layer [115]. They achieved cooling of 12.2°C under ambient temperature without considering non-radiative heat exchange.

Here we emphasize that most of the studies reported on passive radiative coolers have mainly focused on achieving high emissivity in the atmospheric transmittance window [34, 115, 124, 125]. However, it is still *challenging to achieve high reflectance in the solar spectral regime (0.3–2.5 μm) and atmospheric radiation region (2.5–8 μm), besides and high emissivity in the atmospheric transmittance window (8–13 μm), simultaneously* [126].

2.2.3 Research Gaps Identified

The previous subsections presented a detailed literature review, dispensing the current state-of-the-art in the field of nanophotonics and metamaterials for smart window design and solar energy harvesting. This section summarizes the research gaps identi-

fied in the literature.

For smart window applications, firstly, almost all the reported works focus on designing window glasses for specific weather conditions, thereby confining their usage to a specific geographical area. In contrast, a smart window that can regulate solar heat alongside visible transmission could be a better value proposition for application over a wider geographical location. Secondly, most of the designs reported to date are either very expensive or have complex fabrication processes or do not match the figure-of-merit of commercial glasses used in the industry. Therefore, choosing cheaper materials for lithography-free and large-area compatible window designs could reduce the effective cost. In addition, smart tunable windows based on electro-optic materials are yet to be explored.

For solar energy harvesting applications different designs of broadband metamaterial absorbers, selective solar absorbers, and radiative coolers have been discussed. However, most of the reported works on metamaterial absorbers are either narrowband or polarization-dependent or angle-sensitive. Moreover, achieving broadband absorption, especially in the visible and near-infrared regimes, is challenging. Hence, designing an ultra-broadband, polarization-independent, and angle-insensitive absorber in the visible, near-IR, and short-wave IR spectral regimes remains in demand. Concerning spectrally-selective solar absorbers, it is still challenging to design angle- and polarization-independent selective solar absorbers with high absorption in the solar radiation regime but low emission in the mid-IR region (4–13 μm). Moreover, most solar absorbers suffer from low solar-to-heat conversion efficiency at moderately-high temperatures (between 100°C and 400°C). Therefore, spectrally selective, lithography-free solar absorbers with high thermal stability are strongly desired for application in solar thermal engineering. For radiative cooling, most of the studies reported on passive radiative coolers have mainly focused on achieving high emissivity in the atmo-

spheric transmittance window (8–13 μm). However, for operation during the daytime, it is strenuous to design radiative coolers having high reflectance in the solar spectral regime (0.3–2.5 μm) and atmospheric radiation region (2.5–8 μm), besides high emissivity in the atmospheric transmittance window, simultaneously.

Further, it was identified that there is no existing comprehensive theoretical framework for modeling of nanophotonic thin-film optical systems that can accurately predict the optical response of windows and absorbers. The next section of this chapter presents a brief summary of relevant theoretical techniques based on transfer matrix method, transmission line method, Fabry–Perot interferometer, and effective medium theory to calculate the optical responses of different nanophotonic devices. The developed theory could find out the characteristics of optical systems accurately and quickly, eliminating the need to run computationally intensive and time-consuming based numerical simulations.

2.3 Relevant Theoretical Background

Electromagnetic phenomena have excited researchers and scientists for centuries. The contributions of Maxwell, Faraday, Coulomb, and Ampere in the field of electromagnetic theory helped the scientific community to get a deeper insight into the fundamentals of electromagnetic phenomena. The most crucial scientific breakthrough can be attributed to establishing the relation between electric and magnetic fields in the 19th century [127]. Further confinement of these relationships into physical laws by Faraday, Ampere, and Gauss paved the way for James Clerk Maxwell's seminal paper, presented in 1865, which is now well known as the Maxwell's equations of electromagnetics [128]. It is incredible to know that even today, after 150 years, Maxwell's equations are valid in the classical domain, relevant to the field of nanophotonics and metamaterials!

2.3.1 Maxwell's Equations

The institution of Maxwell's equations still remains one of the paramount achievements in the field of modern physics. The set of four Maxwell's equations is self-sufficient to define the dynamics of the electric and magnetic fields in media, either due to the presence of sources (such as charges or currents) or due to incident fields elsewhere. These equations have been extensively explored to study the light–matter interactions over a whole range of electromagnetic spectrum. However, Maxwell's equations are valid in the classical domain and cannot accurately predict quantum phenomena. The Maxwell's equations determining the relationship between the electric, **E**, magnetic, **H**, electric displacement, **D**, and the magnetic induction, **B**, fields, and are given by:

$$\nabla \cdot \mathbf{D} = \rho \tag{2.1a}$$

$$\nabla \cdot \mathbf{B} = 0 \tag{2.1b}$$

$$\nabla \times \mathbf{E} = -\frac{\partial \mathbf{B}}{\partial t} \tag{2.1c}$$

$$\nabla \times \mathbf{H} = \frac{\partial \mathbf{D}}{\partial t} + \mathbf{J} \tag{2.1d}$$

where ρ is the free electric charge density and **J** is the electric current density. These four equations are sufficient to describe electric and magnetic fields in all space and time. However, while considering the macroscopic media where every atom acts as a source, it is impractical to solve the microscopic Maxwell's equations. More often than not, we are much more interested in examining the response of a collective media rather than the response from an individual atom. For the case of microscopic media, **E** and **H** are now representing the averaged fields. The **D** and **B** fields are derived from the relation given by:

$$\mathbf{D} = \epsilon_0 \mathbf{E} + \mathbf{P} \tag{2.2a}$$

$$\mathbf{B} = \mu_0 \mathbf{H} \tag{2.2b}$$

where **P** being the polarization response of the medium, ϵ_0 and μ_0 is the permittivity and permeability of free space, respectively. Since for the case of vacuum there is no polarization response, the above equation becomes $\mathbf{D} = \epsilon_0 \mathbf{E}$ and $\mathbf{B} = \mu_0 \mathbf{H}$. We would like to emphasize that we are considering linear, isotropic, and non-magnetic media for which the polarization is given by:

$$\mathbf{P} = \epsilon_0 \chi_e \mathbf{E} \tag{2.3}$$

where χ_e is the electric susceptibility of the medium. The above equations can be used to rewrite Maxwell's equation to derive the wave equation given by:

$$\nabla^2 \mathbf{E} = \mu_0 \epsilon_0 \epsilon_r \frac{\partial^2 \mathbf{E}}{\partial t^2} \tag{2.4a}$$

$$\nabla^2 \mathbf{H} = \mu_0 \epsilon_0 \epsilon_r \frac{\partial^2 \mathbf{H}}{\partial t^2} \tag{2.4b}$$

One of these wave equations can be used to solve for either the electric or magnetic field for a particular region, and the other can be obtained by utilizing Maxwell's equation. While using frequency domain solvers, we assume the time dependence to be harmonic, such that $\partial/\partial t \rightarrow -i\omega$. In that case, the wave-equation becomes the well-known Helmholtz equation. On the contrary, the time domain solvers use Maxwell's curl equations.

2.3.2 Boundary Conditions

In most practical situations, often one has to solve equations for electromagnetic wave propagation across different media. However, to establish a relation between wave equations in two different media, one needs to solve for boundary conditions at the interface. The Stokes and divergence theorems can be used to find out these boundary conditions using Maxwell's equations, as given below:

$$(\mathbf{D_2} - \mathbf{D_1}) \cdot \mathbf{n} = \rho_s \tag{2.5a}$$

$$(\mathbf{B_2} - \mathbf{B_1}) \cdot \mathbf{n} = 0 \tag{2.5b}$$

$$(\mathbf{E_2} - \mathbf{E_1}) \times \mathbf{n} = 0 \tag{2.5c}$$

$$(\mathbf{H_2} - \mathbf{H_1}) \times \mathbf{n} = \mathbf{J_s} \tag{2.5d}$$

where ρ_s and $\mathbf{J}_s$ are the surface charge density and the surface current density, respectively, at the interface between the two media (1 and 2) and $\mathbf{n}$ being the surface normal [129]. It is important to note that surface charges and currents are absent as the charge carriers' positions are fixed within dielectric media.

2.3.3 Metals and Dispersive Media

The Lorentz oscillator model considers atoms inside metal to be composed of nucleus and electron where the mass of the electron is very small compared to the nucleus. So, one can assume the system to be a harmonic oscillator with the nucleus having infinite mass being fixed and an electron being attached to the nucleus *via* a spring. The equation of motion is given by:

$$m\frac{d^2\mathbf{x}(t)}{dt^2} + \gamma m\frac{d\mathbf{x}(t)}{dt} + K\mathbf{x}(t) = -e\mathbf{E}(t) \tag{2.6}$$

where the second term represents the resultant damping force, the third term rep-

resents the restoring force, and the fourth term represents the driving forces. Also the polarization **P** as a function of Electric field **E** is represented by:

$$\mathbf{P}(\omega) = \frac{ne^2}{m} \frac{\mathbf{E}(\omega)}{\frac{K}{m} - i\gamma\omega - \omega^2} = \epsilon_0 \chi_e \mathbf{E}(\omega) \tag{2.7}$$

Now, one can assume the electrons in the metals are free (unbounded) *i.e.* there is no restoring force, $K = 0$. This is called the Drude model for metals, and the Drude permittivity can be extracted from the expression shown below:

$$\epsilon_{\text{Drude}} = 1 - \frac{\omega_{\text{p}}^2}{\omega^2 + i\omega\gamma} \tag{2.8}$$

where the plasma frequency is given by $\omega_{\text{p}} = \sqrt{ne^2/m\epsilon_0}$. The Drude model still gives an accurate electromagnetic response of metals despite neglecting both the electron–electron and electro–ion interactions. The modified form of Drude model is given by:

$$\epsilon_{\text{Drude}} = \epsilon_\infty - \frac{\omega_{\text{p}}^2}{\omega^2 + i\omega\gamma} \tag{2.9}$$

where ω_{p}, ϵ_∞ and γ represent the plasma frequency, high-frequency dielectric constant, and collision frequency, respectively. One can use these parameters to fit the experimental data of novel plasmonic metals such as gold and silver, as shown in Fig. 2.11. However, the interband transitions limit the validity of the Drude model at visible and higher frequencies [18]. For the case of dielectrics, their permittivity can be derived from the Sellmeier equation, which gives an empirical relationship between refractive index and wavelength for a particular medium.

To summarize, Maxwell's equation and boundary conditions can be applied to metal and dispersive media for designing nanophotonics and metamaterials based tunable optical devices for smart window design and solar energy harvesting. We now move to the analytical modeling section to discuss the different relevant theoretical methods.

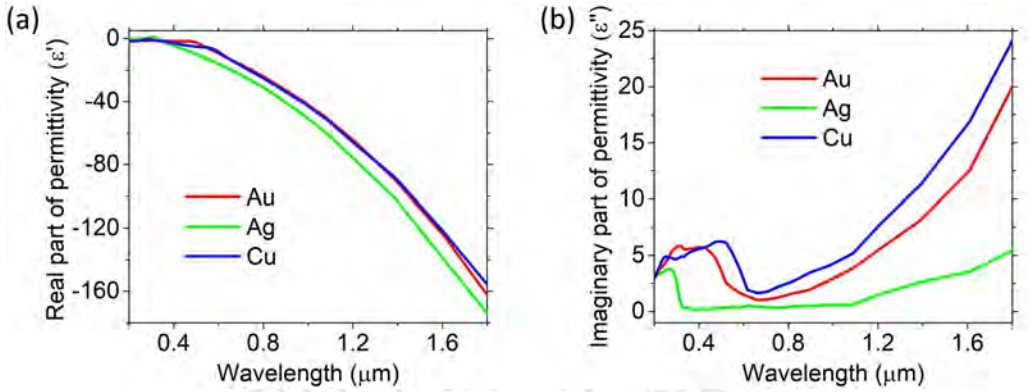

Figure 2.11: Frequency-dependent permittivity of plasmonic metals gold (Au), silver (Ag), and copper (Cu) in ultraviolet, visible, and infrared wavelengths. Data taken from Ref. [130].

2.4 Analytical Methods

This section discusses various theoretical methods in detail for analyzing optical responses of a metallo–dielectric multilayer structure. These theoretical approach can be extended to find absorption, reflection, and transmission across any system having multiple layers for normal as well as oblique angle of incidence.

2.4.1 Transfer Matrix Method

The transfer matrix method (TMM) is used to calculate reflectance and transmittance by analysing the propagation of electromagnetic waves through a multilayered structure. While applying TMM, each layer medium is considered to be homogeneous, linear, and non-magnetic. Consider a TM polarized plane wave incident normally on a multilayered thin-film structure. Taking the example of a metal–dielectric–metal (MDM) multilayer structure, one can approximate this design to consist of four interfaces, represented by q varying between 1 and 4, and five layers: air(0)–dielectric(1)–metal(2)–dielectric(3)–air(4), represented by j, as shown in Fig. 2.12. The incident radiation falling from air medium to MDM thin-film undergoes multiple reflection, partial transmission and absorption and is finally transmitted through the bottom dielectric layer. Note that the boundary consitions require that the tangetial components of **E**

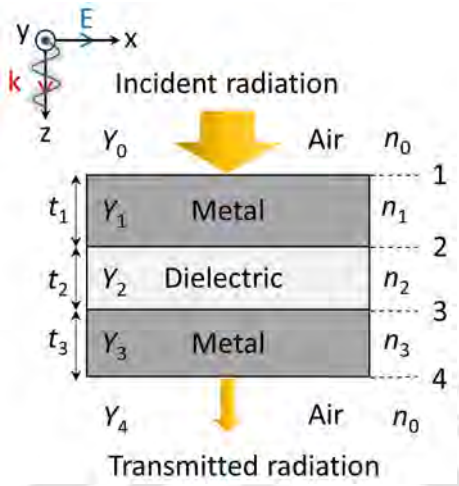

Figure 2.12: Analytical modelling of metal–dielectric–metal multilayer structure using transfer matrix method (TMM). Here, t, Y, and n represent the thickness, admittance, and refractive index of each layer, respectively.

field and **H** field (in the absence of free surface) must be continuous across all the boundaries. For an MDM thin-film, phase shift at each layer is given by [131]:

$$k_j\Lambda = k_0(2n_j t_j \cos\theta_{\mathrm{i},q})/2 \tag{2.10}$$

where, j represents top dielectric (1), metal (2), and bottom dielectric (3) layers, q represents interfaces between j^{th} and $(j+1)^{\mathrm{th}}$ layers, Λ is the optical path length difference between the first two reflected beams from each layer, n, k, and t are the refractive index, propagation wavevector, and thickness of each layer, respectively, and θ_{i} is the angle of incidence. After solving the boundary conditions at each interface, the electric and magnetic fields can be written as:

$$E_q = E_{q+1}\cos k_j\Lambda + H_{q+1}(i\sin k_j\Lambda)/Y_j \tag{2.11a}$$

$$H_q = E_{q+1}Y_j(i\sin k_j\Lambda) + H_{q+1}\cos k_j\Lambda \tag{2.11b}$$

Here, $Y_j = \sqrt{\epsilon_0/\mu_0}\,(n_j\cos\theta_{\mathrm{i},q})$, where Y_j represents the admittance for TE polarization in each layer, μ_0 and ϵ_0 are the permeability and permittivity in free space, respec-

tively. For TM case, $Y_j = \sqrt{\epsilon_0/\mu_0}\,(n_j/\cos\theta_{\mathrm{i},q})$. In matrix form, the relationship between j^{th} and $(j+1)^{\mathrm{th}}$ layer can be written as:

$$\begin{bmatrix} E_q \\ H_q \end{bmatrix} = \mathbf{P}_j \begin{bmatrix} E_{q+1} \\ H_{q+1} \end{bmatrix}, \quad \mathbf{P}_j = \begin{bmatrix} \cos k_j\Lambda & (i\sin k_j\Lambda)/Y_j \\ Y_j i\sin k_j\Lambda & \cos k_j\Lambda \end{bmatrix} \tag{2.12}$$

Here $\mathbf{P}_j$ denotes the characteristics matrix that relates the electric and magnetic fields at the interface across each layer. Therefore, for a five layers media (air–dielectric–metal–dielectric–air) the relation between electric and magnetic fields at interfaces 1 and 4 is given by:

$$\begin{bmatrix} E_4 \\ H_4 \end{bmatrix} = \mathbf{P_1 P_2 P_3} \begin{bmatrix} E_1 \\ H_1 \end{bmatrix} = \mathbf{P} \begin{bmatrix} E_1 \\ H_1 \end{bmatrix} \equiv \begin{bmatrix} p_{11} & p_{12} \\ p_{21} & p_{22} \end{bmatrix} \begin{bmatrix} E_1 \\ H_1 \end{bmatrix} \tag{2.13}$$

Considering TE case, the impedances for the top and the bottom air media are: $Y_0 = \sqrt{\epsilon_0\mu_0}\,(n_0\cos\theta_{\mathrm{i},1})$ and $Y_4 = \sqrt{\epsilon_0\mu_0}\,(n_0\cos\theta_{\mathrm{t},4})$, where θ_{t} is the angle of transmittance, which gives:

$$\begin{bmatrix} E_{\mathrm{i},1} + E_{\mathrm{r},1} \\ (E_{\mathrm{i},1} - E_{\mathrm{r},1})Y_0 \end{bmatrix} = \mathbf{P_1} \begin{bmatrix} E_{\mathrm{t},2} \\ H_{\mathrm{t},2}Y_4 \end{bmatrix} \tag{2.14}$$

Here E_{i}, E_{r}, and E_{t} denote incident, reflected, and transmitted electric fields, respectively. Similarly, H_{t} denotes transmitted magnetic field. Now, the matrices can be expanded to find out transmission (t) and reflection (r) coefficients, given by:

$$t = \frac{2Y_0}{(Y_0p_{11} + Y_0Y_4p_{11}) + (p_{21} + Y_4p_{22})} \tag{2.15a}$$

$$r = \frac{(Y_0p_{11} + Y_0Y_4p_{11}) - (p_{21} + Y_4p_{22})}{(Y_0p_{11} + Y_0Y_4p_{11}) + (p_{21} + Y_4p_{22})} \tag{2.15b}$$

After calculating transmission and reflection coefficients, the transmittance (T) and reflectance (R) can be obtained using $T = |t|^2 \, (n_{\mathrm{t}}\cos\theta_{\mathrm{t}})/(n_{\mathrm{i}}\cos\theta_{\mathrm{i}})$ and $R = |r|^2$, respectively. The absorbance (A) can be calculated using $A = 1 - R - T$.

2.4.2 Transmission Line Method

The transmission line method (TLM) is another theoretical approach to model a multilayer thin-film structure in the form of a circuit. By considering the impedance of different layers of a multilayer structure, TLM can help us to predict the wavelength of maximum transmission (λ_{max}). For a typical MDM structure, a circuital representation for a five-layer media is depicted in Fig. 2.13. Here, Z represents the characteristic impedance of transmission line. Looking from the top towards the bottom, the input impedance at interfaces 2 and 3 is given by [132, 133]:

$$Z_{\mathrm{in},q} = Z_j \frac{Z_{j+1} - iZ_j \tan(k_j t_j)}{Z_j - jZ_{j+1}\tan(k_j t_j)} \tag{2.16}$$

The reflection coefficients at the corresponding metal–dielectric interfaces (2 and 3) can be determined using:

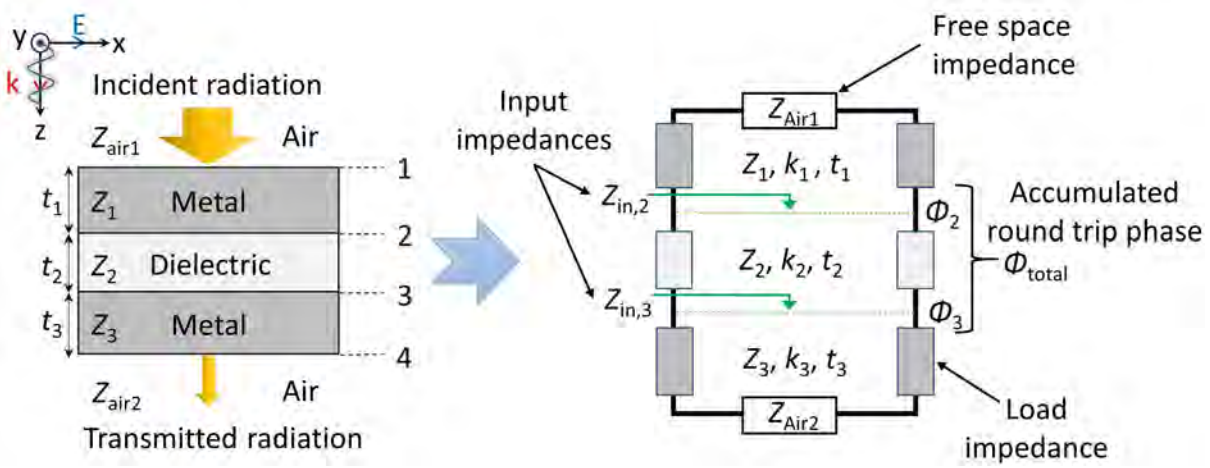

Figure 2.13: Analytical modelling of metal–dielectric–metal multilayer structure using transmission line method. Here, Z, k, and t denote impedance, propagation wavevector, and thickness of each layer, respectively. Note that ϕ denotes phase shift upon reflection at each metal–dielectric interface.

$$r_q = \frac{Z_{\text{in},q} - Z_j}{Z_{\text{in},q} + Z_j} = |r_q| \angle \phi_q \tag{2.17}$$

Here, ϕ_q gives the phase shift upon reflection at each metal–dielectric interface. Figure 2.13 shows the accumulated round trip phase ($\phi_2 + \phi_3$) at interfaces 2 and 3. When this accumulated phase goes to zero, one can get the maximum transmission ($T_{\max}$) at the resonant wavelength [132].

2.4.3 Fabry–Perot Interferometry Technique

Fabry–Perot Interferometry (FPI) is a useful technique that can help us to determine the peak transmission corresponding to the resonant wavelength supported by a cavity sandwiched between two reflective parallel surfaces. For a given MDM multilayer structure, the metallic layer thickness should be such that the electromagnetic radiation can penetrate through it [133]. When an electromagnetic radiation falls on the surface of the top metal, it penetrates through the metallic layer, undergoes multiple back and forth reflections inside the dielectric cavity and eventually a narrowband electromagnetic spectrum is transmitted through the bottom metallic layer. The narrow-band transmission can be attributed to the Fabry–Perot cavity resonance which allows transmission of only those spectral components corresponding to the resonance wavelength of the cavity. This resonance wavelength is given by the following equation [131]:

$$2k_0 n_{\text{D}} t_{\text{D}} + 2\phi = 2\pi m \tag{2.18}$$

where, k_0 is the wavevector defined by $k_0 = 2\pi/\lambda_0$, λ_0 being the resonance wavelength supported by the cavity, n_{D} and t_{D} are the refractive index and thickness of the dielectric layer respectively, and ϕ is the phase shift upon reflection from the bottom and top metallic layers. Lastly, m is an integer value that determines the order of the

cavity resonance. Note that, for the light to be trapped inside the cavity, phase condition in Eq. (2.18) must be satisfied. The underlying principle is that phase accumulated over a complete round trip inside the dielectric cavity must be an integral multiple of 2π to achieve constructive interference, which will eventually lead to the enhanced transmission at specific wavelengths through the bottom metallic layer.

Figure 2.14 depicts a Fabry–Perot resonator cavity for a MDM multilayer structure, where the two metals act as lossy mirrors which are partially transparent and the dielectric can be regarded as the cavity medium. Equation (2.18) depicts the condition for peak transmission which occurs in integral multiples of 2π. The sharpness of the peak is defined by finesse (F), given by [134]:

$$F = 4R/(1-R)^2 \tag{2.19}$$

For this case, transmission through Fabry–Perot cavity is given by:

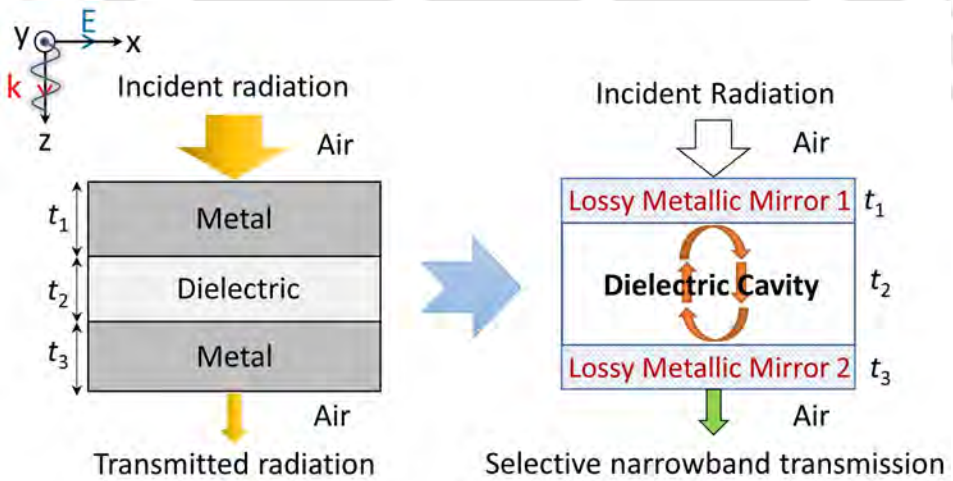

Figure 2.14: Analytical modelling of metal–dielectric–metal multilayer structure using Fabry–Perot interferometer (FPI) technique.

$$T = \kappa/(1 + F\sin^2\delta) \tag{2.20}$$

where, κ is the correction factor which takes care of absorbance (A) due to intrinsic losses in metallic mirrors and can be written as [135]:

$$K = (1 - A - R)/(1 - R) \tag{2.21}$$

The peak transmission condition can be obtained by rewriting Eq. (2.18) in terms of new parameter δ as:

$$\delta = \frac{4\pi}{\lambda_0} n_{\mathrm{D}} t_{\mathrm{D}} \cos\theta_{\mathrm{D}} = 2\pi m \tag{2.22}$$

where, θ_{D} is the angle of incidence inside a dielectric medium.

2.4.4 Effective Medium Theory

The effective medium theory (EMT) can be used to estimate the effective permittivity of a medium comprising of different materials. A homogenized medium's effective permittivity can be calculated using mixing formulae based on the relative fractions and permittivity of different media. For example, as shown in Fig. 2.15, an array of metallic nanoparticles embedded inside the dielectric layer of a MDM multilayer thin-films stack can be assumed to be a homogeneous layer with effective permittivity given by the following set of complementary equations [136]:

$$1/\epsilon_{\perp} = f/\epsilon_{\mathrm{m}}(\omega) + (1 - f)/\epsilon_{\mathrm{d}} \tag{2.23a}$$

$$\epsilon_{\parallel} = f\epsilon_{\mathrm{m}}(\omega) + (1 - f)\epsilon_{\mathrm{d}} \tag{2.23b}$$

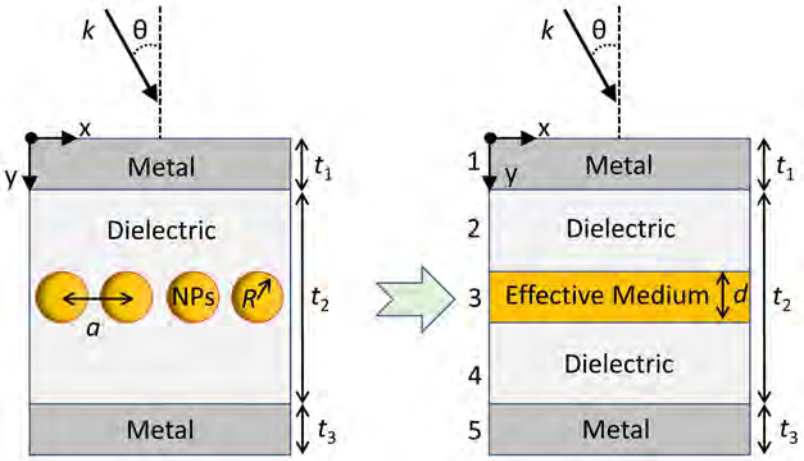

Figure 2.15: (a) A sample design comprising array of metallic nanoparticles (NPs) embedded inside the dielectric layer of a metal–dielectric–metal multilayer thin-films stack. (b) Analytical modelling using effective medium theory.

where ϵ_m and ϵ_d stand for metallic nanoparticles permittivity and dielectric permittivity, respectively; $\epsilon_\perp$ represents effective permittivity along the perpendicular direction and $\epsilon_\parallel$ represents effective permittivity along the parallel direction; f represents the filling ratio of the metallic nanoparticles [137]. This method gives a reasonably accurate approximation and theoretically models any patterned structure at a deep sub-wavelength scale.

2.5 Numerical Techniques

Numerical techniques are needed where the structure of the optical system is too complicated to be analyzed analytically. The finite element method (FEM) and finite difference time domain method (FDTD) are a couple of popular numerical methods that solve Maxwell's equation by dividing the structure's domain into a form of a mesh or grid. These numerical methods are efficient tools for designing complex two- or three-dimensional geometry of nanophotonic devices or a unit cell of metamaterial structures. A parametric sweep can be carried out to find the optimal design parameter, keeping all other parameters constant. More importantly, these numerical tools

can help gaining new physical insight by analyzing the near-field distribution or post-processing the numerically calculated data.

2.5.1 Finite Element Method

The finite element method (FEM) solves partial differential equations to solve boundary value problems and gives an approximate solution. Firstly, it divides the system under consideration into a finite number of elements. Secondly, the governing partial differential Maxwell's equation is solved for each of these individual elements. Thirdly, the boundary conditions are solved for each mesh element, and finally, the partial differential Maxwell's equation is solved for the entire structure. This method's major advantage lies in the system's subdivision into the finite elements (called mesh). These elements can be triangular or quadrilateral depending upon the structure. These elements can accurately model any type of structure, be it spherical, cylindrical, cubical, or elliptical or of any arbitrary shape. Also, depending upon the computational ability of the system, these element sizes can be fine-tuned to divide the structure into a large number of elements to accurately capture fine structural detail in order to be able to estimate its optical responses as accurately as possible.

FEM methods are mainly used to find the solution to two types of problems, scattering problems and eigenvalue problems. Throughout this thesis scattering method is used for numerical calculations. The scattering method forces an incident wave upon the system, producing a complex wave-vector by ensuring a real frequency of the incoming wave. Here the imaginary wave-vector corresponds to the decay of the excited modes in space. This method calculates the system's response by inserting a time-harmonic source, either a plane wave, a waveguide mode, or even a dipole source. The Absorption (A), Reflection (R) and Transmission (T) can be calculated using Poynting vector, $\mathbf{S} = \mathbf{E} \times \mathbf{H}$. Here, the Poynting vector represents the rate of energy transfer of the electromagnetic waves per unit area. The time-averaged energy transfer through

an area A, is given by:

$$S = \int^{A} Re\{\mathbf{E} \times \mathbf{H}^{*}\} \cdot dA \tag{2.24}$$

The final transmission and reflection coefficients can be calculated by finding the flux S due to the scattered field divided by the flux due to the incident field.

For design and simulation of multilayer thin-film optical systems, a commercial finite element method solver, COMSOL Multiphysics®, can simulate over a specific spectral range. Taking an example of multilayer thin films (metal–dielectric–metal) placed on a substrate, a sample two-dimensional view of the unit cell is shown in Fig. 2.16. A plane wave excitation of TM polarization (electric field parallel to xz plane) is applied. Floquet boundary conditions are applied along x and y directions to emulate a large-area thin-film. To capture all the structural details effectively, extra-fine mesh elements are preferred. The air layer thickness is kept at $\lambda_{\max}/2$, where $\lambda_{\max}$ is the maximum wavelength in the considered range. Perfectly matched layers (PML),

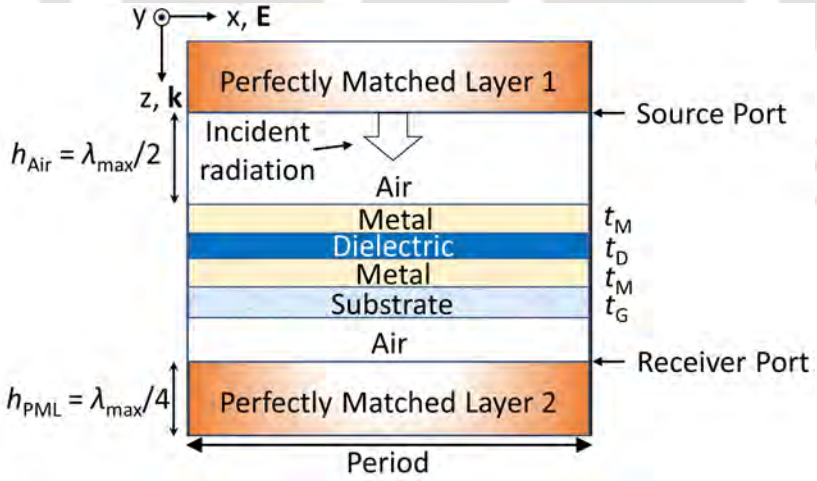

Figure 2.16: A sample three-dimensional schematic view of a unit cell in COMSOL Multiphysics® for designing thin-film based window glasses. Here, $\lambda_{\max}$ is the maximum wavelength in the considered spectral window. Perfectly matched layers (PML) are used at the top and bottom of the unit cell to avoid any anomaly arising from reflections due to confinement of the simulation domain.

each $\lambda_{\max}/4$ thick, are introduced to avoid any anomaly arising from reflections due to confinement of the simulation domain. A plane wave excitation is applied at port 1, representing a 'source' and port 2 representing a 'destination'. Then the overall reflection (R) and transmission (T) is calculated in percentage using the following two equations: $R = 100 \times |S_{11}|^2$ and $T = 100 \times |S_{21}|^2$, where S_{11} and S_{21} are called the scattering (S) parameters. These S parameters (for the two-port network system deployed here) are calculated numerically by the FEM solver over the wavelength range of interest. Using the equation: $A = 100 - R - T$, absorbance (A) in percentage can be further calculated.

2.5.2 Finite Difference Time Domain Method

Contrary to the finite element method (FEM), which works in the frequency domain, the finite difference time domain method (FDTD) solves the time-dependent Maxwell's equations. In FDTD, spatial and time derivatives can be replaced by the two Maxwell's curl equations by using central finite difference approximation (CFDA). For a function *f(x)*, its derivative at x_0 from CDFA is given by:

$$\frac{df(x_0)}{dx} = f(x_0) \cong \frac{f(x_0 + \frac{\Delta x}{2}) - f(x_0 - \frac{\Delta x}{2})}{\Delta x} \tag{2.25}$$

The time-dependent and source free (**J**=0) Maxwell's curl equations in a medium with $\epsilon = \epsilon_0\epsilon_r$ and $\mu = \mu_0\mu_r$ is given by:

$$\frac{\delta \mathbf{E}}{\delta t} = \frac{1}{\epsilon_0\epsilon_r}\nabla \times \mathbf{H} \tag{2.26a}$$

$$\frac{\delta \mathbf{H}}{\delta t} = -\frac{1}{\mu_0\mu_r}\nabla \times \mathbf{E} \tag{2.26b}$$

Now, expanding the curl equations and equating the vector components gives six

equations for the Cartesian coordinate system. So, expanding the first vector curl Eq. (2.26):

$$\frac{\delta \mathbf{E_x}}{\delta t} = \frac{1}{\epsilon_0 \epsilon_r}\left(\frac{\delta \mathbf{H_z}}{\delta y} - \frac{\delta \mathbf{H_y}}{\delta z}\right) \tag{2.27a}$$

$$\frac{\delta \mathbf{E_y}}{\delta t} = \frac{1}{\epsilon_0 \epsilon_r}\left(\frac{\delta \mathbf{H_x}}{\delta z} - \frac{\delta \mathbf{H_z}}{\delta x}\right) \tag{2.27b}$$

$$\frac{\delta \mathbf{E_z}}{\delta t} = \frac{1}{\epsilon_0 \epsilon_r}\left(\frac{\delta \mathbf{H_y}}{\delta x} - \frac{\delta \mathbf{H_x}}{\delta y}\right) \tag{2.27c}$$

Similarly, expanding the 2nd vector curl Eq. (2.26):

$$\frac{\delta \mathbf{H_x}}{\delta t} = \frac{1}{\mu_0 \mu_r}\left(\frac{\delta \mathbf{E_y}}{\delta z} - \frac{\delta \mathbf{E_z}}{\delta y}\right) \tag{2.28a}$$

$$\frac{\delta \mathbf{H_y}}{\delta t} = \frac{1}{\mu_0 \mu_r}\left(\frac{\delta \mathbf{E_z}}{\delta x} - \frac{\delta \mathbf{E_x}}{\delta z}\right) \tag{2.28b}$$

$$\frac{\delta \mathbf{H_z}}{\delta t} = \frac{1}{\mu_0 \mu_r}\left(\frac{\delta \mathbf{E_x}}{\delta y} - \frac{\delta \mathbf{E_y}}{\delta x}\right) \tag{2.28c}$$

Since the FDTD is a time-domain solver, these six electric and magnetic field equations can be solved using the FDTD update equation, considering some simplifying assumptions. For example, the 1D FDTD update equations can be written considering:

(i) Linearly polarized wave along the x-axis exciting an electric field having E_x component only (*i.e.* $E_y = E_z = 0$).

(ii) Wave propagation along z direction having no variation in the x-y plane *i.e.* $\frac{\partial}{\partial x} = 0$ and $\frac{\partial}{\partial y} = 0$

Using the above two conditions, the set of six electric and magnetic field equations from two Maxwell's curl equations can be reduced to two 1D FDTD equations given by:

$$\frac{\delta \mathbf{E_x}}{\delta t} = -\frac{1}{\epsilon_0 \epsilon_r}\frac{\delta \mathbf{H_y}}{\delta z} \tag{2.29a}$$

$$\frac{\delta \mathbf{H_y}}{\delta t} = -\frac{1}{\mu_0 \mu_r}\frac{\delta \mathbf{E_x}}{\delta z} \tag{2.29b}$$

The objective is to observe fields at different places and times by solving these equations in the solution space. Hence, both space and time discretization is needed [129]. After discretizing Eq. (2.29), one can write:

$$\frac{\mathbf{E_x}(k, n+\frac{1}{2}) - \mathbf{E_x}(k, n-\frac{1}{2})}{\Delta t} = -\frac{1}{\epsilon_0 \epsilon_r} \frac{\mathbf{H_y}(k+\frac{1}{2}, n) - \mathbf{H_y}(k-\frac{1}{2}, n)}{\delta z} \tag{2.30a}$$

$$\frac{\mathbf{H_y}(k+\frac{1}{2}, n+1) - \mathbf{H_y}(k+\frac{1}{2}, n)}{\Delta t} = -\frac{1}{\mu_0 \mu_r} \frac{\mathbf{E_x}(k+1, n+\frac{1}{2}) - \mathbf{E_x}(k, 1+\frac{1}{2})}{\delta z} \tag{2.30b}$$

The discretized Eq. (2.30) can be rearranged as a pair of FDTD update equation and can be repeatedly updated in loop to obtain next time instant values of $\mathbf{E_x}(k, n+\frac{1}{2})$ and $\mathbf{H_y}(k+\frac{1}{2}, n+1)$ for 1D case as:

$$\mathbf{E_x}(k, n+\frac{1}{2}) = \mathbf{E_x}(k, n-\frac{1}{2}) - \frac{1}{\epsilon_0 \epsilon_r} \frac{\Delta t}{\Delta z} \{\mathbf{H_y}(k+\frac{1}{2}, n) - \mathbf{H_y}(k-\frac{1}{2}, n)\} \tag{2.31a}$$

$$\mathbf{H_y}(k+\frac{1}{2}, n+1) = \mathbf{H_y}(k+\frac{1}{2}, n) - \frac{1}{\mu_0 \mu_r} \frac{\Delta t}{\Delta z} \{\mathbf{E_x}(k+1, n+\frac{1}{2}) - \mathbf{E_x}(k, 1+\frac{1}{2})\} \tag{2.31b}$$

Alternatively, **E** and **H** fields in space and time domain can be formulated using FDTD method. To calculate $\mathbf{E_x}(k)$, the neighboring values of $\mathbf{H_y}$ at $k - 1/2$ and $k + 1/2$ of the previous time instant are needed. Similarly, to calculate $\mathbf{H_y}(k + 1/2)$, the neighboring values of $\mathbf{E_x}$ at k and k+1 of the previous time instants are needed.

Like the 1D case, the 2D and 3D problems can be solved using FDTD by finding electric and magnetic fields at alternating space and time domains. A schematic representation of the Yee cell demonstrating the discrete **E** and **H** field components for 3D FDTD is shown in Fig 2.17 [138].

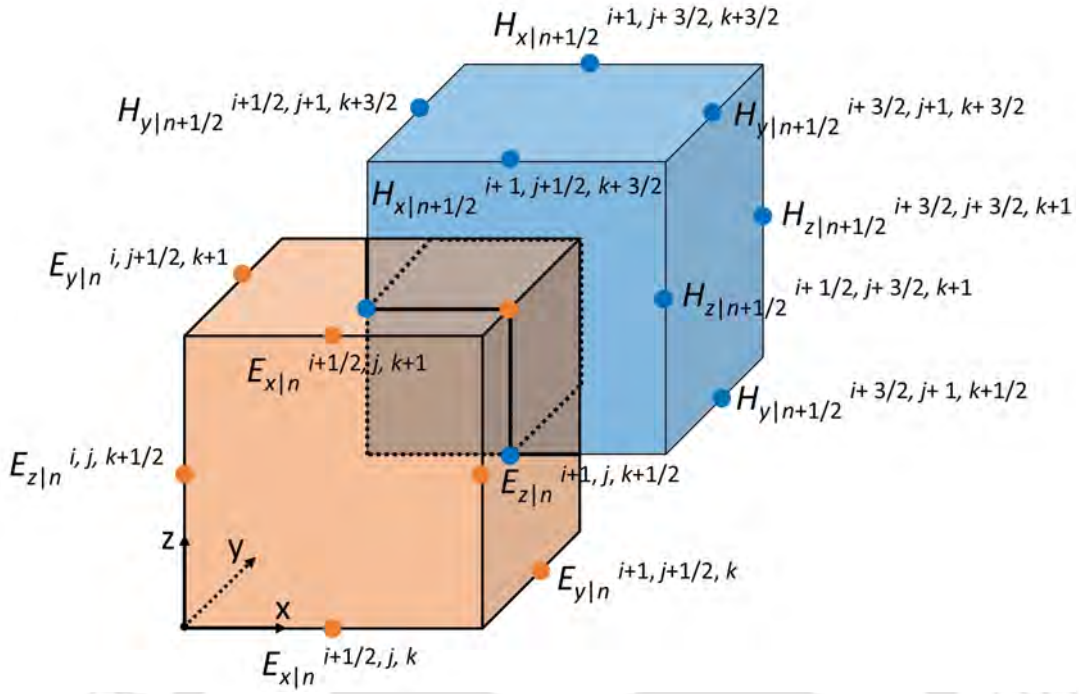

Figure 2.17: Schematic of the Yee cell demonstrating the discretized electric and magnetic field components [138].

2.5.3 Comparison Among Numerical Techniques

FDTD offers several advantages over frequency domain solvers. Since within the FDTD solver, the memory consumption scales only linearly with the system size, it solves in fields for the time t to calculate the fields at $t+\delta t$. In contrast, FEM, a frequency domain solver, solves linear algebra by taking the Fourier transformed Maxwell's equations. This causes the computational memory to scale quadratically with system size [138]. Hence, the computational burden of using finer mesh is much less in FDTD method compared to that of FEM. FDTD, a time domain solver, also allows real-time visualization of the computed electric and magnetic fields, which offers an advantage to realize the output during the run-time. More importantly, in FDTD, non-linear effects can be treated directly, as other differential equations for non-linear media can be directly included. This makes FDTD a potent tool for solving complex problems. At last, even though the FDTD offers a faster computation than FEM, the later produces more

Table 2.2: Comparison chart with pros and cons of a few analytical and numerical techniques. Adapted with permission from [139].

Method	Computational Time	Advantages	Disadvantages
Transfer Matrix Method (TMM)	*Rapid*: a few milliseconds per individual frequency.	• Rapid computation time. • Wide range of geometries supported. • Possible to include a substrate interaction.	• Computations are numerically unstable for elongated or flattened objects.
Finite Element Method (FEM)	*Lengthy*: a compromise made between the computational time and element length.	• Can be used to evaluate the scattering field of any arbitrary shaped particles. • The use of a non-regular tetrahedral adaptive mesh allows more accurate approximation of curved surfaces.	• Computational time is lengthy.
Finite Difference Time Domain Method (FDTD)	*Lengthy*: a compromise made between the computational time and element length.	• Can be used to evaluate scattering parameters from any arbitrary shaped particle.	• Computational time is lengthy. • Permittivity values have to be specified beyond the frequency range of interest. The Drude–Lorentz model may not be an accurate representation of experimental data.

accurate results than its predecessor as FEM solves the Fourier transformed Maxwell's equations. A comparison among a few theoretical and numerical techniques is listed in Table 2.2 with its advantages and disadvantages [139].

3

Climate-Specific Passive Windows Based on Selective Filtering of Solar Radiation

Contents

This chapter presents different designs of climate-specific passive window glasses for selective filtering of visible and infrared radiations from solar spectrum. Section 3.1 introduces a **novel plasmonic 'meta-glass'** that could block infrared radiation efficiently while maintaining good outdoor visibility. Section 3.2 presents **a new design of meta-glass based on nanoparticles** for blocking ultraviolet and infrared radiations. Section 3.3 discusses the design of ultra-thin, multilayered metallo-dielectric passive window glasses where **a unique approach is adopted to design climate-specific passive windows** with desired visible and infrared transmission/blocking capability. Section 3.4 concluded the chapter, where **an innovative approach has been adopted to design transmission-mode nanophotonic windows** as specific color filters, which could be useful for aiding photosynthesis in greenhouses.

3.1 Nanoring Based 'Meta-glass' as Passive Windows

In this section, we introduce plasmonic 'meta-glasses' as infrared-blocking nanophotonic windows that could block up to ∼87% of infrared radiation over a 750–1800 nm spectral window, predominantly responsible for indoor radiative heating, while maintaining a 60% average visible transmission for providing indoor illumination.

3.1.1 Background

A climate-specific design of passive windows requires selective transmission of visible and infrared radiations [140]. The visible radiation provides indoor illumination and visual comfort for the building occupants, whereas IR radiation causes radiative heating inside the room [33]. In the solar irradiance spectrum, almost 90% of the solar energy lies between 400 nm and 1800 nm wavelength spectral regime, consisting of visible (VIS; 400 – 750 nm) and infrared (IR; 750 – 1800 nm) radiations [141]. Therefore, for a typical hot climate condition, passive windows should have high transmission over 400–750 nm wavelengths and low transmission over 750–1800 nm wavelengths.

Recently, a few passive glasses with low-emissivity coatings have been demonstrated to block the solar heat and provide energy-saving to some extent [35, 36, 140]. While some of these reported window coatings based on expensive noble metals such as gold or silver could match the figure of merit used in the industry [31, 46] but failed to do so using relatively inexpensive alternative metals such as copper or aluminium or indium tin oxide [36, 37]. In literature, many broadband absorbers are reported that can completely block infrared radiation, yet blocking infrared radiation while maintaining some visible transmission remained a challenge [25, 142]. Therefore, a design of industry-standard passive windows based on relatively inexpensive material that can efficiently block IR radiation while maintaining standard visible transmission remains largely in demand.

Here, we report a new design of plasmonic 'meta-glasses' comprising a two- dimensional (2D) hexagonal array of tungsten nanorings placed on top of a silica glass substrate. Using the uniform-sized nanoring-based design, we could achieve 80.3% IR blocking over 750–1800 nm wavelength range while maintaining 60% average visible transmission. We further improved the IR blocking efficiency up to 87.1% by introducing two distinct-sized nanorings. We chose tungsten because it has the highest melting point (3422°C), remarkable mechanical strength, and smallest thermal expansion coefficient among all known metals [143]. Unlike gold and silver, tungsten is CMOS compatible, which is crucial for reducing the fabrication cost using conventional lithography techniques for industrial-scale production.

3.1.2 Design and Simulation

Figure 3.1 depicts a 3D schematic view of our nanoring-based plasmonic meta-glass along with its unit cell considered for simulation. This meta-glass comprises a 2D hexagonal array of tungsten nanorings printed on top of transparent silica glass. Note that all the dimensions are specified in Fig. 3.1 caption. We use the wave optics module

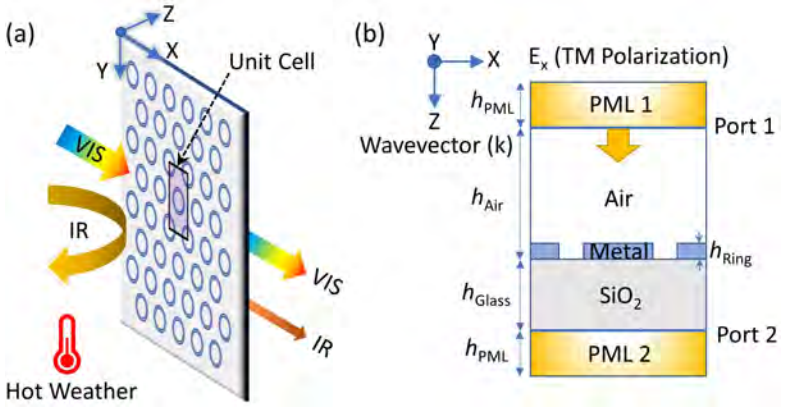

Figure 3.1: Nanoring-based plasmonic 'meta-glass' for a typical hot climate condition in (a) 3D schematic view and (b) a 2D side view of the unit cell simulation model in xz plane. The design consists of a 2D hexagonal array of tungsten nanorings placed on top of silica glass. The incident radiation from port 1 is a plane wave of TM polarization traveling along the z-direction. A couple of perfectly matched layers (PML 1 and PML 2) are used to absorb undue reflections due to the confinement of the simulation domain. Dimensions in nm: $h_{\mathrm{PML}} = 400$, $h_{\mathrm{air}} = 800$, $h_{\mathrm{ring}} = 30$, and $h_{\mathrm{glass}} = 300$.

of a commercial finite element method (FEM) solver, COMSOL Multiphysics®, for full-wave simulations. To capture all the structural details effectively, the maximum and minimum mesh element sizes are taken as 138 nm and ∼0.46 nm, respectively. Floquet boundary conditions are applied along x and y directions to emulate a 2D periodic array of the unit cell. The optical constants for tungsten [144] and silica glass [145] are taken from the literature.

3.1.3 Design I: Uniform-sized Nanorings

For our uniform-sized nanorings based plasmonic glass design, the top view of the rectangular unit cell in xy plane is shown using a shaded region in Fig. 3.2(a). We manually optimize our design in its parametric domain to achieve minimum transmission in the IR regime and maximum transmission in the visible regime. All the dimensions of the optimized design are provided in the figure caption. Figure 3.2(b) shows numerically obtained transmission spectra using FEM and finite difference time domain (FDTD) solvers over the solar spectral regime–showing a near-perfect match. We get

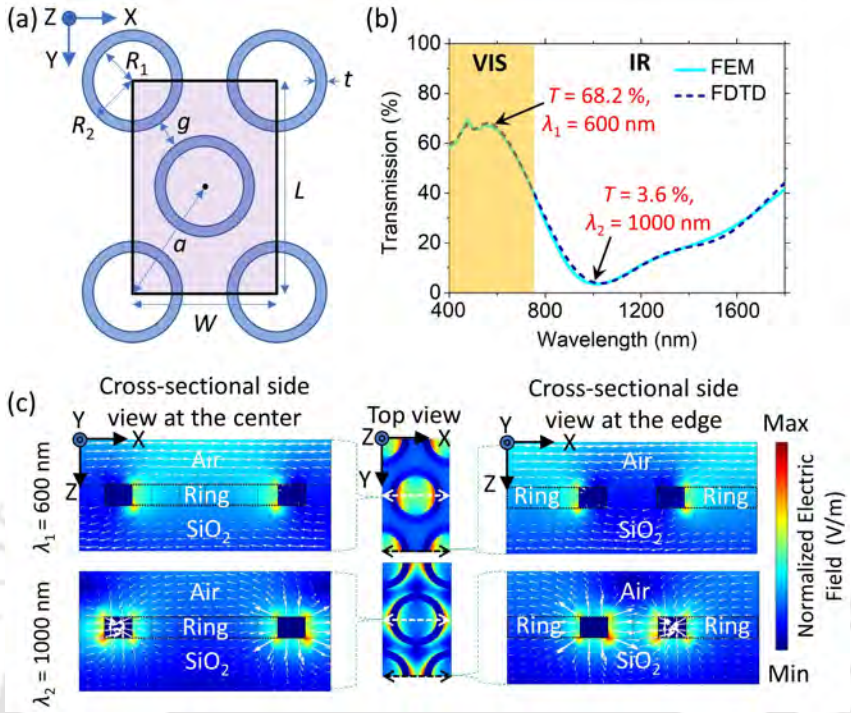

Figure 3.2: Uniform-sized nanoring-based plasmonic glass: (a) top view of a unit cell, shown by shaded region in xy plane. (b) Numerically calculated transmission (T) spectra using finite element method (FEM) and finite difference time domain (FDTD) solvers over solar radiation spectra. (c) Top and side views of the unit cell showing normalized electric field distribution with arrow plots at $\lambda_1 = 600$ nm and $\lambda_2 = 1000$ nm. Dimensions in nm: inner radius of each ring, $R_1 = 105$; outer radius of each ring, $R_2 = 145$; width of each ring, $t = 40$; gap between the rings, $g = R_2/2$; lattice constant, $a = 2R_2+g$; period along y-direction, $L = 2a\cos30°$; and period along x-direction, $W = 2a\sin30°$.

an average transmission of 60.3% in the visible regime with a peak transmission ($T_{\max}$) of 68.2% around λ_1 = 600 nm. Whereas, in the IR regime, we obtain only 19.7% average transmission with a transmission minimum ($T_{\min}$) of 3.6% around λ_2 = 1000 nm. Therefore, we could block 80.3% IR radiations over 750–1800 nm spectral range using a uniform-sized nanoring-based design.

To discuss the underlying principle behind suppression in IR transmission, we show normalized electric field distribution (top view and side views at the center and edge) with arrow plots in Fig. 3.2(c) corresponding to $T_{\max}$ obtained around λ_1 and $T_{\min}$ obtained near λ_2 [see Fig. 3.2(b)]. The top view at λ_2 indicates strong inter-ring

electric field confinement as a result of dipolar charge separation (see side view at λ_2), indicating excitation of localized surface plasmons—leading to significantly suppressed transmission around this resonant wavelength [146, 147]. Whereas at λ_1, the appearance of weak intra-ring electric field confinement (see the top view at λ_1) indicates coupling between opposite inner faces of each nanoring, allowing moderately high transmission through the gap between different nanoring structures [148].

To optimize our design, we study the effect of variation in the gap (g), width (t), thickness (h_{ring}), and outer radius (R_2) of each uniform-sized nanoring, as shown in Fig. 3.3. With a decrease in the gap between these nanorings from 150 nm to 25 nm, we could see a slight redshift in the resonance wavelength and reduced transmission amplitude in the IR regime due to enhanced inter-ring coupling [148], as shown in Fig. 3.3(a). Next, we vary each nanoring width between 10 nm and 60 nm, keeping the outer radius constant. Figure 3.3(b) clearly shows a large blueshift in the resonance

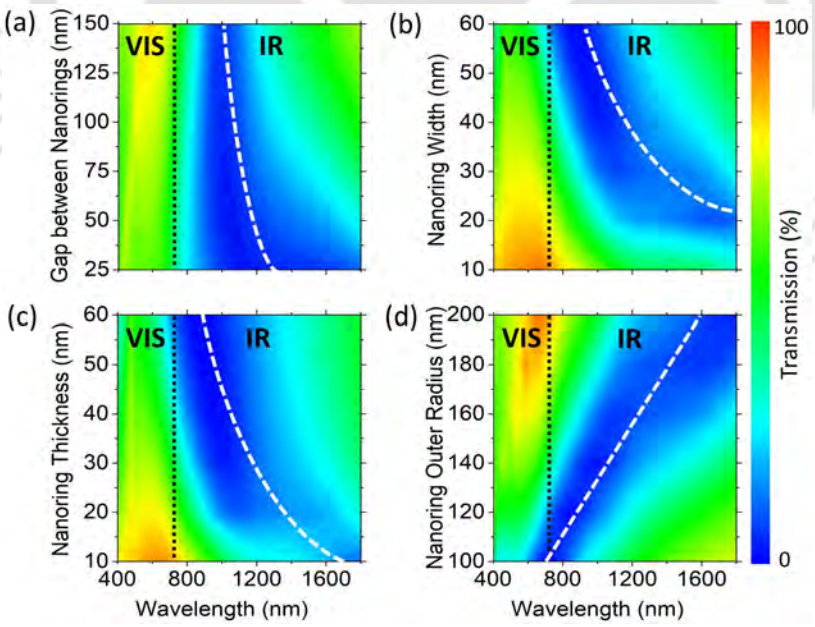

Figure 3.3: Numerically obtained contour plot for our design with uniform-sized nanoring for varying (a) gap between each nanoring, g, (b) width of each nanoring, t, (c) thickness of each nanoring, h_{ring}, and (d) outer radius of each nanoring, R_2. Here, the white dashed lines show the trends for the minimum transmission with changes in the above parameters.

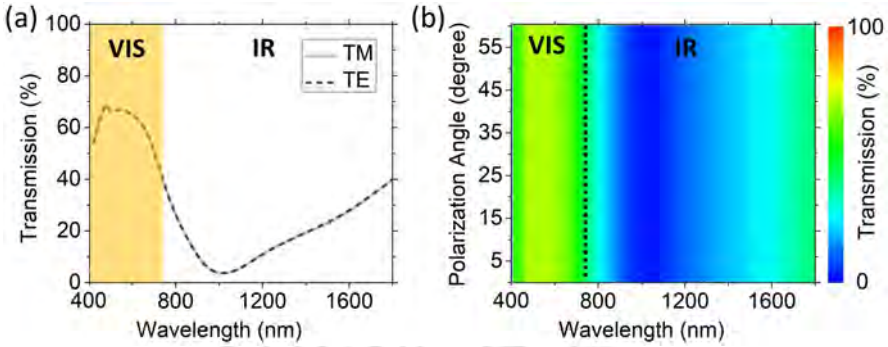

Figure 3.4: Numerically obtained transmission spectra for our uniform-sized nanorings design considering (a) both TM and TE polarization at a normal angle of incidence and (b) contour plot for varying polarization angle between 0 and 60 degrees of the oblique angle of incidence.

wavelength with increased nanoring width due to reduced inner radius dimension. Figure 3.3(c) shows a similar trend of blueshift with an increase in nanoring thickness between 10 nm and 60 nm. Lastly, Fig. 3.3(d) shows a redshift in the resonance wavelength owing to an enlargement in ring dimension with an increase in outer radius between 100 nm and 200 nm while keeping the nanoring width constant. Therefore, by carefully choosing the nanoring's dimension, our meta-glasses can efficiently block the infrared radiation.

To have practical utility, these plasmonic meta-glasses should be polarization- and angle-insensitive to a large extent. Figure 3.4(a) shows a perfect match between numerically calculated spectral response for both TM and TE polarization at a normal angle of incidence—making our design polarization-insensitive. In Fig. 3.4(b), owing to the azimuthal symmetry of the nanorings, the transmission spectra remain unaffected by the change in polarization angle between 0 and 60 degrees, thus, making our design polarization angle-insensitive as well.

3.1.4 Design II: Two distinct-sized Nanorings

For a uniform-sized nanorings based design, we observe excitation of surface plasmon resonance at λ_2. If we could achieve multiple resonances, the entire IR regime can be blocked efficiently [37]. Therefore, we further investigate the spectral response by

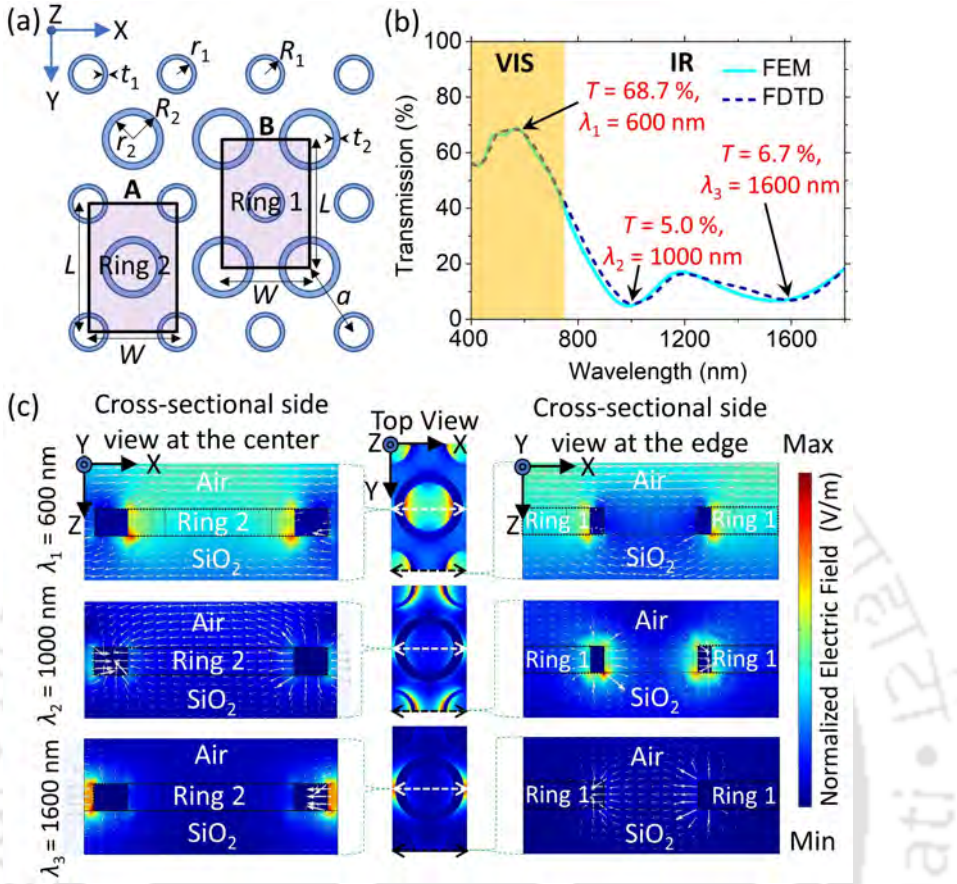

Figure 3.5: Two distinct-sized nanoring-based plasmonic glass depicting (a) choice of unit cells as A or B, shown by shaded region in xy plane. (b) Numerically calculated transmission (T) spectra using FEM and FDTD solvers over solar radiation spectra. (c) Top and side views of the unit cell showing normalized electric field distribution with arrow plots at $\lambda_1 = 600$ nm, $\lambda_2 = 1000$ nm, and $\lambda_3 = 1600$ nm, for choice of unit cell as A. Dimensions in nm: inner radius of corner ring, $r_1 = 100$; outer radius of corner ring, $R_1 = 120$; inner radius of center ring, $r_2 = 125$; outer radius of center ring, $R_2 = 175$; width of corner ring, $t_1 = 20$; width of center ring, $t_2 = 50$; gap between the rings, $g = R_2/2$; lattice constant, $a = 2R_2+g$; period along y-direction, $L = 2a\cos30°$; and period along x-direction, $W = 2a\sin30°$.

introducing two distinct-sized nanorings at the center and corner of the unit cell, depicted using a shaded region for choice of unit cells as A or B in Fig. 3.5(a). Figure 3.5(b) shows numerically obtained transmission spectra using FEM and FDTD solvers over 400–1800 nm wavelengths. We get 59.5% average transmission in the visible regime with a peak transmission of 68.7% around λ_1. While in the IR regime, we obtain only 12.9% average transmission with $T_{\min}$ as low as 5.0% at λ_2 and 6.7% at λ_3 = 1600 nm.

Hence, we could block 87.1% IR radiations over 750–1800 nm spectral range using two distinct-sized nanoring-based designs.

We further study normalized electric field with arrow plots for choice of the unit cell as A in Fig. 3.5(c), corresponding to $T_{\min}$ obtained at λ_2 and λ_3, and $T_{\max}$ obtained near λ_1. The top view at λ_2 and λ_3 indicates strong confinement of electric field due to dipolar charge separation (see side view at λ_2 for corner ring 1 and λ_3 for center ring 2). The reason can be attributed to the excitation of localized surface plasmons at λ_2 for the smaller ring 1 and λ_3 for the larger ring 2, leading to suppressed transmission in the entire IR regime [146,147]. Interestingly, closely spaced resonance wavelengths lead to more broadband and efficient IR radiation blocking than in uniform-sized nanoring-based plasmonic glasses.

3.1.5 Figure of Merit of Our Passive Window Glasses

We now introduce a couple of figure of merit (FOM) used in the industry: visible transmittance (VT) and infrared transmittance (IRT) [37]. VT and IRT represent the portion of visible and infrared radiation transmitted through a glass window over a particular wavelength range, respectively [140]. Mathematically, these can be expressed as:

$$\mathrm{VT} = \frac{\int_{400}^{750} I_{\mathrm{solar}}(\lambda)T(\lambda)\mathrm{d}\lambda}{\int_{400}^{750} I_{\mathrm{solar}}(\lambda)\mathrm{d}\lambda}; \mathrm{IRT} = \frac{\int_{750}^{1800} I_{\mathrm{solar}}(\lambda)T(\lambda)\mathrm{d}\lambda}{\int_{750}^{1800} I_{\mathrm{solar}}(\lambda)\mathrm{d}\lambda} \tag{3.1}$$

where $T(\lambda)$ denotes wavelength-dependent optical transmission through a window. Using VT and IRT values, we calculate the contrast ratio (CR = VT/IRT) that determines the ability of our meta-glasses to simultaneously achieve maximum transmission in the visible regime and minimum transmission in the IR regime [4]. A comparative overview of our design with a few recently reported IR blocking passive glasses [37,140] using alternative low-cost metals (copper, aluminium, titanium nitride

Table 3.1: Figure of merit (FOM) comparative overview with a few recently reported IR blocking passive glasses.[a] Ideal values: VT: 1, IRT: 0, CR: VT/IRT = ∞

Metal (Ref.)	VT	IRT	CR
Cu [37]	0.57	0.19	3.03
Cu [140]	0.59	0.30	1.96
Al [37]	0.27	0.24	1.16
TiN [37]	0.55	0.28	1.93
ITO [140]	0.67	0.30	2.18
AZO [140]	0.67	0.31	2.19
ALON [140]	0.68	0.31	2.20
W (Design I)	0.61	**0.17**	**3.51**
W (Design II)	0.60	**0.16**	**3.75**

[a] VT: Visible Transmittance, IRT: IR Transmittance, CR: Contrast Ratio, Cu: Copper, Al: Aluminium, TiN: Titanium Nitride, ITO: Indium Tin Oxide, AZO: Al-doped Zinc Oxide, ALON: Al Oxynitride, W: Tungsten

etc.) is given in Table 3.1. The theoretically calculated FOM indicates that our proposed plasmonic meta-glasses are likely to outperform the recently reported window glasses in the literature upon practical realization, provided that the on-field performances of the meta-glasses closely follow our theoretical predictions.

3.1.6 Prospective Fabrication Techniques

With the current state-of-the-art nanofabrication technology, the realization of our meta-glasses is indeed feasible. First, a polished silica glass substrate could be spin-coated with polymethylmethacrylate resist layer using electron-beam (e-beam) technique [149]. When the resist is soft-baked, e-beam lithography may be used for exposure resist development. After that, a 30 nm tungsten layer may be deposited using e-beam evaporation technique [150]. After completing the lift-off process, the sample could be rinsed in acetone for a few hours to form nanorings.

3.1.7 Summary

We presented a **novel plasmonic 'meta-glass'** as infrared-blocking nanophotonic windows that could block up to ∼87% infrared radiation over 750–1800 nm spectral range while maintaining 60% average transmission in the visible regime. We achieved an infrared transmittance as low as 0.16 and a contrast ratio as high as 3.75, indicating that our proposed plasmonic glasses could outperform recently reported industry-standard window glasses. By virtue of surface plasmons excitation in the infrared regime, we could achieve selective suppression in the transmission spectrum, which is tailorable by adjusting the dimension of the nanorings. The simulation results obtained using finite element method and finite difference time domain solvers are in good agreement. Our designs are low-cost, easy to fabricate, polarization- and angle-insensitive to a large extent. These plasmonic meta-glasses based on relatively inexpensive material could be useful in places with warm climates.

3.2 Nanoparticles Based Passive Windows

In the previous section 3.1, excellent infrared-blocking was achieved using nanorings based passive windows. This section introduces a new design of 'meta-glass' coatings for passive windows based on a nanoparticles array that can block both ultraviolet and infrared radiations coming from the sun. Such windows would be of huge interests in modern buildings and particularly in automobile industry. A design of an automobile windshield coated with these meta-glasses could increase vehicle mileage by reducing the need for air-conditioning besides providing thermal and visual comfort to passengers and protection from harmful ultraviolet radiation.

3.2.1 Background

The operation of traditional vehicles requires burning of fossil fuels that causes carbon emissions leading to global warming. Keeping in view the sustainable devel-

opment goals, electric vehicles (EVs) have emerged as a promising solution for the future. Unfortunately, limited operating speed, long battery recharge time, and short driving range remain fundamental challenges in the EV industry [151]. A study revealed that passengers' demand for air-conditioning reduces the driving range by 53% and 18% in winter and summer, respectively [152]. A design of passive windows that can block the undesired ultraviolet and infrared radiations while allowing the transmission of visible radiation could improve EV's performance by reducing the need for air conditioning [140, 153].

To address this challenge, we introduce 'meta-glass' coatings to passively control the portion of solar radiation transmitted through it. This coating comprises a two-dimensional (2D) hexagonal array of metallic nanoparticles (NPs) embedded inside the dielectric layer of a metal–dielectric–metal (MDM) multilayer thin-film stack. We use silver (Ag) as the top and bottom metallic layers and silica (SiO_2) as the middle dielectric layer. We explore five different choices of metallic NPs and compare their figure of merit based on industry standards.

3.2.2 Design, Results and Discussions

Figure 3.6(a) shows a 3D perspective view of our proposed meta-glass coating. It comprises a 45 nm thick SiO_2 dielectric layer sandwiched between 8 nm thick top and bottom Ag metallic layers. A 2D hexagonal array of molybdenum (Mo) NPs with a 6 nm radius is embedded inside the dielectric layer. The incident wave is a plane wave of transverse-magnetic polarization propagating along the z-direction. We use a finite element method solver to compute over 200–1800 nm spectral window. This spectral range comprises ultraviolet (UV; 200–400 nm), visible (VIS; 400–750 nm), and a portion of infrared (IR; 750–1800 nm) radiations [141]. Figure 3.6(b) depicts the top view of the design where the shaded region represents the unit cell considered for full-wave simulations. The unit cell parameters are specified in Fig. 3.6 caption. Figure 3.6(c)

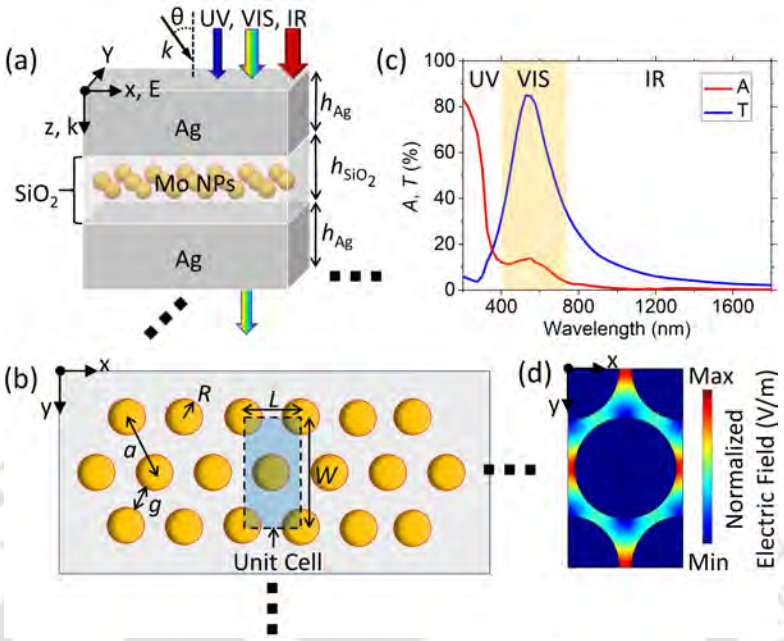

Figure 3.6: (a) A three-dimensional (3D) geometry of meta-glass based on an infinite 2D array of metallic nanoparticles (NPs), (b) top view of the design depicting a unit cell using the shaded region, (c) spectral response showing transmittance (T) and absorbance (A), and (d) normalized electric field distribution of the unit cell at 1000 nm wavelength. In (a) and (b), thickness of top and bottom silver metallic layers, $h_{\mathrm{Ag}} = 8$ nm, thickness of silica dielectric layer, $h_{\mathrm{SiO_2}} = 45$ nm, radius of each NPs, $R = 6$ nm, gap between NPs, $g = R/4$, lattice constant, $a = 2{\times}R{+}g$, Width of the unit cell, $L = 2\mathrm{asin}30°$, and length of the unit cell $W = 2\mathrm{acos}30°$.

shows that the simulated spectral response through our meta-glass design. We could block ∼90% UV and IR radiations while maintaining 60% standard visible transmission. Figure 3.6(d) shows strong localization of the electric field between the NPs at 1000 nm wavelength. Around this wavelength, incident light sees the entire assembly of NPs as a reflective plane–leading to high reflection in near-IR.

Next, the unit cell parameters are tuned to obtain the desired optical response from these meta-glasses. Figure 3.7(a) shows a redshift in the peak transmittance with an increase in the radius (R) of NPs. This is because the larger the NP radius, the resonance is likely to take place at a longer wavelength. Next, when we increase the gap (g) between the NPs, there is a slight blue shift and increase in peak transmittance, as shown in Fig. 3.7(b). This is because light can now see the gaps and easily penetrate

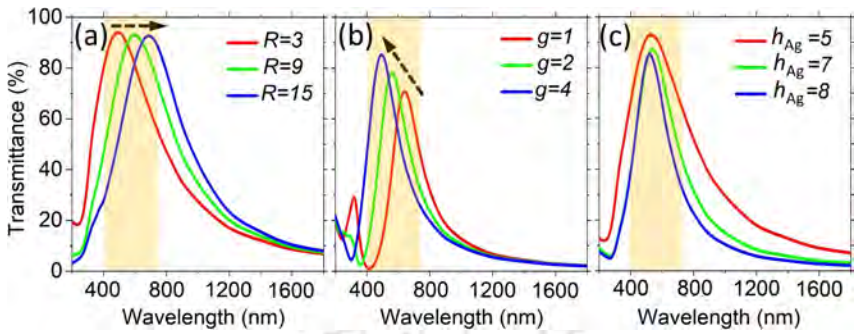

Figure 3.7: Tuning the transmittance spectra by varying the unit cell parameters (all dimensions in nm): (a) radius of NPs, R, (b) gap between NPs, g, and (c) thickness of the top and bottom metallic layers, h_{Ag}.

through the structure. In Fig. 3.7(c), we could see a slight drop in the peak transmittance and narrowing of spectra with an increase in the top and bottom metallic layer thicknesses (h_{Ag}). This is obvious because the larger the thickness of the metallic layer, the lesser will be the transmission of electromagnetic waves through it [132]. Finally, after manually optimizing our design in its parametric domain, we found that R = 6 nm, h_{Ag} = 8 nm , and g = 1.5 nm could be an optimal choice for our meta-glass design.

The portion of UV, VIS, IR, and total solar heat transmitted through a window over a given spectral range is defined as ultraviolet transmittance (UVT), visible transmittance (VT), infrared transmittance (IRT), and solar heat gain coefficient (SHGC), respectively. A general expression for FOM is given by [141]:

$$\mathrm{FOM} = \frac{\int_{\lambda_{\min}}^{\lambda_{\max}} I_{\mathrm{solar}}(\lambda) T(\lambda) \mathrm{d}\lambda}{\int_{\lambda_{\min}}^{\lambda_{\max}} I_{\mathrm{solar}}(\lambda) \mathrm{d}\lambda} \tag{3.2}$$

where $I_{\mathrm{solar}}(\lambda)$ and $T(\lambda)$ are termed as solar irradiance of sun at sea level and wavelength dependent transmission, respectively [37]. The spectral window for UVT, VT, IRT, and SHGC are 200–400 nm, 400–750 nm, 750–1800 nm, and 200–1800 nm, respectively [153]. Since, we optimized our window for typical hot climate condition, ideal values are FOM are: UVT = 0, VT = 1, IRT = 0, and SHGC = 0.43.

Figures 3.8(a)–3.8(e) show numerically obtained spectral response for different choices of metallic NPs: molybdenum (Mo), aluminium (Al), magnesium (Mg), lead (Pb), and Zinc (Zn). In Fig. 3.8(f), we compared their performance by introducing the figure of merit (FOM) used in the industry [7]. Based on these parameters, we find that Mg or Al NPs based meta-glasses are suitable for efficiently blocking the UV portion of the solar radiation. If blocking IR radiation is a priority, then Zn NPs based meta-glasses could be the best choice. However, since we want to maintain visible transmittance around 60%, Mo NPs based meta-glasses could be considered as the best choice among all.

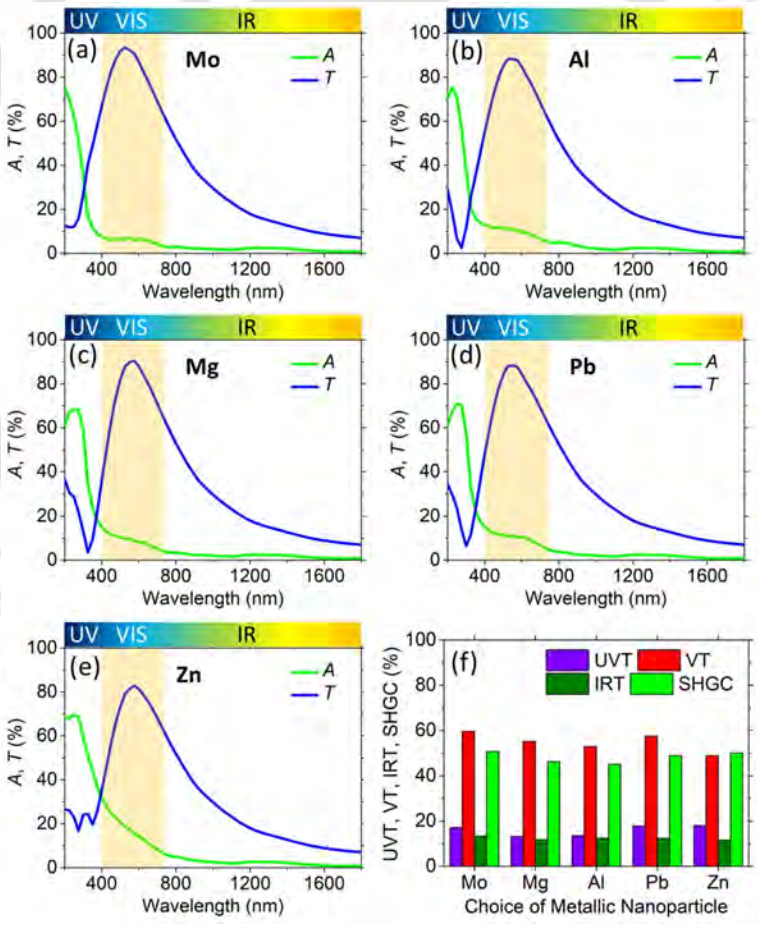

Figure 3.8: Numerically calculated spectral characteristics of meta-glasses for different choices of NPs: (a) molybdenum, (b) aluminium, (c) magnesium, (d) lead, and (e) zinc. Figure of merit comparison among our designs depicted in (a)–(e). Note: ideal values of ultraviolet transmittance (UVT), visible transmittance (VT), infrared transmittance (IRT), and solar heat gain coefficient (SHGC) are 0, 1, 0, and 0.43 over 200–1800 nm spectral range.

3.2.3 Summary

We presented a **new design of meta-glasses** capable of blocking ultraviolet and infrared radiations efficiently. By introducing different choices of metallic nanoparticles inside the dielectric layer of a metal–dielectric–metal cavity, we could achieve more than 90% UV and IR blocking while maintaining 60% visible transmittance. Our thin-film coatings may be applied on vehicle windows to provide ambient indoor temperature and brightness and improve the vehicle's performance.

3.3 Multilayer Thin-film Based Nanophotonic Passive Windows

The previous subsections 3.1 and 3.2 discussed designs of nanoring- and nanoparticle based passive windows, respectively. Although they have good infrared blocking capability, they are suitable only for hot climate conditions. Moreover, the fabrication of such complex structures require either lithography or costly nanofabrication facilities, which will eventually increase the overall cost of production. Therefore, a lithography-free and large-area compatible design of windows is highly desirable.

This section introduces a design based on metal–insulator–metal (MIM) multilayer thin-films for nanophotonic passive windows, where the insulator (dielectric) layer is sandwiched between the two metallic layers. Throughout this thesis, hereafter, the terms 'insulator' and 'dielectric' are used interchangeably. For a simplistic design, we chose to keep top and bottom metal layers identical throughout this work. For metallic layers, we use noble metals [gold (Au) and silver (Ag)] as well as alternative materials [copper (Cu), indium tin oxide (ITO), aluminium-doped zinc oxide (AZO), and aluminium oxynitride (ALON)], considering six separate cases. In each of those cases, we use either silicon dioxide (SiO_2) or titanium dioxide (TiO_2) or silicon (Si) as a dielectric layer to design spectrally selective window glasses. With optimal choice of materials and thicknesses of the metal and the dielectric layers, our lithography-free simple de-

sign could provide climate-specific solutions for passive windows with desired visible and infrared transmission or blocking capability.

3.3.1 Principles behind Controlling the Transmission of Solar and Non-solar Radiations

It is important to note that along with the IR regime, which contributes to 53% of the total solar irradiance, the visible regime also contributes to a significant 44% to the total radiation energy [37]. The solar radiation mainly comprises visible (400–750 nm), near-infrared (NIR; 750–1000 nm), and part of short-wave infrared (SWIR; 1000–1800 nm) wavelengths. Alongside solar radiation, non-solar radiation may also contribute towards radiative heating inside the room [154–156]. The non-solar radiation comprises mid-wave infrared (MWIR; 3–8 μm), long-wave infrared (LWIR; 8–15 μm), and far-infrared (FIR; 15–30 μm) wavelengths. On a hot day, radiation in MWIR and LWIR regime accounts for the non-solar radiation coming from the heated objects (nearby buildings, vehicles, and streets). The non-solar radiation can be attributed to the characteristics blackbody radiation of an object at a particular temperature, emitting at a characteristic wavelength [15]. An ideal window designed for hot climate condition should have strong attenuation in NIR and SWIR, strong reflection in MWIR and LWIR, while allowing good transmission in the visible regime [7, 155, 157]. On the contrary, for cold climate, it might be desirable to allow transmission in visible, NIR, and SWIR, alongside strong reflection in MWIR and LWIR. While majority of the works in the literature focus on designing window glasses only for hot climate condition [37, 41, 155, 157–160], we present solutions for different climatic conditions.

Our objective is to develop a low-cost passive window with improved solar radiation control providing vivid solutions for different climate conditions. Figure 3.9(a) shows an artistic view of our proposed window designs. Our window can operate by either allowing or blocking visible and/or IR radiation, selectively. We propose

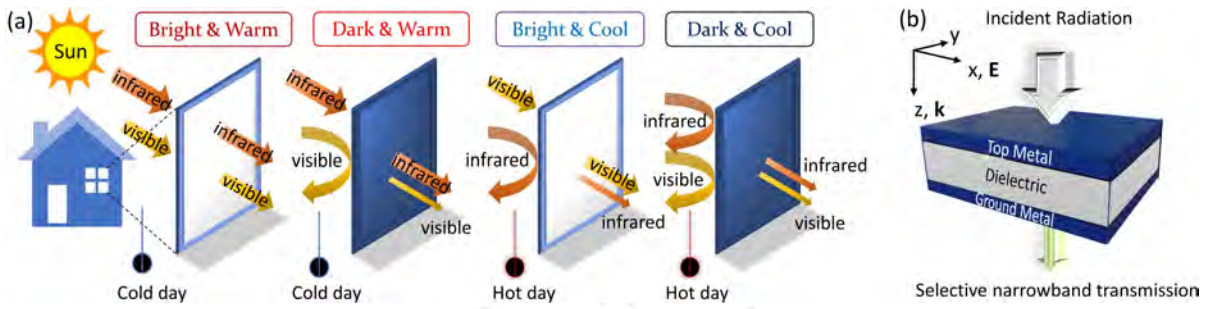

Figure 3.9: (a) Pictorial demonstration of our window operating in different modes in cold and hot climate. For cold climate the window can work in 'bright and warm' (BW) mode (allowing both visible and IR) or 'dark and warm' (DW) mode (blocking visible but allowing IR) when radiative heating is desired with controlled illumination. During hot climate the windows can work in 'bright and cool' (BC) mode (allowing visible but block IR) and 'dark and warm' (DW) mode (blocking both visible and IR) when controlled illumination is desirable but radiative heating is undesirable to maintain ambient room temperature. (b) Metal–insulator–metal (MIM) thin-film in a three-dimensional schematic view. Note that the incident radiation is a plane wave travelling in the z-direction with **E** field aligned along the x-direction (TM polarization).

four possible modes of operations, namely 'bright and warm' (BW) mode (allowing both visible and IR), 'dark and warm' (DW) mode (blocking visible but allowing IR), 'bright and cool' (BC) mode (allowing visible but blocking IR), and 'dark and cool' (DC) mode (blocking both visible and IR). The BW and DW modes are useful for cold climate when radiative heating is desirable inside a cold room to maintain an ambient temperature. In contrast, BC and DC modes which essentially block IR radiation can come handy for hot climate when allowing radiative heat to enter a building becomes undesirable. These window glasses are also capable of controlling indoor illumination by filtering visible radiation. Here, we emphasize that, out of the four possible modes, BC, BW, and DW modes are more significant from window design consideration in homes, offices, and passenger vehicles. Whereas DC mode is more appropriate for applications such as skylight panels for cold storage facilities; that can be addressed using our broadband absorber for solar radiation spectrum; [137, 142] presented in chapter 6 of this thesis.

A 3D schematic view of our proposed design is shown in Fig. 3.9(b). It con-

sists of identical top and bottom metallic layers with a dielectric layer sandwiched between them. The top and bottom metal layers thickness is kept 5 nm throughout this work. Whereas the dielectric thickness is manually optimized from a range of values (between 37 and 75 nm) depending upon the metal–dielectric combination used; to achieve maximum transmission at the desired wavelength. Importantly, the metallic layer thickness should be such that the electromagnetic radiation can penetrate through the MIM structure [133]. When an electromagnetic radiation falls on the surface of the top metal, it penetrates through the metallic layer, undergoes multiple back and forth reflections inside the dielectric cavity and eventually a narrowband electromagnetic spectrum is transmitted through the bottom metallic layer. The narrow-band transmission can be attributed to the Fabry–Perot cavity resonance, which allows transmission of only those spectral components corresponding to the resonance wavelength of the cavity. This resonance wavelength is given by Eq. (2.18) [131]. Note that, for the light to be trapped inside the cavity, phase condition in Eq. (2.18) must be satisfied. The underlying principle is that phase accumulated over a complete round trip inside the dielectric cavity must be an integral multiple of 2π to achieve constructive interference, which will eventually lead to the enhanced transmission at specific wavelengths through the bottom metallic layer.

3.3.2 Simulation and Theoretical Analysis

Figure 3.10(a) depicts a 2D simulation design model of the considered unit cell. The simulation is carried out using the wave optics module of COMSOL Multiphysics® (a commercial FEM solver), over solar (400–1800 nm) as well as non-solar (3–30 μm) radiation spectral range. The refractive indices of dielectrics—SiO_2, TiO_2, and Si are taken as 1.46, 2.54, and 3.57, respectively. Perfectly matched layers (PML) are introduced to avoid any anomaly arising from reflections due to confinement of the simulation domain. The air layer thickness is kept at $\lambda_{max}/2$, where λ_{max} is the maximum wavelength

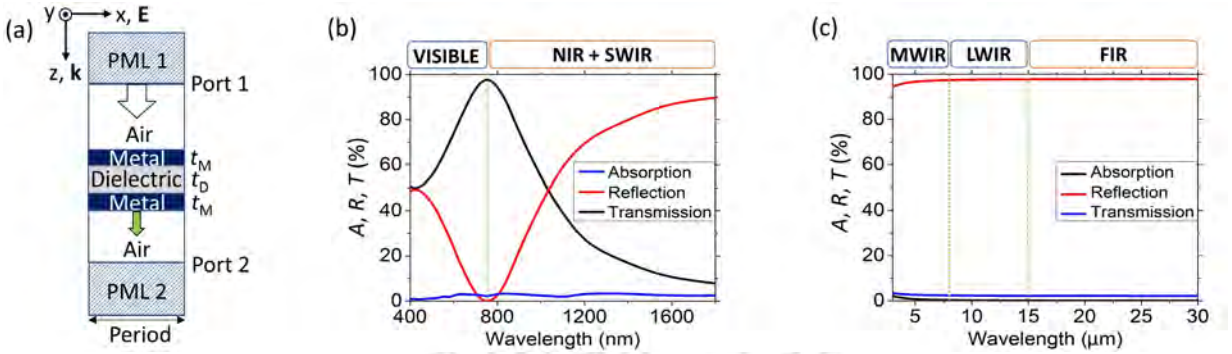

Figure 3.10: Metal–insulator–metal (MIM) thin-film in (a) two-dimensional (2D) simulation model depicting a unit cell. The incident radiation from port 1 is a plane wave travelling in the z-direction with **E** field aligned along the x-direction (TM polarization) and optical response is measured at port 2. Perfectly matched layers (PML) are used at the top and bottom of the unit cell to avoid any anomaly arising from reflections due to confinement of the simulation domain. Simulated absorption, reflection, and transmission spectra are shown for (b) solar and (c) non-solar radiation spectra, considering top and bottom metal as silver, each 5 nm thick, and a dielectric having fixed refractive index ($n_D = 2.2$) and thickness ($t_D = 60$ nm).

in the considered range. Periodicity of the unit cell is considered 200 nm, implemented with Floquet boundary condition. Physics controlled mesh is applied with fine element size for enhanced accuracy. The optical constants for metals such as Au [161], Ag [161], Cu [161], ITO [162], AZO [163], and ALON [164] are taken from the literature.

To understand how light is getting trapped inside our MIM structure, we study transmittance, reflectance, and absorbance profiles considering top and bottom metal layers of silver, each 5 nm thick and a dielectric having fixed refractive index ($n_D = 2.2$) and thickness ($t_D = 60$ nm), for both solar and non-solar radiation spectra. For a linearly polarized plane wave normally incident on the MIM structure, we observe a transmission resonance peak at 750 nm wavelength, as shown in Fig. 3.10(b). For the case of the non-solar spectrum, shown in Fig. 3.10(c), a significant 97.5% of the total incident radiation is reflected from the surface of the MIM structure. This could be useful in attaining and maintaining ambient room temperature.

The magnitude of normalized electric field (**E**) distribution corresponding to resonance wavelength is shown in Fig. 3.11(a), which clearly depicts the presence of reso-

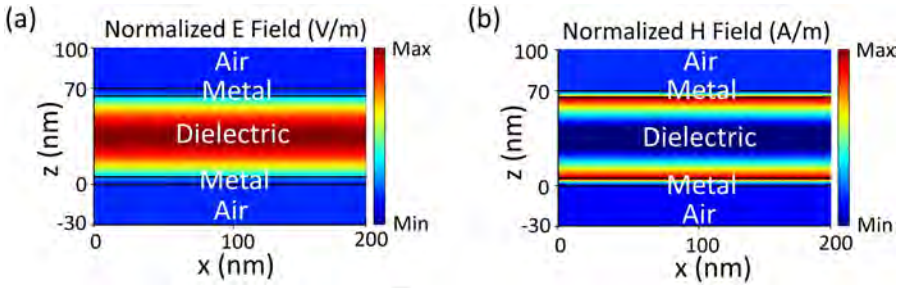

Figure 3.11: Simulated (a) normalized electric field (**E**) and (b) normalized magnetic field (**H**) distribution for the unit cell shown in Fig. 3.10(a), showing presence of electric resonance mode trapped inside the dielectric layer and magnetic resonance mode mostly confined at the metal–dielectric interface along the z-axis at resonance wavelength ($\lambda_0 = 750$ nm).

nant mode trapped inside the dielectric layer. The magnitude of normalized magnetic field (**H**) distribution is depicted in Fig. 3.11(b), showing magnetic resonance, mostly confined at the metal–dielectric interface. However, since we consider metal thickness to be less than the skin depth, these supported resonance modes are leaky and can be coupled to the incident and transmitted electromagnetic radiation. This leads to an enhanced transmission when the resonance condition is satisfied.

To validate our simulation findings, we apply dual theory: transfer matrix method (TMM) and Fabry–Perot interferometer (FPI) technique. Using TMM, we consider a linearly polarized plane wave incident on MIM thin-film structure. The medium is assumed to be linear, homogeneous, and non-magnetic. It is important to note that the incident wave falling from air medium to MIM structure undergoes reflection, transmission, and absorption, multiple times before it is finally transmitted through the bottom metallic layer. To satisfy the boundary conditions, the electric (**E**) and magnetic (**H**) fields must be continuous across the boundaries. For the case of our MIM structure, there are five layers (air–metal–dielectric–metal–air) and four interfaces (1, 2, 3, and 4), as shown in Fig. 3.12(a). For a MIM based design, phase shift at each layer can be represented as [131]:

$$k_{\mathrm{M}}\Lambda = k_0(2\tilde{n}_{\mathrm{M}}t_{\mathrm{M}}\cos\theta_{\mathrm{i},2})/2 \tag{3.3a}$$

$$k_{\mathrm{D}}\Lambda = k_0(2n_{\mathrm{D}}t_{\mathrm{D}}\cos\theta_{\mathrm{i},3})/2 \tag{3.3b}$$

$$k_{\mathrm{M}}\Lambda = k_0(2\tilde{n}_{\mathrm{M}}t_{\mathrm{M}}\cos\theta_{\mathrm{i},4})/2 \tag{3.3c}$$

where, Λ is the optical path length difference between the first two reflected beams from each layer, $\tilde{n}_{\mathrm{M}}$ and t_{M} are the refractive index and thickness of each metallic layer, respectively, θ_{i} is the angle of incidence, k_0, k_{M}, and k_{D} are the propagation wavevectors in air, metal, and dielectric media, respectively. After solving the boundary conditions at each interface, incident and the reflected electric field can be written as:

$$E_1 = E_2\cos k_{\mathrm{M}}\Lambda + H_2(i\sin k_{\mathrm{M}}\Lambda)/Y_1 \tag{3.4a}$$

$$H_1 = E_2Y_1(i\sin k_{\mathrm{M}}\Lambda) + H_2\cos k_{\mathrm{M}}\Lambda \tag{3.4b}$$

$$E_2 = E_3\cos k_{\mathrm{D}}\Lambda + H_3(i\sin k_{\mathrm{D}}\Lambda)/Y_2 \tag{3.4c}$$

$$H_2 = E_3Y_2(i\sin k_{\mathrm{D}}\Lambda) + H_3\cos k_{\mathrm{D}}\Lambda \tag{3.4d}$$

$$E_3 = E_4\cos k_{\mathrm{M}}\Lambda + H_4(i\sin k_{\mathrm{M}}\Lambda)/Y_3 \tag{3.4e}$$

$$H_3 = E_4Y_3(i\sin k_{\mathrm{M}}\Lambda) + H_4\cos k_{\mathrm{M}}\Lambda \tag{3.4f}$$

where,

$$Y_1 = \sqrt{\frac{\epsilon_0}{\mu_0}}\tilde{n}_{\mathrm{M}}\cos\theta_{\mathrm{i},2}, Y_2 = \sqrt{\frac{\epsilon_0}{\mu_0}}n_{\mathrm{D}}\cos\theta_{\mathrm{i},3}, Y_3 = \sqrt{\frac{\epsilon_0}{\mu_0}}\tilde{n}_{\mathrm{M}}\cos\theta_{\mathrm{i},4} \tag{3.5}$$

Here, Y_1, Y_2, and Y_3 represent the admittance in top metal, dielectric, and bottom metal layers, respectively; ϵ_0 and μ_0 are the permittivity and permeability of free space, respectively. Equation (3.5) refers to the TE polarization case when the *E* field is perpendicular to the plane of incidence. Similarly, for TM case when the *E* field is in the plane of incidence, Eq. (3.5) can be rearranged to get:

$$Y_1 = \sqrt{\frac{\epsilon_0}{\mu_0}}\frac{\tilde{n}_{\mathrm{M}}}{\cos\theta_{\mathrm{i},2}}, Y_2 = \sqrt{\frac{\epsilon_0}{\mu_0}}\frac{n_{\mathrm{D}}}{\cos\theta_{\mathrm{i},3}}, Y_3 = \sqrt{\frac{\epsilon_0}{\mu_0}}\frac{\tilde{n}_{\mathrm{M}}}{\cos\theta_{\mathrm{i},4}} \tag{3.6}$$

Writing the above Equations in matrix form we obtain:

$$\begin{bmatrix} E_1 \\ H_1 \end{bmatrix} = \mathbf{P_1}\begin{bmatrix} E_2 \\ H_2 \end{bmatrix}, \begin{bmatrix} E_2 \\ H_2 \end{bmatrix} = \mathbf{P_2}\begin{bmatrix} E_3 \\ H_3 \end{bmatrix}, \begin{bmatrix} E_3 \\ H_3 \end{bmatrix} = \mathbf{P_3}\begin{bmatrix} E_4 \\ H_4 \end{bmatrix} \tag{3.7}$$

where,

$$\mathbf{P_1} = \begin{bmatrix} \cos k_{\mathrm{M}}\Lambda & (i\sin k_{\mathrm{M}}\Lambda)/Y_1 \\ Y_1 i\sin k_{\mathrm{M}}\Lambda & \cos k_{\mathrm{M}}\Lambda \end{bmatrix} \tag{3.8a}$$

$$\mathbf{P_2} = \begin{bmatrix} \cos k_{\mathrm{D}}\Lambda & (i\sin k_{\mathrm{D}}\Lambda)/Y_2 \\ Y_2 i\sin k_{\mathrm{D}}\Lambda & \cos k_{\mathrm{D}}\Lambda \end{bmatrix} \tag{3.8b}$$

$$\mathbf{P_3} = \begin{bmatrix} \cos k_{\mathrm{M}}\Lambda & (i\sin k_{\mathrm{M}}\Lambda)/Y_3 \\ Y_3 i\sin k_{\mathrm{M}}\Lambda & \cos k_{\mathrm{M}}\Lambda \end{bmatrix} \tag{3.8c}$$

Here $\mathbf{P_1}$, $\mathbf{P_2}$ and $\mathbf{P_3}$ denote the characteristics matrices which relate the fields at the interface across each layer. So, for our five layer thin-film system, each having a particular refractive index and thickness, the relation between *E* and *H* field of first and last interface is given by:

$$\begin{bmatrix} E_4 \\ H_4 \end{bmatrix} = \mathbf{P_1 P_2 P_3} \begin{bmatrix} E_1 \\ H_1 \end{bmatrix} = \mathbf{P} \begin{bmatrix} E_1 \\ H_1 \end{bmatrix} \equiv \begin{bmatrix} p_{11} & p_{12} \\ p_{21} & p_{22} \end{bmatrix} \begin{bmatrix} E_1 \\ H_1 \end{bmatrix} \tag{3.9}$$

For air media at the top and towards the bottom, using Eq. (3.5) and considering TE case, we obtain:

$$Y_0 = \sqrt{\frac{\epsilon_0}{\mu_0}} n_0 \cos\theta_{\mathrm{i},1}, Y_4 = \sqrt{\frac{\epsilon_0}{\mu_0}} n_0 \cos\theta_{\mathrm{t},4} \tag{3.10}$$

which gives:

$$\begin{bmatrix} E_{\mathrm{i},1} + E_{\mathrm{r},1} \\ (E_{\mathrm{i},1} - E_{\mathrm{r},1}) Y_0 \end{bmatrix} = \mathbf{P_1} \begin{bmatrix} E_{\mathrm{t},2} \\ H_{\mathrm{t},2} Y_4 \end{bmatrix} \tag{3.11}$$

In order to find out reflection (r) and transmission (t) coefficients, we expand the matrices in above Eq. (3.11) as:

$$r = \frac{(Y_0 p_{11} + Y_0 Y_4 p_{11}) - (p_{21} + Y_4 p_{22})}{(Y_0 p_{11} + Y_0 Y_4 p_{11}) + (p_{21} + Y_4 p_{22})} \tag{3.12}$$

$$t = \frac{2Y_0}{(Y_0 p_{11} + Y_0 Y_4 p_{11}) + (p_{21} + Y_4 p_{22})} \tag{3.13}$$

Finally, the reflection (R) and transmission (T) can be obtained using $R = |r|^2$ and $T = |t|^2 (n_\mathrm{t} \cos\theta_\mathrm{t})/(n_\mathrm{i} \cos\theta_\mathrm{i})$, respectively. The absorption (A) can be obtained by using $A = 1 - R - T$.

Alongside TMM, we have also used FPI technique to determine the resonant wavelength of the cavity. The structure shown in Fig. 3.12(b) can be considered similar to a Fabry–Perot resonator cavity, where the two metals act as lossy mirrors which are partially transparent and the dielectric can be regarded as the cavity medium. Eq. (2.18) depicts the condition for peak transmission which occurs in integral multiples of 2π.

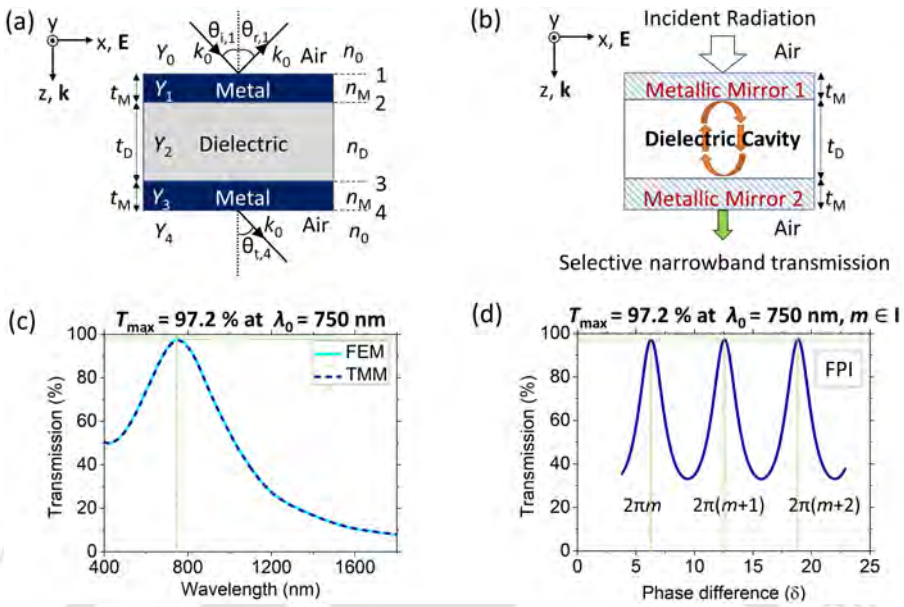

Figure 3.12: Detailed schematic of the proposed structure using (a) TMM and (b) FPI technique. Here, t, Y, n, and k represent the thickness, admittance, refractive index, and wavevector of the corresponding layer, respectively. The transmission spectra in (c) show a comparison between FEM and TMM. Using FPI technique, the condition for peak transmission which occurs in integral multiples of 2π is shown in (d). All methods accurately predict the resonance condition at $\lambda_0 = 750$ nm with a peak transmission of 97.2%, highlighted by dotted green cross lines.

The sharpness of the peak is defined by finesse (F), given by: $F = 4R/(1-R)^2$ [134]. For this case, transmission through Fabry–Perot cavity is given by: $T = \kappa/(1 + F\sin^2\delta)$ where, κ is the correction factor which takes care of absorbance (A) due to intrinsic losses in metallic mirrors and can be written as: $K = (1 - A - R)/(1 - R)$ [135]. The peak transmission condition can be obtained by rewriting Eq. (2.18) in terms of new parameter δ as:

$$\delta = \frac{4\pi}{\lambda_0} n_{\mathrm{D}} t_{\mathrm{D}} \cos\theta_{\mathrm{D}} = 2\pi m \tag{3.14}$$

where, θ_{D} is the angle of incidence inside a dielectric medium. In this section, we presented an in detail theoretical analysis for a five-layer thin-film system. This theory can be extended to find absorption, reflection, and transmission across any system

having multiple layers for normal as well as the oblique angle of incidence.

For applications such as color filter and switching, which require low tunability but high quality-factor (narrowband resonance), thick metal is desirable [165]. However, for designing our window glasses, a low quality-factor (broadband resonance) is desirable to achieve high peak transmission at the resonance wavelength and cover a larger spectrum of visible and IR radiation. Specific dimensions of the metal and dielectric layers are obtained after manually optimizing the design in its parametric domain, as discussed in the parametric analysis subsection.

3.3.3 Verification of Simulation Results using Theoretical Model

A comparison among FEM, TMM, and FPI transmission spectra at normal incidence is shown in Figs. 3.12(c) and 3.12(d). Here, we consider top and bottom metal as silver, each 5 nm thick and a dielectric having fixed refractive index (n_{D} = 2.2) and thickness (t_{D} = 60 nm). An excellent agreement is seen between simulation (FEM) and theory (TMM). It can be predicted from Eq. (3.14) that, FPI technique accurately predicts the resonant wavelength ($\lambda_0 = 750$ nm), with a peak transmission of 97.2%, which exactly matches with TMM and FEM transmission peaks [see Figs. 3.12(c) and 3.12(d)]. Such a good agreement, indeed, validates our simulation results. For the rest of our work, TMM and FEM will be used to produce theoretical and simulation results. Pleasantly in all the studies, TMM and FEM spectra are in excellent agreement.

3.3.4 Parametric Analysis of Layer Thickness and Refractive Index

To optimize our MIM thin-film design, we study the effect of the device dimensions and explore different materials that can help us obtain desirable optical properties. The resonance wavelength can be tuned by changing either the refractive index (n_{D}) or the thickness (t_{D}) of the dielectric layer. To cross-check, we studied three cases by taking n_{D} as 1.5, 2.25, and 3, keeping other parameters constant (top and bottom metal is gold

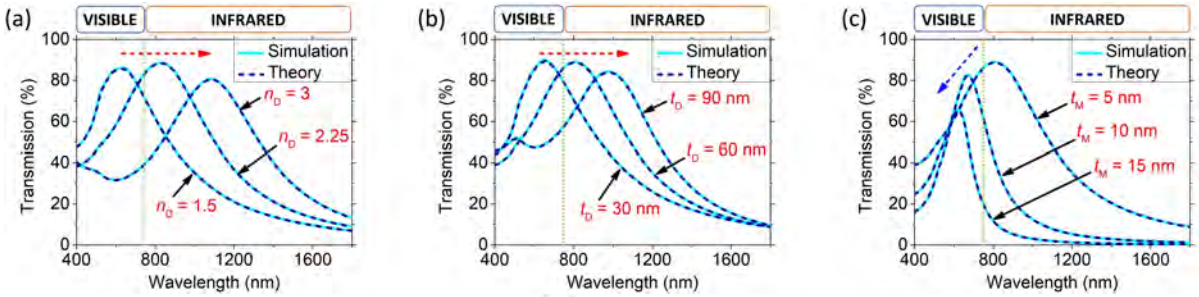

Figure 3.13: Parametric study of MIM structure for varying (a) refractive index of the dielectric, n_{D}, (b) thickness of the dielectric, t_{D}, and (c) thickness of top and bottom metal, t_{M}, keeping other parameters constant in each case. Note that the top and bottom metals are chosen as gold in each case.

(Au), each 5 nm thick, and dielectric layer being 60 nm thick). We observe a clear redshift in the resonance wavelength with an increase in the refractive index of the dielectric [see Fig. 3.13(a)]. The reason can be attributed to the slow propagation of light with an increase in the refractive index of the medium, or in other words light virtually covers a longer path [166]. Hence, a mode with a larger resonant wavelength is supported by the cavity. Similar reasoning can be applied to understand the effect of the increase in the thickness of the dielectric t_{D}, which shows a prominent redshift [see Fig. 3.13(b)]. Here we take t_{D} as 30 nm, 60 nm, and 90 nm, keeping other parameters unchanged (top and bottom metal are Au each 5 nm thick, with a dielectric having n_{D} = 1.5).

Next, we change the thickness of both top and bottom metal layers by taking t_{M} as 5 nm, 10 nm, and 15 nm for each, keeping other parameters constant (top and bottom metal is Au, with a dielectric having n_{D} = 2.2 and t_{D} = 60 nm). We observe a clear drop in the overall transmission profile [see Fig. 3.13(c)]. This is quite obvious as increasing the metal thickness will cause a decrease in the transmission amplitude [129]. Importantly, change in metal thickness changes the quality-factor of the transmission profile. Hence, we choose the top and bottom metal layer thickness as 5 nm each for all our future designs, unless specified.

3.3.5 Passive Climate-specific Window Glasses

To operate under different modes, the key idea is to choose appropriate material for the dielectric layer that gives resonance peak at the desired wavelength. Here we focus on designing MIM thin-film based passive window glasses that can work in three different modes of operation namely BC, BW, and DW modes. The transmission spectra obtained using different metal and dielectric combinations are shown in Fig. 3.14. For instance, in BW mode, 750 nm is the desired resonance wavelength to achieve maximum transmission in both visible and IR spectral regimes. We found that refractive indices of SiO_2, TiO_2, and Si, make them suitable candidates for our passive glasses to operate under different modes.

For our first design, shown in Fig. 3.14(a), we choose Au as top and bottom metal layers, each 5 nm thick, and a dielectric layer of 37 nm thickness. Here, Au–SiO_2–Au based glass works in BC mode which essentially allows visible but blocks IR radiation. Similarly, Au-TiO_2-Au based glass works in BW mode which allows both visible and IR radiation. Lastly, Au–Si–Au based glass works in DW mode which effectively blocks visible but allows IR radiation. Using gold based design, a peak transmission up to 90% is achieved at the resonance wavelength—making gold a suitable choice for passive window glasses.

Although a very thin-film of metal is used for our design, gold being an expensive metal can increase the overall cost of large-area devices—limiting the widespread acceptance of our passive window technology. To reduce the overall cost of production, we explore the possibility of using relatively-inexpensive metals (such as silver and copper). Similar to the previous case with gold, for our second and third design, we use 5 nm thick silver and copper as metallic layers, having dielectric thickness of 45 nm and 41 nm, respectively. Using silver, we observe exceptional performance with over 97% peak transmission at the resonance wavelength [see Fig. 3.14(b)]. Similarly,

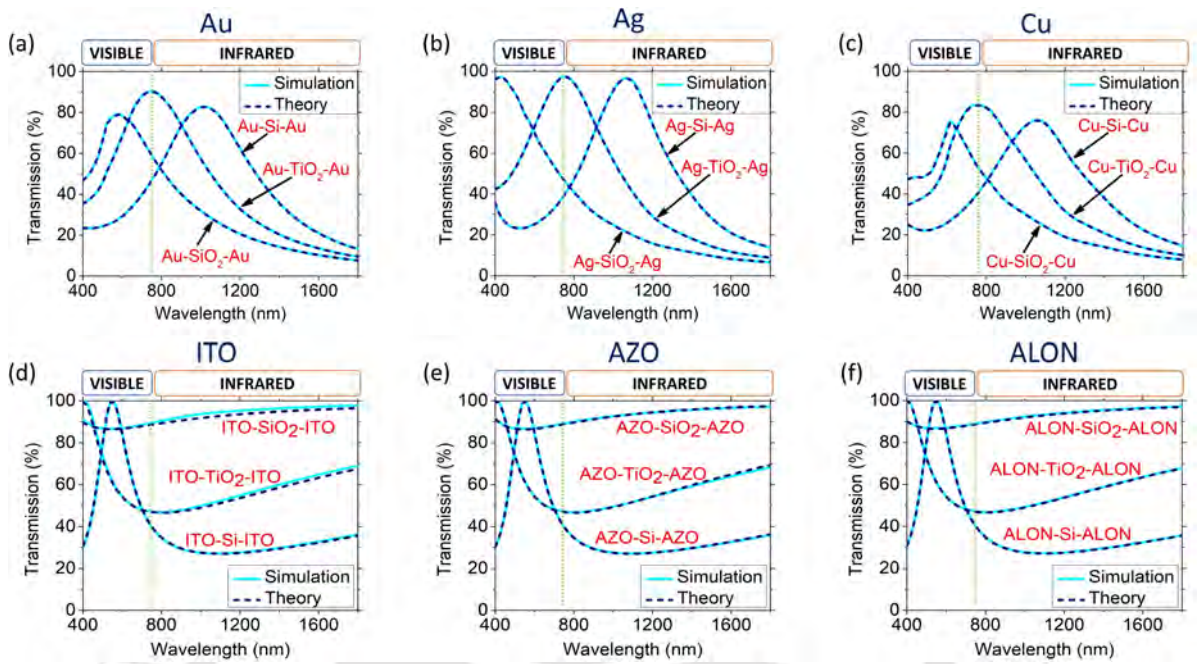

Figure 3.14: Design of MIM thin-films choosing metal as (a) gold, (b) silver, and (c) copper, which can work in three different modes of operation by choosing dielectric as SiO_2 for BC mode (useful in hot climate with illumination), TiO_2 for BW mode (useful in cold climate with illumination), and Si for DW mode (useful in cold climate without illumination). Similarly, design with metal as (d) ITO, (e) AZO, and (f) ALON can work in BC mode using silicon (Si), BW mode using SiO_2, and intermediate mode (useful in spring/autumn with illumination) using TiO_2. Here, each metallic layer is 5 nm thick, and dielectric layer thicknesses in (a), (b), (c), (d), (e), and (f) are 37 nm, 45 nm, 41 nm, 75 nm, 75 nm, and 75 nm, respectively.

copper also performed fairly well with up to 83% peak transmission at the resonance wavelength and can be considered as a cheaper alternative to both gold and silver [see Fig. 3.14(c)].

To further explore the possibility of making the design low-cost, we also explored the use of transparent conductive oxides (TCOs) as metallic layers. We observe that optically transparent metal oxides such as ITO, AZO, and ALON can provide some unique optical responses. In contrast to the previous case with noble metals (Au, Ag, and Cu), TCOs offer a precise control over the amount of IR radiation allowed to pass through our passive window. For example, ITO–SiO_2–ITO based glass allows almost 95% IR transmission while maintaining visible transmission at 88%, useful during win-

ter [see Fig. 3.14(d)]. In contrast, ITO–Si–ITO based glass allows only 30% IR transmission, keeping visible transmission still high at 65%, useful during summer. The intermediate solution is given by ITO–TiO_2–ITO based glass which can be useful during pleasant spring/autumn. Therefore, an efficient and precise control over IR blocking make such MIM based glasses suitable for providing climate-specific solution. Similar results are obtained using AZO as metal [see Fig. 3.14(e)].

However, with the ever-growing popularity of ITO and AZO among the research community, the industry demand has also grown up exponentially [162]. Consequently, the prices of these metals are bound to rise in the near future. Here, we introduce ALON, which is a low-cost, abundant, lightweight, and toughest poly-crystalline transparent glass available in the market [167]. Its performance is at par with ITO and AZO [see Fig. 3.14(f)]. Unique optical and mechanical properties make it suitable for high performance, portable, bulletproof, and blast-resistant windows that can be used for military vehicles, fighter aircrafts, and submarine applications [168]. A summary of passive window glass specifications including its design parameters and different modes of operation is listed in Table 3.2.

3.3.6 Effect of Different Polarizations and Incident Angles

As our passive window will face sunlight at diverse incident angles throughout the day, analysis of such structure is incomplete without studying the effects of polarization and incident angle of solar radiation on the window's performance. Hence, we also study both TM and TE polarizations using Ag (5 nm) as metal and SiO_2 as a dielectric for BC mode, TiO_2 for BW mode, and Si for DW mode, each 45 nm thick. Figure 3.15(a) confirms that the transmission profile is not affected by the change in polarization, making our design polarization-independent. Besides, we also study the angle sensitivity, ranging over 0 – 85 degrees of angle of incidence using Ag–TiO_2–Ag based glass. Figures 3.15(b) and 3.15(c) show that the transmission efficiency for both

Table 3.2: Detailed specifications of our MIM thin-films for passive windows[a,b]

Choice of Metal	Mode of Operation	MIM Structure (thickness in nm)	λ_{max} (nm)	T_{max} (%)	T_{wings} (%)		θ_{max} (degree)	
					Left	Right	TM	TE
Au	BC	Au (5)–SiO_2 (37)–Au (5)	580	79.3	46.9	7.7	77	77
	BW	Au (5)–TiO_2 (37)–Au (5)	750	90.3	35.4	9.5	77	77
	DW	Au (5)–Si (37)–Au (5)	1020	82.8	23.7	13.3	78	78
Ag	BC	Ag (5)–SiO_2 (45)–Ag (5)	430	97.2	96.4	6.6	76	77
	BW	Ag (5)–TiO_2 (45)–Ag (5)	750	97.5	42.5	8.7	77	77
	DW	Ag (5)–Si (45)–Ag (5)	1070	96.6	35.8	13.7	78	78
Cu	(BC	Cu (5)–SiO_2 (41)–Cu (5)	615	75.5	47.2	7.9	77	77
	BW	Cu (5)–TiO_2 (41)–Cu (5)	750	83.4	34.6	10.0	77	77
	DW	Cu (5)–Si (41)–Cu (5)	1060	76.1	25.3	14.7	78	78
ITO	BW	ITO (5)–SiO_2 (75)–ITO (5)	1800	96.5	89.7	96.5	80	80
	IMD	ITO (5)–TiO_2 (75)–ITO (5)	400	99.2	99.2	67.6	83	83
	BC	ITO (5)–Si (75)–ITO (5)	550	99.9	30.8	35.6	82	82
AZO	BW	AZO (5)–SiO_2 (75)–AZO (5)	1800	97.5	91.3	97.5	80	80
	IMD	AZO (5)–TiO_2 (75)–AZO (5)	400	99.3	99.3	69.4	83	83
	BC	AZO (5)–Si (75)–AZO (5)	550	99.9	30.4	36.3	82	82
ALON	BW	ALON (5)–SiO_2 (75)–ALON (5)	1800	96.9	90.1	96.9	80	80
	IMD	ALON (5)–TiO_2 (75)–ALON (5)	400	99.9	99.9	67.2	83	83
	BC	ALON (5)–Si (75)–ALON (5)	550	99.9	30.9	35.6	82	82

[a] All the values are calculated for solar spectral regime over 400 – 1800 nm wavelengths.
[b] λ_{max}: wavelength of the maximum transmission, T_{max}: maximum transmission, T_{wings}: transmission at the left and right wings taken at 400 nm and 1800 nm, respectively, θ_{max}: the angle of incidence up to which the average transmittance is $\geq$ 90% over solar spectral regime, BC: Bright and Cool, BW: Bright and Warm, DW: Dark and Warm, IMD: **i**nter**med**iate.

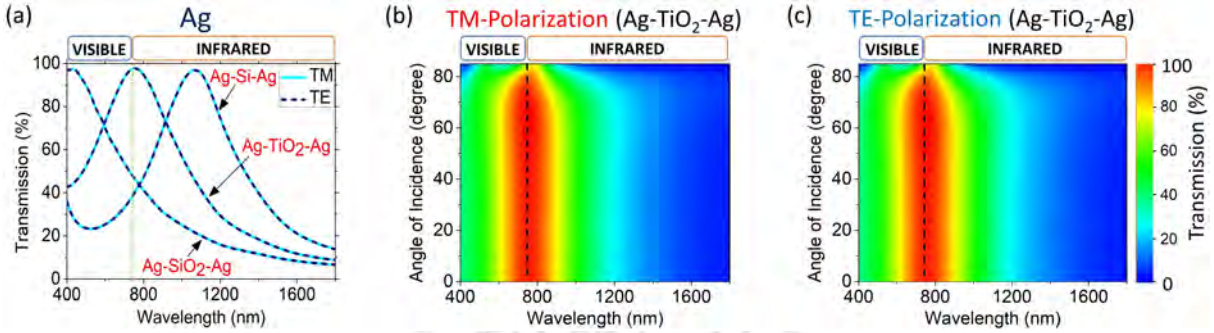

Figure 3.15: Simulated transmission plot showing (a) both TM and TE polarization using Ag (5 nm) as metal and SiO_2 as a dielectric for BC mode, TiO_2 for BW mode, and Si for DW mode, (each dielectric layer being 45 nm thick); showing polarization insensitivity. Contour plot for incident-angle dependent transmission spectrum of Ag–TiO_2–Ag based MIM structure showing over 90% transmission efficiency for a wide angle of incidence (up to 77 degrees) for both (b) TM, and (c) TE case.

TM and TE cases remain over 90% for a wide angle of incidence (up to 77 degrees), hence making our structure highly angle-insensitive. For the rest of the designs, the data are provided in Table 3.2. Practically, such a wide angle-insensitivity also indicates that the viewer is less likely to observe any color shift while viewing through the window glass. Thus, above properties make our structure highly efficient for daytime operation.

3.3.7 Figure of Merit of Our Passive Window Glasses

To compare the performance of our MIM thin-film based passive window glasses with previously reported and existing commercial windows, here, we introduce figure of merit (FOM) used in the industry [7, 157, 158]. The three main parameters include visible transmittance (VT), IR transmittance (IRT), and solar heat gain coefficient (SHGC), which basically gives the fraction of visible, infrared, and total solar radiation transmitted through a window glass over a specific wavelength window, respectively [37]. For our window glass design, the spectral range of VT, IRT, and SHGC lies within 400–750 nm, 750–1800 nm, and 400–1800 nm, respectively.

Alongside controlling the amount of heat radiatively transferred through the win-

dow glasses, illumination inside the room is equally an important aspect of a window design. For the case when maximum illumination inside the room is desirable, an ideal window designed for hot climate condition should have visible transmittance as high as possible, and IR transmittance as low as possible (VT $\rightarrow$ 1, IRT $\rightarrow$ 0), which corresponds to our BC mode. Whereas for cold climate, both VT and IRT should be as high as possible (VT, IRT $\rightarrow$ 1), which corresponds to our BW mode. On the contrary, for the case when minimum illumination is required for cold climate, ideally, VT should be as low as possible, and IRT should be as high as possible (VT $\rightarrow$ 0, IRT $\rightarrow$ 1), which corresponds to our DW mode. For calculating SHGC value of an ideal window in BC mode, we consider $T_{\text{visible}}(\lambda)$ = 1, and $T_{\text{IR}}(\lambda)$ = 0, which results in SHGC = 0.55, within 400 – 1800 nm spectral range. Similarly, for the case of BW and DW modes, the ideal SHGC value is 1 and 0.45, respectively, for the same spectral range. However, it is important to note that SHGC value for practical purposes may vary depending upon the geographical location.

Figure 3.16 shows a comparison among the figure of merit data obtained for various window glasses in BC, BW, and DW modes. The figure of merit obtained using our relatively inexpensive metals (Ag, Cu, ITO, AZO, and ALON) show overall better performance compared to those of industry-standard commercial windows and previously reported infrared-blocking plasmonic glasses, in terms of VT, IRT, and SHGC values obtained. Most of the previously reported works focus solely on blocking IR radiation and allowing visible radiation, which eventually falls under BC mode. Figure 3.16(a) shows a comparison of figure of merit for BC mode among our MIM thin-film based glasses and three double pane argon low-emissivity coating commercial windows (CW I, CW II, and CW III) [7, 8, 154]. The figure of merit obtained using our relatively inexpensive metals—specifically silver outperforms industry-standard commercial window glasses.

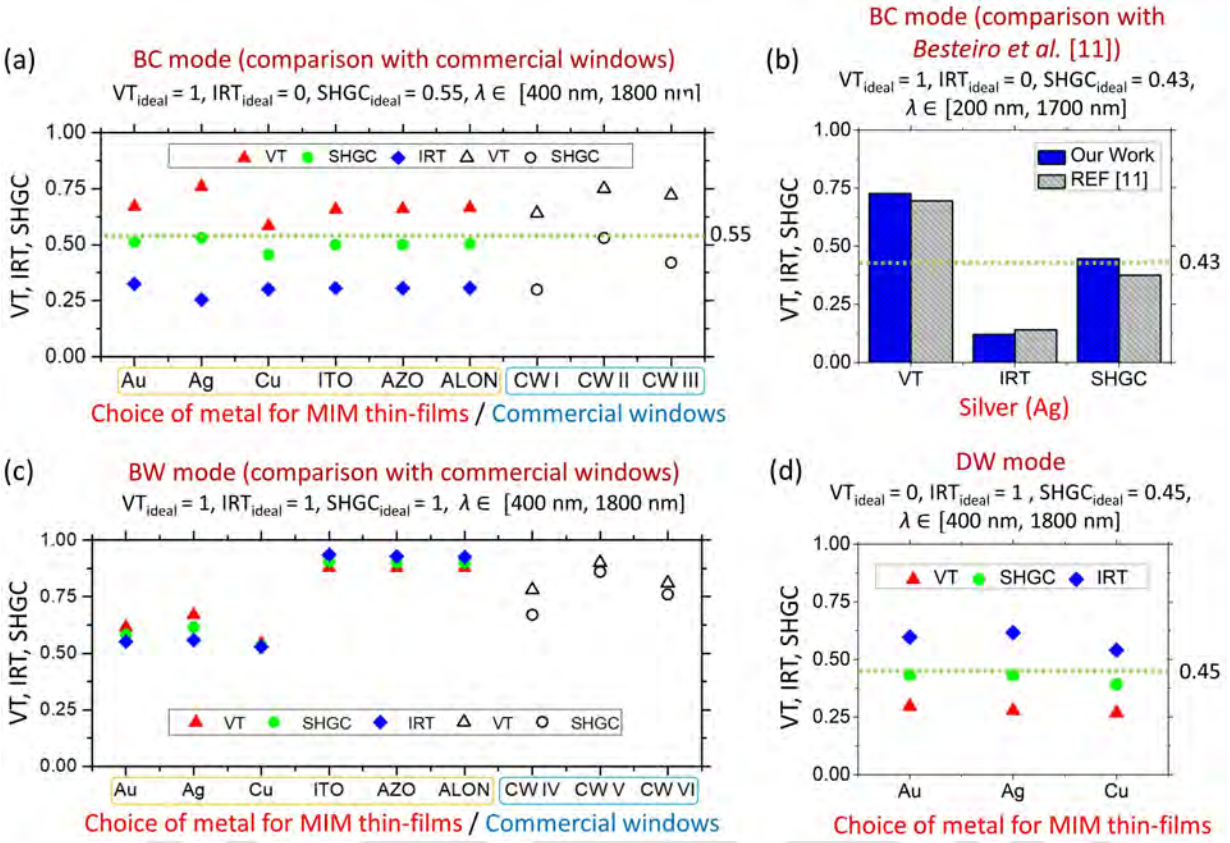

Figure 3.16: Figure of merit showing VT, IRT, and SHGC values for (a) BC mode, comparing our MIM thin-films (where, SiO_2 is used a dielectric layer for Au, Ag, and Cu based design, and Si is used as dielectric layer for ITO, AZO, and ALON based design) with three commercial double-pane argon low-emissivity coating glasses (CW I, CW II, and CW III) [7,154,157], (b) BC mode, comparing our Ag–SiO_2–Ag based glasses with Ag nanoshell based plasmonic glasses [37], (c) BW mode, comparing our MIM thin-films (where, TiO_2 is used as a dielectric layer for Au, Ag, and Cu based design, and SiO_2 is used as a dielectric layer for ITO, AZO, and ALON based design) with commercial double-glazed, high-solar-gain low-emissivity glass (CW IV), single- and double-pane clear glasses (CW V and CW VI) [7, 157], and (d) new DW mode, comparison among noble metals used in our MIM thin-films (Si is used as a dielectric layer).

Besteiro *et al.* reported the design of IR blocking plasmonic glasses using nanoshell, nanorod, and nanocup over 200 – 1700 nm spectral regime [37]. Out of the three cases, silver nanoshell based IR blocking plasmonic glasses produced the best result in terms of VT, IRT, and SHGC values obtained. Hence for comparison, we consider silver nanoshell based plasmonic glasses of Ref. [37] by taking the mean values of manually and computationally obtained data. For a fair comparison, we manually optimized the

design parameters of our silver-based MIM thin-film over the same spectral range *i.e.* 200 – 1700 nm, considering top and bottom Ag layer, each 8 nm thick; with 80 nm thick SiO_2 layer in between. The calculated ideal SHGC value over this spectral range is 0.43. Figure 3.16(b) shows that our silver based MIM thin-films show better performance in all the three parameters (VT, IRT, and SHGC) compared to silver nanoshell based plasmonic glasses of Ref. [37]. Especially, the SHGC values obtained by our design are very close to the ideal SHGC value.

Figure 3.16(c) shows figure of merit for BW mode, comparing our MIM thin-film based glasses with commercial double-glazed, high-solar-gain low-emissivity glass (CW IV), single and double pane clear glass windows (CW V and CW VI) [7, 157]. For this case, our alternative inexpensive materials (ITO, AZO, and AZO) outperform the commercial glasses in terms of figure of merit obtained. At last, for our new DW mode, silver shows overall better performance than gold and copper considering ideal VT, IRT, and SHGC values [see Fig. 3.16(d)]. Hence, the figure of merit obtained using our MIM thin-film based passive glasses is promising and these category of glasses can be used as a viable solution for different climate conditions.

3.3.8 Prospective Fabrication Techniques, Application, and Future Scope

For practical application, ordinary glasses may be coated with our prescribed MIM thin-films. These thin-films can be fabricated by successive electron beam (e-beam) evaporation method [169, 170]. Using this method, the bottom metallic layer of 5 nm thickness may be coated on a silica glass substrate, typically 5 mm thick [132]. Then the dielectric layer of appropriate thickness may be deposited on the top surface of the metal–substrate layer. At last, 5 nm thick top metallic layer may be coated at the top surface of dielectric–metal–substrate layer using an e-beam evaporator [171].

Passive glasses are cheap, durable, and require low maintenance compared to commercially available smart glasses [7, 34, 154]. Although, passive glasses do not offer

dynamic tunability, their transmission profiles can be adjusted to any of our specific modes according to the site requirement. These advantages can facilitate a wide acceptance of our passive window technology and can dramatically reduce the need for air-conditioning system [172].

3.3.9 Summary

We theoretically demonstrated metal–insulator–metal thin-film based passive windows for **uniquely controlling the amount of transmitted visible and infrared radiation, depending upon different specific climate conditions**. We explored noble metals (Au, Ag, Cu) alongside alternative materials (ITO, AZO, and ALON) to provide a cheaper alternative to commercially available windows. The figure of merit obtained for our passive glasses using relatively inexpensive materials (such as Ag, Cu, ITO, AZO, and ALON) outperform industry-standard commercial windows and previously reported infrared-blocking plasmonic glasses. The theoretical results obtained using transfer matrix method and Fabry–Perot interferometer technique perfectly match those of finite element method based full-wave numerical simulations. Our design is simple, lithography-free and hence large-area compatible, ultra-thin, polarization-independent, and angle insensitive (up to 83 degrees). These passive glasses can be integrated into security panels, privacy windows, advertising screens, room partitions, electronic curtains, and solar control skylight panels. Aluminium oxynitride based window glasses are suitable for high performance, portable, bullet-proof, and blast-resistant windows that can be used in high security buildings, military vehicles, fighter aircrafts, and submarine applications. A preliminary work towards the experimental realization of these passive windows is briefly mentioned in appendix A of this thesis.

3.4 Nanophotonic Passive Windows as Color Filters

As an extension of the work from the previous section 3.3, this section introduces spectrally selective transmission-mode nanophotonic color-filter windows. Such windows could be of huge interests in greenhouses. By providing suitable micro-climate inside greenhouses for photosynthesis, these polarization- and angle-insensitive color filters coated greenhouse glasses could significantly improve yield and quality of crop and reduce its maturation period.

3.4.1 Background

To meet the livelihood demands of the ever-growing world population, there is a dire need to look beyond conventional agriculture practices. For long-term sustainability, greenhouses can play a pivotal role to improve the yield and quality of crops which are otherwise difficult to grow locally [173]. It is worth mentioning that exposure to some particular wavelengths of visible light can remarkably improve crop yield and reduce the maturation period. For instance, for photosynthesis, plants utilize only those specific wavelengths of light which are related to absorption characteristics of different pigments such as chlorophyll A, chlorophyll B, and the carotenoids [174]. Among these pigments, chlorophyll A has absorption peaks at 430 nm and 662 nm wavelengths and considered as the primary pigment that accounts for nearly 75% of the photosynthetic activity [175]. Therefore, a design of spectrally selective transmission-mode color filter whose peak transmission exactly matches the peak absorption wavelengths, can significantly improve crop yield and reduce the maturation period. Reduced maturation period may bring down the water usage, electricity requirements, maintenance cost, and time to market.

Here, we present designs of metal–dielectric–metal (MDM) based transmission-mode color filters. Our objective is to design spectrally selective passive filters such

that peak transmission wavelength coincides with the peak absorption wavelengths of chlorophyll pigment A. For two different absorption peaks at 430 nm and 662 nm wavelengths, two different transmission-mode color filters are designed having peak transmission at those wavelengths. Here, we use silver (Ag) as the identical top and bottom metallic layers. The middle dielectric layer is made of visibly transparent polymethyl methacrylate (PMMA). By finding an optimal choice of dielectric thickness, the peak transmission of the MDM color filter is tuned to match the absorption peaks of chlorophyll pigment A.

3.4.2 Design, Results, and Discussion

Figure 3.17(a) depicts a three-dimensional (3D) artistic view of a greenhouse, where glasses A and B are chosen as reference for demonstrating designs of blue (design A) and red (design B) color transmission-mode filters. Figure 3.17(b) depicts a 2D schematic side view of MDM passive filter, where design A consists of Ag(27 nm)–PMMA(86 nm)–Ag(27 nm) thin-film to selectively transmit blue portion of the visible

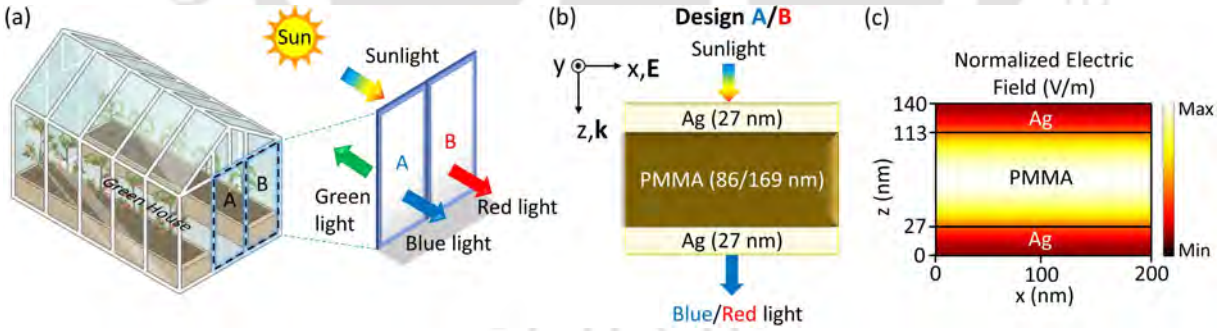

Figure 3.17: (a) A 3D artistic view of a greenhouse showing adjacent glasses A and B (taken as a reference) coated with metal-dielectric-metal (MDM) thin-film to selectively transmit blue and red portions of the visible spectra, respectively. (b) A 2D schematic side view of MDM thin-film, where the incidence radiation is a plane wave of TM polarization (**E** parallel to the plane of incidence) travelling along z-direction. Here, design A consists of Ag(27 nm)–PMMA(86 nm)–Ag(27 nm) thin-film to selectively transmit blue portion of the visible radiation. Similarly, design B consists of Ag(27 nm)–PMMA(169 nm)–Ag(27 nm) thin-film to selectively transmit red portion of the visible radiation. (c) normalized electric field (**E**) distribution for design A at 430 nm wavelength showing **E** field is mostly confined inside the dielectric layer.

radiation. Similarly, design B consists of Ag(27 nm)–PMMA(169 nm)–Ag(27 nm) thin-film to selectively transmit red portion of the visible radiation. These MDM thin-films can be approximated as a Fabry–Perot cavity where the top and bottom metallic layers are considered to be lossy metals and the middle dielectric layer acts as a resonator cavity. The resonance wavelength can be determined using [140]: $2Kn_{\mathrm{D}}t_{\mathrm{D}} + 2\phi = 2\pi m$ where, wavevector, $K = 2\pi/\lambda_{\mathrm{max}}$, λ_{max}: resonance wavelength for maximum transmission, t_{D} and n_{D} are the thickness and refractive index of the PMMA layer, respectively, the order of cavity resonance is given by integer value m, and ϕ denotes the total phase shift after reflection from the identical top and bottom metallic layers. The incident sunlight falls on the surface of the top Ag layer, penetrates through it, undergoes back and forth reflections inside the PMMA layer, and finally transmitted through the bottom Ag layer. When the accumulated phase becomes an integral multiple of 2π, the maximum transmission is allowed at that resonance wavelength [132]. Figure 3.17(c) shows normalized electric field distribution for design A at 430 nm wavelength showing electric field is mostly confined inside the dielectric layer.

For simulation we use COMSOL Multiphysics®, a finite element method solver, to obtain transmission spectra over the visible regime *i.e.* 400–750 nm wavelengths. For theoretical modelling we use transfer matrix method (TMM) to calculate the overall transmission through a multilayer structure [141]. Figure 3.18(a) shows transmission spectra obtained for both designs A and B. It is clearly evident that the wavelength of peak absorption for chlorophyll pigment A at 430 nm and 662 nm perfectly overlaps with the wavelength of peak transmission for our designs A and B, respectively. A close match between simulation and theoretical results validates our findings. Figure 3.18(b) shows numerically obtained transmission spectra for designs A and B for both TM and TE polarization. A near-perfect match indicates that our design is polarization-independent and suitable for application in greenhouses that receives unpolarized so-

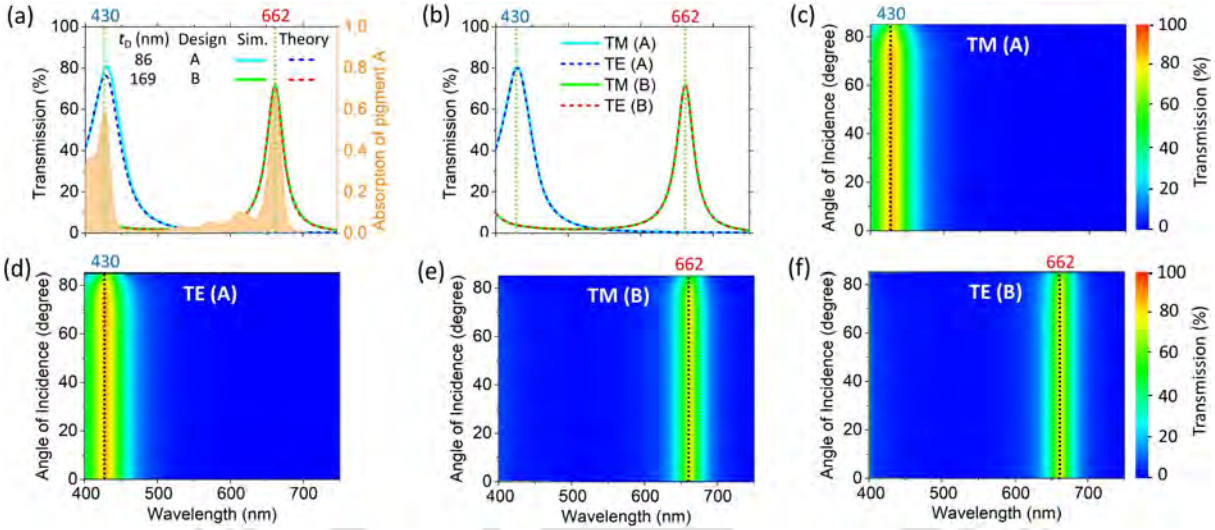

Figure 3.18: Transmission spectra for design A ($t_M = 27$ nm, $t_D = 86$ nm) and B ($t_M = 27$ nm, $t_D = 169$ nm) depicted in Fig. 3.17 showing (a) peak transmission at 430 nm and 662 nm, exactly matching the wavelengths of the peak absorption for chlorophyll pigment A. (b) shows numerically obtained transmission spectra for design A and design B, for both TM and TE polarization. Numerically obtained contour plot by varying angle of incidence ranging over 0–85 degrees for both TM and TE polarization in design A: (c) & (d) and design B: (e) & (f).

lar radiation.

In Figs. 3.18(c) and 3.18(d), we show transmission contour plots for design A over 0–85 degrees of angle of incidence. We observe that the transmission spectra remain unaltered till 75 degrees of angle of incidence. Moreover, we get over 90% transmission efficiency up to 80 degrees of angle of incidence, making our design angle-insensitive to a great extent. Similarly, in Figs. 3.18(e) and 3.18(f), we show transmission contour plot for design B over 0–85 degrees of angle of incidence. Such a good angle-insensitivity will ensure that our design is suitable for dynamic daylight situations. It also indicates that glasses coated with these passive color filters are less likely to show color shift even at a grazing angle of incidence.

3.4.3 Summary

To conclude, we theoretically demonstrated designs of MDM-based blue and red transmission-mode color filters, where **an innovative approach has been adopted to**

design transmission-mode nanophotonic windows as specific color filters, which could be crucial for applications in greenhouses. The peak transmission of two passive filters A and B were optimized to perfectly match the wavelength of peak absorption spectra for chlorophyll A and B at 430 nm and 662 nm, respectively. Our theoretical results agree well with the simulation findings. Our design is ultra-thin, easy to fabricate, lithography-free, large-area compatible, polarization-independent, and angle-insensitive up to 80 degrees of angle of incidence. For practical application, designs of blue and red transmission-mode color filters can be individually coated on the exterior or interior surface of adjacent glasses in a greenhouse. Greenhouses coated with these spectrally selective passive color filters could reduce the maturation period of plants by enhancing the rate of photosynthesis [176]. Reduced maturation period will eventually bring sustainability by reducing the carbon footprint of heating and cooling systems used in greenhouses.

4

Electrotunable Nanophotonic Windows Based on Metal–Insulator–Metal Multilayer Thin-films

Contents

Chapter 3 introduced designs of passive windows based on nanoring, nanoparticle, and multilayered nanophotonic thin-films. Among them, only the latter could provide different solutions for different climate conditions. Moreover, those multilayered designs are large-area compatible and lithography-free—making those the most promising candidates for fabricating large-area windows or changing weather conditions. However, passive windows once fabricated cannot be tuned to our specific needs. In this regard, tunable windows are better which can dynamically control the intensity of transmitted solar radiation.

This chapter introduces a couple of tunable windows based on metal–insulator–metal multilayer thin-films. Section 4.1 discusses a **unique approach to design all-weather electrotunable windows** that can dynamically control the intensity of transmitted solar radiation, depending upon the weather condition. Section 4.2 concludes this chapter with a discussion on designs of electrotunable, absorption- and transmission-mode color filters for application as electrochromic windows, **with significantly reduced voltage requirements**.

4.1 All-weather Electrotunable Windows

This section investigates a design of electrotunable windows using noble metals as well as their relatively-inexpensive alternatives. A lithography-free design approach is adopted using multilayer metallo-dielectric structure, that can dynamically control the intensity of transmitted solar radiation, depending upon the weather conditions. An electro-optic polymer is used as the dielectric layer, which on applying voltage, changes the effective refractive index by virtue of electro-optic effect, allowing tunable filtering of visible and infrared radiation over a voltage range of -15 V to +15 V.

4.1.1 Background

In literature, tunable filters have been designed by applying either external thermal or electrical energy. For thermal tuning, phase change materials (PCMs), such as vanadium dioxide (VO_2) could be used [177], which changes its state from insulator to metal at a transition temperature of 68°C. This transition induces an abrupt change in optical transmittance, particularly in the near-infrared wavelength regime. However, for smart window applications, the typical transition temperature of VO_2 is too high (68°C). Electrically tunable filters can be designed using electro-optic (EO) polymers [165], epsilon-near-zero (ENZ) materials [162], and graphene [178]. Here, the electro-optic polymers work on the principle of changing refractive index in response to the applied external electric field [179]. Coming to the ENZ materials such as indium tin oxide, they can be doped to achieve a transition from dielectric-like to metal-like properties in the near-infrared regime for optical intensity modulation [180]. However, such materials have not been explored to date in the context of smart windows for selectively filtering visible and infrared radiations, to the best of our knowledge.

In the present scenario, both passive and tunable windows are used globally. Among them, passive windows are suitable only for fixed climate conditions. For example, a passive window optimized to block the heat and allow the transmission of visible light could be suitable for places like Chennai in India which has moderate to hot climate condition. Whereas, places such as Delhi in India experience both extreme hot and cold weather conditions, where such passive windows would not be a practical choice. Such places demand a tunable window that can selectively filter visible and infrared radiations depending upon the dynamically changing weather conditions. To address this problem, we present a design of electrotunable windows for dynamically controlling the transmission of solar radiation as per our convenience.

4.1.2 Principles behind Controlling the Transmission of Solar and Non-Solar Radiations

An artistic view of our **m**ulti**l**ayer **m**etallo-**d**ielectric (MLMD) thin-films based smart window for a hot weather condition is shown in Fig. 4.1(a). These smart windows can control portions of solar radiation transmitted and reflect the non-solar radiation coming from the heated objects such as streets, vehicles, and nearby buildings [15]. For hot weather condition, when illumination is desirable inside the room, ideally, a window should allow transmission of visible radiation and block the transmission of IR radiation [7, 155, 157]. Whereas, for cold weather, the transmission of both visible and IR radiation becomes desirable.

As per the dynamic weather condition, our window can either allow or block solar radiation besides reflecting the non-solar radiation in either case. In section 3.3 of chapter 3, we introduced four possible modes of operation, namely, 'Bright and Cool' (BC)

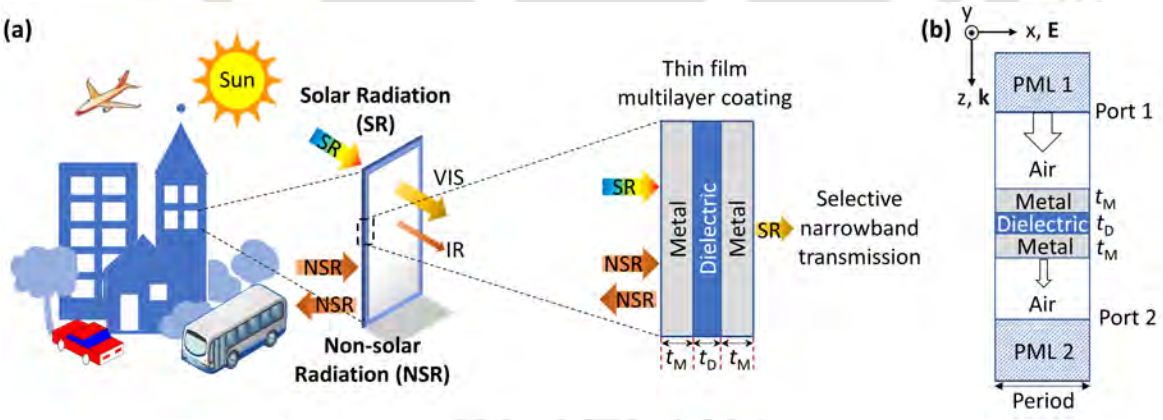

Figure 4.1: Artistic outlook depicting a hot weather condition showing (a) 3D side view of our multilayer metallo-dielectric window glass, capable of selective filtering of visible (VIS) and infrared (IR) radiation, reflecting non-solar radiations coming from the heated objects (streets, vehicles, and nearby buildings) in mid-wave and long-wave infrared wavelength regime, and (b) 2D simulation model showing a unit cell. The incident radiation from port 1 is a plane wave of transverse magnetic (TM) polarization traveling along the z-direction. A couple of perfectly matched layers (PML) are deployed at the top and bottom of the unit cell to avoid undue reflections arising due to confinement of the simulation domain. Note that the thickness of metallic layers at the top and bottom (t_{M}) and dielectric (t_{D}) may vary depending upon the type of materials used.

mode (allowing visible but blocking IR), 'Bright and Warm' (BW) mode (allowing both visible and IR), 'Dark and Warm' (DW) mode (blocking visible but allowing IR), and 'Dark and Cool' (DC) mode (blocking both visible and IR). During hot weather, BC and DC modes are useful when radiative heating of a cold room becomes undesirable. On the contrary, during cold weather, BW and DW modes are convenient when radiative heating of a cold room is desirable to maintain ambient room temperature. Moreover, by filtering visible radiation, these smart windows can also control indoor illumination to ensure sufficient visible light transmission useful for day-to-day activities [162].

4.1.3 Design and Simulation

To keep our design simple, we use MLMD planar structure, where a dielectric layer is inserted between the two metallic layers, and the top and bottom metallic layers are kept identical throughout. A two-dimensional model of unit cell under consideration is shown in Fig. 4.1(b). We use finite element method (FEM) solver of the COMSOL Multiphysics®, particularly the wave optics module to simulate absorption, reflection, and transmission spectra over the solar (400–1800 nm) and non-solar (3–30 μm) spectral regime, shown in Figs. 4.2(a) and 4.2(b). The solar regime includes visible (VIS; 400–750 nm), near-infrared (NIR; 750–1000 nm), and a part of short-wave infrared (SWIR; 1000–1800 nm) wavelengths. The non-solar regime includes mid-wave infrared (MWIR; 3–8 μm), long-wave infrared (LWIR; 8–15 μm), and a part of far-infrared (FIR; 15–30 μm) wavelengths.

For the MLMD structure we assumed gold as a material for the top and bottom metallic layers, each being 5 nm thick, and a dielectric layer with thickness, t_{D} = 50 nm, of a material having a refractive index, n_{D} = 2.2. To obtain accurate results, we deployed wavelength domain solver with physics-controlled extra-fine meshing, where the maximum and the minimum allowed mesh element sizes are 21.4 nm and $\sim$ 0.1 nm, respectively, to be able to effectively model all structural detail. Each air layer (at the

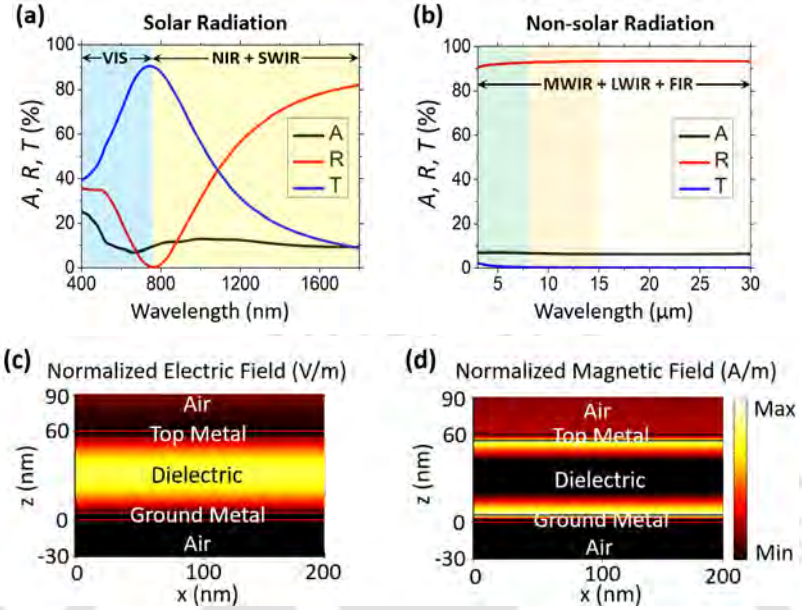

Figure 4.2: Numerically calculated absorption, reflection, and transmission spectra for multilayer metallo-dielectric glass for both (a) solar and (b) non-solar radiation spectra, taking top and bottom metallic layers (t_{M}) as gold, each being 5 nm thick, and dielectric with thickness, t_{D} = 50 nm and refractive index, $n_{\mathrm{D}} = 2.2$. For our study, the solar radiation spectra span over 400–1800 nm, including visible (VIS; 400–750 nm), near-infrared (NIR; 750–1000 nm), and a part of short-wave infrared (SWIR; 1000–1800 nm) wavelengths. The non-solar radiation spectra span over 3–30 μm, including mid-wave infrared (MWIR; 3–8 μm), long-wave infrared (LWIR; 8–15 μm), and a part of far-infrared (FIR; 15–30 μm) wavelengths. The presence of resonance mode is depicted by magnitude of (c) normalized electric field (**E**), and (d) normalized magnetic field (**H**) distribution, corresponding to the resonance wavelength (λ_0 = 750 nm).

top and bottom) is considered to be 400 nm thick. To avoid undue reflections, arising due to confinement of the simulation domain, perfectly matched layers (PML) of 200 nm thickness are used at the top and bottom of the unit cell. Periodicity of the unit cell along both lateral directions is taken to be 200 nm, implemented using Floquet boundary condition. Note that the optical constants of gold (Au) [161], silver (Ag) [161], copper (Cu) [161], indium tin oxide (ITO) [162], aluminium-doped zinc oxide (AZO) [163], and aluminium oxynitride (ALON) [164] are taken from the literature.

The normalized electric (**E**) and magnetic (**H**) field distribution corresponding to the resonant wavelength, depicted in Figs. 4.2(c) and 4.2(d), clearly show the existence of resonant mode confined inside the dielectric layer. As we consider metal layer

thickness less than the skin depth [133], the enhanced transmission is achieved at resonance condition since the supported resonant modes are leaky and can couple with the incident and transmitted electromagnetic radiation.

4.1.4 Theoretical Analysis

To support our simulation results, we apply transfer matrix method (TMM), transmission line method (TLM), and Fabry–Perot interferometer (FPI) technique. Here, we take top and bottom metallic layers as silver, each being 5 nm thick, and dielectric with thickness, t_{D} = 60 nm and refractive index, n_{D} = 2.2. For TMM case, we consider five layers and four interfaces, assuming a plane wave of linear polarization falling on top of our multilayered glass, as shown in Fig. 4.3(a). Here, n, Y, and t represent the refractive index, admittance, and thickness of the corresponding layer, respectively. We assume medium to be linear, non-magnetic, and homogeneous [131]. The transmission spectra obtained using TMM is shown in Fig. 4.3(d).

For TLM, a simplified circuit model is shown in Fig. 4.3(b). Here, Z, k, and t are characteristic impedance, propagation constant, and the thickness of the transmission line, respectively, corresponding to the identical (top and bottom) metallic and dielectric layers. The input impedance at interfaces 3 and 2 seen from the top towards the bottom, can be obtained using [133, 165]:

$$Z_{\mathrm{in},3} = Z_{\mathrm{M}} \frac{Z_0 - jZ_{\mathrm{M}}\tan(k_{\mathrm{M}}t_{\mathrm{M}})}{Z_{\mathrm{M}} - jZ_0\tan(k_{\mathrm{M}}t_{\mathrm{M}})} \tag{4.1a}$$

$$Z_{\mathrm{in},2} = Z_{\mathrm{D}} \frac{Z_{\mathrm{in},3} - jZ_{\mathrm{D}}\tan(k_{\mathrm{D}}t_{\mathrm{D}})}{Z_{\mathrm{D}} - jZ_{\mathrm{in},3}\tan(k_{\mathrm{D}}t_{\mathrm{D}})} \tag{4.1b}$$

where Z_0 is free space impedance of air. The corresponding reflection coefficients at metal–dielectric interfaces are:

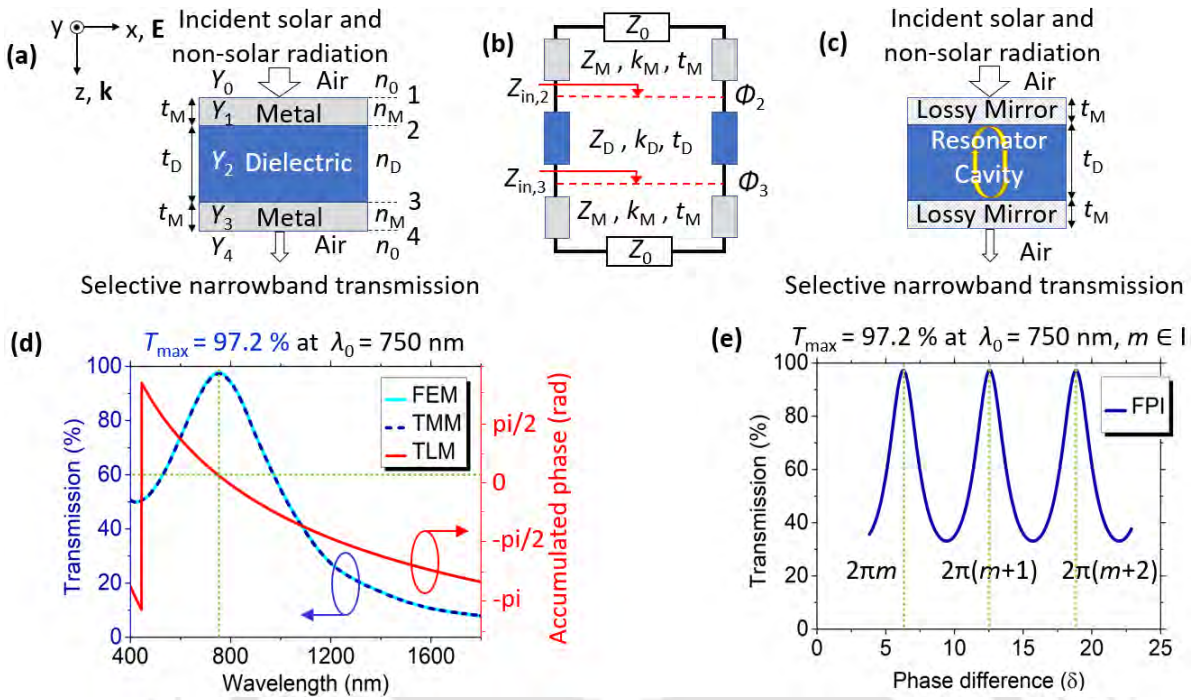

Figure 4.3: Detailed schematic of the proposed design shown in Fig. 4.1, analyzed using (a) transfer matrix method (TMM), (b) transmission line method (TLM), and (b) Fabry–Perot interferometer (FPI). For all three cases, we take metallic layers at the top and bottom as silver, each being 5 nm thick (t_{M}), and dielectric with thickness, $t_{\mathrm{D}} = 60$ nm and refractive index, $n_{\mathrm{D}} = 2.2$. In (a) Y and n represent the admittance and refractive index of the corresponding layer, respectively. In (b) Z_{in}, Z, k, and ϕ are input impedance, characteristic impedance, propagation constant, and phase shift upon reflection at the interface of the transmission line, respectively. (d) shows comparison between transmission spectra of finite element method (FEM) and TMM. TLM accurately predicts the resonant wavelength ($\lambda_0 = 750$), when the accumulated round trip phase becomes zero (represented by green square dot cross lines). (e) FPI accurately predicts the peak transmission ($T_{\max} = 97.2\%$; represented by green square dot cross lines) corresponding to the resonant wavelength which occurs in integral multiples of 2π, exactly matches with FEM and TMM transmission peaks. Note that in (d), we have taken 10 nm wavelength step for our theoretical calculations to match the number of samples taken for the full-wave simulations.

$$r_3 = \frac{Z_{\mathrm{in},3} - Z_{\mathrm{D}}}{Z_{\mathrm{in},3} + Z_{\mathrm{D}}} = |r_3| \angle \phi_3 \tag{4.2a}$$

$$r_2 = \frac{Z_{\mathrm{in},2} - Z_{\mathrm{D}}}{Z_{\mathrm{in},2} + Z_{\mathrm{D}}} = |r_2| \angle \phi_2 \tag{4.2b}$$

Here, ϕ_3 and ϕ_2 denote the phase shift upon reflection at metal–dielectric interfaces 3 and 2, respectively. The accumulated round trip phase ($\phi_3 + \phi_2$) upon reflection is

shown in Fig. 4.3(d). When the accumulated round trip phase becomes zero, maximum transmission ($T_{\max}$) is allowed at the resonant wavelength $\lambda_0 = 750$ nm [165].

Next, we use FPI method to determine $T_{\max}$ corresponding to the resonant wavelength supported by the cavity [see Fig. 4.3(c)]. Here identical top and bottom metallic layers represent lossy mirrors and the dielectric layer can be considered as a resonator cavity medium. The condition for maximum transmission occurs in integral multiples of 2π as shown in Fig. 4.3(e).

A comparison among FEM, TMM, TLM, and FPI is shown in Figs. 4.3(d) and 4.3(e). An excellent agreement between simulation (FEM) and theory (TMM) is seen for the entire solar spectral regime. TLM allows us to accurately predict the resonant wavelength ($\lambda_0 = 750$ nm) when the accumulated round trip phase becomes zero. FPI technique accurately predicts the peak transmission ($T_{\max}$ = 97.2%) at the resonant wavelength ($\lambda_0 = 750$ nm), which exactly matches with TMM and FEM transmission peaks. Hence, a perfect match between simulation and theory, indeed, validates our findings. From the next subsection, we will use TMM and FEM to compare theoretical and simulation results.

4.1.5 Parametric Analysis

To obtain a desirable optical response, we optimize the design of our MLMD glass by studying the effect of change in device dimensions. Figure 4.4 shows the contour plot for varying refractive index (n_{D}) and thickness (t_{D}) of dielectric layer as well as varying thickness of metallic layers (t_{M}). For each of the cases, we consider top and bottom metallic layers as gold. Figures 4.4(a) and 4.4(b) depict a redshift with increase in the dielectric refractive index (considering t_{M} = 5 nm and t_{D} = 50 nm) and dielectric thickness (considering t_{M} = 5 nm and n_{D} = 2.2), respectively. The reason can be attributed to the increases in the effective path length of electromagnetic waves with increase in refractive index or thickness of the medium, leading to slow propagation

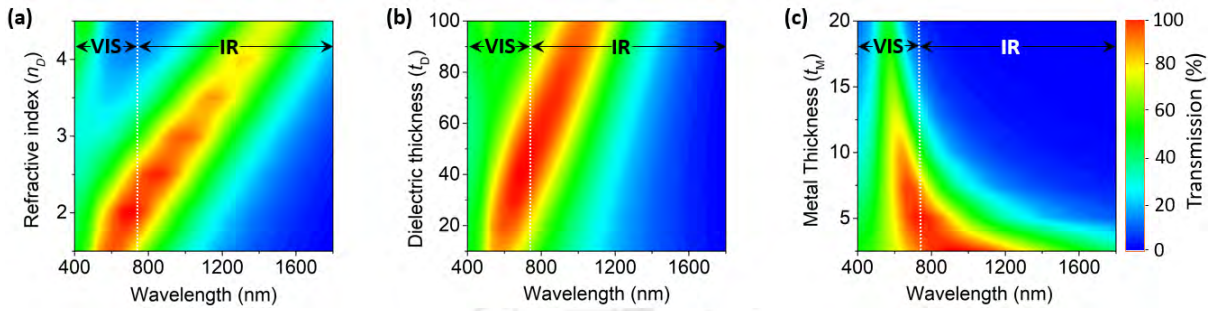

Figure 4.4: Simulation based parametric study showing contour plot to optimize our MLMD glass design for varying (a) refractive index of dielectric layer, n_{D} (considering $t_{\mathrm{M}} = 5$ nm and $t_{\mathrm{D}} = 50$ nm), (b) thickness of dielectric layer, t_{D} (considering $t_{\mathrm{M}} = 5$ nm and $n_{\mathrm{D}} = 2.2$), and (c) thickness of top and bottom metallic layers, t_{M} (considering $n_{\mathrm{D}} = 2.2$ and $t_{\mathrm{D}} = 50$ nm). In each case, top and bottom metallic layers are chosen as gold (Au).

of wave inside, indicating, a mode with a larger resonant wavelength is supported by the cavity [166]. Figure 4.4(c) depicts a dip in overall transmission spectra with increase in metal thickness (considering n_{D} = 2.2 and t_{D} = 50 nm). This is because, the larger the thickness of the metal, the lesser will be the transmission of electromagnetic waves through it [181]. However, in our case, to cover a larger spectrum of visible and IR radiation, metallic layers with lower thickness is desirable for a broadband response [165]. Therefore, for all our future designs, top and bottom metallic layers are chosen to be 5 nm thick. Also, to achieve transmission peak exactly at the desired resonance wavelength, the dielectric thickness is adjusted in each case (between 50 and 90 nm).

4.1.6 Electrotunable Glasses for All-weather Conditions

To achieve transmission peak at the desired wavelength, either the the thickness (t_{D}) or refractive index (n_{D}) of dielectric needs to be changed. For example, to achieve maximum transmission in both visible and IR spectral regime (BW mode), 750 nm is the desired resonance wavelength for peak transmission. For this purpose, many different types of EO materials are mentioned in the literature [182]. The comparison among a few EO materials that may be considered for our smart window design is shown in

Table 4.1: Comparison among a few different EO materials that may be considered for our smart window design [182]

EO Materials	$\frac{dn}{du}$ (nm/V)	IC Compatibility	Remarks
$LiNbO_3$	0.160	No	high melting point (>900 °C), limited bandwidth, and good stability.
Doped Polymers	0.125	Yes	good bandwidth but temperature sensitive.
DAST	3.410	Yes	high melting point (259 °C), large bandwidth, and good stability.

Note: $\frac{dn}{du}$: electro-optic (EO) coefficient.

Table 4.1. In this work, we choose 4-dimethyl-amino-N-methyl-4-stilbazoliumtosylate (DAST), an EO polymer having tunability near-visible regime. This polymer possesses a large EO coefficient (3.41 nm/V) that is desirable to attain maximum tunability with minimum bias voltage. The refractive index of DAST as a function of the applied voltage is given by [165]:

$$n_{\mathrm{D}} = n_0 + \frac{dn}{du}\frac{V}{t_{\mathrm{D}}} \tag{4.3}$$

where n_0 = 2.2 is the refractive index of DAST polymer at zero bias, $\frac{dn}{du}$ = 3.41 nm/V being EO coefficient with u being the applied electric field, V is the applied voltage, and t_{D} denotes the thickness of the DAST polymer. A two-dimensional schematic diagram of electrotunable MLMD glass with bias voltage supply is shown in Fig. 4.5(a) (see Appendix I for more details). The transmission plot for a varying bias voltage is shown in Fig. 4.5(b) at arbitrarily chosen nine discrete values between −20 V and +20 V in steps of 5 V. Here, we considered the top and bottom metal layers as gold, each 5 nm thick and a 50 nm thick dielectric layer of DAST polymer.

In Fig. 4.5(b), it can be seen that between −20 V and +20 V, there is a gradual spectral shift in the transmission peak towards longer wavelengths. This is because of a shift

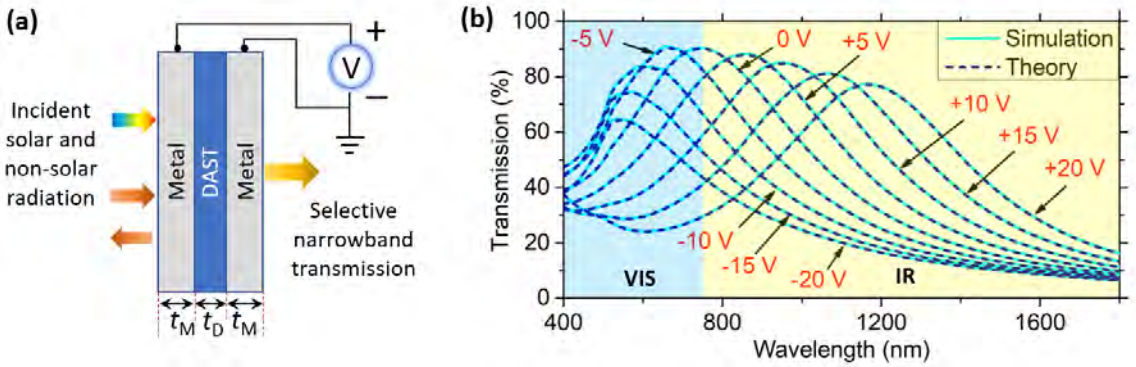

Figure 4.5: (a) 2D schematic diagram of electrotunable MLMD glass with bias voltage supply, and (b) transmission plot showing the effect of change in bias voltage at arbitrarily chosen nine discrete values between −20 V and +20 V in steps of 5 V, considering top and bottom metal of gold, each 5 nm thick (t_M) and dielectric being DAST polymer, 50 nm thick (t_D).

in the resonance frequency due to a change in the refractive index of the electro-optic polymer, used as an insulator layer (see Appendix I for more details). Here, our idea is to set BW mode at zero bias (0 V) which allows both visible and IR transmission. Then we achieve BC and DW modes simply by shifting the transmission peak into either visible or IR regime, respectively. Ideally, with a larger applied potential, a larger shift in the transmission peak towards either visible or IR regime is expected. This will result in a larger transmission in one regime, *e.g.* either visible (at negative bias) or IR (at positive bias), along with a stronger blocking in the other regime. For a low-power design, considering symmetric positive and negative bias voltages, here we chose −15 V for BC mode and +15 V for DW mode, for demonstrating the proof-of-the concept. Note that there is a trade-off between a larger operating voltage and a mode's performance in selective filtering of radiation.

For our first three MLMD based window glass design, we choose top and bottom metallic layers both to be either Au or Ag or Cu and DAST polymer as dielectric layer, for all the three cases [see Figs. 4.6(a), 4.6(b), and 4.6(c)]. These electrotunable glasses can operate under BC, BW, and DW modes over a voltage range of −15 V to +15 V. For instance, considering Au–DAST–Au based glasses, when we apply a negative bias

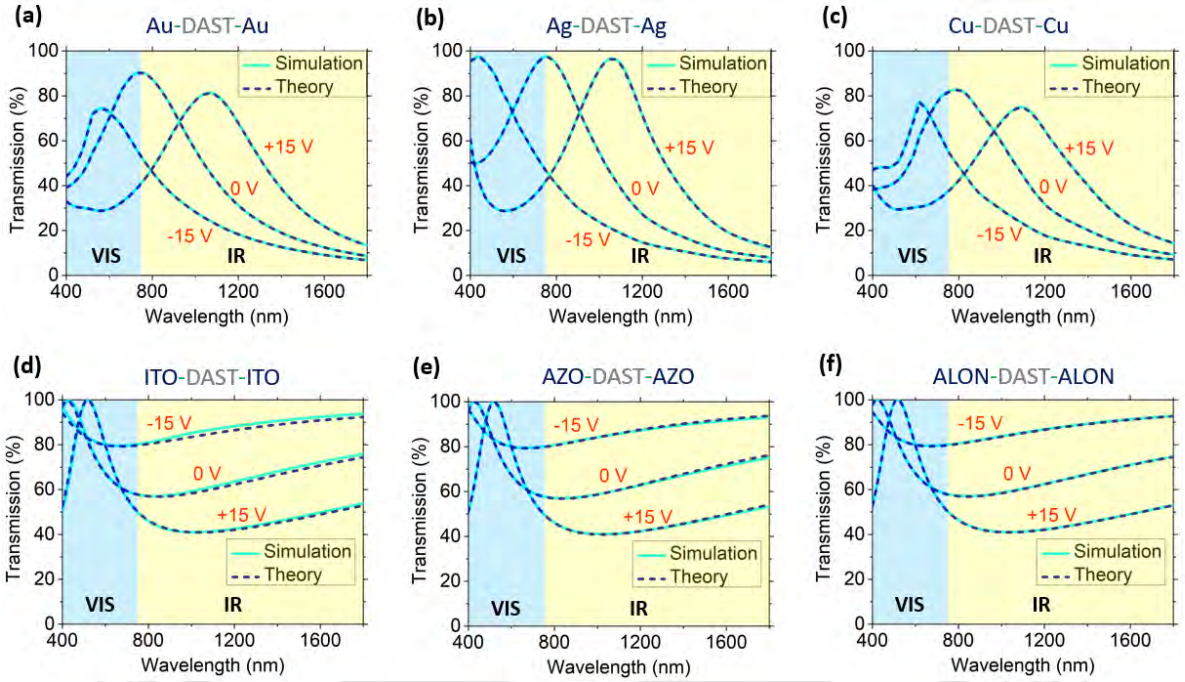

Figure 4.6: Transmission spectra for our electrotunable glasses choosing top and bottom metallic layers, both made of either (a) gold, (b) silver, or (c) copper, and dielectric layer as DAST polymer in each case, with an applied bias voltage of −15 V, 0 V, and +15 V working in BC (Bright and Cool; useful in hot weather with illumination), BW (Bright and Warm; useful in cold weather with illumination), and DW (Dark and Warm; useful in cold weather without illumination) modes, respectively. Similarly, design with choice for metallic layers at top and bottom to be either (d) ITO, (e) AZO, or (f) ALON, and dielectric layer as DAST polymer in each case, with an applied bias voltage of −15 V, 0 V, and +15 V works in BW, intermediate (useful in autumn/spring with illumination), and BC modes, respectively.

(−15 V) our smart window works in BC mode, useful during summer when maximum indoor illumination with minimum radiative heating is desired. Whereas, on applying a positive bias (+15 V) our window works in DW mode, useful during winter when minimum indoor illumination with maximum radiative heating is desired. By default (no bias applied *i.e.* 0 V) it works in BW mode, which is useful during winter when maximum indoor illumination with maximum radiative heating is desirable.

For a low-cost design, we further explore the use of transparent conductive oxides (TCOs) as metallic layers. Among the three TCOs considered, ALON is abundant, low-cost, toughest, and lightweight material [167], suitable for designing military-grade,

Table 4.2: Detailed Specifications of Our Electrotunable Window Glasses

Structure (thickness in nm)	Mode of Operation	Remarks
Au(5)–DAST(50)–Au(5)	BC, BW, DW	$T_{\text{peak}} = 90.4\%$, ultra-compact, expensive.
Ag(5)–DAST(60)–Ag(5)	BC, BW, DW	$T_{\text{peak}} = 97.5\%$, high tunability, less expensive compared to Au.
Cu(5)–DAST(60)–Cu(5)	BC, BW, DW	$T_{\text{peak}} \sim 80.0\%$, relatively inexpensive compared to Au and Ag.
ITO(5)–DAST(90)–ITO(5)	BW, IMD, BC	$T_{\text{IR,BW}} = 88.3\%$, $T_{\text{IR,BC}} = 45.6\%$, relatively inexpensive.
AZO(5)–DAST(90)–AZO(5)	BW, IMD, BC	Performance same as ITO, relatively inexpensive.
ALON(5)–DAST(90)–ALON(5)	BW, IMD, BC	Performance same as ITO, cheapest, lightweight, and toughest.

Note: BC: Bright and Cool; BW: Bright and Warm; DW: Dark and Warm; IMD: **i**nter**med**iate; Mode of Operation at -15 V, 0 V, and $+15$ V power supply.

bulletproof, portable, and blast-resistant windows [168]. On careful investigation, we observe that glasses based on ITO, AZO, and ALON can provide some unique optical response by applying a bias voltage across the DAST layer [see Figs. 4.6(d), 4.6(e), and 4.6(f)]. For example, ITO–DAST–ITO based glass on application of negative bias (-15 V), works in BW mode, allows over 88% of IR and over 83% visible transmission, desirable during winter. Whereas, on application of positive bias (+15 V), it works in BC mode, where ∼75% visible and merely 45% IR radiation is transmitted—desirable during summer. If we can further increase the bias voltage (say up to +45 V), IR transmission falls below 20%. When no bias (0 V) is applied, we get an intermediate solution, useful during spring / autumn / rainy season when both indoor illumination and radiative heating are desired to some extent. Such excellent control over IR blocking capabilities makes MLMD glasses suitable for designing an all-weather smart window. Detailed specifications of our smart glasses are provided in Table 4.2.

4.1.7 Effect of Different Polarizations and Incident Angles

To ensure that our design is suitable for daytime operation, we study both TM and TE polarization using Au–DAST–Au based design with a bias voltage of ±15 V. Figure

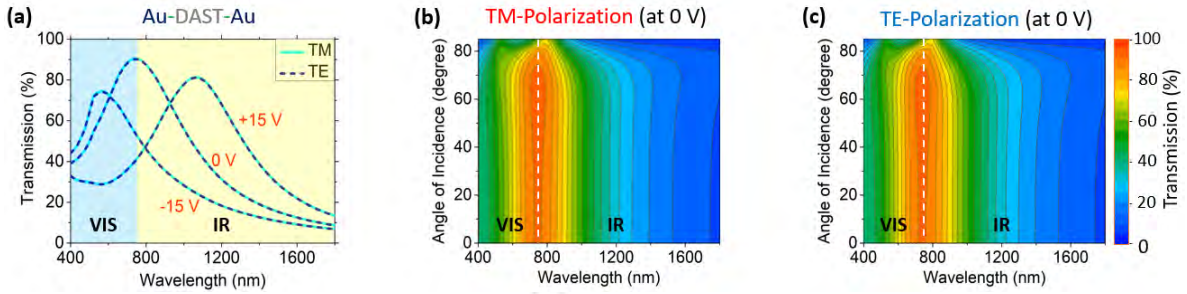

Figure 4.7: Simulated transmission spectra showing (a) both TM and TE polarization for Au (5 nm)–DAST (50 nm)–Au (5 nm) structure under three modes of operation at −15 V, 0 V, and +15 V bias voltage, showing polarization insensitivity. Contour plot for angular transmission spectrum of the same structure at 0 V bias, showing over 90% transmission efficiency for a wide angle of incidence (up to 75 degrees) for both (b) TM and (c) TE polarization.

4.7(a) shows that even after applying voltage over −15 V to +15 V, transmission spectra remain unaffected by change in polarization of the incident wave, hence, showing polarization-insensitivity. To account for the effect of dynamically changing position of the sun, we also study for varying angle of incidence, ranging over 0–85 degrees at 0 V bias. Figures 4.7(b) and 4.7(c) show that our design is angle-insensitive up to 75 degrees of angle of incidence for both TM and TE cases, with over 90% transmission efficiency, hence, making our smart glasses a practical choice for daytime operation.

4.1.8 Figure of Merit of Our Electrotunable Window Glasses

To meet industry standards, we evaluate the performance of our electrotunable glasses, by calculating their figure of merit [7, 157, 158]. The three most commonly used parameters: visible transmittance (VT), infrared transmittance (IRT), and solar heat gain coefficient (SHGC) were introduced in subsection 3.3.8 of chapter 3. An ideal window designed for hot weather condition should have VT value as high as possible and IRT value as low as possible. In contrast, for cold weather, both VT and IRT values should be as high as possible. For SHGC value calculation in BC mode over 400–1800 nm wavelength range, we take $T_{\text{visible}}(\lambda) = 1$, and $T_{\text{IR}}(\lambda) = 0$, which gives ideal SHGC value as 0.55. Similarly, for BW and DW modes within the same spectral

Table 4.3: VT, IRT, and SHGC Ideal Values, $\lambda \in [400\text{ nm}, 1800\text{ nm}]$

Mode of operation	VT	IRT	SHGC
BC Mode	1	0	0.55
BW Mode	1	1	1
DW Mode	0	1	0.45

Note: BC: Bright and Cool; BW: Bright and Warm; DW: Dark and Warm; VT: Visible Transmittance; IRT: IR Transmittance; SHGC: Solar Heat Gain Coefficient.

regime, the ideal SHGC value comes out to be 1 and 0.45, respectively. VT, IRT, and SHGC ideal values are listed in Table 4.3.

Figure of merit calculations for BC, BW, and DW modes, comparing our MLMD based smart glasses with a few commercial glasses and previously reported infrared-blocking plasmonic glasses are shown in Fig. 4.8. A comparison of figure of merit for BC mode among our smart glasses and two double-pane argon low-emissivity coating commercial windows (CW I, and CW II), is shown in Fig. 4.8(a) [7, 8, 154]. In this case, our relatively inexpensive metals such as Ag, ITO, AZO, and ALON outperform industry-standard commercial window glasses.

Recently, *Besteiro et al.* designed thin-film plasmonic glasses to block IR radiations over 200–1700 nm spectral range [37]. Out of all the materials considered, their figure of merit calculation revealed that silver nanoshell based plasmonic glasses produced the best results. Figure 4.8(b) shows a comparison between our silver based smart glasses and their silver nanoshell based plasmonic glasses. For a fair comparison, we take the mean value of their calculated and simulation data and optimize our design over the same spectral range (200–1700 nm) by considering 8 nm thick top and bottom silver layers alongside 95 nm thick DAST layer. For their spectral range, the calculated ideal SHGC value is 0.43. The figure of merit calculations reveals that our silver based smart glasses can outperform their silver nanoshell based plasmonic glasses in all the

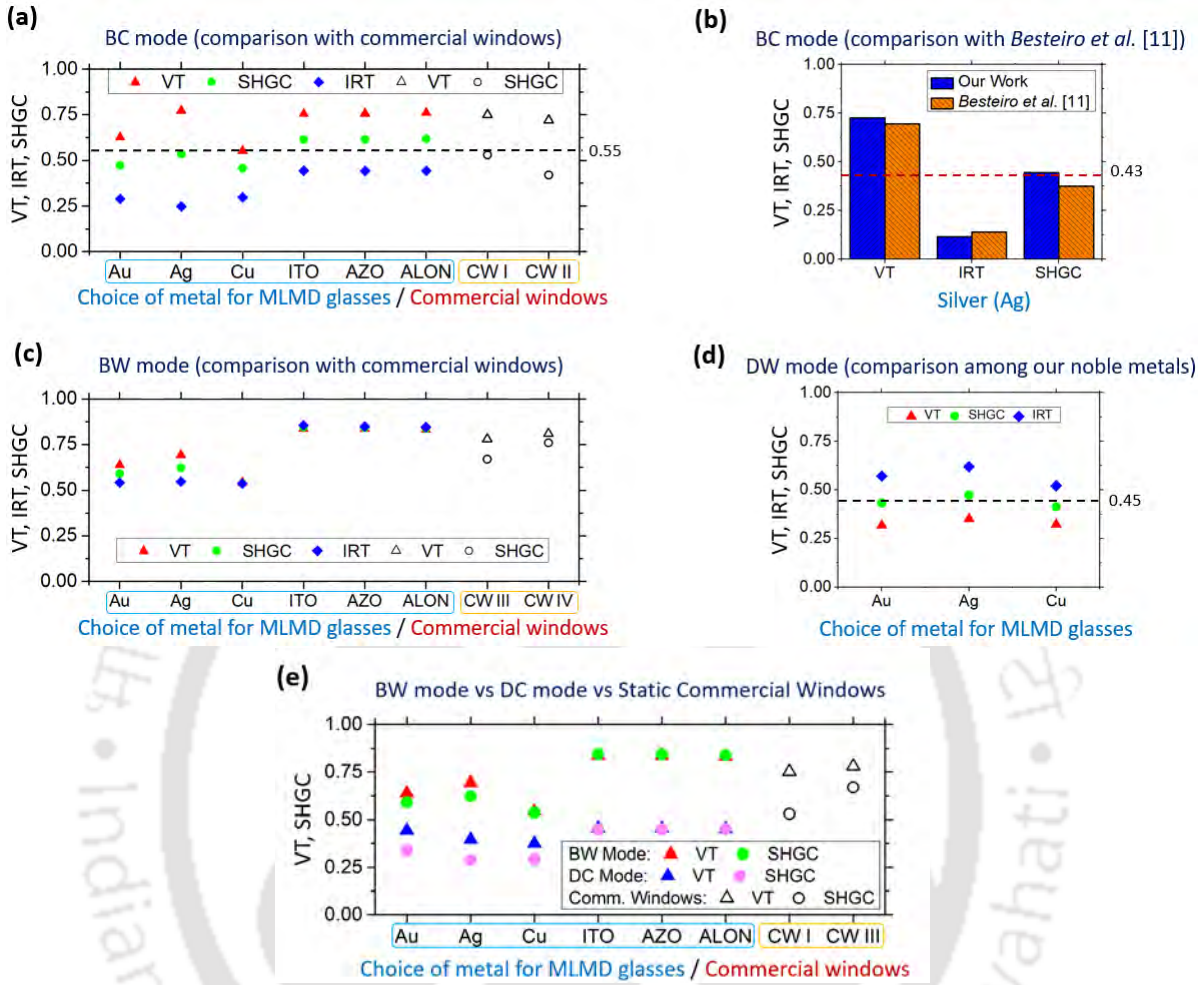

Figure 4.8: Figure of merit representation for (a) BC mode, comparing our smart glasses with two commercial double-pane argon low-emissivity coating glasses (CW I and CW II) [7, 8, 154], (b) BC mode, comparison between our silver based smart glasses and silver nanoshell based IR-blocking plasmonic glasses [37], (c) BW mode, comparing our smart glasses with commercial double-glazed, high-solar-gain low-emissivity glass and double-pane clear glasses (CW III and CW IV) [7, 8], (d) new DW mode, comparison among our gold, silver, and copper based smart glasses, and (e) comparison between BW and DC modes of our glasses and the static commercial windows (CW I and CW III). In each case, DAST polymer is used as dielectric layer. Note that in (a), (b), and (d) the short dashed horizontal lines represent the corresponding ideal SHGC value in each case.

three parameters (VT, IRT, and SHGC).

A comparison among our smart glasses, commercial double-glazed high-solar-gain low-emissivity glass, and double-pane clear glass windows (CW III and CW IV) is shown in Fig. 4.8(c) [7,8]. In this case, our smart glasses based on relatively inexpensive

metals such as ITO, AZO, and ALON outperform the industry-standard commercial window glasses. For the DW mode, a comparison among our Au-, Ag-, and Cu-based smart glasses is shown in see Fig. 4.8(d). In this case as well, silver shows overall better performance compared to gold. Figure 4.8(e) shows a comparison between the BW and DC modes of our glasses and the static commercial windows (CW I and CW III). Note that DC mode requires biasing of -30 V for Au, Ag, and Cu based designs and +50 V for ITO, AZO, and ALON based designs. The figure of merit calculation revealed that the overall performance of our relatively inexpensive metals (Ag, Cu, ITO, AZO, and ALON) is better compared to Au and also meets industry standards. Therefore, our MLMD based glasses could be a suitable choice for large scale commercial production of all-weather smart windows.

4.1.9 Effect of Substrate

From a practical point-of-view, an ideal implementation of our MLMD film would be its integration with an insulated glass unit (IGU) used in buildings. This IGU will allow us to find out the rate of heat loss through a window, defined as U-value [7,8,154]. Therefore, it will be interesting to compare the performance of our MLMD glass, with and without an optically transparent silica (SiO_2) glass substrate. Figure 4.9(a) shows a 2D schematic diagram of our electrotunable MLMD film (with bias voltage supply) coated on a silica glass substrate. Here, the thicknesses of the metallic layer (t_M), the dielectric layer (t_D), and silica glass substrate (t_G) are considered to be 8 nm, 90 nm, and 5 mm, respectively. Note that the thicknesses of metal and dielectric layers are manually optimized for coating on the glass substrate. To evaluate the performance, we calculate the figure-of-merit parameters in BC mode using Ag–DAST–Ag based glass. Figure 4.9(b) shows a comparison of the VT, IRT, SHGC parameters obtained in BC mode among our Ag–DAST–Ag based smart glasses (with and without silica glass substrate) and a couple of commercial double-pane argon low-emissivity coating

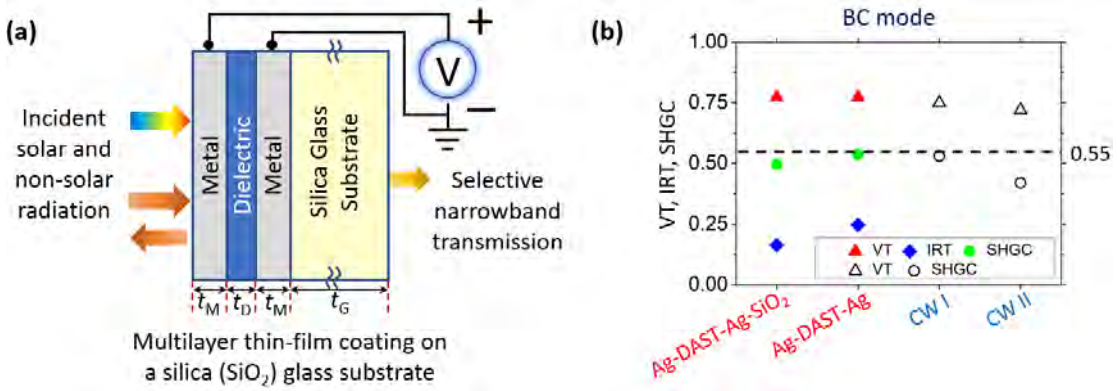

Figure 4.9: (a) 2D schematic diagram (not to scale) of an electrotunable MLMD thin-film (with terminals for bias voltage supply) coated on optically-transparent silica (SiO_2) glass substrate. Here, the thicknesses of metal (t_M), dielectric (t_D), and silica glass substrate (t_G) are considered to be 8 nm, 90 nm, and 5 mm, respectively. (b) The figure of merit representation for BC mode showing a comparison among our Ag–DAST–Ag based smart glasses (with and without silica glass substrate) and a couple of commercial double-pane argon low-emissivity coating glasses (CW I and CW II) [7, 8, 154].

glasses (CW I and CW II) [7,8,154]. We observe that our proposed windows still exhibit overall better performance than the commercial windows when our MLMD glasses are coated on a single-pane glass substrate. Therefore, our MLMD based glasses could be a better and cheaper alternative to commercial double- or triple-pane low-emissivity glasses.

4.1.10 Prospective Fabrication Method and Fabrication Imperfection Tolerance Study

With the existing state-of-the-art nanoscale fabrication facilities, the fabrication of our proposed MLMD glass design is feasible. For instance, Ag–DAST–Ag based MLMD glass can be fabricated by successive electron beam (e-beam) evaporation technique [169–171, 182]. First, a silver metal layer of 5 nm thickness needs to be coated on the top surface of a two-sided polished silica glass substrate (typically 5 mm thick) using an e-beam evaporator [41]. Then a 60 nm thick DAST layer may be deposited as a single crystal over a large-area in a certain orientation on the top surface of the bottom silver layer. The graphoepitaxy technique may be used to control the orientation and

Table 4.4: Fabrication tolerance study for Ag–DAST–Ag based MLMD glass in BC, BW, and DW modes, showing variation in VT, IRT, and SHGC values over solar radiation spectral regime *i.e.* $\lambda \in$ [400 nm, 1800 nm], with $\pm 5\%$ variation in thicknesses of top / bottom Ag layer (5 nm thick) and DAST layer (60 nm thick)

MLMD Layer (Thickness)	Variation in Thickness	BC Mode			BW Mode			DW Mode		
		VT	IRT	SHGC	VT	IRT	SHGC	VT	IRT	SHGC
Top / Bottom Ag (5 nm)	Upper Limit (+5%)	0.76	0.24	0.52	0.70	0.53	0.62	0.35	0.62	0.47
	Optimum Dimension	**0.77**	**0.25**	**0.54**	**0.69**	**0.55**	**0.62**	**0.35**	**0.62**	**0.47**
	Lower Limit (−5%)	0.79	0.26	0.55	0.69	0.56	0.63	0.35	0.62	0.48
DAST (60 nm)	Upper Limit (+5%)	0.80	0.26	0.56	0.67	0.57	0.62	0.36	0.61	0.48
	Optimum Dimension	**0.77**	**0.25**	**0.54**	**0.69**	**0.55**	**0.62**	**0.35**	**0.62**	**0.47**
	Lower Limit (−5%)	0.74	0.24	0.51	0.72	0.53	0.63	0.34	0.63	0.47

Note: BC: Bright and Cool; BW: Bright and Warm; DW: Dark and Warm; VT: Visible Transmittance; IRT: IR Transmittance; SHGC: Solar Heat Gain Coefficient.

solidification of the DAST crystals [182]. Finally, another 5 nm thick silver layer may be deposited at the top surface of DAST–Ag coating using the e-beam evaporation technique. For optical characterization, a microscope integrated with a spectrometer or a Fourier Transform Infrared (FT-IR) microscope and an electron multiplication charge-coupled device (CCD) camera may be used [169, 170]. It is important to note that the optical response from such MLMD glasses is subjected to controlled environmental conditions during fabrication. However, fabrication imperfections may arise depending upon the deposition techniques employed and the surface smoothness of different materials used. Therefore, it is important to further analyze the effect of such imperfections on the design's performance.

Table 4.4 lists the results of the fabrication-tolerance study conducted for Ag–DAST–Ag based MLMD glass in BC, BW, and DW modes. Variations in VT, IRT, and SHGC values are shown over the solar radiation spectral regime with $\pm 5\%$ variation in thick-

nesses of top/bottom Ag layer (5 nm thick) and DAST layer (60 nm thick). We found that the performance parameters (VT, IRT, and SHGC) vary only marginally with ±5% variation in the thickness of each layer. This finding shows that our proposed MLMD glass designs are robust and the overall window performance is less prone to fabrication imperfections. Here we like to mention that ± 5% tolerance for 5 nm thick Ag could be too small a tolerance. In practical cases, lumps and islands of Ag will be formed and an appropriate air filling fraction needs to be considered.

4.1.11 Application in Smart Windows

Smart windows coated with our suggested MDLM based thin-film can be controlled *via* smart-home systems to provide security and privacy features alongside dynamic tuning, with only ±15 V supply. However, the major challenge lies in the durability of such electrotunable windows compared to ordinary windows. In this work, we have used DAST polymer as an EO material. This polymer possesses one of the largest EO coefficients among all those organic crystals available today [182]. DAST also has a large melting point (259 °C), a large electrical bandwidth, and exhibits stability up to 250 °C. Hence, it is expected that DAST based devices will be durable. As shown in Table 4.1, alternative EO materials such as lithium niobate ($LiNbO_3$) or doped polymers may also be used, but they may require a very high voltage because of their small EO coefficients. Therefore, it is always desirable to look for more such EO materials that have certain optical absorption in the non-powered state to achieve different modes as per the requirement of the geographical location.

It is important to note that the temperature in the gap of an insulated glass unit of a window may exceed (90 °C) or even go below the freezing point in a few geographical places that face extreme weather conditions [183]. Therefore, it is equally important that EO material exhibits matched mechanical as well as thermal properties. This will ensure that its coefficient of thermal expansion closely matches with the metals used

in the MLMD glasses, therefore, reducing the mechanical strain during expansion or cooling down. To have longevity and practical value, the EO material should also offer resistance to ultraviolet radiation, high humidity, exposure to direct sunlight, *etc*.

4.1.12 Summary

We presented a theoretical design of metal–dielectric–metal based electrotunable smart glasses, **where a unique approach is adopted** for dynamically controlling the amount of transmitted solar radiation depending on weather conditions. We explored noble metals as well as their relatively inexpensive alternatives as metallic layers. An electro-optic polymer is used as a dielectric layer to make the system tunable by using a bias voltage ranging from −15 V to +15 V. The figure-of-merit calculations show that our relatively inexpensive materials (Ag, Cu, ITO, AZO, and ALON) can outperform industry-standard commercial glasses and previously reported infrared-blocking plasmonic glasses. Our design is robust, low-cost, ultra-compact (60–100 nm thick), lithography-free, large-area compatible, polarization-independent, and angle-insensitive (up to 75 degrees). Our theoretical results obtained using transfer matrix method, transmission line method, and Fabry–Perot interferometer technique agree well with those of finite element method based full-wave simulations which validate our results. These ultra-thin smart glasses can be integrated into privacy windows, security panels, solar control skylight panels, *etc*. Aluminium oxynitride based glasses can be used in fighter aircraft, military vehicles, high security buildings, and submarine applications.

4.2 Tunable Color Filters as Electrochromic Windows

In chapter 2, it was discussed that electrochromic window glasses are considered the best candidate among photochromic, thermochromic, and electrochromic windows. This section presents low-power electrotunable absorption- and transmission-mode color filters as electrochromic windows. In line with the previous section, the design

comprises metal–dielectric–metal multilayer thin-film structure. By applying a voltage across an electro-optic polymer, used as a dielectric layer, tunable color filtering is achieved over a voltage range of −10 V to +10 V.

4.2.1 Background

Manipulation of light–matter interactions at the nanoscale enables controlled spectral absorption, reflection, and transmission through an optically engineered material. In particular, spectrally selective structural color filters based on plasmonic metamaterials, photonic crystals, and metasurfaces have attracted substantial attention because of their potential in achieving easy scalability, excellent sustainability, improved efficiency, and low-cost design [9–11]. By selective absorption/transmission of a narrowband visible spectrum, such structural color filters can be used for a wide range of applications, such as biological and chemical sensing [184, 185], color decoration and printing [186, 187], displays [188], light-emitting diodes (LEDs) [9, 10], and electrochromic windows [189].

Naturally, structural color filters can be seen in the wings of some specific types of animals and birds, such as beetles, butterflies, moths, *etc.* [190, 191]. Recently, metamaterial was introduced that enabled the realization of compact, high resolution, and high color-efficiency based artificial color filters [169,192,193]. A few plasmonic nanostructures based on metallic nanorod arrays [194], nanohole arrays on metal film [195], nanoring arrays of metal on glass substrate [149], and sub-wavelength gratings [196] have been explored for color filtering application. However, structural color filters based on symmetric/asymmetric metal–dielectric–metal (MDM) structure gained attention due to simple and compact design, large-area compatibility, design flexibility, and low-cost thin-film nanofabrication techniques involved [197]. For example, Yoon *et al.* demonstrated a transmission-mode color filter based on MDM Fabry–Perot cavity which can generate blue, green, and red colors by adjusting the thickness of the cav-

ity [198]. Unfortunately, such MDM based color filters once fabricated, can only filter a fixed color (either blue or green, or red), which limits their ability to dynamically tune the color filters for absorption/transmission over a wide spectral range [169, 197, 199]. If the absorption/transmission can be controlled in real-time, then this may open up avenues for designing highly-efficient electrochromic windows and high-contrast optical switches [200–203].

Some recently reported absorption- and transmission-mode tunable color filters are dynamically controllable either by polarization of the incident light [204, 205] or by electrical power supply [200, 201, 206]. For electrical tuning, epsilon-near-zero (ENZ) material [170, 201, 207, 208], graphene [209, 210], n-type indium antimonide (n-InSb) [200], liquid crystals [211,212], Ge2Sb2Te5 (GST225) [213], vanadium oxide (VO_2) [214], and electro-optic (EO) polymer [165, 201] can be used. However, most of the proposed structures either require complex lithography-based fabrication processes due to the type of nanostructure patterning used or require very high supply voltage to cover a wide spectral range under consideration. For example, Mirshafieyan *et al.* proposed the design of an electrically tunable perfect light absorber, which utilizes 50 V power supply for 40 nm spectral shift of the resonance wavelength in the visible regime [200]. Similarly, the design proposed by Bibbo *et al.* [207], used 160 V power supply to achieve less than 50 nm spectral shift of the resonance wavelength in the visible regime. Also, the design proposed by Qian *et al.* [206], used 70 V power supply to achieve less than 100 nm spectral shift in the near-infrared regime. Therefore, a need for power-efficient design of both absorption- and transmission-mode color filters and optical switches, in visible and near-infrared regime, respectively, remained largely in demand.

To bridge that gap in the literature, here, we introduce theoretical design of electrotunable absorption- and transmission-mode colour filters based on MDM structure. Our structure comprises top and bottom metallic layers with a dielectric layer sand-

wiched in between. Here, we use silver (Ag) as the top and bottom metallic layers, and 4-dimethyl-amino-Nmethyl-4-stilbazoliumtosylate (DAST), an electro-optic (EO) polymer, as the dielectric layer. For illustration purpose, we design three distinct absorption- and transmission-mode color filters (blue, green, and red).

4.2.2 Design Schematic

A 2D schematic side view of our absorption-mode color filter based on MDM structure is shown in Fig. 4.10(a). It consists of Ag–DAST–Ag based thin-film multilayered structure. The top Ag layer is 40 nm thick, middle DAST layer is 80 nm thick, and the bottom Ag layer is 125 nm thick. Note that the bottom Ag layer is kept optically thick to completely block the transmission through the structure, for designing an absorption-mode color filter. This asymmetric MDM structure can be approximated as a Fabry–Perot cavity [135], which absorbs the light completely at the resonance wavelength, hence, forming a 'perfect absorber'. The DAST layer forms a resonator cavity sandwiched between the top and bottom lossy Ag layers. The condition of resonance wavelength is given by Eq. (2.18) [131]. The normalized electric (**E**) field distribution

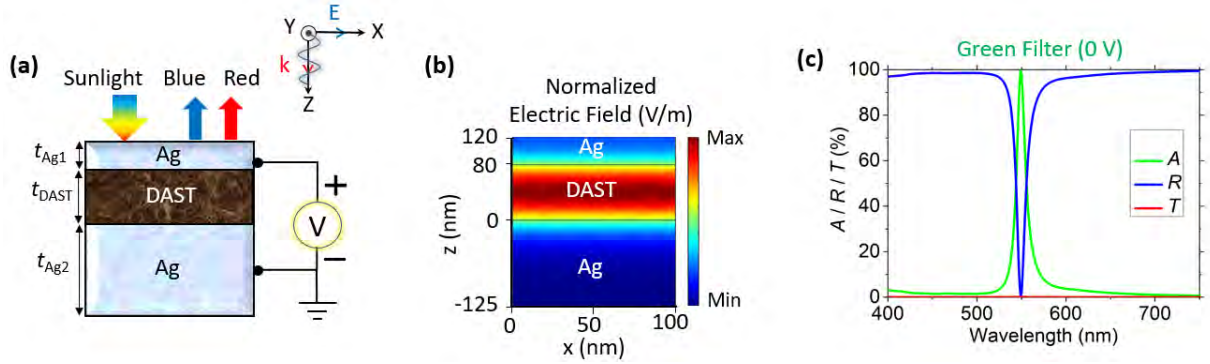

Figure 4.10: An asymmetric metal–dielectric–metal (MDM) based absorption-mode color filter showing (a) 2D schematic side view with bias voltage supply, (b) normalized electric field (**E**) distribution, showing the existence of resonant mode trapped inside the dielectric layer corresponding to the resonance wavelength $\lambda_0 = 550$ nm with 0 V power supply, and (c) absorption (A), reflection (R), and transmission (T) spectra showing perfect absorption at the resonance wavelength with 0 V power supply.

corresponding to the resonant wavelength λ_0 = 550 nm, shown in Fig. 4.10(b), clearly depicts the presence of resonant mode trapped inside the DAST layer, which validates our Fabry–Perot cavity approximation.

4.2.3 Simulation Model

We use finite element method (FEM) solver, COMSOL Multiphysics® wave optics module, to simulate over 400–750 nm visible spectral range for color filters and 1400–1750 nm near-infrared spectral range for optical switches. By considering an incident plane wave of TM polarization, we study absorption, reflection, and transmission spectra. The optical constants of Ag are taken from [130]. Perfectly matched layers are used at the top and bottom of the considered unit cell, each having a thickness of $\lambda_{max}/4$ (where λ_{max} is the upper limit of wavelength range under consideration), to avoid unwanted reflections as a result of the confinement of the simulation domain. The periodicity of the unit cell is considered to be 100 nm. The reflectance (R) and transmittance (T) are measured from the S parameters. Finally, absorbance (A) can be calculated using $A = 1 - R - T$. For absorption-mode color filter, as we take optically thick bottom Ag layer, at the resonance wavelength λ_0 = 550 nm, we see a perfect absorption of green color at 0 V power supply, while other parts of the visible spectrum (blue and red) are reflected back through the optically thin top Ag layer, as shown in Fig. 4.10(c).

4.2.4 Theoretical Framework

To support our simulation results, we apply transfer matrix method (TMM) and transmission line method (TLM). For TMM case, we consider five layers (Air–Ag–DAST–Ag–Air) and four interfaces (1, 2, 3, and 4), assuming medium to be linear, non-magnetic, and homogeneous. We consider a plane wave of linear polarization incident on the top Ag layer, as shown in Fig. 4.11(a). Here, Y, n, and t represent the

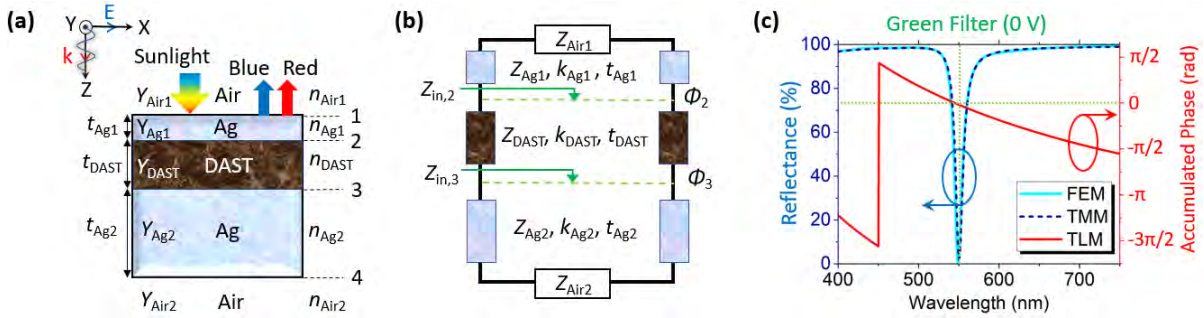

Figure 4.11: Detailed 2D schematic of the proposed absorption-mode color filter using (a) transfer matrix method (TMM) model, (b) transmission line method (TLM) model, and (c) a comparison among finite element method (FEM; light blue solid line), TMM (dark blue short dashed line) and TLM (red solid line). Simulation (FEM) and theory (TMM) show perfect match for the reflectance spectra over 400–750 nm wavelength range, supported by TLM, which accurately predicts the resonant wavelength $\lambda_0 = 550$ nm, when the accumulated round trip phase shift becomes zero (light green square dot cross line).

admittance, refractive index, and thickness of the corresponding layer, respectively. For Ag1–DAST–Ag2 (bottom layer) based design, phase shift at each layer can be written as [131]:

$$k_{\mathrm{Ag1}}h = k_0(2\tilde{n}_{\mathrm{Ag1}}t_{\mathrm{Ag1}}\cos\theta_{\mathrm{i,2}})/2 \tag{4.4a}$$

$$k_{\mathrm{DAST}}h = k_0(2n_{\mathrm{DAST}}t_{\mathrm{DAST}}\cos\theta_{\mathrm{i,3}})/2 \tag{4.4b}$$

$$k_{\mathrm{Ag2}}h = k_0(2\tilde{n}_{\mathrm{Ag2}}t_{\mathrm{Ag2}}\cos\theta_{\mathrm{i,4}})/2 \tag{4.4c}$$

where, k_0 represents the propagation wavevector in free space. Solving the boundary condition for E and H field at each of the interface, we obtain:

$$E_1 = E_2\cos k_{\mathrm{Ag1}}h + H_2(i\sin k_{\mathrm{Ag1}}h)/Y_1 \tag{4.5a}$$

$$H_1 = E_2Y_1(i\sin k_{\mathrm{Ag1}}h) + H_2\cos k_{\mathrm{Ag1}}h \tag{4.5b}$$

$$E_2 = E_3\cos k_{\mathrm{DAST}}h + H_3(i\sin k_{\mathrm{DAST}}h)/Y_2 \tag{4.5c}$$

$$H_2 = E_3Y_2(i\sin k_{\mathrm{DAST}}h) + H_3\cos k_{\mathrm{DAST}}h \tag{4.5d}$$

$$E_3 = E_4 \cos k_{\mathrm{Ag2}} h + H_4 (i \sin k_{\mathrm{Ag2}} h)/Y_3 \tag{4.5e}$$

$$H_3 = E_4 Y_3 (i \sin k_{\mathrm{Ag2}} h) + H_4 \cos k_{\mathrm{Ag2}} h \tag{4.5f}$$

where,

$$Y_{\mathrm{Ag1}} = \sqrt{\frac{\epsilon_0}{\mu_0}} \tilde{n}_{\mathrm{Ag1}} \cos\theta_{\mathrm{i},2} \tag{4.6a}$$

$$Y_{\mathrm{DAST}} = \sqrt{\frac{\epsilon_0}{\mu_0}} n_{\mathrm{DAST}} \cos\theta_{\mathrm{i},3} \tag{4.6b}$$

$$Y_{\mathrm{Ag2}} = \sqrt{\frac{\epsilon_0}{\mu_0}} \tilde{n}_{\mathrm{Ag2}} \cos\theta_{\mathrm{i},4} \tag{4.6c}$$

Here, Y_{Ag1}, Y_{DAST}, and Y_{Ag2} represent the admittance in top Ag, DAST, and bottom Ag layers, respectively. The above Eq. (4.6) is valid for the TE polarization case. For TM case, Eq. (4.6) can be modified to get:

$$Y_{\mathrm{Ag1}} = \sqrt{\frac{\epsilon_0}{\mu_0}} \tilde{n}_{\mathrm{Ag1}} / \cos\theta_{\mathrm{i},2} \tag{4.7a}$$

$$Y_{\mathrm{DAST}} = \sqrt{\frac{\epsilon_0}{\mu_0}} n_{\mathrm{DAST}} / \cos\theta_{\mathrm{i},3} \tag{4.7b}$$

$$Y_{\mathrm{Ag2}} = \sqrt{\frac{\epsilon_0}{\mu_0}} \tilde{n}_{\mathrm{Ag2}} / \cos\theta_{\mathrm{i},4} \tag{4.7c}$$

Connecting Eq. (4.5) in matrix form we obtain:

$$\begin{bmatrix} E_1 \\ H_1 \end{bmatrix} = \mathbf{P_1} \begin{bmatrix} E_2 \\ H_2 \end{bmatrix} \tag{4.8a}$$

$$\begin{bmatrix} E_2 \\ H_2 \end{bmatrix} = \mathbf{P_2} \begin{bmatrix} E_3 \\ H_3 \end{bmatrix} \tag{4.8b}$$

$$\begin{bmatrix} E_3 \\ H_3 \end{bmatrix} = \mathbf{P_3} \begin{bmatrix} E_4 \\ H_4 \end{bmatrix} \tag{4.8c}$$

where,

$$\mathbf{P_1} = \begin{bmatrix} \cos k_{\mathrm{Ag1}} h & (i \sin k_{\mathrm{Ag1}} h)/Y_{\mathrm{Ag1}} \\ Y_{\mathrm{Ag1}} i \sin k_{\mathrm{Ag1}} h & \cos k_{\mathrm{Ag1}} h \end{bmatrix} \tag{4.9a}$$

$$\mathbf{P_2} = \begin{bmatrix} \cos k_{\mathrm{DAST}} h & (i \sin k_{\mathrm{DAST}} h)/Y_{\mathrm{DAST}} \\ Y_{\mathrm{DAST}} i \sin k_{\mathrm{DAST}} h & \cos k_{\mathrm{DAST}} h \end{bmatrix} \tag{4.9b}$$

$$\mathbf{P_3} = \begin{bmatrix} \cos k_{\mathrm{Ag2}} h & (i \sin k_{\mathrm{Ag2}} h)/Y_{\mathrm{Ag2}} \\ Y_{\mathrm{Ag2}} i \sin k_{\mathrm{Ag2}} h & \cos k_{\mathrm{Ag2}} h \end{bmatrix} \tag{4.9c}$$

Here the characteristics matrices denote by $\mathbf{P_1}$, $\mathbf{P_2}$,and $\mathbf{P_3}$ relate the fields at the interface across each layer. So, for our five layers (Air–Ag–DAST–Ag–Air) thin-film system, the relation between E and H field of the first and the last interface can be written as:

$$\begin{bmatrix} E_4 \\ H_4 \end{bmatrix} = \mathbf{P_1 P_2 P_3} \begin{bmatrix} E_1 \\ H_1 \end{bmatrix} \tag{4.10}$$

The final characteristics matrix $\mathbf{P}$, incorporating $\mathbf{P_1}$, $\mathbf{P_2}$,and $\mathbf{P_3}$ is the resultant of 2×2 matrices:

$$\mathbf{P} = \mathbf{P_1 P_2 P_3} = \begin{bmatrix} p_{11} & p_{12} \\ p_{21} & p_{22} \end{bmatrix} \tag{4.11}$$

For the top and bottom air media, using Eq. (4.6) and considering the TE case, we obtain:

$$Y_{\mathrm{Air1}} = \sqrt{\frac{\epsilon_0}{\mu_0}} n_{\mathrm{Air1}} \cos\theta_{\mathrm{i},1} \tag{4.12a}$$

$$Y_{\mathrm{Air2}} = \sqrt{\frac{\epsilon_0}{\mu_0}} n_{\mathrm{Air2}} \cos\theta_{\mathrm{t},4} \tag{4.12b}$$

By rewriting Eqs. (4.8) and (4.12) in terms of boundary conditions:

$$\begin{bmatrix} E_{\mathrm{i},1} + E_{\mathrm{r},1} \\ (E_{\mathrm{i},1} - E_{\mathrm{r},1})Y_{\mathrm{Air1}} \end{bmatrix} = \mathbf{P_1} \begin{bmatrix} E_{\mathrm{t},2} \\ H_{\mathrm{t},2}Y_{\mathrm{Air2}} \end{bmatrix} \tag{4.13}$$

To obtain reflection (r) and transmission (t) coefficients, we expand the matrices in Eq. (4.13) as:

$$r = \frac{(Y_{\mathrm{Air1}}p_{11} + Y_{\mathrm{Air1}}Y_{\mathrm{Air2}}p_{11}) - (p_{21} + Y_{\mathrm{Air2}}p_{22})}{(Y_{\mathrm{Air1}}p_{11} + Y_{\mathrm{Air1}}Y_{\mathrm{Air2}}p_{11}) + (p_{21} + Y_{\mathrm{Air2}}p_{22})} \tag{4.14}$$

$$t = \frac{2Y_{\mathrm{Air1}}}{(Y_{\mathrm{Air1}}p_{11} + Y_{\mathrm{Air1}}Y_{\mathrm{Air2}}p_{11}) + (p_{21} + Y_{\mathrm{Air2}}p_{22})} \tag{4.15}$$

Finally, the reflection (R) and transmission (T) can be obtained using $R = |r|^2$ and $T = \frac{n_{\mathrm{t}}\cos\theta_{\mathrm{t}}}{n_{\mathrm{i}}\cos\theta_{\mathrm{i}}}|t|^2$ respectively. The absorption (A) can be obtained by using $A = 1 - R - T$. The reflectance spectra obtained using TMM is shown in Fig. 4.11(c).

For the case of TLM, Ag–DAST–Ag based MDM design can be approximated as a transmission line. A simplistic circuit model is shown in Fig. 4.11(b). Here, k, Z, and t are propagation constant, characteristic impedance, and the thickness of the transmission line, respectively, corresponding to the (top and bottom) Ag and the DAST layers. The input impedance at interfaces 3 and 2 looking downward, can be obtained using [133, 165]:

$$Z_{\mathrm{in},3} = Z_{\mathrm{Ag2}}\frac{Z_{\mathrm{Air2}} - jZ_{\mathrm{Ag2}}\tan(k_{\mathrm{Ag2}}t_{\mathrm{Ag2}})}{Z_{\mathrm{Ag2}} - jZ_{\mathrm{Air2}}\tan(k_{\mathrm{Ag2}}t_{\mathrm{Ag2}})} \tag{4.16a}$$

$$Z_{\mathrm{in},2} = Z_{\mathrm{DAST}}\frac{Z_{\mathrm{in},3} - jZ_{\mathrm{DAST}}\tan(k_{\mathrm{DAST}}t_{\mathrm{DAST}})}{Z_{\mathrm{DAST}} - jZ_{\mathrm{in},3}\tan(k_{\mathrm{DAST}}t_{\mathrm{DAST}})} \tag{4.16b}$$

where Z_{Air} is free space impedance of air. The corresponding reflection coefficients at Ag–DAST interfaces are:

$$r_3 = \frac{Z_{\mathrm{in},3} - Z_{\mathrm{DAST}}}{Z_{\mathrm{in},3} + Z_{\mathrm{DAST}}} = |r_3|\angle\phi_3 \tag{4.17a}$$

$$r_2 = \frac{Z_{\mathrm{in},2} - Z_{\mathrm{DAST}}}{Z_{\mathrm{in},2} + Z_{\mathrm{DAST}}} = |r_2|\angle\phi_2 \tag{4.17b}$$

Here, ϕ_3 and ϕ_2 denote the phase shift upon reflection from the bottom and top Ag layers. The accumulated round trip phase ($\phi_3 + \phi_2$) upon reflection from the bottom and top Ag layers is shown in Fig. 4.11(c). When the accumulated round trip phase becomes zero, maximum transmission ($T_{\max}$) is allowed at the resonant wavelength $\lambda_0 = 550$ nm [165].

A comparison among FEM, TMM, and TLM is shown in Fig. 4.11(c). An excellent agreement between simulation (FEM) and theory (TMM) is seen for the entire visible spectral regime. TLM allows us to accurately predict the resonant wavelength $\lambda_0 = 550$ nm when the accumulated round trip phase becomes zero. Hence, a perfect match between simulation and theory, indeed, validates our findings. Note that the theoretical derivations shown in this paper can be modified to find the optical response across any thin-film multilayered system for normal as well as the oblique angle of incidence. From the next subsection, we will use TMM and FEM to compare theoretical and simulation results.

4.2.5 Parametric Analysis

In order to achieve perfect absorption/transmission at the desired wavelength, ideally, the thicknesses of all three layers (top Ag, DAST, and bottom Ag) need to be optimized. Figure 4.12 shows the contour color plot for parameter optimization of absorption-mode color filter for varying thickness of top Ag, DAST, and bottom Ag layers. To find the minimum optimized thickness of the top Ag layer, a parametric sweep over 5–60 nm thickness is carried out, as shown in Fig. 4.12(a). With an increase in top Ag layer thickness, we observe a slight blueshift and a gradually increasing dip in the reflectance spectrum at the resonance wavelength. The reflectance reaches zero for 40 nm Ag layer thickness, shown by dotted light green cross line in Fig. 4.12(a), and then gradually increases. The reason can be attributed to an increase in Ag layer thickness, making it difficult for light to penetrate through the optically thick structure [129].

Additionally, a gradual decrease in the reflection bandwidth is also observed with an increase in top Ag layer thickness. This can be explained using Fabry–Perot cavity theory, where an increase in lossy Ag layer thickness increases the quality factor of the reflection spectra and hence, makes the spectral bandwidth narrower [131]. For color filtering application, a narrowband design is considered more suitable for precise color filtering capability, and hence, 40 nm thickness is taken as the optimum value for the top Ag layer thickness to achieve perfect absorption with a very narrow bandwidth of 12 nm.

Next, we vary the thickness of the DAST layer from 40 nm to 120 nm, in steps of 10 nm, as shown in Fig. 4.12(b). We observe a linear trend in the redshift of the resonance wavelength with an increase in DAST layer thickness. The reason can be explained by considering a thicker dielectric cavity, where a longer wavelength mode

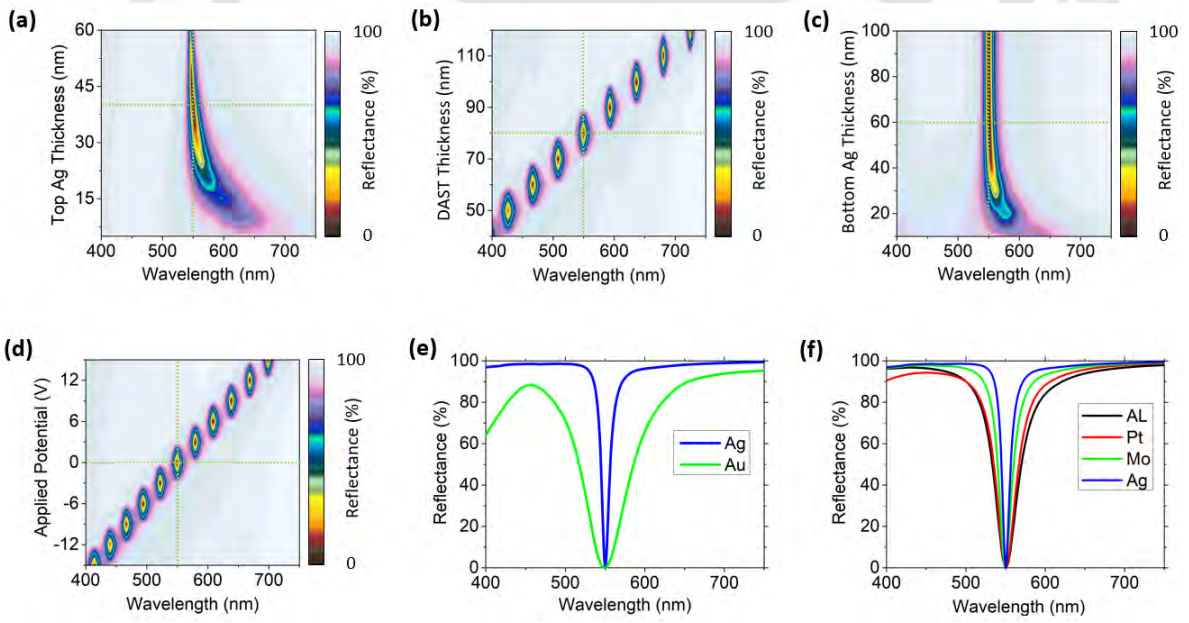

Figure 4.12: Contour colour plot for parameter optimization of absorption-mode color filter for varying thickness of (a) top silver (Ag), (b) DAST, and (c) bottom Ag layers; (d) Effect of applied voltage across the DAST layer, and reflectance spectra obtained using (e) gold (Au) / Ag as the top metal, and (f) aluminium (Al) / platinum (Pt) / molybdenum (Mo) / Ag as the bottom metal.

is supported by the medium [166]. We can see that by varying the thickness of DAST layer from 40 nm to 120 nm, the entire visible spectral range can be covered, and hence, any color filter can be designed as per demand. For example, for the design of a green color filter at 550 nm wavelength, 80 nm DAST layer thickness is the optimum value, shown by dotted light green cross line in Fig. 4.12(b).

Thereafter we vary the bottom Ag layer thickness from 10 nm to 100 nm. Similar to the case for top Ag layer, we observe a slight blueshift and a gradually increasing dip in the reflectance spectra at the resonance wavelength, with an increase in the bottom Ag layer thickness. The reflectance reaches near-zero value at 60 nm thickness, shown by dotted light green cross line in Fig. 4.12(c), and then the reflectance gradually becomes constant. Hence, for designing an absorption-mode color filter, minimum recommended bottom Ag layer thickness is 60 nm. For completely blocking the transmission, we consider bottom Ag layer thickness as 125 nm.

We then study the effect of the applied voltage across the DAST layer, as shown in Fig. 4.12(d). DAST, an EO polymer, having tunability near-visible regime and possessing a large EO coefficient (3.41 nm/V), is desirable to attain maximum tunability with minimum bias voltage. The refractive index of DAST as a function of the applied voltage is given by Eq. (4.3) [165]. By varying the applied potential, over a range of voltage, from -15 V to +15 V, in steps of 3 V, we observe a prominent redshift with a linear trend, as shown in Fig. 4.12(d). We found that by using just ± 10 V power supply, all types of color filters (blue/green/red) can be realized. When no power is supplied, by default the device acts as a green filter, shown by dotted light green cross line in Fig. 4.12(d).

Finally, we explored different materials to find a suitable choice for the top and the bottom metallic layers. For the case of top metallic layer, we found that only gold (Au) can be used as a possible alternative for Ag. However, the reflectance spectra obtained

using Au is poor compared to Ag, as shown in Fig. 4.12(e). Moreover, Au is much more expensive and gives a very broad bandwidth, hence, not a suitable choice for low-cost and high quality-factor absorption-mode color filter design. For the case of bottom metallic layer, we found many cheaper alternatives to Ag, such as aluminium (Al), platinum (Pt), and molybdenum (Mo). As can be seen in Fig. 4.12(f), Ag outperforms all the metals, in terms of high-quality factor obtained, followed by Mo, Pt, and Al. Nevertheless, such materials can still be used as a cheaper alternative to Ag to reduce the overall cost of our design, since a relatively thick bottom metallic layer is used for the design of absorption-mode color filter.

4.2.6 Absorption-mode Color Filters

To achieve perfect absorption at the desired wavelength, either the thickness or the refractive index of DAST needs to be changed. As seen in the parametric analysis section, a variation in DAST thickness between 40 and 120 nm can cover the entire visible range. However, such MDM based color filters once fabricated can filter only a fixed color (either blue or green, or red), which limit their ability to dynamically tune the color filtering characteristics over a broad spectral range.

In order to control the light absorption dynamically, the refractive index of DAST can be changed by providing sufficient power supply. For illustration purposes, shown in Fig. 4.13(a), we design three distinct absorption-mode color filters (blue, green, and red), and show that only ± 10 V power supply should be sufficient to realize any intermittent color filter in the visible regime. A near-perfect absorbance is achieved with a very narrow bandwidth (12 nm) for each of the absorption-mode color filters. To obtain near-perfect absorption for all three color filters shown, the thickness of each layer is optimized. The top Ag layer is 45 nm thick, middle DAST layer is 80 nm thick, and the bottom Ag layer is 125 nm thick.

Further, to ensure that our design is suitable for dynamic daylight situation, we

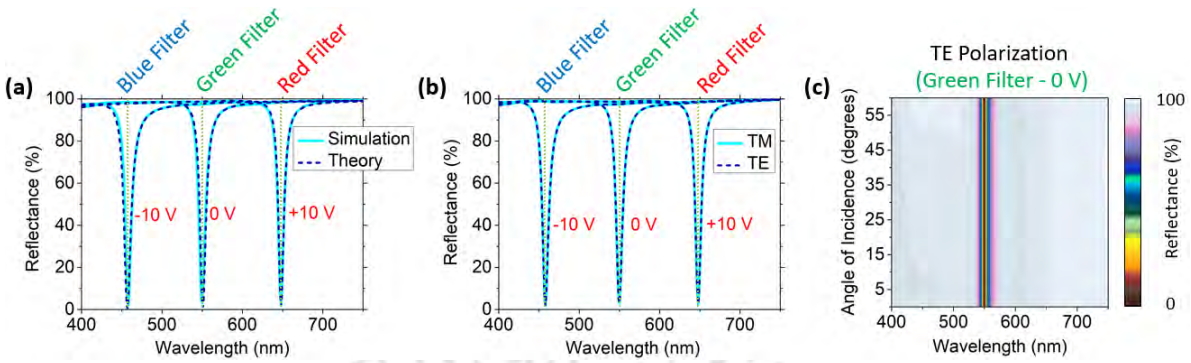

Figure 4.13: Ag–DAST–Ag based absorption-mode color filter showing reflection spectra for (a) realization of blue, green, and red color filters over a voltage range of −10 V to +10 V, (b) both TM and TE polarization, and (c) contour plot over 0–60 degrees of oblique angle of incidence at 0 V bias, showing angle-insensitivity considering TE polarization.

study both TM and TE polarization using Ag–DAST–Ag based design with a bias voltage of ±10 V. Figure 4.13(b) shows that even after applying voltage over −10 V to +10 V, transmission spectra remain unaffected by the change in polarization of the incident wave, hence, showing polarization insensitivity. To account for the effect of dynamically changing position of the sun, we also study for varying angles of incidence, ranging over 0–60 degrees at 0 V bias, considering TE case. Figure 4.13(c) shows that the reflection spectra are not affected for varying angles of incidence, hence, making our color filter design angle insensitive to a great extent. A comparative overview of a few recently reported absorption-mode color filters in the visible spectral regime is shown in Table 4.5, showing that our design is much more power-efficient compared to some of the recently reported works in literature.

4.2.7 Transmission-mode Color Filters as Electrochromic Windows

Similar to the case of absorption-mode color filters, transmission-mode color filters can also be designed by tweaking the bottom Ag layer thickness enough to allow the passage of light through the MDM structure. A 2D schematic side view of our transmission-mode color filter is shown in Fig. 4.14(a). The top and bottom Ag layers, each 32 nm thick and middle DAST layer, 77 nm thick are considered for this design.

Table 4.5: A comparative overview of a few recently reported absorption-mode color filters in the visible spectral regime

References	Structural Design	Spectral Shift	Applied Potential
Mirshafieyan *et al.* [200]	Ag–InSb(n)–TiO_2–Ag	20/40 nm	50 V
Guo *et al.* [201]	ITO–DAST–ITO	85 nm	±20 V
Bibbo *et al.* [207]	Au–$LiNbO_3$–ITO	50 nm	160 V
Park *et al.* [170]	ITO–HfO_2–Au	40 nm	50 V
Yi *et al.* [208]	ITO–Si_3N_4–Au	10 nm	20 V
This Work	Ag–DAST–Ag	190 nm	± 10 V

In contrast to the case of absorption-mode color filter, for the design of transmission-mode color filter, the bottom Ag layer thickness is kept optically thin to allow a narrowband transmission through the structure, when the Fabry–Perot resonance condition is satisfied at the resonance wavelength. The normalized electric (**E**) field distribution corresponding to the resonant wavelength, shown in Fig. 4.14(b), clearly depicts the presence of resonant mode trapped inside the DAST cavity. Similar to the case of absorption-mode color filter, we demonstrate three distinct transmission-mode

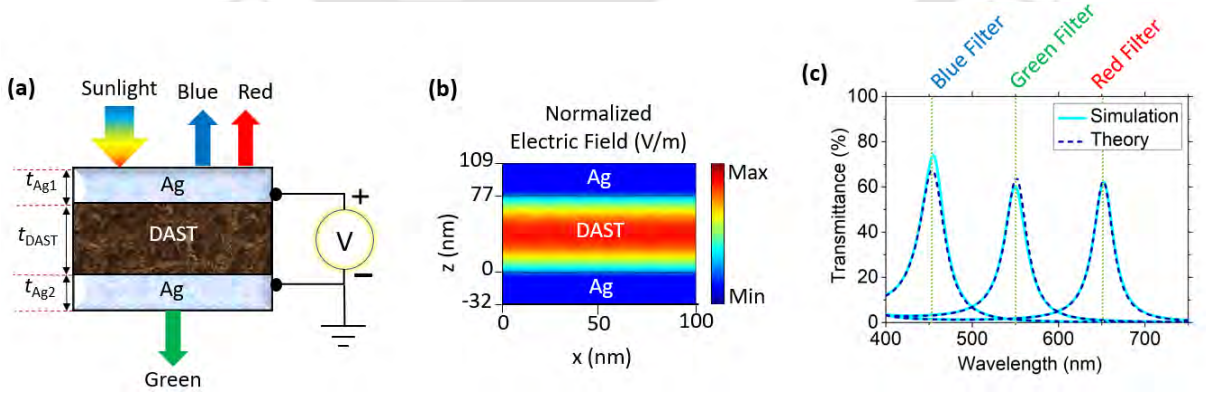

Figure 4.14: (a) A symmetric Ag–DAST–Ag based transmission-mode color filter showing (a) 2D schematic side view with bias voltage supply, (b) normalized electric field (**E**) distribution, showing the existence of resonant mode trapped inside the DAST layer corresponding to the resonance wavelength ($\lambda_0 = 550$ nm), and (c) realization of blue, green, and red color filters over a voltage range of −10 V to +10 V.

color filters (blue, green, and red), and show that only ±10 V power supply should be sufficient to realize any intermittent transmission-mode color filter in the visible regime. As shown in Fig. 4.14(c), a transmission peak of over 60% is achieved with moderate bandwidth (approx. 32 nm) for each of the transmission-mode color filters. The transmission peak can be further enhanced by sacrificing the quality factor of the transmission spectra.

4.2.8 Prospective Fabrication Method and Characterization Technique

A typical fabrication flow for the realization of our theoretically proposed design is rather straightforward. MDM based devices, composed of multilayer thin films of Ag–DAST–Ag can be fabricated by successive electron beam (e-beam) evaporation technique [169–171]. For the realization of an absorption-mode color filter, first, a 125 nm thick Ag layer needs to be coated on a smooth silicon (Si) wafer [170]. Thereafter, 80 nm thick DAST layer needs to be deposited on top of Ag–Si layer. Finally, 45 nm thick Ag layer can be deposited on top of DAST–Ag–Si layer. For the case of a transmission-mode color filter, top and bottom Ag layers, each 32 nm thick, need to be coated on top and bottom surfaces of a two-sided polished DAST layer of 77 nm thickness [169,171]. For optical characterization, Fourier Transform infrared (FT-IR) microscope or a microscope integrated with a spectrometer and an electron multiplication charge-coupled device (CCD) camera of prescribed specifications given in [169,170] may be used.

4.2.9 Summary

We presented a theoretical design of electrotunable absorption- and transmission-mode nanophotonic windows as specific color filter based on metal–dielectric–metal (MDM) structure **with significantly reduced voltage requirements**. We illustrated the design of three color filters (blue, green, and red) to show that only ±10 V power supply should be sufficient to realize any intermittent color filter in the visible regime.

Our theoretical results obtained using transfer matrix method and transmission line method agree well with those of finite-element-method based full-wave simulations, which validates our results. For practical realization, our design is power-efficient, large-area compatible, lithography-free, angle-insensitive, polarization-independent, and has extremely narrow-bandwidth.

5

Static and Electrotunable Windows Based on Insulator–Metal–Insulator Multilayer Thin-films

Contents

In chapters 3 and 4, we mainly focused on the designs of passive and electrotunable windows, respectively, based on metal–insulator–metal multilayer thin-films. We showed that the optimal performances of those windows were obtained using metallic layers which were 5 nm in thickness. Today, with the existing nanofabrication technology, it is still very challenging to deposit uniform 5 nm thin top and bottom metallic layers in a metal–insulator–metal structure. However, with rapid advancement in nanofabrication technology we believe that soon it may be possible in the near future. So, keeping in mind the current state-of-the-art nanofabrication technology, we explored alternative designs of passive and electrotunable windows based on insulator–metal–insulator (IMI) multilayer thin-films, which would allow the use of a thicker metal film that would be easier to fabricate.

This chapter presents the designs of static and electrotunable 'smart' windows, followed by a comparative study between those. **A unique approach is adopted** to design insulator–metal–insulator thin-films, deposited over a silica glass substrate to filter visible and infrared solar radiation selectively. For static windows, we optimize our design to operate in diverse climatic conditions by choosing different combinations and thicknesses of metal and insulator layers. Whereas for electrotunable windows, we use an electro–optic polymer as the insulator layers to dynamically control portions of transmitted solar radiation over a voltage range of -12 V to +12 V.

5.0.1 Background

In literature, many visible or infrared filters based on metal–insulator–metal (MIM) thin-films have been reported [197–199]. However, there is a lack of work on insulator–metal–insulator (IMI) thin-films based filters. Moreover, such thin-films have not been explored in the context of smart windows that simultaneously require filtering of visible and infrared radiations. Here, it is important to highlight that the MIM structures significantly block the transmission of electromagnetic radiation through it due to the

use of two metallic layers at the top and bottom. Since smart window applications demand transmission-mode filters with high visible transmittance, the metallic layer thickness should be minimal in MIM structures to achieve desired visible light transmission. Unfortunately, such ultra-thin layers of metals are very challenging to realize even with the existing state-of-the-art nanofabrication facilities. In this context, IMI thin-films could be a more practical choice due to the use of a single metallic layer (that could be comparatively thicker than those used in MIM structures), sandwiched between two insulator layers.

Here we present a comparative study on insulator–metal–insulator (IMI) thin-films based static and electrotunable windows. We use noble metals [gold (Au), silver (Ag), and copper (Cu)] as well as their relatively inexpensive alternatives [lithium (Li), titanium nitride (TiN), and aluminium oxynitride (ALON)] as a choice for the metallic layer. For static windows, we make use of different dielectrics [such as, silica (SiO_2), titanium oxide (TiO_2), and silicon (Si)] as a choice for both the top and bottom insulator layers. For electrotunable windows, we use an electro–optic polymer: 4-dimethylamino-N-methyl-4-stilbazoliumtosylate (DAST), as the insulator layers, which would allow to dynamically control the portions of transmitted solar radiation over a voltage range of -12 V to +12 V [132].

5.0.2 Design and Working Principles

A three-dimensional (3D) schematic of our smart window coated with IMI thin-film is depicted in Fig. 5.1(a). This nanocoated thin-film consists of a metallic layer sandwiched between two insulator layers. Smart windows based on this IMI thin-film can control portions of solar radiation transmitted and reflect the non-solar radiation coming from the heated objects nearby. Figure 5.1(b) depicts an artistic view of our smart window, which can ideally work in four possible configurations, discussed in detail in section 3.3 of chapter 3. Configuration I refers to 'Bright–Cool' (BC) mode, which es-

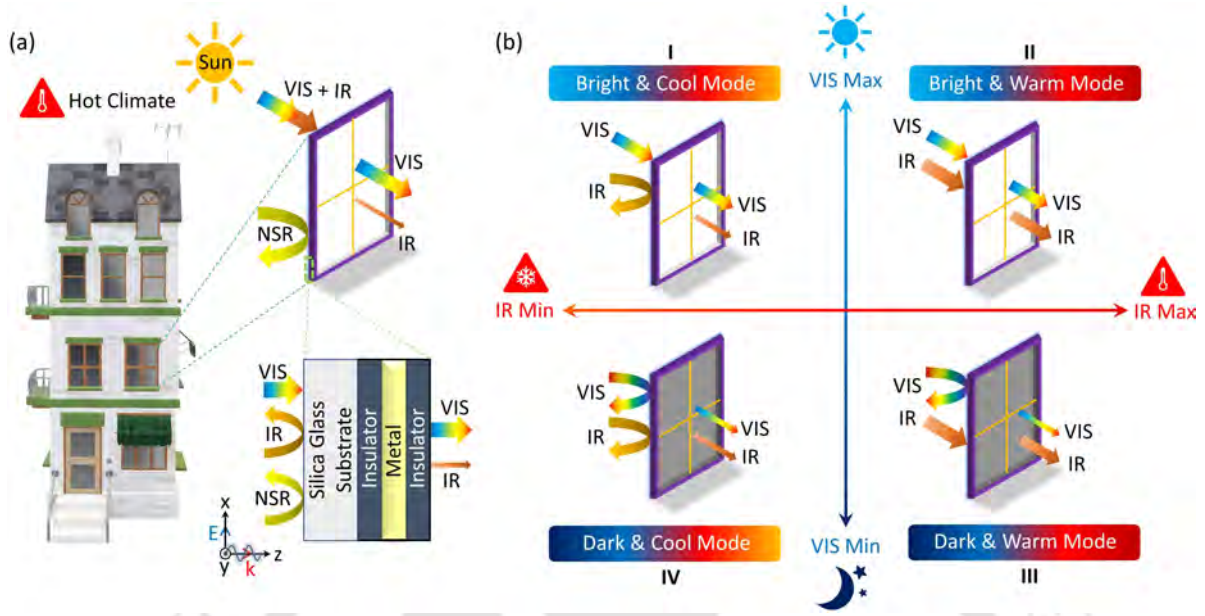

Figure 5.1: A three-dimensional (3D) visual demonstration of our smart window coated with insulator–metal–insulator thin-film depicting (a) a hot climatic condition, where these windows allow transmission of the visible (VIS) radiation, block infrared (IR), and reflect the non-solar radiation (NSR) coming from the blackbody radiation of the nearby objects. (b) Graphical representation depicting four possible modes of operation by transmitting or blocking visible/IR radiation.

sentially allows visible but blocks IR transmission—useful in warm climate conditions with high illumination. Configuration II refers to 'Bright–Warm' (BW) mode, which essentially allows both visible and IR transmission—useful in cool climate conditions with high illumination. Configuration III refers to 'Dark–Warm' (DW) mode, which essentially blocks visible but allows IR transmission—useful in cool climate conditions with low illumination. Lastly, configuration IV refers to 'Dark–Cool' (DC) mode, which essentially blocks both visible and IR transmission—useful in warm climate conditions with low illumination. Note that DC mode is suitable for application in cold storage facilities, skylight panels, and radiative cooling [217,218], which we have addressed in chapters 6 and 7 of this thesis.

5.0.3 Simulation Methods

A 2D schematic view of IMI thin-films is depicted in Fig. 5.2(a). Figures 5.2(b) and 5.2(c) show numerically obtained absorption, reflection, and transmission spectra over solar and non-solar radiation. This figure illustrates that these IMI thin-films can selectively filter the solar radiation and completely reflect the non-solar radiation. Here, we consider identical top and bottom insulators layers made of TiO_2, each 53 nm thick and having a fixed refractive index (n_D = 2.2). The metallic layer is composed of 17 nm thick silver.

We use wave optics module of a commercial finite element method solver, COMSOL Multiphysics®, to simulate over solar and non-solar spectral ranges. To capture all the structural details effectively, we prefer extra-fine mesh elements with the maximum and minimum mesh element sizes of 22.2 nm and $\sim$ 0.1 nm, respectively. We consider the period to be 200 nm and apply Floquet boundary conditions along x and y directions to emulate a large-area thin-film. Note that the optical constants for metal and metal oxides such as Au [161], Ag [161], Cu [161], Li [219], TiN [220], ALON [164] are taken from the literature.

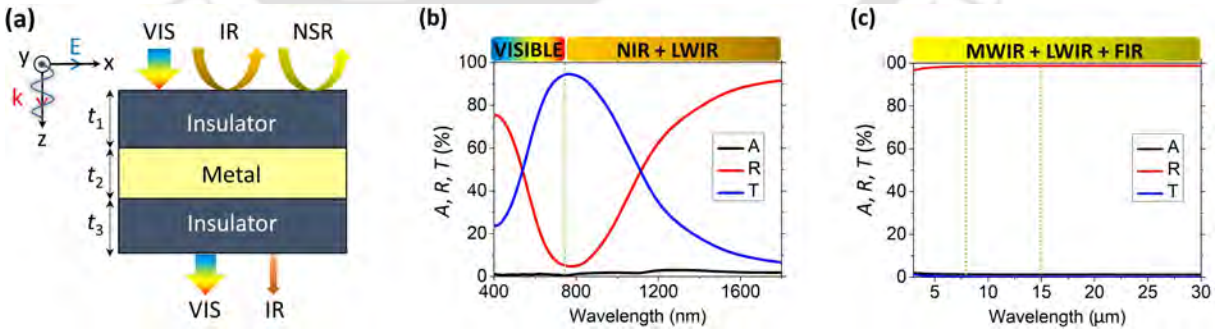

Figure 5.2: Insulator–metal–insulator thin-film in (a) a 2D schematic side view that can selectively transmit solar radiation (VIS+IR) and reflect non-solar radiation (NSR). Here, the incident light is a plane wave of TM polarization (electric field parallel to xz plane) travelling along z-direction. Numerically calculated absorption (A), reflection (R), and transmission (T) spectra over (b) solar radiation (400–1800 nm) and (b) non-solar radiation (3–30 μm). Note that in (b) and (c), the top and bottom insulators layers are made of TiO_2, each 65 nm thick and having fixed refractive index (n_D = 2.2). The metallic layer is made of 17 nm thick silver.

5.0.4 Theoretical validation

A comparison between simulation (FEM) and theory (TMM and TLM) is shown in Fig. 5.3. We observe a near-perfect match between FEM and TMM transmission spectra over the entire solar radiation spectral regime. The phase response obtained using TLM helps us to find the wavelength of maximum transmission ($\lambda_{\max} = 750$ nm). For instance, when the accumulated round trip phase goes to zero, TMM and FEM predict the maximum transmission, which further consolidates our findings. Note that for above studies, we consider 17 nm thick Ag as the metallic layer. The top and bottom insulator layers have fixed thickness and refractive index (t_{D} = 65 nm, n_{D} = 2.2). In the subsequent sections, FEM and TMM are used to compare between simulation and theoretical results.

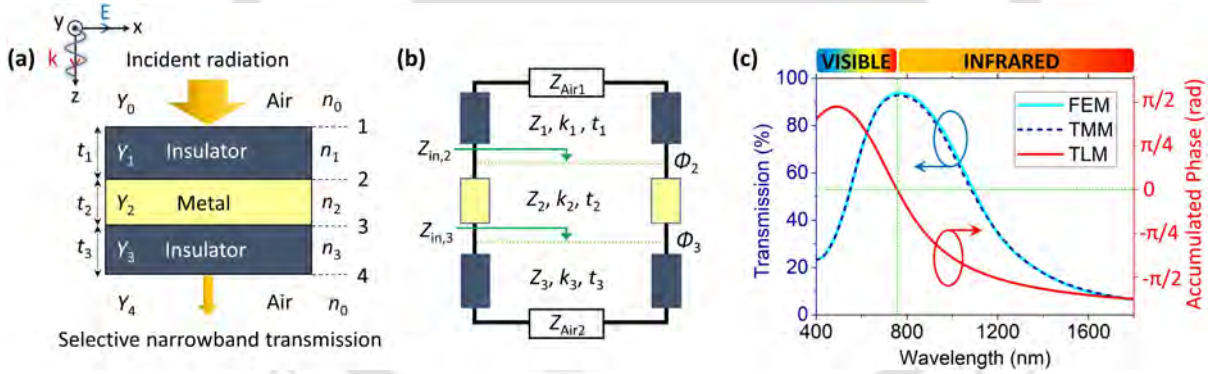

Figure 5.3: Analytical modelling of insulator–metal–insulator thin-film using (a) transfer matrix method (TMM) and (b) transmission line method (TLM). (c) Spectral and phase response comparison among finite element method (FEM; solid cyan line), TMM (dashed blue line), and TLM (solid red line) methods. Here, we consider 17 nm thick Ag as the metallic layer, and the top and bottom insulator layers have fixed thickness and refractive index (t_{D} = 65 nm, n_{D} = 2.2).In (a) t, Y, and n represent the thickness, admittance, and refractive index of each layer, respectively. In (b) Z and k denote impedance and propagation wavevector at each layer; ϕ denotes phase shift upon reflection at each metal–insulator interface.

5.0.5 Parametric Analysis

To optimize our design, we study the effect of change in each layer's material thickness and refractive index in IMI thin-film. First, we vary the thickness of the metallic

layer between 5 and 50 nm. Here, for reference, we take Ag as the metallic layer keeping top and bottom insulator layers thicknesses and refractive indices fixed (t_1, t_3 = 42 nm, n_1, n_3 = 2.2). The color contour plot in Fig. 5.4(a) shows that with an increase in metal thickness, the amplitude of the transmission spectra decreases, becomes narrower, and finally, transmission becomes negligible after 50 nm thickness. This is because at optical frequencies, metals are highly reflective and do not allow the penetration of electromagnetic waves through it beyond a particular thickness [18]. Therefore, for application such as colour filters or sensors which require high quality factor, a relatively thick metal is desirable [132, 221]. Whereas for smart windows, which require high transmission over a broad spectral regime, relatively thin metal is desired. In general, a metal thickness between 15 and 30 nm could be suitable depending upon the choice of metal used.

Next, we vary the thickness of the identical top and bottom insulator layers between 10 and 60 nm, keeping their refractive index as 2.2 and metallic layer thickness as 20 nm. Figure 5.4(b) shows a shift in the peak transmission towards IR regime with an increase in dielectric layer thickness shown by the dotted white line. Lastly, we vary

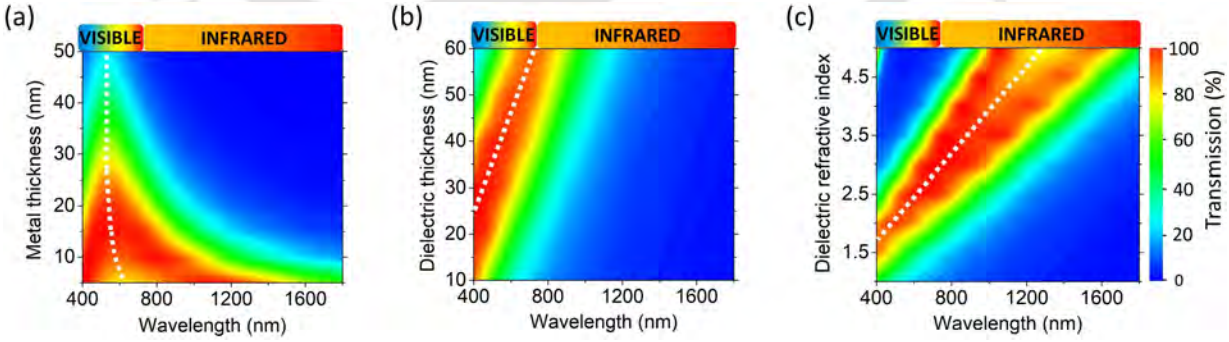

Figure 5.4: Numerically calculated parametric analysis for insulator–metal–insulator thin-film showing transmission over solar radiation spectra using colour contour plot for varying (a) thickness of metallic layer (t_2), (b) thickness of dielectric layer (t_1 and t_3), and (c) refractive index of dielectric layer (n_1 and n_3). Here, the white dotted lines show the trends for the maximum transmission with change in thickness and refractive index of different layers. Note that in each case silver is chosen as the metallic layer.

the dielectric refractive index between 1 and 5, choosing insulator and metallic layer thicknesses as 42 nm and 20 nm, respectively. Figure 5.4(c) clearly shows that with an increase in insulator refractive index, the peak transmission broadens and shifts towards the IR regime. The reason can be attributed to an increase in the path length as the medium becomes denser. Now, if we want to optimize our design for BC, BW, and DW modes, the key idea is to have peak transmission in the visible, interface of visible–IR, and IR regimes, respectively. To achieve this objective, either the thickness or the refractive index of the dielectric need to be altered. We found that for BC, BW, and DW modes, silicon dioxide (SiO_2), titanium dioxide (TiO_2), and silicon (Si), respectively, could be a suitable choice as the top and bottom insulator layers.

5.1 Insulator–Metal–Insulator Thin-films Based Static Windows

A comprehensive idea about all the design parameters, discussed under parametric analysis section, allows us to design customized passive windows based on site requirement. In Figs. 5.5(a)–5.5(f), we demonstrate six different designs of thin-film based passive windows, by choosing different combinations of metal and insulator layers. Figure 5.5(a) shows design of thin-film based passive windows using SiO_2–Ag–SiO_2 for BC mode (useful in summer season with high illumination), TiO_2–Ag–TiO_2 for BW mode (useful in winter season with high illumination), and Si–Ag–Si for DW mode (useful in summer season with low illumination). The basic idea is to keep peak transmission in the middle of the visible regime for BC mode, at the transition interface of visible–IR regime for BW mode, and in the middle of IR regime for BW mode. A similar approach has been adopted using alternative materials such as Cu, Li, and TiN, for providing a low-cost passive window.

Comparing the transmission spectra in Figs. 5.5(a) and 5.5(e), it is evident that Ag based thin-films windows outperform Au based thin-film windows. For Ag based

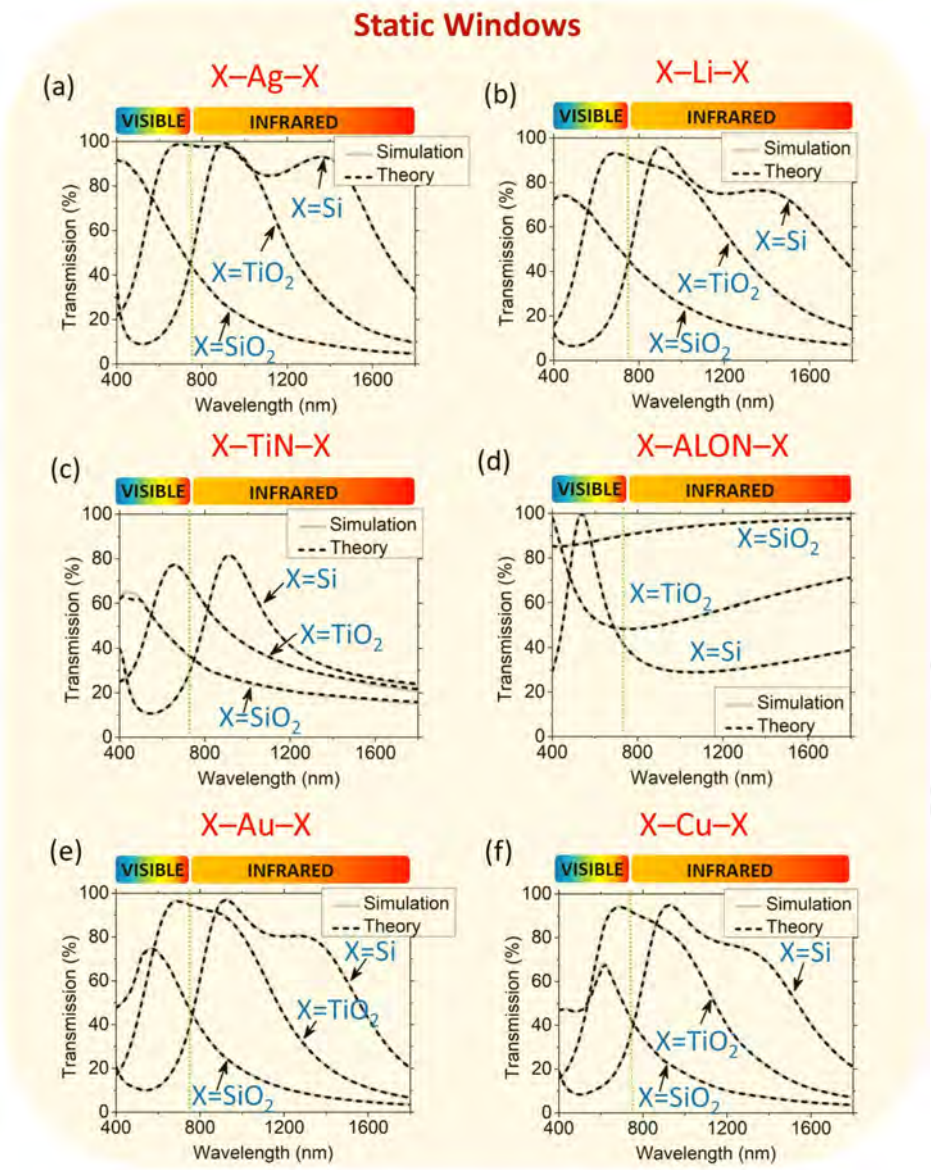

Figure 5.5: Design of insulator–metal–insulator thin-film based passive window glasses using metal as silver (Ag), lithium (Li), titanium nitride (TiN), aluminium oxynitride (ALON), gold (Au), and copper (Cu). In (a), (b), (c), (e), and (f), passive windows could operate in BC mode—choosing dielectric as silicon dioxide (SiO_2); useful in summer season with high illumination, BW mode—choosing dielectric as titanium dioxide (TiO_2); useful in winter season with high illumination, and DW mode—choosing dielectric as silicon (Si); useful in winter season with low illumination. Whereas in (d), these passive windows with metal as ALON could operate in BC mode—choosing dielectric as Si, BW mode—choosing dielectric as SiO_2, and intermediate mode—choosing dielectric as TiO_2; useful in spring/autumn with high illumination. Thicknesses of metal (t_M) and insulator (t_D) layers in nm: (a) $t_M = 15$, $t_D = 53$, (b) $t_M = 24$, $t_D = 49$, (c) $t_M = 18$, $t_D = 54$,(d) $t_M = 5$, $t_D = 35$, (e) $t_M = 18$, $t_D = 53$, (f) $t_M = 18$, $t_D = 53$.

Table 5.1: Specifications for insulator–metal–insulator thin-films based static windows.

Metal	Insulator	IMI Structure (thickness in nm)	Mode	λ_{max} (nm)	T_{max} (%)	θ_{max} (degree)
Au	SiO_2	SiO_2 (53)–Au (18)–SiO_2 (53)	BC	570	75.0	80
	TiO_2	TiO_2 (53)–Au (18)–TiO_2 (53)	BW	690	96.6	82
	Si	Si (53)–Au (18)–Si (53)	DW	920	97.2	83
Ag	SiO_2	SiO_2 (53)–Ag (15)–SiO_2 (53)	BC	400	92.0	81
	TiO_2	TiO_2 (53)–Ag (15)–TiO_2 (53)	BW	700	99.1	82
	Si	Si (53)–Ag (15)–Si (53)	DW	900	99.7	83
Cu	SiO_2	SiO_2 (53)–Cu (18)–SiO_2 (53)	BC	610	68.6	80
	TiO_2	TiO_2 (53)–Cu (18)–TiO_2 (53)	BW	690	94.2	82
	Si	Si (53)–Cu (18)–Si (53)	DW	920	95.1	84
Li	SiO_2	SiO_2 (49)–Li (24)–SiO_2 (49)	BC	440	74.5	81
	TiO_2	TiO_2 (49)–Li (24)–TiO_2 (49)	BW	680	93.4	82
	Si	Si (49)–Li (24)–Si (49)	DW	900	96.0	84
TiN	SiO_2	SiO_2 (54)–TiN (18)–SiO_2 (54)	BC	440	65.0	82
	TiO_2	TiO_2 (54)–TiN (18)–TiO_2 (54)	BW	650	77.5	84
	Si	Si (54)–TiN (18)–Si (54)	DW	910	81.4	84
ALON	SiO_2	SiO_2 (35)–ALON (5)–SiO_2 (35)	BW	1800	98.1	85
	TiO_2	TiO_2 (35)–ALON (5)–TiO_2 (35)	IMD	400	98.5	84
	Si	Si (35)–ALON (5)–Si (35)	BC	540	99.9	83

Note that all above parameter values are evaluated over solar spectral range *i.e.* 400–1800 nm wavelengths. Here, λ_{max}: wavelength of the peak transmission, T_{max}: peak transmission, θ_{max}: the maximum angle of incidence for unpolarized light—having average transmittance $\geq$ 90% over 400–1800 nm wavelengths, BC: Bright–Cool, BW: Bright–Warm, DW: Dark–Warm, and IMD: **i**nter**med**iate.

thin-films, a peak transmission up to 92.0%, 99.1%, and 99.7% is achieved in BC, BW, and DW modes, respectively. Apart from silver, Cu, Li, and TiN performed reasonably well and can be considered a reasonable, cost-effective alternative for a large-scale window design. Unlike the five metals, ALON based thin-film windows [shown in Fig. 5.5(d)] could work in BW mode using SiO_2–ALON–SiO_2, intermediate mode using TiO_2–ALON–TiO_2 (useful in spring/autumn season with high illumination), and BC mode using Si–ALON–Si. Therefore, precise control over IR transmission gives a customizable solution to design a climate-specific window. Note that ALON is abundant, low-cost, toughest, and lightweight poly-crystalline transparent glass [167] suitable for bulletproof, portable, and blast-resistant windows that can be used for fighter aircraft, military vehicles, and submarines [168]. A detailed specification of our thin-film based passive windows is provided in Table 5.1.

5.2 Insulator–Metal–Insulator Thin-films Based Electrotunable Windows

While thin-film based static window glasses could provide low-cost windows customizable for different climate conditions, static windows cannot be tuned once fabricated. Therefore, we looked for an electro–optic material that can be used as top and bottom insulator layers and can match the refractive indices of SiO_2, TiO_2, and Si by tuning voltage supply. In literature, various electro-optic materials have been reported, but most of them have a small value of electro-optic coefficient [141]. A low value of electro-optic coefficient will result in significantly less tunability of peak transmission, and consequently, very high voltage will be required to cover the entire solar radiation spectral regime. DAST, an EO polymer having tunability near-visible regime and possessing a very large EO coefficient (3.41 nm/V) was reported by Geis *et al.* [182].

Figure 5.6(a) shows a 2D schematic view of IMI thin-film with an applied bias voltage (V). It consists of 65 nm thick top and bottom DAST layers, used as the electro–optic

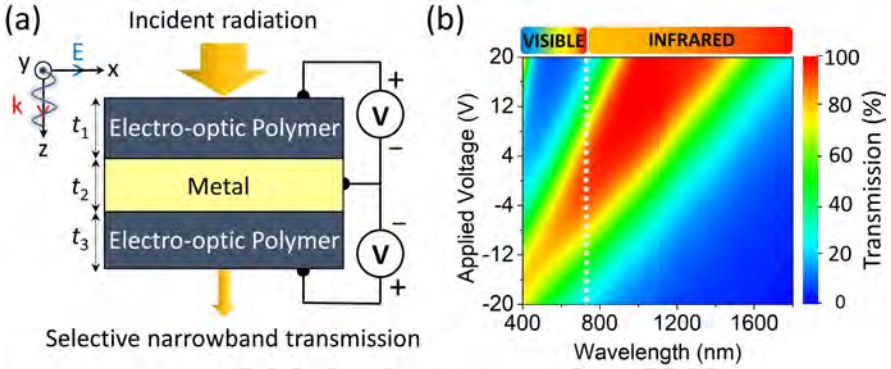

Figure 5.6: (a) 2D schematic side view of insulator–metal–insulator thin-film with bias voltage supply. (b) Colour contour transmission spectra for varying bias voltage between −20 V and +20 V. Here, 17 nm thick Ag is used as the metallic layer and 65 nm thick DAST polymer is used as the top and bottom dielectric layers.

polymer, and a 17 nm thick middle metallic layer made of gold. During the experiment, metal contacts can be placed on the outer surfaces of the top and bottom electro-optic (EO) polymer layers, as also demonstrated in the literature for other EO polymers such as lithium niobate ($LiNbO_3$) [222–224]. Figure 5.6(b) shows the effect of change in bias voltage between −20 V and +20 V. We see that the peak transmission shifts towards IR, and also the transmission spectrum gets broader. We choose the thickness of metal and insulator layers such that at no bias condition (0 V), the peak transmission lies precisely at the transition interface of the visible and IR regime. When we apply positive bias (e.g. +12 V), the peak transmission shifts towards IR. Whereas, with negative bias (e.g. −12 V), the peak transmission shifts towards visible. For a low-power design, we estimate that −12 V, 0 V, and +12 V, could be suitable for windows operating in BC, BW, and DW modes, respectively.

Based on the above understanding, in Figs. 5.7(a)–5.7(f), we show six different designs of thin-film based electrotunable windows using different choices of metals. In each case, DAST is used as the top and bottom insulator layers. For the case of Au, Ag, Cu, Li, and TiN, when we apply −12 V, 0 V, and +12 V power supply, these windows can work in BC, BW, and DW modes, respectively. Ag gives the best results like the

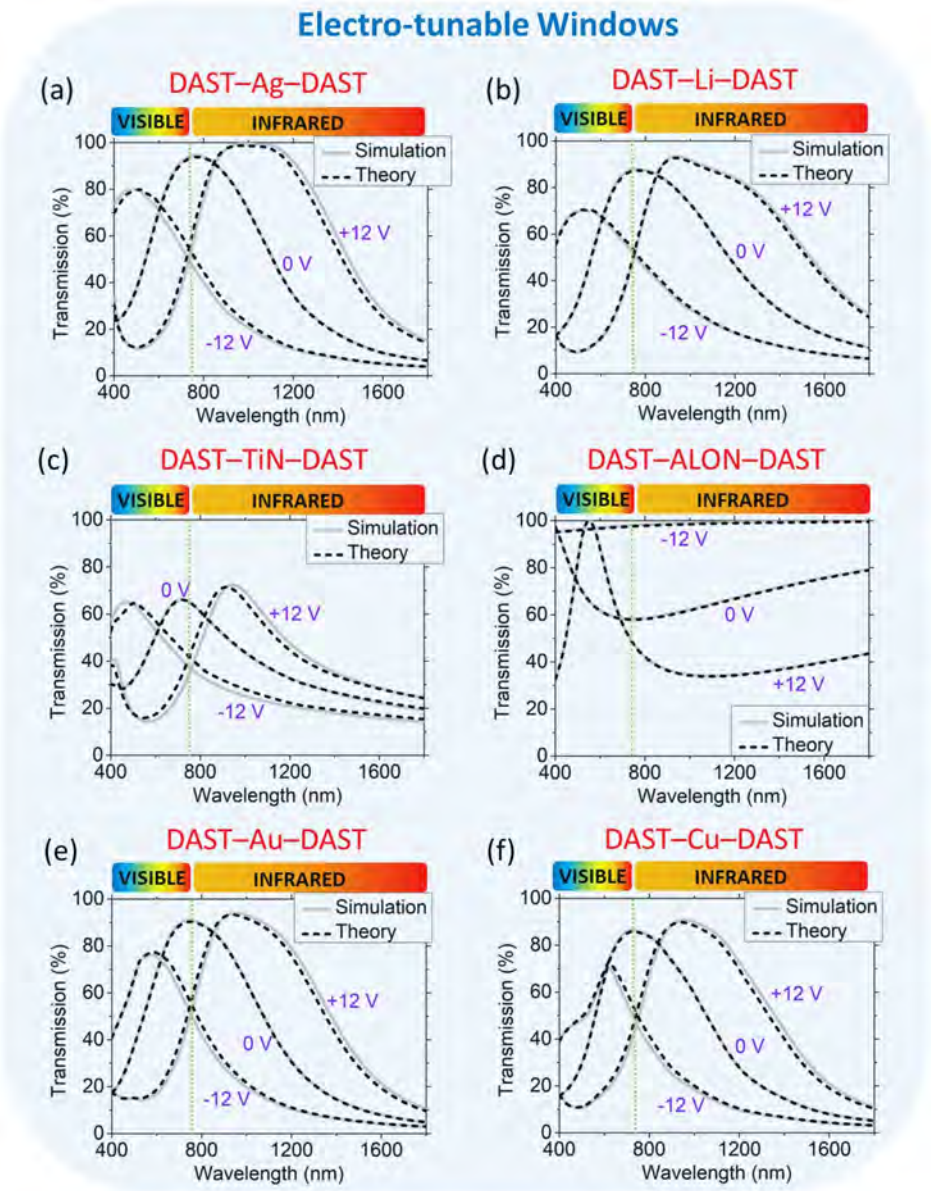

Figure 5.7: Design of insulator–metal–insulator thin-film based electrotunable window glasses in using metal as silver (Ag), lithium (Li), titanium nitride (TiN), aluminium oxynitride (ALON), gold (Au), and copper (Cu). Here, an electro–optic polymer: 4-dimethyl-amino-N-methyl-4-stilbazoliumtosylate (DAST) is used as the top and bottom insulator layers. In (a), (b), (c), (e), and (f), these tunable windows could operate in BC, BW, and DW modes by choosing −12 V, 0 V, and +12 V power supply, respectively. Whereas in (d), ALON based tunable windows could operate in BC, intermediate, and BW modes by choosing +12 V, 0 V, and −12 V power supply, respectively. Thicknesses of metal (t_M) and insulator (t_D) layers in nm: (a) t_M = 17, t_D = 65, (b) t_M = 26, t_D = 62, (c) t_M = 20, t_D = 70, (d) t_M = 5, t_D = 40, (e) t_M = 20, t_D = 65, (f) t_M = 20, t_D = 65.

Table 5.2: Specifications for insulator–metal–insulator thin-film based electrotunable windows.

Metal	IMI Structure (thickness in nm)	Mode	Potential (Volts)	λ_{max} (nm)	T_{max} (%)	θ_{max} (degree)
Au	DAST (65)–Au (20)–DAST (65)	BC	−12	580	76.2	83
		BW	0	750	91.0	83
		DW	+12	950	94.1	84
Ag	DAST (65)–Ag (17)–DAST (65)	BC	−12	490	80.0	83
		BW	0	760	94.5	83
		DW	+12	980	99.5	84
Cu	DAST (65)–Cu (20)–DAST (65)	BC	−12	610	70.9	83
		BW	0	720	86.6	83
		DW	+12	950	90.7	84
Li	DAST (62)–Li (26)–DAST (62)	BC	−12	520	70.7	83
		BW	0	760	88.0	84
		DW	+12	940	93.4	84
TiN	DAST (70)–TiN (20)–DAST (70)	BC	−12	470	65.0	81
		BW	0	720	66.2	83
		DW	+12	940	72.3	84
ALON	DAST (40)–ALON (5)–DAST (40)	BW	−12	1800	99.9	84
		IMD	0	400	97.8	84
		BC	+12	550	99.9	83

Note that all above parameter values are evaluated over solar spectral range *i.e.* 400–1800 nm wavelengths. Here, λ_{max}: wavelength of the peak transmission, T_{max}: peak transmission, θ_{max}: the maximum angle of incidence for unpolarized light—having average transmittance $\geq 90\%$ over 400–1800 nm wavelengths, BC: Bright–Cool, BW: Bright–Warm, DW: Dark–Warm, and IMD: **i**nter**med**iate.

case of a static window, followed by Au, Li, Cu, and TiN. For Ag based thin-films, a peak transmission up to 80.0%, 94.5%, and 99.5% is achieved in BC, BW, and DW modes, respectively. Unlike these five metals, when we apply −12 V, 0 V, and +12 V, ALON based designs work in BW, intermediate, and BC modes. Although for proof of the concept, we have demonstrated three instants *i.e.* −12 V, 0 V, and +12 V, these electrotunable glasses give an extra degree of freedom to tune the spectral response using any voltage between −12 V and +12 V. Therefore, we believe that these smart windows could be a suitable all-weather solution. The dimension of each layer concerning electrotunable window is provided in Table 5.2.

5.2.1 Effect of Different Polarizations and Incident Angles

In a practical scenario, these static and electrotunable windows may face sunlight at a diverse angle of incident depending upon day time. Therefore, to have practical utility, the design should be polarization and angle insensitive to some extent. The structure we considered is azimuthally symmetric, and hence, it is polarization independent. When light of arbitrary polarization is incident from the top, it encounters a planar multilayer structure that is symmetrical along both x and y orthogonal directions [225]. Figure 5.8(a) shows spectral response obtained for silver thin-film based static windows, considering both TM and TE polarizations. A perfect match between both the polarizations proves that our design is polarization insensitive.

Physically, light impinging on a multilayer system at an oblique angle of incidence has two orthogonal electric field vector components: parallel and perpendicular to the top surface of the multilayer stack, for any arbitrary polarization. For the angle study shown in Figs. 5.8(b) and 5.8(c), we consider TiO_2–Ag–TiO_2 thin-film based static windows. We see that these static windows are angle insensitive up to 80 degrees of angle of incidence. However, the overall transmission through our multilayer design drops significantly at a grazing angle of incidence (80 degrees and beyond).

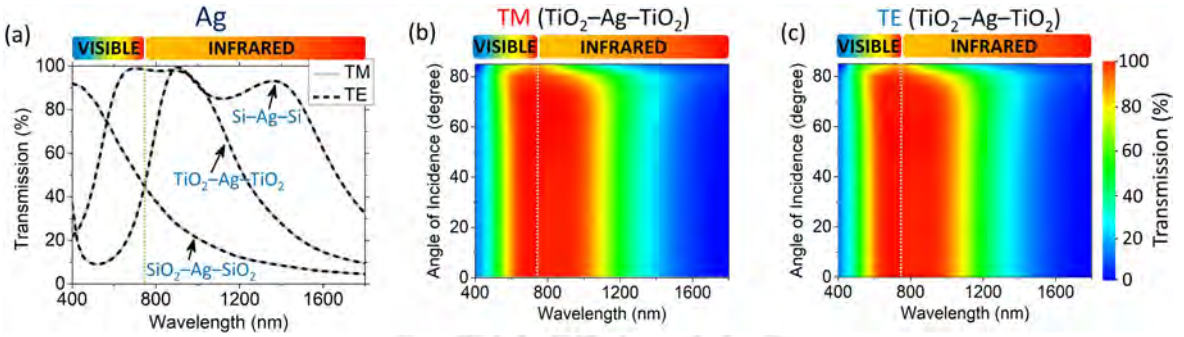

Figure 5.8: (a) Numerically calculated transmission spectra for insulator–metal–insulator thin-film based passive windows: (a) depicts transmission spectra for both TM and TE polarization at normal angle of incidence, (b) and (c) show transmission colour contour plot for TM and TE polarization, respectively, for varying angle of incidence between 0 and 85 degrees. Here, the metal and insulator layers are considered to be 15 nm and 53 nm thick, respectively.

This is because the perpendicular component of the electric field tends to penetrate the multilayer structure, leading to scattering of incident radiation at those angles, hence reducing the overall transmission through a multilayer system. Nevertheless, such a good angle insensitivity suggests that our design could be robust against color shift even at a grazing angle of incident solar radiation.

For electrotunable windows, we show spectral response obtained for gold based thin-films. Figure 5.9(a) shows transmission spectra for both TM and TE polarizations. We see a perfect match between both polarizations at -12 V, 0 V, and 12 V power supply. This indicates that change in polarization does not affect tunability, making our thin-film-based electrotunable windows polarization independent. For studying angle insensitivity, we vary the angle of incidence between 0 and 85 degrees at 0 V power supply. In Figs. 5.9(b) and 5.9(c), we see that the transmission peak remains above 90% even at 80 degrees of angle of incidence, hence, making our electrotunable window angle insensitive to a great extent. For the rest of the static and electrotunable window designs, the angle studies are listed in Tables 5.1 and 5.2, respectively.

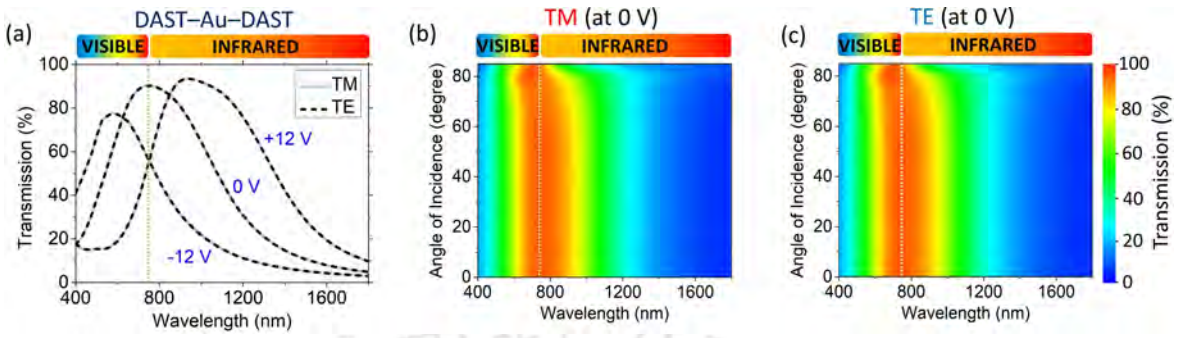

Figure 5.9: (a) Numerically calculated transmission spectra for insulator–metal–insulator thin-film based electrotunable windows (DAST–Au–DAST): (d) depicts transmission spectra for both TM and TE polarization at normal angle of incidence, (b) and (c) show transmission colour contour plot for TM and TE polarization, respectively, for varying angle of incidence between 0 and 85 degrees. Here, the metal and insulator layers are considered 20 nm and 65 nm thick, respectively.

5.3 Static versus Electrotunable Windows

We now compare the performance of our static and electrotunable windows with commercial windows used in the industry [7,8,154]. The three most widely used figure of merit (FOM) in the industry are visible transmittance (VT), infrared transmittance (IRT), and solar heat gain coefficient (SHGC), introduced in section 3.3 of chapter 3. In practice, an ideal window for hot climate conditions should have high VT and low IRT values. Whereas, for cold climate conditions, both values should be high. The ideal VT, IRT, and SHGC values are given in Table 4.3 of chapter 4. Apart from VT, IRT, and SHGC, contrast ratio (CR) is also an important optical parameter that gives the spectral transmission modulation [4]. We express CR using VT and IRT as: $\mathrm{CR_{VT}} = \mathrm{VT_{BC}}/\mathrm{VT_{DW}}$ and $\mathrm{CR_{IRT}} = \mathrm{IRT_{BC}}/\mathrm{IRT_{DW}}$, respectively.

Figures 5.10(a) and 5.10(d) show FOM comparison among our different designs of static and electrotunable windows, respectively, based on the choices of metal and a couple of commercial windows. We notice that the FOM obtained using our relatively inexpensive metals (Ag, Li, TiN, Cu, and ALON) fair well against two double-pane argon low-emissivity coating commercial windows (CW I, and CW II) [7, 8, 154]. In

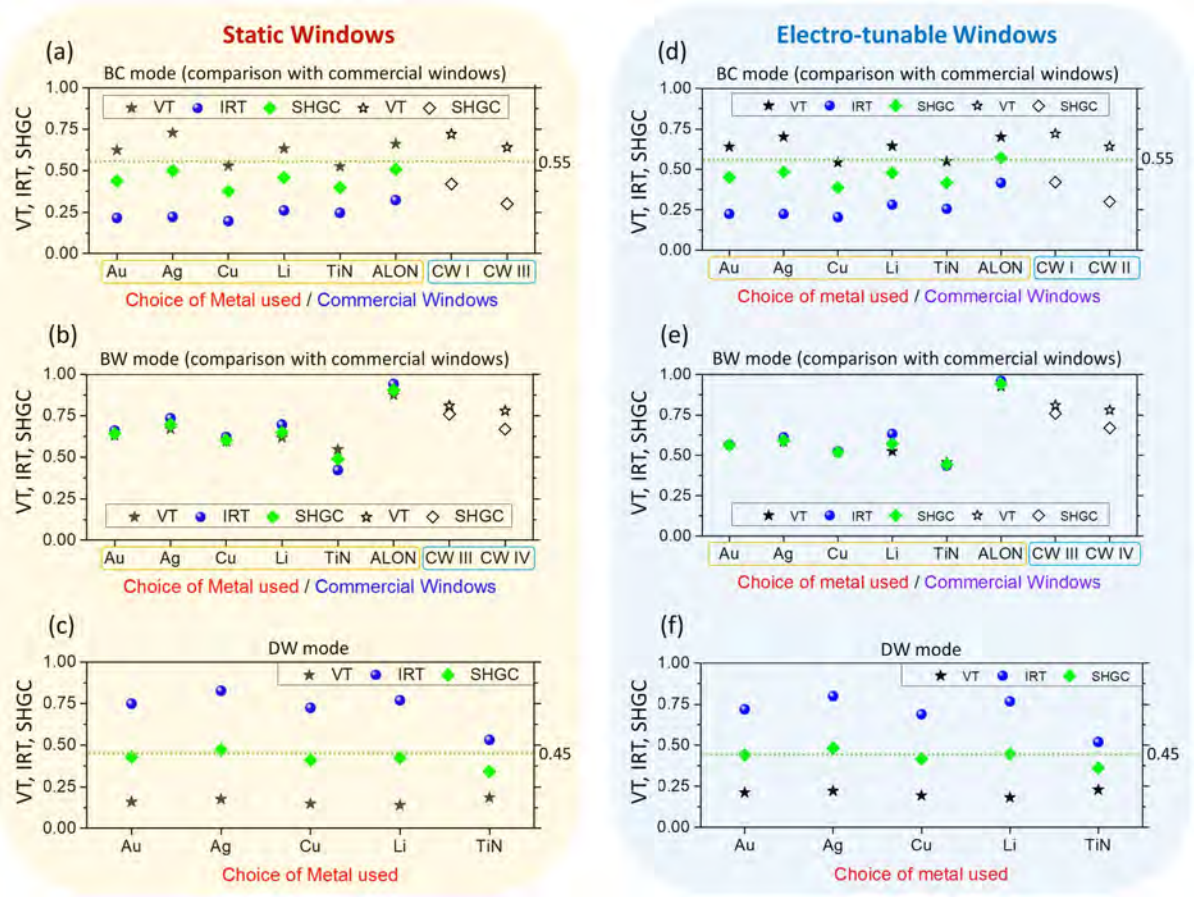

Figure 5.10: Theoretically calculated figure of merit for passive window glasses in (a)–(c) and electrotunable window glasses in (d)–(f), showing VT, IRT, and SHGC values. In (a) BC mode, comparing our insulator–metal–insulator thin-film based glasses with two commercial glasses (CW I and CW II) having double-pane argon low-emissivity coating [7, 8, 154], (b) BC mode, comparing our silver based insulator–metal–insulator thin-film glasses with silver nanoshell based IR blocking plasmonic glasses [37], (c) BW mode, comparing our insulator–metal–insulator thin-film based glasses with commercial glasses (CW III: double-glazed with high-solar-gain low-emissivity coating, and CW IV: double-pane clear glass) [7,8], and (d) new DW mode, comparison among our five insulator–metal–insulator thin-film based glasses. In (a), (b), and (c), SiO_2, TiO_2, and Si, are used as the top and bottom dielectric layers, respectively. In (d), (e), and (f), DAST polymer is used as top and bottom dielectric layers.

fact, our design based on Ag as a choice of metal could outperform commercial windows. Figures 5.10(b) and 5.10(e) show a comparison of FOMs for static and electrotunable windows and two commercial double-glazed, high-solar-gain low-emissivity glass and double pane clear glass windows (CW III and CW IV) [7, 8] in BW mode. In this case, ALON based static and electrotunable windows could outperform com-

Table 5.3: Contrast ratio (CR) for VT and IRT values between BC and DW modes, for gold, silver, and copper based electrotunable windows, $\lambda \in$ [400 nm, 1800 nm]

FOM	This Work			Ref. Work [141]		
	DAST–Au–DAST	DAST–Ag–DAST	DAST–Cu–DAST	Au–DAST–Au	Ag–DAST–Ag	Cu–DAST–Cu
VT_{BC}	0.64	0.70	0.54	0.63	0.77	0.55
VT_{DW}	0.21	0.22	0.19	0.32	0.35	0.32
CR_{VT}	**3.03**	**3.18**	**2.81**	**1.97**	**2.20**	**1.71**
IRT_{BC}	0.22	0.22	0.20	0.29	0.25	0.30
IRT_{DW}	0.72	0.80	0.69	0.57	0.62	0.52
CR_{IRT}	**3.20**	**3.58**	**3.38**	**1.97**	**2.50**	**1.75**

Note: $CR_{VT} = VT_{BC}/VT_{DW}$; $CR_{IRT} = IRT_{BC}/IRT_{DW}$; VT: Visible Transmittance; IRT: IR Transmittance; BC: Bright and Cool; DW: Dark and Warm; FOM: Figure of Merit.

mercial windows. Figures 5.10(c) and 5.10(f) show a comparison of FOMs among our static and electrotunable windows in DW mode. Here, Ag gives the best performance followed by Li, Au, Cu, and TiN. Hence, the FOM obtained for both static and electrotunable windows indicate that these thin-film smart windows based on relatively inexpensive materials (Ag, Li, TiN, Cu, and ALON) could be a suitable low-cost alternative to existing expensive commercial windows.

For electrotunable windows, we examine the contrast ratio (CR) for VT and IRT values between BC and DW modes. Table 5.3 shows a comparison of FOM for our IMI electrotunable glasses with MIM electrotunable glasses recently reported in the literature [141]. The calculated CR values for this work are nearly 1.5 to 2 times better than the previous works. Practically it signifies that our IMI based thin-film windows could operate efficiently under diverse weather conditions.

5.3.1 Effect of Size-dependent Metallic Losses

Until now, the spectral response for our IMI thin-films was calculated by considering bulk lossy metal. However, when the thickness of the metallic-layer is less than the mean free path of electrons, size-dependent metallic losses need to be taken into account, in order to accurately predict the spectral response [226]. The permittivity of the middle metallic layer can be expressed using the following Drude–Lorentz dispersion relation [226–228]:

$$\epsilon(\omega) = \epsilon_{\infty} - \frac{\omega_{\mathrm{D}}^2}{\omega^2 + i\omega(\gamma + \nu_{\mathrm{F}}/\delta)} - \frac{\Delta\epsilon\omega_{\mathrm{L}}^2}{\omega^2 - \omega_{\mathrm{L}}^2 + i\omega\Gamma_{\mathrm{L}}} \tag{5.1}$$

where high-frequency permittivity, ϵ_{∞} = 3.7180; plasma frequency, ω_{D} = 2.1059 $\times$ 10^{15} rad/s; plasma frequency associated with intraband transition, ω_{L} = 1.0359 $\times$ 10^{15} rad/s; oscillator strength, $\Delta\epsilon$ = 0.4242; optical frequency of incident radiation, $\omega = 2\pi\, c/\lambda$; bulk collision frequency, γ = 1.05 $\times$ 10^{14} rad/s; damping coefficient associated with Lorentz model, Γ_{L} = 8.2937 $\times$ 10^{13} rad/s; Fermi velocity, ν_{F} = 1.4 $\times$ 10^{6} m/s; size-dependent parameter, δ, represents effective mean free path of electron.

Figure 5.11 depicts the numerically calculated spectral response and respective FOM calculated with and without size-dependent metallic losses consideration for both static and electrotunable windows. Figures 5.11(a) and 5.11(b) show the transmission spectra for passive and electrotunable windows, respectively, in BC, BW, and DW modes, with and without size-dependent metallic losses using Ag based IMI thin-film. As expected, the inclusion of size-dependent metallic losses leads to a slight broadening in the transmission spectra [229]. The corresponding FOM are depicted in Figs. 5.11(c) and 5.11(d), respectively. It is evident from the calculated FOM that there is only a marginal variation in VT, IRT, and SHGC values. In fact, the VT values improved because of an increase in transmission in the visible regime. Therefore, through this size-dependence analysis, we conclude that the performance of smart windows is unlikely to degrade during experimental realization.

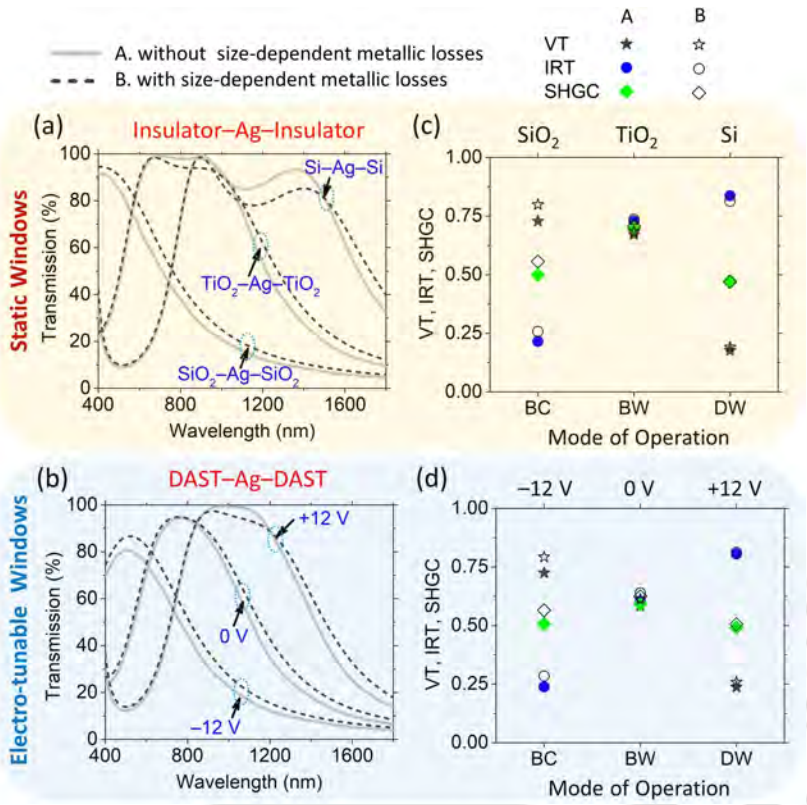

Figure 5.11: Numerically studied effect of size-dependent metallic losses on spectral response and their corresonding FOM for silver-based insulator–metal–insulator thin-film passive windows in (a), (c) and electrotunable windows in (b), (d). In (a) and (c), SiO_2, TiO_2, and Si are used as the top and bottom dielectric layers in BC, BW, and DW modes, respectively. In (b) and (d), DAST polymer is used as top and bottom dielectric layers. Thicknesses of metal (t_M) and insulator (t_D) layers in nm: (a) $t_M = 15$, $t_D = 53$, (b) $t_M = 17$, $t_D = 65$.

5.3.2 Substrate Effect on Transmission Spectra

In practice, our IMI thin-films need to be integrated with a single-pane clear glass or an insulated glass unit (IGU)—used in buildings for designing thin and lightweight windows with desired visible and infrared transmission/blocking capability. Therefore, it is imperative to study the effect of an optically transparent glass substrate. A 2D schematic diagram of our IMI thin-film coated on the inside of a transparent glass made of silica (SiO_2) is shown in Fig. 5.12(a). For this study, we consider 17 nm thick Ag metallic layer, 65 nm thick top SiO_2 layer, and 5 mm thick bottom SiO_2 layer. Figure 5.12(b) shows transmission spectra for SiO_2–Ag–SiO_2 based window glass over solar

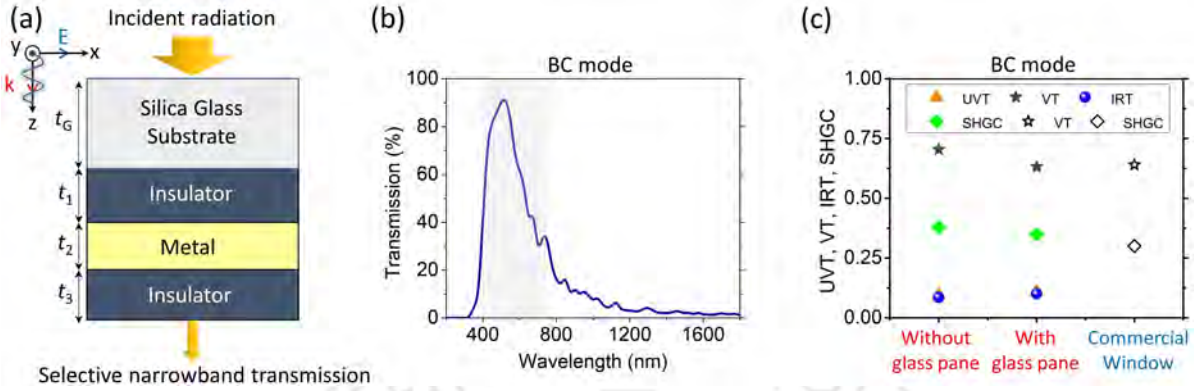

Figure 5.12: (a) 2D schematic side view of insulator–metal–insulator thin-film coated on the inside of silica glass substrate, (b) transmission spectra for SiO_2–Ag–SiO_2 based window glass in BC mode, and (c) figure of merit in BC mode showing UVT, VT, IRT, and SHGC values, comparing our insulator–metal–insulator thin-film based glasses (with and without silica glass substrate) with a commercial glass (double pane argon with low-E coating) [7]. Here, $t_1 = t_3 = 65$ nm, $t_2 = 17$ nm, and $t_G = 5$ mm.

spectral regime. We observe that the transmission spectra profile remained similar to without substrate case. In fact, coating over glass substrate blocks the harmful UV radiation completely. We also found that the optical response remained unaltered even when the IMI thin-film was coated outside the silica glass substrate. However, coating thin-film towards the inside will protect these films from external heat and moisture from rains, thereby increasing the lifetime of these smart glasses. In Fig. 5.12(c), we compute the FOM in BC mode for IMI thin-films with and without glass substrate and show comparison with a commercial double-pane argon low-emissivity coating glasses [7, 8, 154]. It is evident that these IMI thin-films coated on glass substrate still preserve an excellent FOM. Here, we introduce UV transmittance (UVT), which denotes the portion of UV radiation transmitted through a glass window over a 200–400 nm wavelength range. We found the UVT values to be 0.10 and 0.09, with and without a glass pane, respectively. Such low UVT values indicate that these window glasses can block ∼90% of the incident UV radiation. Therefore, we believe that such a glass category could provide a better and cost-effective alternative than the existing commercial double-pane or triple-pane low-emissivity glass windows.

5.3.3 Thin-film Coating for Blocking UV Radiations

We optimise our thin-film glasses for applications that exclusively require thin-film glasses with good UV blocking abilities by adding additional UV blocking coating layers. Figure 5.13(a) shows a new 2D schematic design of our IMI thin-films. Here, the top and bottom insulator layers consist of three dielectrics—5 nm thick SiO_2 layer, 15 nm thick TiO_2 layer, and 5 nm thick Si layer. The idea here is to choose the refractive indices of top and bottom insulator layers to act as an anti-reflective coating that will enhance transmission in the visible and block harmful UV radiations completely. Figure 5.13(b) shows the corresponding transmission spectra for BC mode over the solar spectral regime. We see an excellent UV and IR blocking with a very high visible transmission. We believe that this design can be customized for any mode with different choices of metal and dielectrics proposed in this work. Recently Besteiro *et al.* reported various designs of IR blocking plasmonic glasses out of which silver nanoshell based glasses produced the best result [37]. We took the mean value of their manually and computationally obtained data. For a fair comparison, we optimised our design

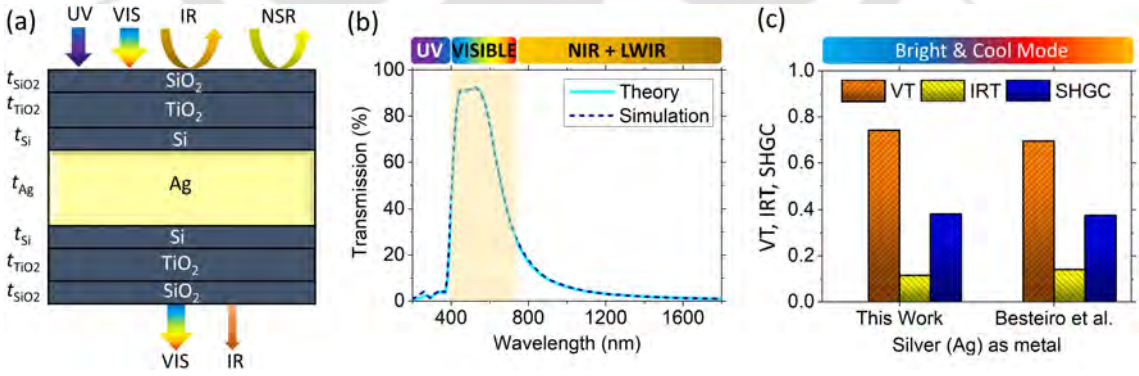

Figure 5.13: (a) 2D schematic side view of insulator–metal–insulator thin-film coated with UV blocking thin-film layers, (b) transmission spectra in BC mode using SiO_2–TiO_2–Si–Ag–SiO_2–TiO_2–Si multilayered design, and (c) figure of merit comparison in BC mode between our Ag-based insulator–metal–insulator thin-film with Ag nanoshell based plasmonic glasses [37] over 200-1700 nm wavelength regime. Dimensions (nm): $t_{SiO_2} = 5$, $t_{tiO_2} = 15$, $t_{Si} = 5$, and $t_{Ag} = 28$ nm.

over 200–1700 nm wavelength regime by considering metal thickness as 28 nm. In Fig. 5.13(c) we compare the FOM of our silver based IMI thin-films glasses with Ag nanoshell based glass. It is evident that our Ag based glasses outperform their Ag nanoshell based glasses in terms of VT, IRT, SHGC values obtained.

5.3.4 Prospective Fabrication Technique

With the continuous advancement in nanoscale fabrication technology, we believe that the experimental realization of our proposed thin-film based smart windows is indeed feasible. For fabricating SiO_2–Ag–SiO_2 based static window design, first, we need to take a one-side polished glass substrate made of silica typically 5 mm thick. Then silver metal needs to be deposited on top of silica using electron beam (e-beam) evaporation technique [132, 169–171]. Again 65 nm thick silica needs to be deposited on the top of Ag–SiO_2 stack using spin coating or e-beam evaporation technique. For fabricating an electrotunable window, DAST needs to be deposited over a large-area as a single crystal in a certain orientation, in place of SiO_2. To control the solidification and orientation, the graphoepitaxy technique can be used [182]. For optical characterization, UV-VIS or IR spectroscopy may be used to cover the entire solar radiation regime [169, 170].

5.3.5 Summary

We presented insulator–metal–insulator multilayer thin-films based designs of static and electrotunable 'smart' windows, which are **uniquely designed to filter visible and infrared solar radiation selectively**. Our design is robust, lithography-free, large-area compatible, polarization-independent, and angle-insensitive up to 80 degrees of oblique incidence. Our theoretical results are in close agreement with simulation findings. The theoretically calculated figure of merit indicates that our static and electrotunable smart windows could be a better value proposition than industry-standard

commercial windows. In addition, we obtained a better contrast ratio for diverse climatic conditions that significantly improved for smart window's efficiency. Our size-dependence analysis revealed that the performance of our smart windows is unlikely to degrade during practical realization. We found that the optical response remained unaltered when the IMI thin-film was coated on the inside or outside the silica glass substrate. We have also shown that a multilayer coating may be used to block the harmful ultraviolet radiation completely. A detailed fabrication technique is provided to show the experimental feasibility.

6

Broadband Metamaterial Absorbers for Solar Energy Harvesting

Contents

Chapters 3, 4, and 5 presented different designs of windows for selective filtering of solar light and heat from the solar radiation. This chapter is dedicated to investigating different designs for harvesting heat from the solar radiation. These absorbers have implications in solar cells, thermophotovoltaics, *etc*. Section 6.1 introduces **a new design of plasmonics based broadband metamaterial absorber in a 400–1100 nm spectral window** that could be used to improve the efficiency of silicon solar cells. Since plasmonic metals such as gold and silver exhibit plasmon resonance in ultraviolet–visible regimes, it is challenging to achieve ultrabroadband absorption over the entire solar radiation regime. To overcome this problem, refractory metals (such as molybdenum or tungsten) may be used. Utilizing these metals, sections 6.2 presents the design of a one-dimensional grating-based wide-angle and ultrabroadband metamaterial absorber which has been optimized to provide an **unprecedented ∼99% average absorption in a 400–2500 nm spectral range** for solar energy harvesting. Here, one should note that a design of 'perfect' absorber must be polarization- and angle-insensitive besides having near-perfect absorption over a broad spectral range. Unfortunately, one-dimensional grating-based structures are polarization-sensitive due to a lack of symmetry from the top. To overcome this limitation, section 6.3 focuses on **a new design of two-dimensional grating based ultrabroadband 'perfect' metamaterial absorber over a wider spectral regime of 300–4500 nm**, which may have considerable implications in the thermophotovoltaics application.

6.1 Plasmonics Based Broadband Metamaterial Absorbers

In this section, we present a wide-angle and polarization-independent design of broadband plasmonic metamaterial absorbers. We report 96.9% average absorption over 400–1100 nm wavelengths. Improving solar cell efficiency is crucial for moving towards green energy while meeting the ever-growing global energy demand. An in-

tegrated design of broadband absorbers into photovoltaic-modules could significantly enhance solar cell efficiency.

6.1.1 Background

It is well known that photovoltaic (PV) cells absorb only those photons which have energy greater than the bandgap of the semiconductor materials used [230]. Therefore, a typical PV cell can utilize only a portion of the solar radiation received on the earth's surface. For example, silicon and organic solar cells absorb photons over 400–1100 nm and 400–650 nm wavelengths, respectively [147]. A design of a spectrally selective broadband absorber could remarkably improve solar cell efficiency.

Here, we present a design of broadband plasmonic metamaterial absorber, consisting of a two-dimensional array of cross–ring shaped metallic layers embedded inside dielectric layer, followed by ground metallic layer, and silicon (Si) substrate. We use titanium nitride (TiN) as the metallic layer and polymethyl methacrylate (PMMA) as the dielectric layer.

6.1.2 Design, Results and Discussion

Figure 6.1(a) depicts a unit cell in a two-dimensional schematic side- and top views of cross–ring based broadband plasmonic metamaterial absorber. Here, both cross and ring are made of TiN, each 50 nm thick, embedded at the center of 130 nm thick PMMA dielectric layer. The width (w) and length (L) of the cross are 60 nm and 120 nm, respectively. The inner (r_1) and outer radii (r_2) of the ring are 110 nm and 160 nm, respectively. The ground metal is made of TiN having 150 nm thickness. Note that 300 nm thick Si substrate is used for demonstration only and has no role in broadband absorption. The periodicity of the unit cell is 400 nm. The full-wave simulations are performed using commercial three-dimensional (3D) FDTD solver, Lumerical FDTD®. The refractive index of PMMA is taken as 1.49, and optical constants of TiN are taken

from the literature [220].

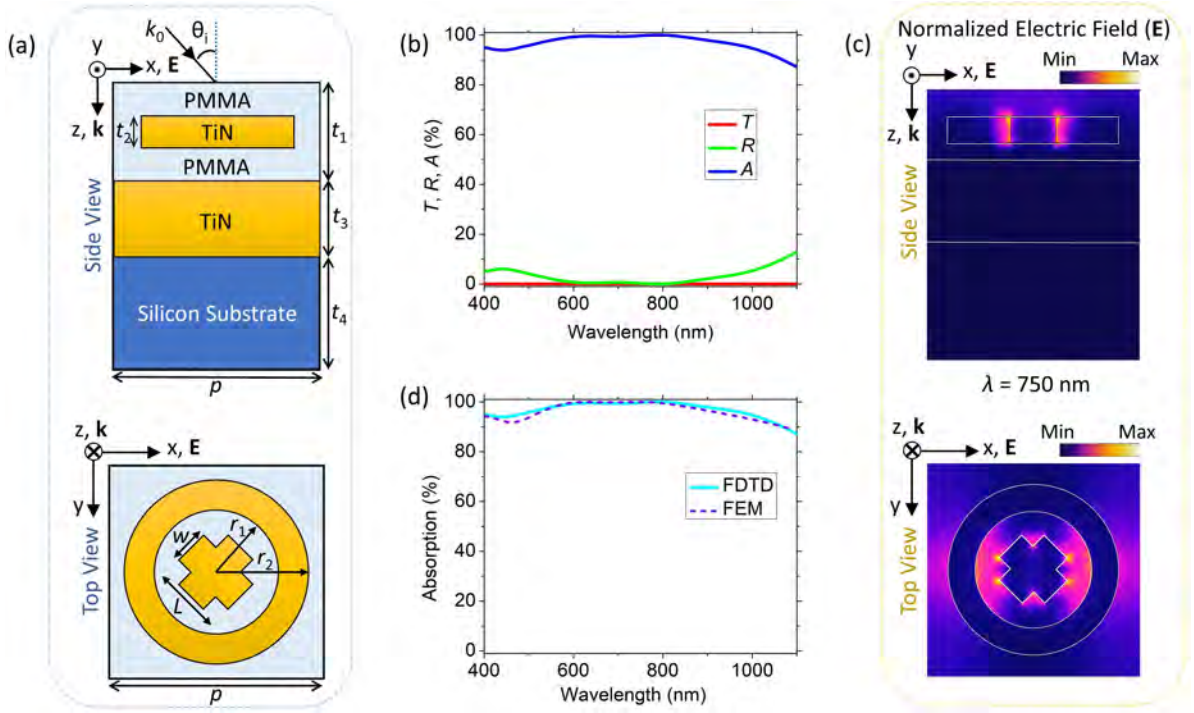

Figure 6.1: Our design of broadband plasmonic metamaterial absorber depicting a unit cell in (a) two-dimensional schematic side and top views. (b) Numerically calculated [using FDTD solver] spectral response over 400–1100 nm wavelengths. (c) Normalized electric (**E**) field distribution shown for top and side view at the wavelength of peak absorption *i.e.* $\lambda = 750$ nm. (d) A comparison between spectral response obtained using FDTD and FEM solvers. Dimensions (nm): $t_1 = 130$, $t_2 = 50$, $t_3 = 150$, $t_4 = 300$, $w = 60$, $L = 120$, $r_1 = 110$, $r_2 = 160$, and $p = 400$.

The numerically calculated spectral response for our cross–ring based absorber design is shown in Fig. 6.1(b). We could achieve an average absorption of 96.9% over 400–1100 nm wavelengths. We optimized our design to achieve a maximum of 99.9% absorption at 750 nm wavelength that corresponds to the wavelength of peak absorption of silicon solar cells. The electric (**E**) field distribution at the wavelength of peak absorption is depicted in Fig. 6.1(c). The strong localization of **E** field indicates excitation of surface plasmons [147]. Unlike noble metals (such as gold, silver, and copper) that exhibit plasmon resonance in ultraviolet–visible regimes, TiN has plasmon resonance located in visible–near infrared regimes—resulting in continuous broadband

absorption over a wide spectral range [141]. Since TiN is less metallic compared to noble metals, the field confinement due to plasmon resonance is weaker [231]. Therefore, a ground metal of TiN is used to enhance the absorption over a broad wavelength regime. Between 400 nm and 550 nm wavelengths, TiN acts as a lossy dielectric allowing more light to penetrate through it [220, 231]. At those wavelengths, PMMA dielectric layer encapsulated over TiN acts as an anti-reflection layer—allowing high absorption without any plasmonic resonance. To verify our findings, we simulate over the same spectral range (400–1100 nm wavelengths) using a FEM solver, COMSOL Multiphysics® [132, 140]. Figure 6.1(d) shows a close agreement in spectral response obtained using FDTD and FEM-based solvers.

For thermophotovoltaics application, the design of broadband absorber should be polarization-independent and angle insensitive to a large extent [142]. Figure 6.2(a) depicts simulated spectral response for both TM and TE polarization at a normal angle of incidence. A perfect match between TM and TE polarization spectra indicates that our design is polarization-independent. To check angle dependency, we study absorption spectra by varying angle of incidence between 0 and 85 degrees, as depicted in Figs. 6.2(b) and 6.2(c), showing both TM and TE polarization, respectively. The average absorption obtained for TM, TE, and unpolarized radiation, is shown in Fig. 6.2(d). We obtain over 90% average absorption up to 75 degrees of oblique incidence angle. Such a wide-angle insensitivity could practically lead to efficient absorption of solar radiation for dynamically changing sun's position, even at a grazing angle of incidence. We believe that our design can be easily fabricated using the current state-of-the-art nanofabrication technology [25, 132, 142]. To obtain sharp edges around cross–ring-shaped structures, electron beam lithography and DC magnetron sputtering may be used [231].

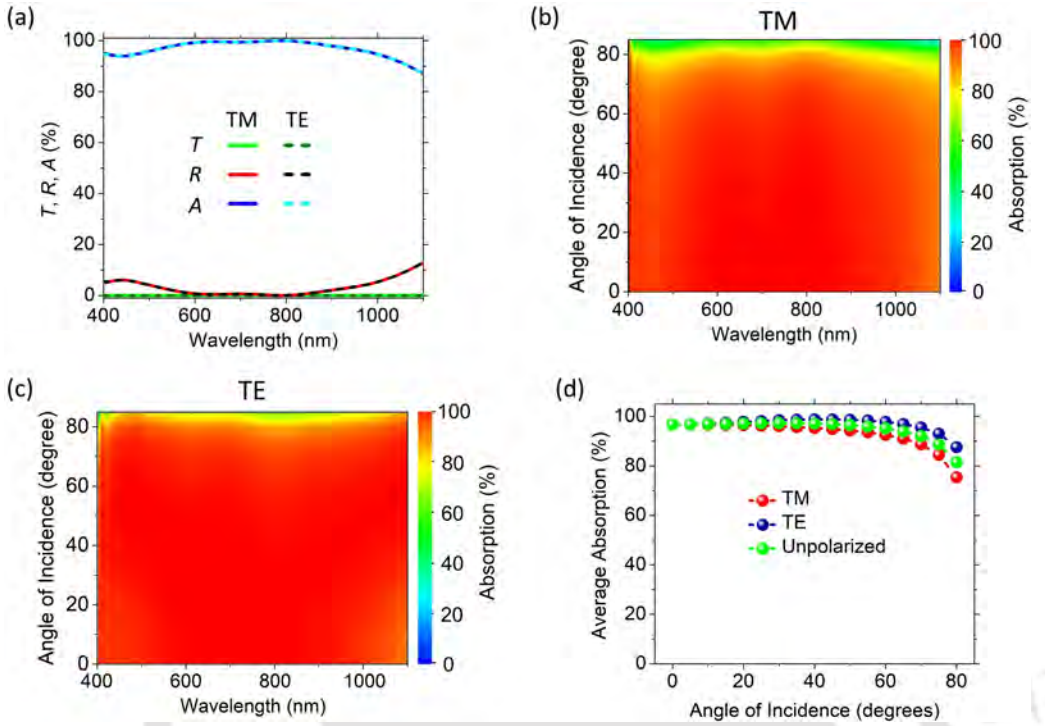

Figure 6.2: Simulated transmission (T), reflection (R), and absorption (A) spectra (using FDTD solver), over 400–1100 nm wavelengths at normal angle of incidence for (a) both TM and TE polarization. Color contour absorption spectra for varying angle of incidence between 0 and 85 degrees for both TM and TE polarization in (b) and (c), respectively. (d) Average absorption obtained for TM, TE, and unpolarized radiation, showing 90% average absorption up to 75 degrees of oblique incidence angle.

6.1.3 Summary

We investigated a **new design of cross–ring based broadband plasmonic metamaterial absorber**. An average absorption of 96.9% is achieved over 400–1100 nm wavelengths with a peak absorption of 99.9% at 750 nm wavelength—perfectly matching the wavelength of peak absorption by silicon solar cell [147]. A close agreement between absorption spectra obtained using finite difference time domain solver and finite element method solver validates our findings. Our design is polarization-independent and provides 90% average absorption up to 75 degrees of oblique incidence angle. Practically, these thin-film broadband absorbers can be integrated into photovoltaics modules for enhancing efficiency of silicon as well as organic solar cells [137, 142].

6.2 1D-Grating Based Ultrabroadband Metamaterial Absorbers

The previous section discussed plasmonics based broadband metamaterial absorbers which could be very useful for enhancing the efficiency of silicon or organic solar cells. Since the absorption band only covers 400–1100 nm spectral window, it may not be that useful for solar energy harvesting as it doesn't cover the entire solar irradiance regime. In this section, we introduce an ultrabroadband metallo-dielectric grating-based metamaterial absorber. It consists of a one-dimensional periodic grating of multilayered, alternating molybdenum (metal)–germanium (dielectric) layers. This design offers over 99% absorption over 400–2500 nm spectral window at normal angle of incidence using 64 pairs of metallo-dielectric layer.

6.2.1 Design, Simulation, and Theory

Our simulation model, shown in Fig. 6.3, consists of 20 pairs of alternating metallo-dielectric layers, terminated by a bottom metallic plate supported by a silicon substrate. Metal layers are made of molybdenum (Mo), each 13 nm thick. The dielectric layers are made of germanium (Ge), each with a thickness of 7 nm. The thickness of

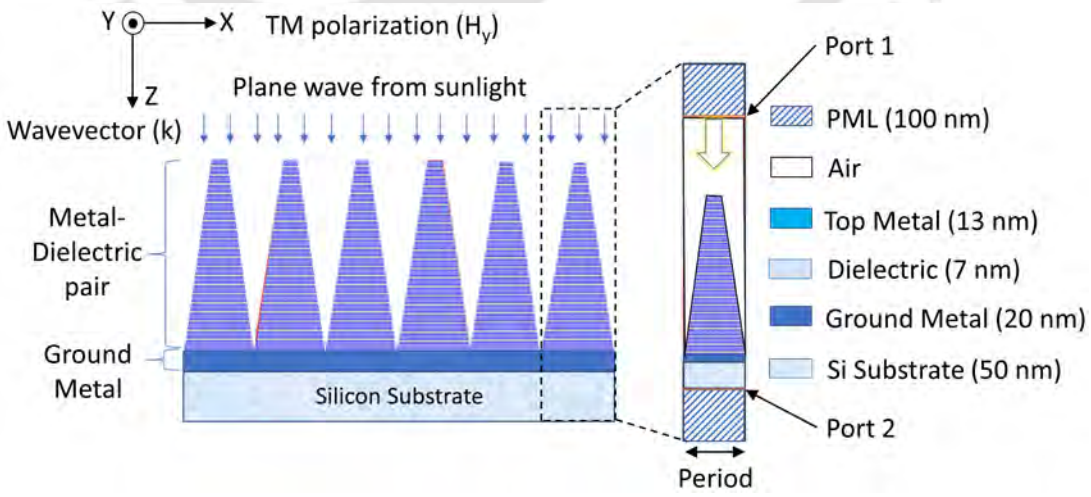

Figure 6.3: Design geometry and unit cell of the ultrabroadband tapered metallo-dielectric grating-based metamaterial absorber. The dimensions are specified within parenthesis.

the bottom molybdenum plate is 20 nm. The width of the top and bottom metallo-dielectric pair is 30 nm and 120 nm, respectively. A periodicity (P) of 120 nm is considered along the x-axis. The number of metallo-dielectric pairs is denoted by L, varied from 1 to 64. Port 1 acts as the source of light propagating along z-axis. Port 2 acts as a detector to allow calculation of transmittance and reflectance from S parameters, from which absorbance can be obtained. The simulation is carried out using a finite element method solver, COMSOL Multiphysics®, over a spectral range of 400–2500 nm. The spectral response shown in Fig. 6.4(a) depicts a near-perfect absorption (A > 98%) considering L = 20.

We deploy effective medium theory (EMT) where each metallo-dielectric pair can be considered as a homogeneous material with an effective permittivity given by the following set of complementary equations [136]:

$$1/\epsilon_{\perp} = f/\epsilon_{\mathrm{m}}(\omega) + (1-f)/\epsilon_{\mathrm{d}} \tag{6.1a}$$

$$\epsilon_{\parallel} = f\epsilon_{\mathrm{m}}(\omega) + (1-f)\epsilon_{\mathrm{d}} \tag{6.1b}$$

where ϵ_{m} and ϵ_{d} stand for metal and dielectric permittivity, respectively; $\epsilon_{\perp}$ represents effective permittivity along the perpendicular direction and $\epsilon_{\parallel}$ represents effective permittivity along the parallel direction of metallo-dielectric interfaces; f represents the filling ratio of the metal given by: $f = t_{\mathrm{m}}/(t_{\mathrm{m}} + t_{\mathrm{d}})$, where t_{m} and t_{d} denote the thickness of metal and dielectric layers, respectively. Here, we considered molybdenum and germanium to form alternating metallo-dielectric pair with filling ratio of f = 0.65 (t_{m} = 13 nm and t_{d} = 7 nm). Our analysis shows that the EMT model has an absorption spectrum [Fig. 6.4(b), dashed line] very similar to the one obtained from numerical simulations [Fig. 6.4(b), solid line]. An excellent agreement is seen up to 1200 nm, beyond which the approximations of EMT tend to become inaccurate [84]. Nevertheless, such a good agreement, indeed, validates our simulation results.

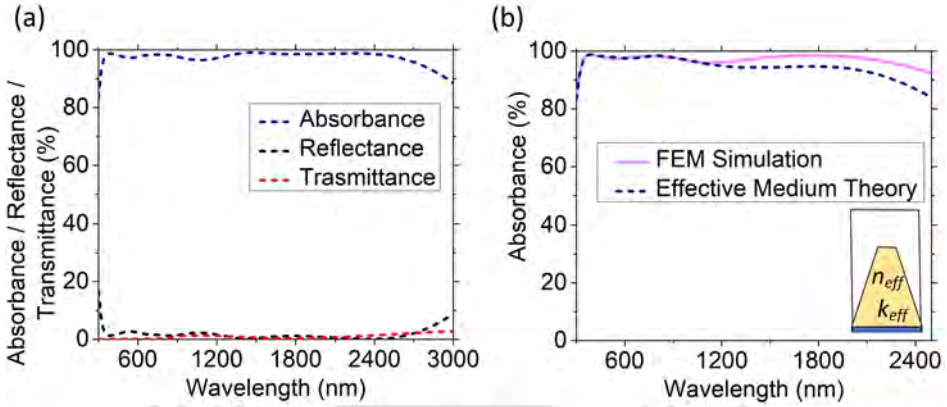

Figure 6.4: (a) Absorbance, reflectance, and transmittance spectra with 98.2% average absorbance between 400–2500 nm using $L = 20$ pairs of alternating molybdenum–germanium with bottom molybdenum layer on top of Si substrate, (c) Comparison between simulation model and effective medium theory (EMT) for $L = 20$.

6.2.2 Physical Mechanism

In order to understand how light is getting absorbed by our structure at such a wide range of wavelength, we have studied normalized magnetic field distributions (colour maps) and energy flow (arrow maps) at the plane of y = 0 at different incident wavelengths [see Fig. 6.5]. We observed that most of the incident wave first propagates downwards along the z-axis through the air gap and whirls into the structure (Fig. 6.5 arrow map). The vortex created due to magnetic field concentration (Fig. 6.5 colour maps) can be explained with the concept of slow light. It is defined as light propagating at very low group velocity compared to the speed of the light in vacuum. Hence, the modes propagate very slowly and get absorbed at different layer thickness [84].

Figure 6.5 clearly shows the presence of a fundamental order slow-light mode at longer wavelengths of λ = 1.5 μm, 1.75 μm, 2 μm, 2.25 μm, and 2.5 μm. As we reduce the wavelength, the bright colour spot goes up to the middle part of the structure (at λ = 2 μm) and finally goes to the top (at λ = 1.5 μm). This is called the 'trapped rainbow' effect as reported in the gold-based broadband absorber [76]. The bottom metallic layer plays a key role as reflector, forcing the long-wavelength waves to travel back into the

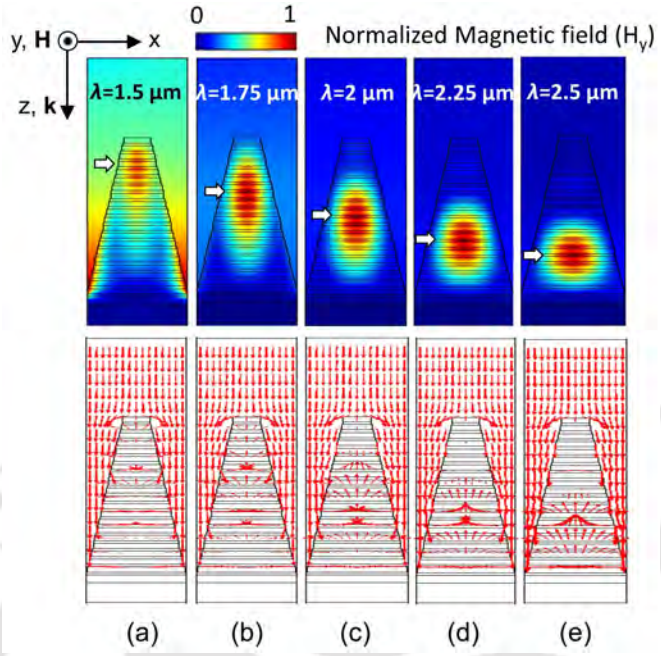

Figure 6.5: Distributions of normalized magnetic field (colour maps) and energy flow (arrow maps) in tapered metallo-dielectric grating-based metamaterial absorber at different incident wavelengths: (a) $\lambda = 1.5$ μm, (b) $\lambda = 1.75$ μm, (c) $\lambda = 2$ μm, (d) $\lambda = 2.25$ μm, and (e) $\lambda = 2.5$ μm for a model with $L = 20$.

metallo-dielectric multilayer waveguide instead of getting transmitted through. The reflected wave then gets fully absorbed, allowing us to further extend the absorbance spectra into mid-IR regime, up to 3 μm.

Since at shorter wavelength (less than 1 μm), there is no such excitation of slow-light waveguide modes, the mechanism of the observed high-efficiency absorption may be attributed to the anti-reflection effect. For shorter wavelengths, the real part of the relative permittivity of molybdenum is positive, allowing it to act as a lossy dielectric. This property accounts for the natural anti-reflection of light due to its tapered profile [84]. However, at longer wavelengths, the real part of the relative permittivity of molybdenum is highly negative. This accounts for the severe light reflection attributed to its metallic property. It is the combination of the trapped rainbow effect and the anti-reflection effect that creates the presented ultrabroadband absorber with high efficiency.

6.2.3 Parametric Analysis and Tolerance Study

Here, we emphasize that the design of such an ultrabroadband absorber is non-trivial and requires careful choice of device dimension and materials. For our design, the contour plot of parametric analysis is shown in Fig. 6.6. Ideally, the thickness of each material needs to be minimized for reducing the overall cost and time of fabrication, eventually, making the structure ultra-thin. In order to find the minimum thickness of the top metal, a parametric sweep from 5 to 20 nm thickness is carried out. It is observed that with an increase in top metal thickness (t_{M1}), the absorption efficiency first increases and then gradually decreases after t_{M1} = 13 nm (see white dashed line in Fig. 6.6(a). Hence, an intermediate size of 13 nm is the optimum thickness to achieve maximum absorbance efficiency.

For the case of dielectric thickness (t_D), the absorption efficiency first increases and

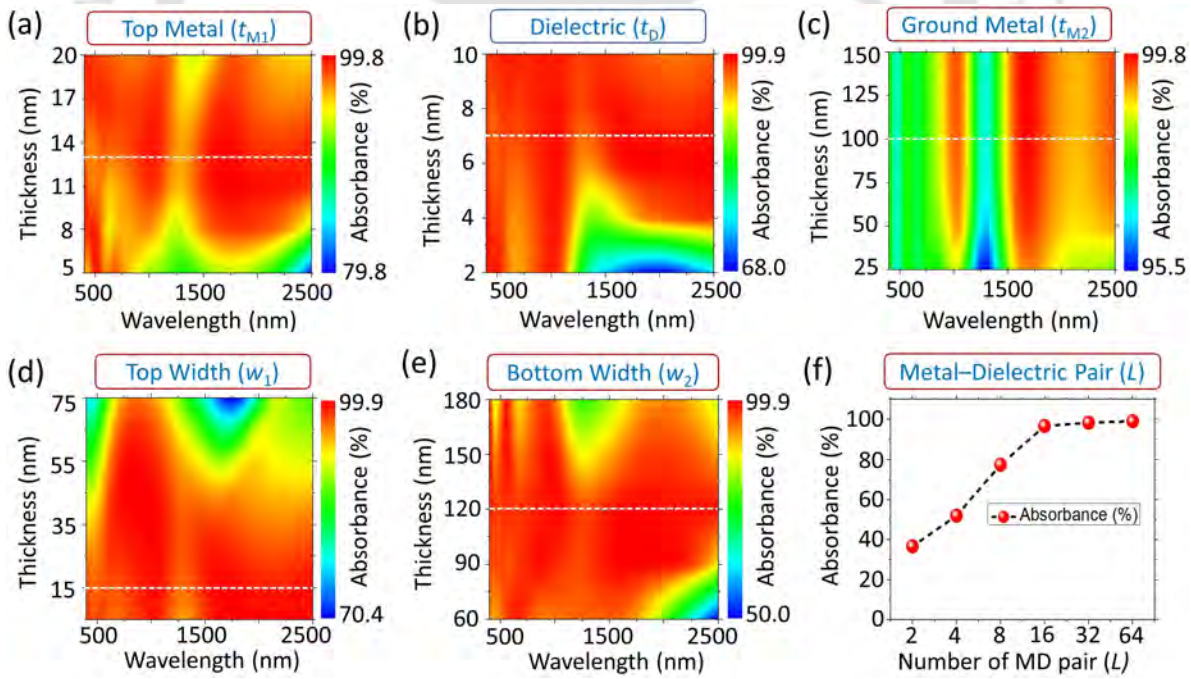

Figure 6.6: Parametric analysis showing contour plot for varying thickness of (a) top metal (t_{M1}), (b) dielectric (t_D), (c) ground metal (t_{M2}), (d) top width (w_1), and (e) bottom width (w_2). The white dashed lines show the optimized parameter value in each case. (f) Variation of average absorption efficiency with number of metallo-dielectric pairs (L).

Table 6.1: Optical fabrication tolerance limit obtained using $L = 20$ pair with $\pm 0.5\%$ maximum allowable variance in average absorption efficiency (in %) considering five parameters (all dimensions are in nm)

Fabrication tolerance	t_{M1}	t_D	t_{M2}	w_1	w_2
Upper limit	16	9	No limit	30	125
Lower limit	10	5	25	No limit	100
Optimum dimension	**13**	**7**	**100**	**15**	**120**

Note: t_{M1}: Top metal thickness, t_D: Dielectric thickness, t_{M2}: Ground metal thickness, w_1: Top width, and w_2: Bottom width.

then becomes nearly constant after t_D = 7 nm, making it a suitable thickness for dielectric layer [see Fig. 6.6(b)]. Similarly, the optimum ground metal thickness (t_{M2}) is chosen as 100 nm [see Fig. 6.6(c)]. To account for the role of tapered grating structure, we optimize the top and bottom width, w_1 and w_2, respectively, of the structure [see Figs. 6.6(d) and 6.6(e)]. We find that a ratio of 1:8 between the top and bottom width (w_1 = 15 nm and w_2 = 120 nm) is the right choice to achieve efficient broadband absorption. The field coupling can be improved (minimized) by reducing (increasing) the gap between the grating columns. Another way could be by changing the gradient of the columnar structure. Further, changing the dielectric layer thickness can also change the field coupling between grating columns.

To account for fabrication errors, we also study optical fabrication tolerance limit for Design I obtained using $L = 20$ pair with $\pm 0.5\%$ maximum allowable variance in average absorption efficiency, shown in Table 6.1. The upper and lower limits obtained for device dimension reveal that our design is robust and deviation in absorbance efficiency is less prone to fabrication imperfections.

6.2.4 Role of Metallo-Dielectric Pairs in the Ultrabroadband Absorption

Ideally, with increasing number of metallo-dielectric pairs, average absorbance must saturate to a certain level. We further evaluated average absorbance as a function of L, as shown in Fig. 6.6(f), for optimizing the absorber film's thickness, fabrication cost and performance. We observe a gradual rise in absorbance with an increase in L till 16, beyond which there is a trend of saturation in average absorbance. Our design with L = 16 offers 96.7% average absorbance, whereas the design in [76] could achieve 95% average absorbance with L = 20. Moreover, we could achieve an unprecedented 99.13% average absorbance with L = 64, the highest absorption reported till date in 400–2500 nm range, to the best of our knowledge. So, there is a clear tradeoff between the thickness of an absorber and its maximum absorbance. With L = 20, the structure is 470 nm thick and it offers 98.2% absorbance; whereas for L = 64, 99.13% absorbance can be achieved but the structure needs to be roughly three times thicker. Thicker structure adds to the cost and time for fabrication. Hence, we chose L = 20 for our analyses presented in this work.

6.2.5 Choices of Different Materials as Metal and Dielectric Layers

We started our work with noble metals like gold (Au) and silver (Ag) and found that the absorber made of gold–germanium or silver–germanium tapered metallo-dielectric pairs showed excellent absorption in near IR regime but performed fairly at the visible regime. The real part of the germanium is very dispersive, whereas the imaginary part is large, implying high absorbing capability. A series of investigations with high

Table 6.2: Average absorbance (%) for various metals calculated in 400–2500 nm range using a simulation model with number of stack pairs, L = 20.

Wavelength (400-2500nm)	Au	Ag	Cu	Al	Ti	W	Ni	V	Mo	Zr	Hf
Absorbance (%)	97.447	97.098	97.644	98.144	94.682	97.048	97.949	97.115	98.201	79.598	79.064

lossy refractory metals were performed. These metals outperformed the noble metals in terms of average absorbance over a wide band region (see Table 6.2). It was found that aluminium–germanium and molybdenum–germanium based absorbers showed over 98% absorbance in entire visible and near IR regime using a model with L = 20. High lossy metals or low bandgap semiconductors are key to realizing a good absorber [21]. We choose molybdenum, a high loss metal instead of noble metal to form the tapered metallo-dielectric grating, because of its mechanical and thermal stability. Firstly, its coefficient of thermal expansion is the lowest of the engineering materials [232]. Secondly, it provides mechanical stability to our metamaterial absorber because of its strength and hardness. Also, it has a high melting point of 2623°C and thus, proving itself to be a right choice of material for solar energy harvesting application.

6.2.6 Effect of Different Incident Angles

To evaluate the angle sensitivity of the proposed structure we simulated over a range of incident angles, from 0 to 85 degrees. We achieved an efficiency of over 90% for up to 60 degrees of incident angle [see Fig. 6.7], making it an excellent candidate for absorbing solar spectrum throughout the daytime. With the help of today's state-of-

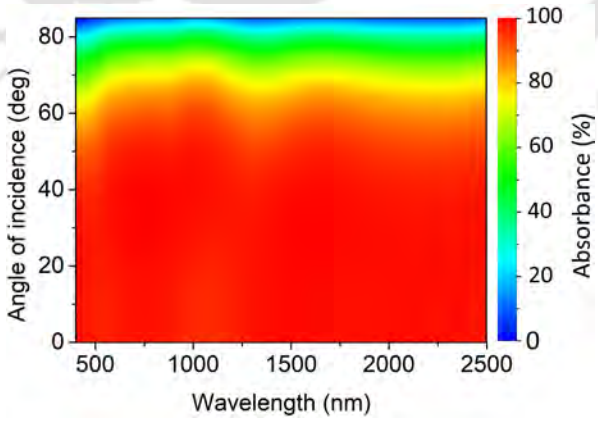

Figure 6.7: Contour plot for the angular absorption spectrum with $L = 20$, where L denotes number of metallo-dielectric pairs in the model, showing over 90% absorption efficiency for a wide angle of incidence, up to 60 degrees.

the-art nano-fabrication technologies, such structures can be easily fabricated. In the simulation, we have ignored minor surface roughness which may arise due to fabrication imperfections, resulting in slight variance in the measured values of absorbance to those obtained from simulations [65].

6.2.7 Summary

We designed and simulated an ultrabroadband absorber based on a one-dimensional periodic array of metallo-dielectric alternating multilayered tapered structure. It can absorb radiation over the whole visible and near-infrared spectrum, ranging from 400–2500 nm, *i.e.*, over entire solar spectrum. The average absorption of 98.2% was achieved by 20 pairs of alternating molybdenum–germanium based tapered structure. The **absorbance was further enhanced to over 99%** using more number of metallo-dielectric layers (64 pairs). The broadband absorption is attributed to multiple slow-wave modes getting absorbed at different layers. The trapped rainbow effect and the anti-reflection effect together give broadband absorbance with high efficiency. Additionally, our simulation model shows angle insensitivity up to 60 degrees. Absorbance spectra, obtained from effective medium theory, agree well with our simulation results. Our presented work can be utilized in a wide range of applications such as solar energy harvesting, thermophotovoltaics, stealth technology, camouflage, and thermal emitters.

6.3 2D-Grating Based Ultrabroadband Metamaterial Perfect Absorbers

The previous section discussed a one-dimensional array of grating based ultrabroadband metamaterial absorber with a fundamental limitation of polarization- sensitivity due to lack of symmetry from the top of the structure. To overcome this limitation, in this section, we present a polarization-independent ultrabroadband perfect metamaterial absorber comprising a two-dimensional array of hemi-ellipsoid shaped metallo-dielectric multilayered structure. An unprecedented average absorbance of

~99% is theoretically demonstrated over a spectral range between 300 nm and 4500 nm at normal incidence. The proposed design has potential application in thermophotovoltaics for solar energy harvesting.

6.3.1 Design Schematic and Simulation Model

A three-dimensional (3D) schematic representation of our design is shown in Fig. 6.8(a). Our design comprises 20 pairs of alternating metallo-dielectric layer, with metal being molybdenum (each 78 nm thick), and dielectric being germanium (each 42 nm thick). This metallo-dielectric stack is terminated by a ground metal tungsten (300 nm thick), supported by a silicon (Si) substrate (200 nm thick). Note that the Si substrate is shown for demonstration purposes only. This substrate has no role in simulation as the ground metal is thick enough to block the penetration of electromagnetic waves through it. The length of each minor axis (d) of a prolate hemi-ellipsoid is 400 nm. A 20

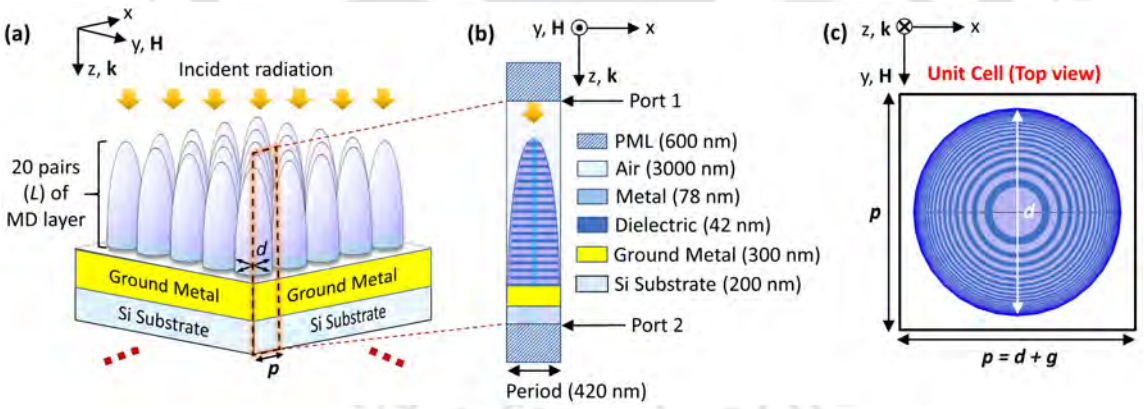

Figure 6.8: Design of an infinite two-dimensional array of hemi-ellipsoid shaped metallo-dielectric multilayered structure showing (a) 3D schematic representation along with (b) side- and (c) top view of its unit cell considered for 3D numerical simulation. We consider TM polarization, where, **H** field is aligned along y-axis. Plane wave propagates along the z-axis from port 1 and optical response is measured using S parameters. This design consists of 20 pairs (L) of metallo-dielectric layer [made of molybdenum (Mo)–germanium (Ge)], with tungsten (W) as the ground metal, standing over a silicon substrate. A perfectly matched layer (PML) is applied at the top and the bottom of the unit cell. In (a) and (c), d (400 nm): length of each minor axis of a prolate hemi-ellipsoid, g (20 nm): the gap between the base of two adjacent hemi-ellipsoids, and p (420 nm): the period of the unit cell. In (b), the thickness of each layer of the simulation model is mentioned within the parentheses.

nm gap (g) is considered between the base of two adjacent hemi-ellipsoids to account for any error arising due to their misalignment during fabrication. The unit cell has a periodicity (p) of 420 nm along both x-axis and y-axis, implementing the Floquet boundary conditions to simulate a 2D array.

Figure 6.8(b) and 6.8(c) show the side- and top view, respectively, of the unit cell considered for 3D numerical simulation. We simulate the unit cell using the RF module of the commercially available finite element method (FEM) based solver, COMSOL Multiphysics®, over 300–5000 nm spectral window. The optical constants for molybdenum [144, 233], germanium [234, 235], and tungsten [144, 233] are taken from the literature. A wavelength-domain solver is deployed with fine physics-controlled meshing, where the maximum and the minimum allowed mesh element sizes are $\lambda_{\max}/20$ (where $\lambda_{\max}$ is the maximum wavelength of the considered range in vacuum) and $\sim$18 nm, respectively, which could accurately model the structural details. To minimize the effect of undue reflections arising due to confinement of the simulation domain, perfectly matched layers (PML), each 600 nm thick, were introduced above Port 1 and below Port 2. For TM case, perfect electric conductor boundary condition is applied along the x-direction and periodic boundary condition is applied along the y- boundaries. Whereas for TE case, periodic boundary condition is applied along the x-direction and perfect electric conductor is applied along the y- boundaries.

6.3.2 Spectral Response Analysis

The numerically calculated spectra for absorbance, reflectance, and transmittance for our design are shown in Fig. 6.9(a). For 20 pairs (L) of metallo-dielectric layer, we obtain an unprecedented average absorbance of $\sim$99% at normal incidence, the highest average absorbance reported so far between 300 nm and 4500 nm spectral range, to the best of our knowledge. A small wobbling seen in the middle of the absorption spectra arises due to imperfect overlap of the fundamental order slow-light modes (discussed

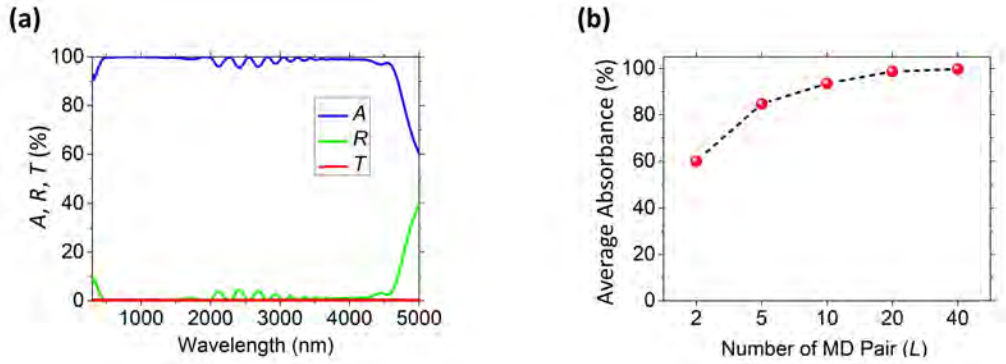

Figure 6.9: Numerically calculated spectral response for our design showing (a) absorbance (A), reflectance (R), and transmittance (T) for design with 20 pairs (L) of metallo-dielectric layer between 300 nm and 5000 nm spectral window at normal incidence, and (b) trend for gradually increasing average absorbance with increasing number of metallo-dielectric pair (L) at five discrete values between 2 and 40. Note that the average absorbance is calculated between 300 nm and 4500 nm spectral range at normal incidence.

in detail under working principle subsection) [84]. For optimizing the absorber's cost, performance, and overall thickness, we also study the average absorbance of our design at five discrete values of L between 2 and 40, as shown in Fig. 6.9(b). With an increasing number of metallo-dielectric pair, ideally, average absorption should increase and eventually, must saturate. Till L = 20, a gradual rise in average absorption can be seen, beyond which there is a trend towards saturation. Hence, a design with L = 20 is chosen as the optimized model for our work.

6.3.3 Working Principle

To understand the physical principle behind ultrabroadband absorption, we study normalized magnetic and electric field distribution (colour plot) with corresponding energy flow (arrow plot), over ten discrete incident frequencies, f (wavelengths, λ) between 67 THz and 750 THz (between 400 nm and 4500 nm), using 20 pairs (L) of metallo-dielectric layer, as shown in Fig. 6.10. For longer wavelengths (between 2000 nm and 4500 nm), it is evident from the arrow plot that before entering the structure, the incident light propagates along the z-direction (downwards) *via* air gaps,

swivels, and then enters the structure. As shown in Fig. 6.10(a), the confinement of magnetic field creates a vortex (shown using colour plot), which can be described using slow-light concept. It is defined as the propagation of light at very low group velocity, leading to the generation of fundamental order modes, as the slow-waves get trapped across different locations of the structure [25]. While the magnetic field is confined inside the structure, the electric field at the corresponding wavelength is mostly confined in the air gap between the adjacent hemi-ellipsoids, as shown by dotted white circles in Fig. 6.10(b). The confinement of electric field in the air gap indicates mode interaction between the adjacent hemi-ellipsoids, similar to the findings reported in [236].

For longer wavelengths, the existence of slow-light mode of fundamental order can be seen in Fig. 6.10(a). At 4500 nm wavelength, magnetic resonance mode formation is supported at the lowest part of the structure. This mode moves upward towards the center of the structure at 3500 nm wavelength and finally reaches the topmost part at 2000 nm wavelength. Thereafter, the presence of higher-order magnetic resonance modes is observed between 1500 nm and 2000 nm spectral range, of which one instance is shown at λ = 1600 nm. The pattern of electric modes, shown in Fig. 6.10(b), originating from near-field interaction between the adjacent hemi-ellipsoids, follow a similar trend with change in incident wavelength, as seen for the magnetic modes in Fig. 6.10(a). As previously reported, the underlying principle can be understood using trapped rainbow effect [237, 238]. For longer wavelengths, molybdenum possesses highly negative real part of the relative permittivity, making it behave more like metal—causing severe light reflection. However, no excitation of slow-wave mode is observed at shorter wavelengths ($\lambda < 1500$ nm).

At shorter wavelengths, the mechanism behind efficient absorption can be ascribed to anti-reflection effect [239]. This effect can be seen as enhanced light transmission inside the structure due to the gradual change of effective indexes, attributed to gra-

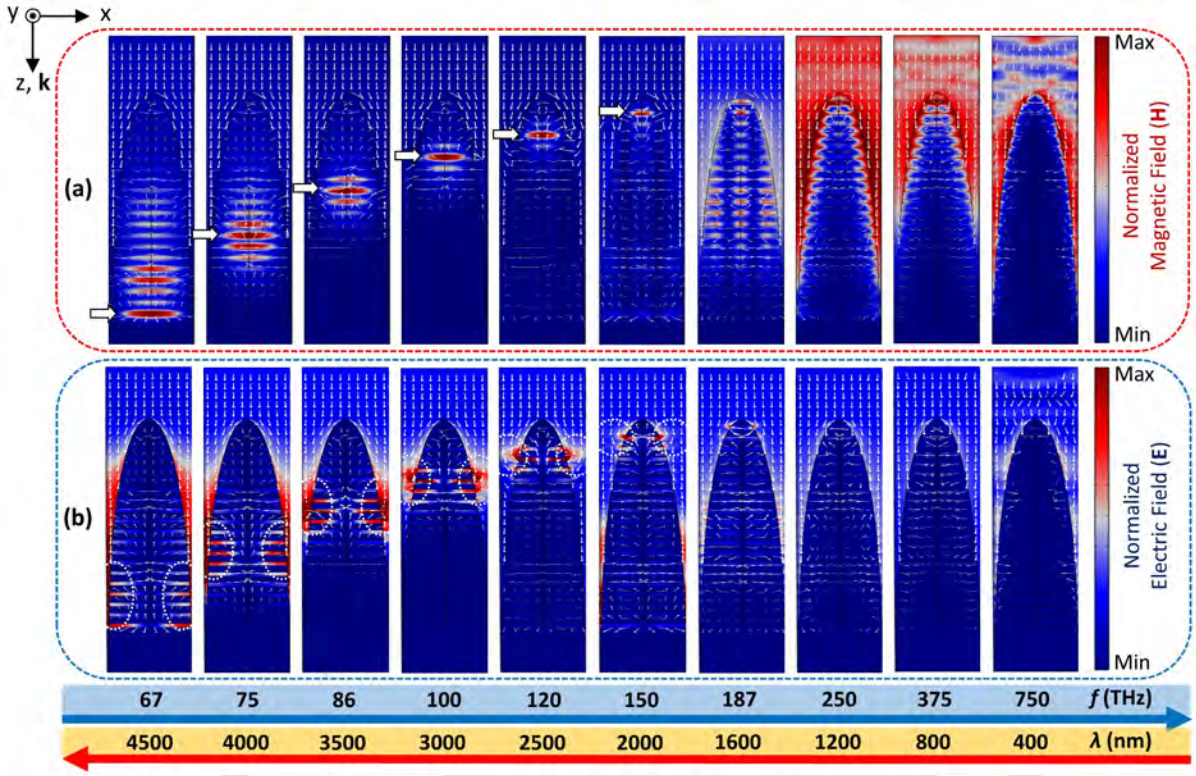

Figure 6.10: Normalized (a) magnetic- and (b) electric field distribution (colour plots) with corresponding energy flow (arrow plot) at arbitrarily chosen incident frequencies, f (wavelengths, λ) between 67 THz and 750 THz (between 400 nm and 4500 nm), simulated for 20 pairs (L) of metallo-dielectric layer. In (a), for the incident wavelengths between 2000 nm and 4500 nm, the presence of fundamental order magnetic resonance modes is clearly shown at different locations of the structure using horizontal white arrows (pointing towards right). At $\lambda = 1600$ nm, higher-order resonance modes can be seen in the magnetic field plot. In (b), dotted white circles highlight the electric modes, corresponding to the magnetic resonance modes in (a), which depict the pattern of near-field interaction between adjacent hemi-ellipsoids with incident wavelength.

dient in design from the top to bottom [25]. It is observed that at shorter wavelengths, molybdenum behaves as a lossy dielectric, as its real part of relative permittivity is positive [233], leading to anti-reflection effect. Thus, the anti-reflection effect (for $\lambda < 1500$ nm) and the trapped rainbow effect (for $\lambda > 1500$ nm) together give efficient absorption over the entire solar spectral regime.

Since the hemi-ellipsoid shaped absorber has a higher gradient in design in the upper half compared to the lower half, the fundamental order magnetic mode resonances for the upper half is not perfectly overlapping. This is because of the considerable

change in the width of each metallo-dielectric pair as we move from the top towards the middle section of the absorber, creating enough gap between each resonance peak to become non-overlapping. This is the cause of wobble arising in the middle of the absorbance spectra between 2000 nm and 3500 nm wavelengths [see Fig. 6.9(a)]. These wobbles can be completely removed by sacrificing the absorption bandwidth [84].

For the lower half of the absorber, the gradient in design becomes lesser and lesser as we go down from middle section towards the bottom. This causes a gradual reduction in the wobble size due to overlapping fundamental order magnetic mode resonances, resulting in near-perfect absorption between 3500 nm and 4500 nm wavelengths [see Fig. 6.9(a)]. Note that the metallo-dielectric layers are followed by ground metal, which acts as a reflector for the longer wavelengths, forcing them to travel back and get fully absorbed inside the metallo-dielectric multilayer structure, hence, further increasing our range of absorption up to 5000 nm.

6.3.4 Theoretical Modelling and Verification

To validate our simulation results, we use effective medium theory (EMT) approximation, where each metallo-dielectric pair is assumed to be a homogeneous layer with effective permittivity given by Eq. (6.1). For our design, we consider a filling ratio of f = 0.65 (t_m = 78 nm and t_d = 42 nm), with molybdenum and germanium forming the alternating metallo-dielectric pair. A comparison between numerically calculated absorbance spectra for L = 20 (solid line) and EMT approximation (dashed line) over 300–5000 nm spectral range at normal incidence, is shown in Fig. 6.11(a). Between 400 nm and 1900 nm spectral range, shown by the shaded region, the absorbance spectra obtained using EMT approximation are in close agreement with L = 20, beyond which EMT approximation gradually becomes inaccurate.

To understand the underlying cause, we study normalized magnetic field distribution (colour plot) and energy flow (arrow plot) using EMT approximation at arbitrarily

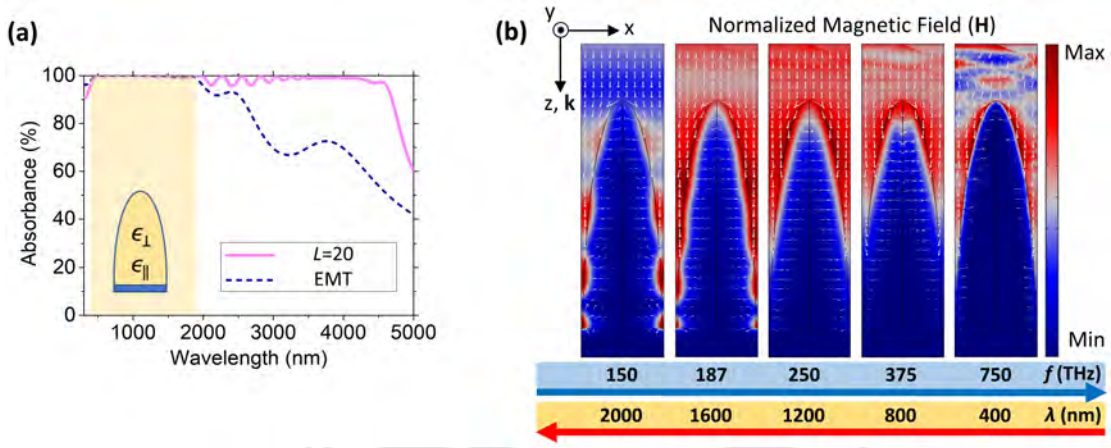

Figure 6.11: (a) Comparison of numerically calculated absorbance spectra between 20 pairs (L) of metallo-dielectric layer (solid line) and effective medium theory (EMT) approximation (dashed line) over 300–5000 nm spectral range at normal incidence, and (b) normalized magnetic field ($\mathbf{H}$) distribution (colour plot) and energy flow (arrow plot) using EMT approximation at arbitrarily chosen incident frequencies, f (wavelengths, λ) between 150 THz and 750 THz (between 400 nm and 2000 nm). Note that in (a), the EMT approximation is valid between 400 nm and 1900 nm spectral range, shown by the shaded region.

chosen incident frequencies, f (wavelengths, λ) between 150 THz and 750 THz (between 400 nm and 2000 nm), as shown in Fig. 6.11(b). We observe that the magnetic field distributions at λ = 400 nm, 800 nm, and 1200 nm are similar for both L = 20 and EMT approximation, as shown in Figs. 6.10 and 6.11(b), respectively. However, at λ = 1600 nm (and beyond), the formation of magnetic resonance modes can be seen for L = 20 due to the presence of discrete metallo-dielectric pair, which is otherwise missing in our EMT approximation. Since no such formation of magnetic resonance modes is seen in the EMT approximation, therefore, this approximation is only applicable up to 1900 nm wavelength, beyond which the effect of magnetic resonance modes becomes increasingly significant.

In the UV region *i.e.* 300–400 nm wavelength range, we observe slightly more dip in the absorbance spectra for L = 20 compared to EMT approximation, as shown in Fig. 6.11(a). The reason may be attributed to enhanced reflections inside the hemi-ellipsoid absorber due to the presence of discrete metallo-dielectric pair in L = 20 [see

Fig. 6.9(a) for reference], leading to a larger dip in the absorbance spectra. Nevertheless, a close agreement between L = 20 and EMT approximation over 400–1900 nm spectral range, indeed validates our results. A close agreement between them also suggests that our proposed design is robust and will have little impact due to deformity arising out of fabrication imperfections.

6.3.5 Parametric Analysis and Tolerance Study

For designing an ideal broadband absorber, the key aspect is to choose such material which has large real and imaginary parts of frequency-dependent refractive index (n and k). A high value of n ensures that the incident light travels slowly inside a medium, hence allowing more time for light to get absorbed. The imaginary part k accounts for the loss in a medium. Having a high value of k will ensure more loss over the same optical path.

For our design, the contour plot of parametric analysis is shown in Fig. 6.12. Ideally, the thickness of each material needs to be minimized for reducing the overall cost and time of fabrication, eventually, making the structure ultra-thin. In order to find the minimum thickness of the metal (t_{M1}), a parametric sweep from 10 nm to 100 nm thickness is carried out, keeping all other parameters constant. We observe that with an increase in metal thickness, the absorption bandwidth keeps on increasing, as shown in Fig. 6.12(a). Hence, t_{M1} = 78 nm is chosen as the optimum thickness to achieve maximum average absorbance between 300 nm and 4500 nm, shown using white dashed line in Fig. 6.12(a). On the contrary, with an increase in the dielectric thickness (t_{D}), the absorption bandwidth goes on decreasing. Therefore, t_{D} = 42 nm is the suitable thickness for dielectric layer, as shown in Fig. 6.12(b).

To account for the role of gradient in design of the hemi-ellipsoid absorber, we vary the length of each minor axis (d) between 100 nm and 800 nm, as shown in Fig. 6.12(c). It is observed that with an increase in the length of each minor axis, the absorption

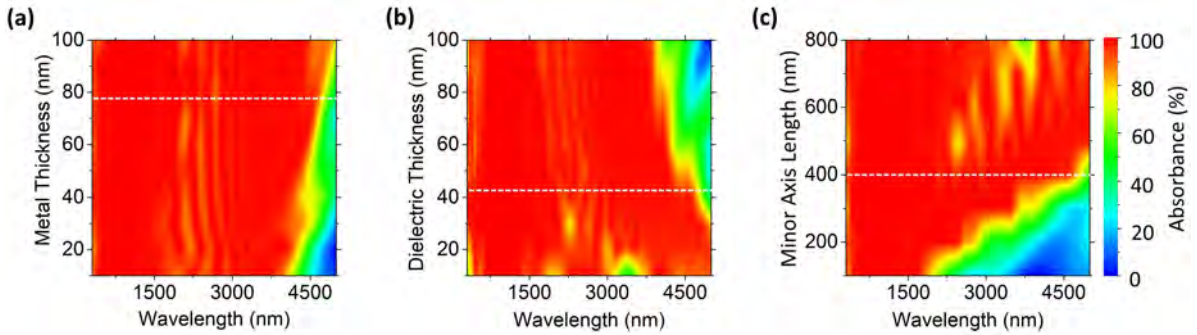

Figure 6.12: Simulation based parametric analysis of our design showing colour contour plot for varying (a) metal thickness, t_{M1}, (b) dielectric thickness, t_D, and (c) length of each minor axis, d, while keeping all other parameters constant for each case. The white dashed lines show the optimized parameter value between 300 nm and 4500 nm spectral range in each case.

bandwidth keeps on increasing. This indicates that absorption bandwidth can be further extended beyond 4500 nm wavelength. However, for designs with larger bandwidth, a dip in the middle of the absorbance spectrum can be seen with an increase in the length of each minor axis [see Fig. 6.12(c)], arising due to the increasingly imperfect overlap of the fundamental order resonance modes. This may result in a decrease in the overall average absorbance much below 99%. Hence, d = 400 nm is the right choice for our design to achieve maximum average absorbance between 300 nm and 4500 nm, suitable for application in thermophotovoltaics.

To account for fabrication errors, we also study optical fabrication tolerance limit for our design obtained using L = 20 pair with $\pm$0.5% maximum allowable variance on average absorbance, as shown in Fig. 6.13. The ends of the shadowed region depict the upper and lower limit of tolerance for varying thickness of metallic layer (t_{M1}), dielectric layer (t_D), and length of each minor axis (d). The values obtained for upper limit, lower limit, and optimized dimension of the absorber are listed in Table 6.3. The upper and lower limits for device dimension reveal that our design is robust and deviation in average absorbance is less prone to fabrication imperfections.

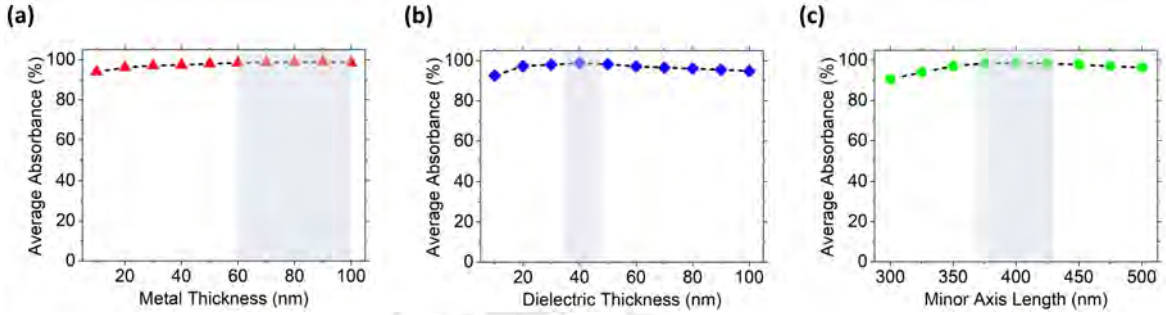

Figure 6.13: Numerically calculated optical fabrication tolerance of our design showing average absorbance between 300 nm and 4500 nm spectral range at normal incidence for varying (a) metal thickness, t_{M1}, (b) dielectric thickness, t_D, and (c) length of each minor axis, d, while keeping other parameters constant in each case. The shadowed regions show the tolerance limit for our design with $\pm 0.5\%$ maximum allowable variance on average absorbance.

Table 6.3: Fabrication tolerance limit for our design shown in Fig. 6.8 with $\pm 0.5\%$ maximum allowable variance on average absorbance (all dimensions are in nm)

Fabrication tolerance	**Metal thickness (t_{M1})**	**Dielectric thickness (t_D)**	**Length of each minor axis (d)**
Upper limit	100	47	430
Lower limit	60	35	370
Optimum dimension	**78**	**42**	**400**

6.3.6 Effect of Different Incident Angles and Polarizations

A broadband absorber for solar energy harvesting is only useful if the design is polarization-insensitive and can offer high average absorbance even at a wide angle of incidence considering dynamic daylight situations. Our design is symmetrical along both x and y directions. This provides a perfect match between TM and TE polarization spectra at normal incidence, making the structure polarization-insensitive, as shown in Fig. 6.14(a). To check angle-sensitivity, we study colour contour plot (for both TM and TE polarization) between 300 nm and 4500 nm spectral regime over a wide range of incident angles, between 0 and 60 degrees, as shown in see Figs. 6.14(b) and 6.14(c).

Figure 6.14(d) shows the average absorbance (between 300 nm and 4500 nm spectral range) for TM, TE, and unpolarized waves at a varying angle of incidence. A close

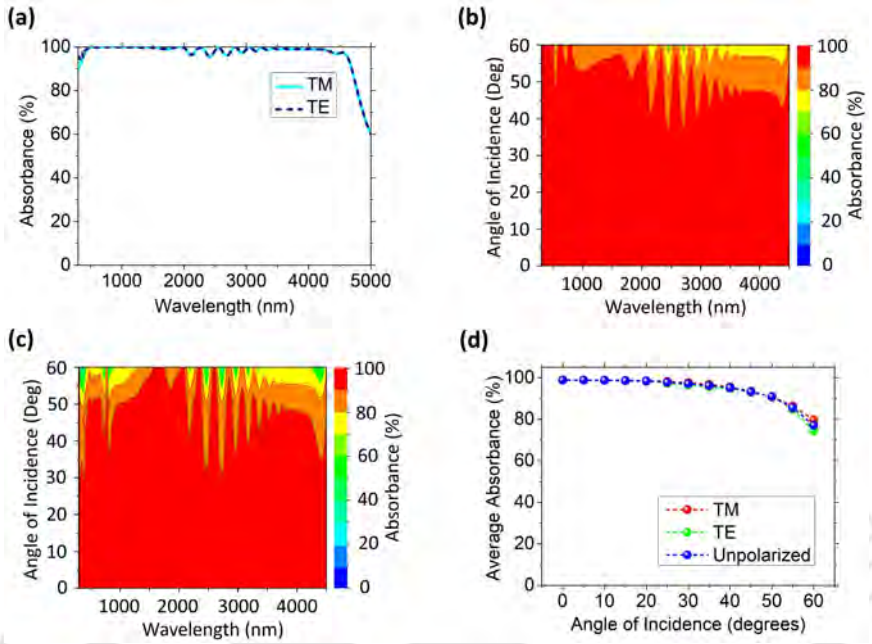

Figure 6.14: Simulation results for our design showing (a) absorbance spectra (between 300 nm and 4500 nm) for both TM and TE polarizations at normal incidence; contour plot of absorbance spectrum for (b) TM and (c) TE polarization as a function of incident angle, ranging from 0 to 60 degrees, and (d) average absorbance (between 300 nm and 4500 nm) for TM, TE, and unpolarized waves incident at different angles, showing over 90% average absorbance efficiency (η) for the oblique angle of incidence up to 50 degrees and nearly 80% absorption efficiency for the oblique angle of incidence up to 60 degrees.

match among their average absorbance values indicates that the performance for TE, TM, and unpolarized waves are expected to be very similar for the oblique angle of incidence, up to 60 degrees. It also shows that over 90% absorption efficiency (η) can be achieved for the oblique angle of incidence up to 50 degrees and nearly 80% absorption efficiency for the oblique angle of incidence up to 60 degrees, over 300–4500 nm wavelength range. This drop in the absorption efficiency becomes more significant at the grazing angles, primarily due to the enhanced reflections from the surfaces. From the fabrication point of view, we choose the gap (g) between the base of two adjacent hemi-ellipsoids to be 20 nm. However, if we can reduce the gap below 20 nm, absorbance efficiency can be further improved. Nevertheless, such a good absorption efficiency over a wide-angle makes our design angle-insensitive to a great extent. The

Table 6.4: Comparative overview of a few recently reported broadband absorbers for solar energy harvesting

References	Structural Design	Range (nm)	Avg. A (%)	P.I.	A.I. (up to)	η
Liu *et al.* [64]	(Ti/V/W)–SiO_2–(Ti/V/W)	280–4000	91	Yes	NA	NA
Hoa *et al.* [65]	Au–Si–Au	400–1600	∼90	Yes	Yes (60°)	0.9
Soydan *et al.* [66]	TMC/TMN–Al_2O_3 (multilayer)	300–2500	90	No	Yes (60°)	0.8
Aalizadeh *et al.* [67]	Ti–Mn–Al_2O_3–Ti	480–3280	90	Yes	Yes (40°)	0.9
Lin *et al.* [68]	Graphene–SiO_2 (multilayer) –Ag	300–2500	85	Yes	Yes (60°)	0.7
Gao *et al.* [69]	SiO_2–TiN–SiO_2–TiN	200–1200	90	Yes	Yes (40°)	0.9
This Work	Mo–Ge (20 pairs) –W	300–4500	∼99	Yes	Yes (60°)	0.8

Note: A: Absorbance (%); P.I.: Polarization-Insensitive; A.I.: Angle-Insensitive; η: Absorption Efficiency; NA: Not Available.

above studies predict that our design is an excellent choice for solar energy harvesting throughout the daytime. A comparative overview of a few recently reported broadband absorbers for solar energy harvesting is listed in Table 6.4.

6.3.7 Prospective Fabrication Methodology and Future Scope

Today, with the fast advancement in nano-scale fabrication facilities, it is indeed feasible to fabricate our proposed design. First, a base needs to be prepared by depositing 100 nm thick molybdenum film using RF magnetron sputtering over a flat Si substrate [236]. In the next step, 20 pairs of alternating molybdenum and germanium layers should be deposited on top of bottom metallic layer (molybdenum) using sputtering. The one-dimensional tapered-grating array (typically 10 μm × 10 μm dimension) can be obtained by milling alternating molybdenum and germanium layers with Focused Ion Beam (FIB) technology. For precise control over tapered angle, grayscale bitmaps can be used to pattern the nano-design by controlling beam dose [236].

For making a two-dimensional tapered array, the one-dimensional tapered array needs to be milled orthogonally, to realize a polarization-insensitive absorber [240]. The non-uniform gradient in design can be obtained by precisely-controlled grayscale bitmaps and proper beam doses adjustments during the milling process. Note that during this fabrication process, defects may arise due to imperfect quality of the materials used, leading to surface roughness. Also, the fabrication error of patterns may arise due to the deposition of milled away particles in the fabricated grooves. Such errors cannot be completely avoided and hence a dimension tolerance study is important to compensate for the fabrication errors without affecting the final absorbance efficiency beyond the acceptable limit. Hence, the information provided in Table 6.3 is very useful for designing a robust absorber. Besides, we also introduced a 20 nm gap between two hemi-ellipsoid shaped structures, to account for any error arising due to their misalignment during fabrication. Another technique for fabricating molybdenum–germanium multilayer structure is nano-imprint lithography using an electron beam physical vapour deposition technique [241]. Compared to FIB technology, the nano-imprint and lift-off approach are parallel processes, and large-area design (typically in cm dimension) can be easily realized. Moreover, the nano-imprint and lift-off methods can produce nano-tapered array (period $\sim$200 nm), suitable for fabricating absorbers for solar energy harvesting.

Here it is important to note that the metals used in grating columns of the broadband absorbers introduce joule heating during absorption of incident radiation, which causes a photothermal effect on geometric configuration [242]. The high absorption happens due to a large imaginary part of the dielectric constant [243, 244]. Conventional metals used in broadband absorbers have weak stability at high operating temperatures, which may alter the dielectric constant and hence may not produce the desired optical response. In this work, we have used refractory metals (such as tungsten

and molybdenum) and germanium as the dielectric material, which have very high melting points, good mechanical and thermal stability, and large imaginary part of the dielectric constant [144, 233–235]. Although actual performance can be evaluated after fabrication and testing of the prototype, but we may expect our design to be robust and operate efficiently at high temperatures.

6.3.8 Summary

In this work, we presented **a new design of ultrabroadband 'perfect' absorber** consisting of a 2D array of hemi-ellipsoid shaped metallo-dielectric (MD) multilayered structure, due to lateral symmetry this design is polarization-insensitive, which was not achieved in the previous design using 1D array. **An unprecedented average absorbance of $\sim$99% is achieved at normal incidence between 300 nm and 4500 nm spectral range.** We used 20 pairs of molybdenum–germanium metallo-dielectric layer, with tungsten as ground metal. The ultrabroadband absorption is attributed to the anti-reflection effect (for $\lambda < 1500$ nm) and the trapped rainbow effect (for $\lambda > 1500$ nm). Our design is polarization-independent as well as angle-insensitive (up to 60 degrees). Our theoretical calculations agree well with those of full-wave simulation results. A perspective prospective fabrication methodology and fabrication-imperfection tolerance study are also discussed for the practical realization of our proposed design. The figure-of-merit calculations show that our 'perfect' absorber can outperform some of the broadband absorbers, recently reported in the literature. A potential application of our presented broadband metamaterial absorber includes integration into solar devices for solar energy harvesting using thermophotovoltaics.

7

Solar Absorbers and Radiative Coolers for Waste Heat Management

Contents

Chapter 6 discussed trapping of the solar heat using broadband absorbers. This chapter investigates multilayer thin-films based designs of spectrally selective solar absorbers and passive radiative coolers for utilizing the waste heat. Section 7.1 investigates a generic multilayer design of selective solar absorbers that has been specifically optimized by choosing appropriate materials, number of layers required and their thicknesses to obtain an **exceptional solar-to-thermal energy conversion efficiency of 87% with a total absorbed power of 889.4** Wm^{-2}. Section 7.2 further investigates another multilayer design of a passive radiative cooler, which has been optimized to provide an **unprecedented cooling capacity of 115** Wm^{-2} **with a temperature reduction up to 60K below ambient temperature**.

7.1 Selective Solar Absorbers for Waste Heat Management

Selective solar absorbers harnessing solar energy as heat and converting it into thermal energy have gained much attention, specifically in solar thermophotovoltaic and solar thermoelectric generator systems. However, most of these solar absorbers suffer from low solar-to-heat conversion efficiency at moderately-high temperatures (100–400°C) and require complex nanofabrication techniques such as focused ion beam milling or electron beam lithography, hindering large-scale production. This section presents a lithography-free and large-area compatible design of selective solar absorber for waste heat management.

7.1.1 Design and Simulation

A three-dimensional (3D) schematic of our proposed solar absorber is shown in Fig. 7.1. Our multilayer design comprises a stack of five layers: 125 nm thick silica (SiO_2), 50 nm thick titanium dioxide (TiO_2), 10 nm thick silicon (Si), 25 nm thick germanium (Ge), and 200 nm thick chromium (Cr) layers placed on top of a Si substrate. Note that the Si substrate has no role in broadband absorption. The full-wave simu-

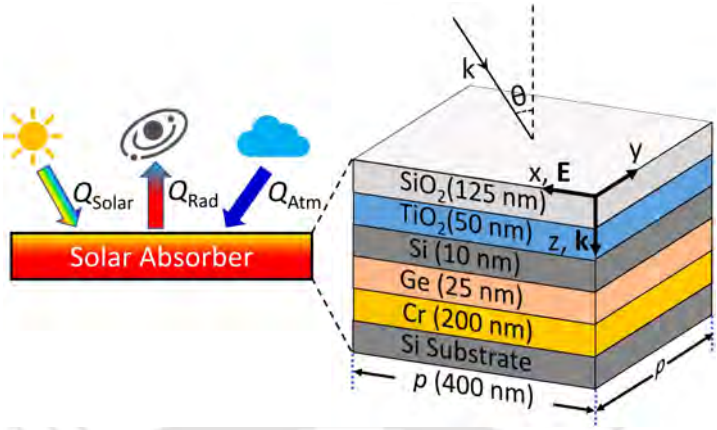

Figure 7.1: Proposed multilayer selective solar absorber in a 3D schematic view of geometry (not to scale). Here, the incident radiation is a plane wave of TM polarization travelling along z-direction. Note that all the dimensions are specified within parenthesis.

lations are performed using a FEM solver, COMSOL Multiphysics® over 0.3–14 μm wavelength range. To effectively capture all the structural details, we use extra fine mesh elements with the maximum and minimum mesh element sizes being 38 nm and 0.2 nm, respectively. The periodicity (p) of the unit cell is 400 nm. Floquet boundary conditions are applied along x and y directions to emulate a large-area thin film. The optical constants for SiO_2 [145, 245], TiO_2 [245], Si [235], Ge [234, 235], and Cr [246] are taken from the literature.

7.1.2 Analytical Modelling

We use transfer matrix method (TMM) to verify our simulation results. While applying TMM, we assume the medium to be linear, non-magnetic, and homogeneous [132]. We consider a TM polarized plane wave incident normally on a five-layer thin film stack of the solar absorber. We approximate our design to consist of six interfaces, represented by q varying between 1 and 6, and seven layers: air(0)–SiO_2(1)–TiO_2(2)–Si(3)–Ge(4)–Cr(5)–Si Substrate(6), represented by j. The incident radiation falling on top of this multilayer stack undergoes multiple reflection, transmission, and absorption inside each layer. Note that **E** and **H** fields must be continuous across all the

boundaries to satisfy the boundary conditions. The phase shift at each layer is given by [131]: $k_j\Lambda = k_0(2n_j t_j \cos\theta_{i,q})/2$ where, j value between 1 and 5 represents SiO_2, TiO_2, Si, Ge, and Cr layers, and q value between 2 and 6 represents interfaces between j^{th} and $(j+1)^{th}$ layers, respectively; Λ is the optical path length difference between the first two reflected beams from each layer; t, k, and n are the thickness, propagation constant, and refractive index of each layer, respectively, and θ_i is the angle of incidence. After solving the boundary conditions at each interface, the electric and magnetic fields can be written as:

$$E_q = E_{q+1}\cos k_j\Lambda + H_{q+1}(i\sin k_j\Lambda)/Y_j \tag{7.1a}$$

$$H_q = E_{q+1}Y_j(i\sin k_j\Lambda) + H_{q+1}\cos k_j\Lambda \tag{7.1b}$$

Here, $Y_j = \sqrt{\epsilon_0/\mu_0}\,(n_j\cos\theta_{i,q})$, where Y_j represents the admittance for TE polarization in each layer, μ_0 and ϵ_0 are the permeability and permittivity in free space, respectively. For TM case $Y_j = \sqrt{\epsilon_0/\mu_0}\,(n_j/\cos\theta_{i,q})$. In matrix form, the relationship between j^{th} and $(j+1)^{th}$ layer can be written as:

$$\begin{bmatrix} E_q \\ H_q \end{bmatrix} = \mathbf{P}_j \begin{bmatrix} E_{q+1} \\ H_{q+1} \end{bmatrix}, \quad \mathbf{P}_j = \begin{bmatrix} \cos k_j\Lambda & (i\sin k_j\Lambda)/Y_j \\ Y_j i\sin k_j\Lambda & \cos k_j\Lambda \end{bmatrix} \tag{7.2}$$

Here $\mathbf{P}_j$ denotes the characteristics matrix that relates the electric and magnetic fields at the interface across each layer. Therefore, for a seven-layer stack, the relation between electric and magnetic fields at interfaces 1 and 6 is given by:

$$\begin{bmatrix} E_6 \\ H_6 \end{bmatrix} = \mathbf{P_1P_2P_3P_4P_5} \begin{bmatrix} E_1 \\ H_1 \end{bmatrix} = \mathbf{P} \begin{bmatrix} E_1 \\ H_1 \end{bmatrix} \equiv \begin{bmatrix} p_{11} & p_{12} \\ p_{21} & p_{22} \end{bmatrix} \begin{bmatrix} E_1 \\ H_1 \end{bmatrix} \tag{7.3}$$

Considering TE case, the impedances for top air medium and bottom Si substrate are: $Y_0 = \sqrt{\epsilon_0\mu_0}\,(n_0\cos\theta_{i,1})$ and $Y_6 = \sqrt{\epsilon_{Si}\mu_0}\,(n_{sub}\cos\theta_{t,6})$, respectively, where θ_t is the

transmission angle, which gives:

$$\begin{bmatrix} E_{\mathrm{i},1} + E_{\mathrm{r},1} \\ (E_{\mathrm{i},1} - E_{\mathrm{r},1})Y_0 \end{bmatrix} = \mathbf{P_1} \begin{bmatrix} E_{\mathrm{t},2} \\ H_{\mathrm{t},2}Y_6 \end{bmatrix} \tag{7.4}$$

Here E_{i}, E_{r}, and E_{t} denote incident, reflected, and transmitted electric fields, respectively. Similarly, H_{t} denotes transmitted magnetic field. Now, we expand the matrices to find out transmission (t) and reflection (r) coefficients, given by:

$$t = \frac{2Y_0}{(Y_0 p_{11} + Y_0 Y_6 p_{11}) + (p_{21} + Y_6 p_{22})} \tag{7.5a}$$

$$r = \frac{(Y_0 p_{11} + Y_0 Y_6 p_{11}) - (p_{21} + Y_6 p_{22})}{(Y_0 p_{11} + Y_0 Y_6 p_{11}) + (p_{21} + Y_6 p_{22})} \tag{7.5b}$$

Then, the transmission (T) and reflection (R) in percentage can be obtained using $T = 100 \times |t|^2 (n_{\mathrm{t}} \cos\theta_{\mathrm{t}})/(n_{\mathrm{i}} \cos\theta_{\mathrm{i}})$ and $R = 100 \times |r|^2$, respectively. The absorption (A) can be calculated using $A = 100 - R - T$.

7.1.3 Spectral Characteristics

Figure 7.2(a) shows spectral irradiance of solar energy at sea level and thermal radiation of a surface at 300°C. Ideally, selective solar absorbers are designed to have

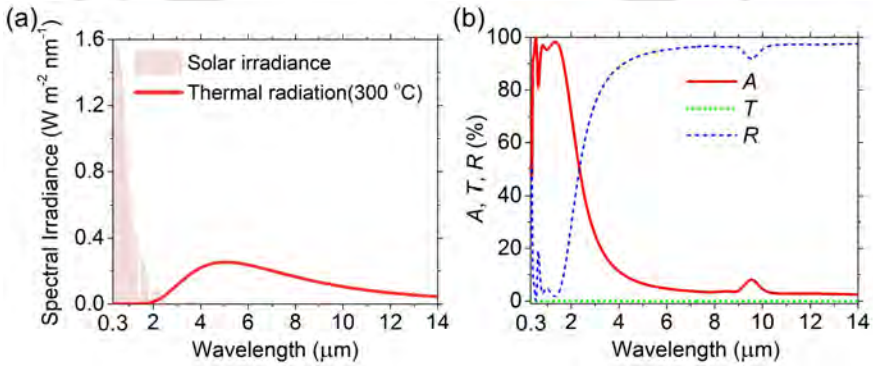

Figure 7.2: (a) Spectral irradiance of solar energy and thermal radiation of the solar absorber's surface at 300°C, (b) numerically calculated spectral characteristics of our proposed selective solar absorber showing absorption (A), transmission (T), and reflection (R) spectra over 0.3–14 μm wavelength range.

high absorption in ultraviolet (UV), visible (VIS), and near-IR ranges (0.3–2.5 μm) and low emission in the mid-IR regime (4–13 μm) [91]. Figure 7.2(b) shows the absorption, transmission, and reflection spectra from 0.3 to 14 μm. We achieve 93.6% average absorption between 0.4 μm and 1.8 μm wavelengths, where more than 90% of the total solar energy is received on the earth's surface [141]. In contrast, the average emissivity between 4 μm and 13 μm wavelengths is only 4.5%. The above results indicate that our proposed selective solar absorber exhibits near-perfect spectral characteristics in the solar and thermal radiation regimes.

7.1.4 Verification using Theoretical Analysis

Figure 7.3(a) shows a six-layer 2D stack depicting theoretical design of our proposed selective solar absorber. As shown in Fig. 7.3(b), a perfect match between the numerically (FEM) and theoretically (TMM) calculated absorption spectra over the entire 0.3–14 μm spectral range indeed validates our simulation findings.

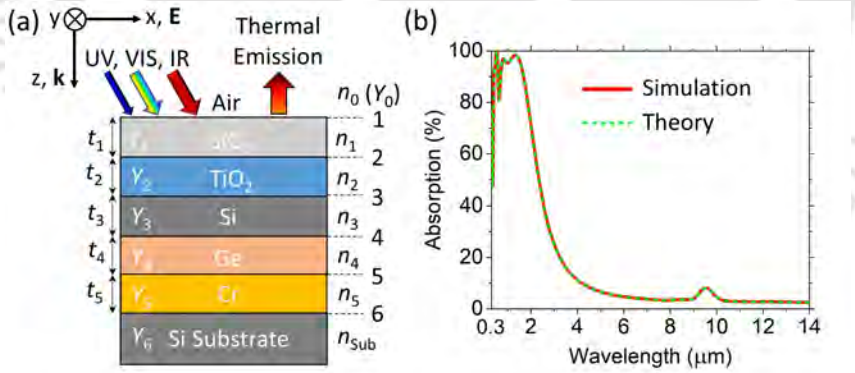

Figure 7.3: Theoretical modelling of our selective solar absorber design using transfer matrix method (TMM): (a) 2D stack of air–SiO_2–TiO_2–Si–Ge–Cr–Si substrate, and (b) simulated versus theoretical absorption plot in 0.3–14 μm wavelength range. In (a), t, Y, and n are each layer's thickness, admittance, and refractive index, respectively. Here, $t_1 = 125$ nm, $t_2 = 50$ nm, $t_3 = 10$ nm, $t_4 = 25$ nm, $t_5 = 200$ nm.

7.1.5 Physical Mechanism

To explain the physical mechanism, we show normalized power loss density at arbitrarily chosen wavelengths in UV, visible, and IR ranges, as shown in Fig. 7.4. It is clearly evident that Si and Ge layers play a major role in absorption in UV (λ = 0.3 μm) and visible (λ = 0.6 μm) spectral regimes, respectively. At the same time, Cr metallic layer with high n and k values in the IR regime helps in broadband absorption in near-IR and reflection in the thermal radiation regime [142]. Note that the top SiO_2 and TiO_2 layers act as anti-reflection coatings to enhance the absorption in the visible spectrum of solar radiation.

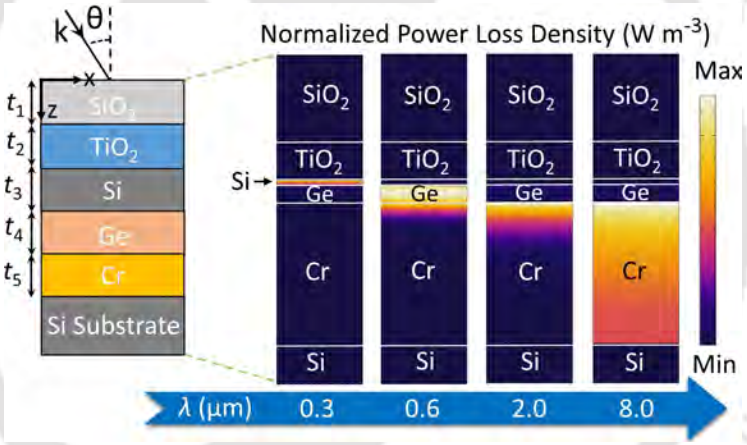

Figure 7.4: Numerically calculated normalized power loss density at arbitrarily chosen wavelengths in UV, visible and IR regimes: $\lambda = 0.3$ μm (UV), 0.6 μm (visible), 2 μm (short wave-IR), and 8 μm (long wave-IR).

7.1.6 Fundamental Theory of Energy Conversion

The solar-to-thermal energy conversion efficiency (η), considering no losses due to conduction and convection, is calculated using the following equation [90]:

$$\eta = \frac{\alpha_{\text{abs}} CF.Q - \epsilon_{\text{abs}}(\sigma T_{\text{abs}}^4 - \sigma T_{\text{amb}}^4)}{CF.Q} \tag{7.6}$$

$$\text{here } \alpha_{\text{abs}} = \frac{\int_0^\infty \alpha'_{\lambda,\text{abs}} I_{\text{AM1.5}}(\lambda) d\lambda}{\int_0^\infty I_{\text{AM1.5}}(\lambda) d\lambda}, \epsilon_{\text{abs}} = \frac{\int_0^\infty \varepsilon'_{\lambda,\text{abs}} I_{\text{BB}}(T_{\text{abs}}, \lambda) d\lambda}{\int_0^\infty I_{\text{BB}}(T_{\text{abs}}, \lambda) d\lambda} \tag{7.7}$$

CF is the concentration factor which is the ratio of solar collector area and absorber surface area, *Q* is solar radiative heat flux *i.e.* AM 1.5 Global tilt spectrum, σ is Stefan–Boltzmann constant, $\alpha'_{\lambda,\text{abs}}$ and $\varepsilon'_{\lambda,\text{abs}}$ are wavelength-dependent absorption and emission coefficients, respectively, T_{abs} is the operational temperature of the absorber, T_{amb} is the ambient temperature, $I_{\text{AM1.5}}(\lambda)$ is spectral irradiance of solar radiation at AM 1.5, and $I_{\text{BB}}(T_{\text{abs}}, \lambda)$ is spectral blackbody radiation at the operational temperature [141]. For simple theoretical calculations, the spectral range considered for integral limit is 0.3–4 μm for $\alpha'_{\lambda,\text{abs}}$ and 4–13 μm for $\varepsilon'_{\lambda,\text{abs}}$. When non-radiative heat component is ignored, the net absorbing power per unit area by the solar absorber under the direct influence of solar radiation is calculated by [247]:

$$Q_{\text{net}}(T_{\text{abs}}, T_{\text{amb}}) = Q_{\text{solar}}(T_{\text{abs}}) + Q_{\text{atm}}(T_{\text{amb}}) - Q_{\text{rad}}(T_{\text{abs}}) \tag{7.8}$$

Here, Q_{solar} is the solar power absorbed per unit area by the absorber, given by:

$$Q_{\text{solar}}(T_{\text{abs}}) = CF \int_0^\infty \alpha_{\text{abs}}(T_{\text{abs}}, \lambda) I_{\text{AM1.5}}(\lambda) d\lambda \tag{7.9}$$

Q_{atm} is the power absorber per unit area by the solar absorber due to the thermal radiation of the atmosphere which is characterized by the ambient temperature of the atmosphere:

$$Q_{\text{atm}}(T_{\text{amb}}) = \int_0^\infty \alpha_{\text{abs}}(T_{\text{abs}}, \lambda) \epsilon_{\text{atm}}(\lambda) I_{\text{BB}}(T_{\text{amb}}, \lambda) d\lambda \tag{7.10}$$

Finally, $Q_{\mathrm{rad}}(T_{\mathrm{abs}})$ is the power radiated per unit area by the absorber i.e the thermal energy lost due to radiative heat transfer, and it is calculated by:

$$Q_{\mathrm{rad}}(T_{\mathrm{abs}}) = \int_0^\infty \epsilon_{\mathrm{abs}}(T_{\mathrm{abs}}, \lambda) I_{\mathrm{BB}}(T_{\mathrm{abs}}, \lambda) d\lambda \tag{7.11}$$

The thermal performance calculations for our selective solar absorber will be discussed next subsection.

7.1.7 Efficiency Calculations

The solar-to-thermal conversion efficiency of our selective solar absorber can be evaluated using Eq. (7.6). On solving, we obtain 87% solar-to-thermal conversion efficiency when the surface temperature of selective solar absorber is at 100°C, and the concentration factor is one sun. Further, the thickness of each layer is manually optimized based on two parameters: absorption and emission coefficients. A multilayer structure is deemed to be temperature-independent below 600°C [91]. The absorption coefficient achieved is 0.9 and the emission coefficient is reported to be 0.04 at 100°C. The efficiency can be increased by placing a solar concentrator on top of the multilayer structure [89].

Figure 7.5 shows that as the temperature of the structure increases, the conversion efficiency decreases because of the blue shift of thermal radiation as per Wien's displacement law [141]. The temperature at which the system reaches equilibrium *i.e.* the solar absorption is equal to the absorber's thermal radiation, is called stagnation temperature. The designed solar absorber exhibits a stagnation temperature of 378°C when the concentration factor is one sun. Table 7.1 shows that a net power of 889.4 Wm^{-2} can be achieved by the solar absorber when its surface temperature is at 100°C.

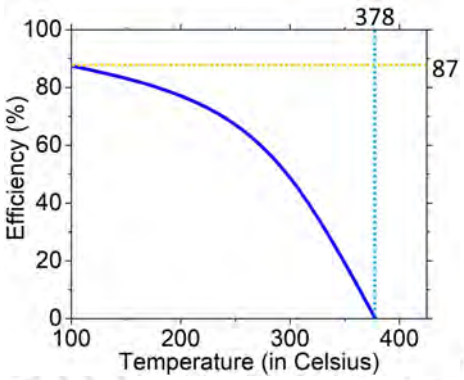

Figure 7.5: Calculated solar-to-thermal energy conversion efficiency as a function of the surface temperature of the selective solar absorber.

Table 7.1: Heat components of designed selective solar absorber considering temperature of absorber as 100°C and ambient temperature of 24°C.

Radiative Component	Q_{solar}	Q_{atm}	Q_{rad}	Q_{net}
Power per unit area (Wm^{-2})	899.0	0.5	10.1	889.4

7.1.8 Effect of Different Polarizations and Incident Angles

As the incident radiation from the sun may fall at oblique angles and can be of any polarization, a solar absorber design should be polarization- and angle-insensitive to a great extent. Figure 7.6(a) depicts a close match between TE and TM polarized absorption spectra for a normal angle of incidence, thus making our design polarization-independent. Figures 7.6(b) and 7.6(c) depict absorption contour plots for varying inci-

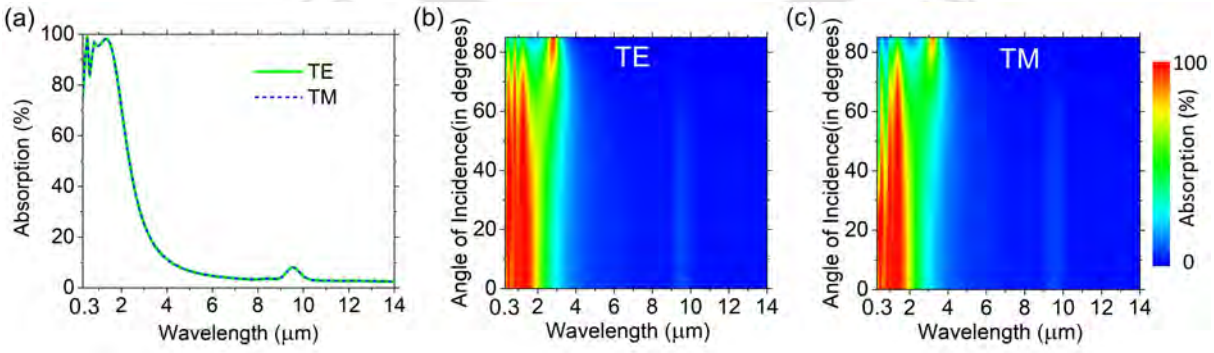

Figure 7.6: Numerically calculated absorption spectra for (a) TE and TM polarization at a normal angle of incidence, and contour plot of absorption spectra for a varying angle of incidence from 0 to 85 degrees of angle of incidence for (b) TE and (c) TM modes.

dence angles. We can see that the absorption remains reasonably high till 60 degrees of oblique incidence angle for both TM and TE polarization. For further analysis, we plot average absorption with varying angle of incidence over the solar and mid-IR regimes for TM, TE, and unpolarized incident radiation. From Fig. 7.7(a), it is clearly evident that the average absorption over the solar regime remains more than 90% till 40 degrees of angle of incidence and nearly 80% at 60 degrees of angle of incidence. In contrast, the average absorption remains below 4% over the mid-IR region. The above findings indicate that our design could be suitable for solar absorber applications which require high angle-insensitivity [68, 142]. In Fig. 7.7(b) we examine the relationship between the angle of incidence and the converted thermal energy. Initially, with an increase in the angle of incidence, the solar-to-thermal conversion efficiency increases marginally and then gradually drops to nearly 80% at 60 degrees of angle of incidence considering the unpolarized incident radiation. The thermal energy conversion efficiency is directly linked with the absorption and emission coefficients, which is directly related to average absorption over a given spectral range. Therefore, as we gradually increase the oblique angle of incidence, the average absorption slowly decreases [see Fig. 7.7(a)], owing to a gradual increase in reflection at glazing angles, thereby reducing the solar-

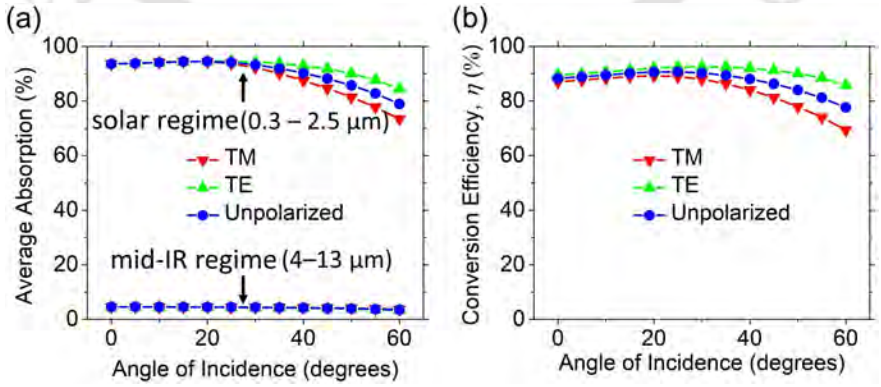

Figure 7.7: (a) Average absorbance over solar (0.3–2.5 μm) and mid-infrared (4–13 μm) regimes and (b) solar-to-thermal energy conversion efficiency (η), calculated numerically with increasing angle of incidence for TM, TE, and unpolarized incident radiation.

to-thermal conversion efficiency.

7.1.9 Prospective Fabrication Technique and Tolerance Study

With the continuous advancement in nanofabrication technology, the practical realization of our thin film multilayer solar absorber should be relatively simple. To begin, a Si wafer of suitable thickness can be taken to form the substrate. Next, an e-beam evaporator may be used to deposit Cr metallic layer under controlled pressure (typically 2×10^{-3} Pa) and deposition rate (0.5 nm/s) [248]. Other common materials such as Ge, Si, TiO_2, and SiO_2 can also be deposited in order *via* e-beam evaporator by controlling the deposition rate between 0.03 nm/s and 0.5 nm/s, depending on the thickness of each layer [248]. Alternatively, keeping in view the cost of manufacturing for end-use application, these materials can be deposited over a large area *via* chemical and physical vapor deposition techniques such as plasma enhanced chemical vapor deposition and magnetron sputtering, respectively [249, 250]. These types of equipment are fully compatible with the industrial-scale glass manufacturing processes. Optical characterization can be performed using UV–VIS–NIR and Fourier Transform-IR spectrometers for measuring spectral characteristics over 0.3–14 μm spectral range [112].

Note that our primary objective is to improve the optical performance of these solar absorbers for solar thermal engineering applications. However, under practical scenarios, the net absorbed power and solar-to-thermal conversion efficiency are expected to alter depending upon several challenging factors such as geographical location, cloudiness, humidity, and so on [251]. In addition, a solar absorber has to withstand elevated temperatures and humidity inside the collector. So, for long-term durability, the stack layers of solar absorbers should offer protection from exposure to direct sunlight, high humidity, ultraviolet radiation, *etc*. Keeping technological challenges in mind, we have meticulously chosen chemically inert and stable materials such as SiO_2 and Si having matched thermal and mechanical properties for reduced mechanical strain during ther-

mal expansion or cooling [252,253]. These materials are widely used in semiconductor fabrication processes as passivation layers. Our proposed selective solar absorbers could essentially manifest superior mechanical robustness, which in turn may protect the device from harsh external environmental conditions for a relatively longer lifespan outdoors [112].

With the continuous advancement in nanofabrication technology, the practical realization of our thin film multilayer solar absorber is relatively simple. To begin, a Si

Table 7.2: Study of fabrication tolerance of the proposed selective solar absorber design with ±10% change in thickness of each layer.

Layer (thickness)	α_{abs}	ϵ_{abs}	$Q_{\text{net}}(\text{Wm}^{-2})$	η
t_1 + 10%	0.89	0.04	880.9	86.6
SiO_2 (t_1 = 125 nm)	0.90	0.04	889.4	87.0
t_1 − 10%	0.91	0.04	896.3	88.3
t_2 + 10%	0.90	0.04	887.5	87.3
TiO_2 (t_2 = 50 nm)	0.90	0.04	889.4	87.0
t_2 − 10%	0.90	0.04	888.1	87.4
t_3 + 10%	0.90	0.04	888.9	87.4
Si (t_3 = 10 nm)	0.90	0.04	889.4	87.0
t_3 − 10%	0.90	0.04	889.1	87.5
t_4 + 10%	0.89	0.04	882.5	86.8
Ge (t_4 = 25 nm)	0.90	0.04	889.4	87.0
t_4 − 10%	0.90	0.04	894.3	88.0
t_5 + 10%	0.90	0.04	889.2	87.5
Cr (t_5 = 200 nm)	0.90	0.04	889.4	87.0
t_5 − 10%	0.90	0.04	888.9	87.4

Note: α_{abs}: absorption coefficient, ϵ_{abs}: emission coefficient, Q_{net}: net absorbed power, η: solar-to-thermal conversion efficiency.

wafer of suitable thickness can be taken to form the substrate. Next, an e-beam evaporator may be used to deposit Cr metallic layer [248]. Then Ge, Si, TiO_2, and SiO_2 layers can be deposited in order *via* chemical vapour deposition [250]. Optical characterization can be performed using UV–VIS–NIR and Fourier Transform-IR spectrometers for measuring spectral characteristics over 0.3–14 μm wavelength range [112].

Obtaining a smooth coating could be challenging during fabrication. Minor surface roughness may lead to some alteration in the estimated net absorbing power and solar-to-thermal conversion efficiency of our device. In this regard, the tolerance study shown in Table 7.2 reveals that the net absorbing power and solar-to-thermal conversion efficiency of these solar absorbers experience marginal variation with $\pm 10\%$ change in each layer thickness. Hence, one can safely assume that our proposed solar absorber design is robust to fabrication imperfections.

7.1.10 Summary

We theoretically presented a design of multilayer thin film based selective solar absorbers for solar thermal engineering applications. Our polarization- and angle-insensitive design **offers 87% solar-to-thermal energy conversion efficiency with a total absorbed power of 889.4** $\mathrm{Wm^{-2}}$ when the temperature of the solar absorber is at 100°C. The absorption coefficient achieved is 0.90 and the emission coefficient is reported to be 0.04. Our proposed solar absorber manifests a stagnation temperature of 378°C. A perfect match between our theoretical and simulation results validates our findings. A detailed prospective fabrication technique is discussed to show the feasibility of the proposed design. Our proposed solar absorber could be useful in larger-scale engineering applications such as electricity generation, water desalination, air conditioning, industrial heating, just to name a few.

7.2 Thermal Emitters for Passive Daytime Radiative Cooling

Passive radiative coolers, which pump excess heat to cold exterior space *via* thermal radiation, have emerged as a promising energy-free technology in cooling buildings, thermal power plants, and photovoltaics. However, designing a 'daytime' passive radiative cooler is challenging due to the simultaneous requirement of high reflectance in the solar spectral regime (0.3–2.5 μm) and high emissivity in the atmospheric transmittance window (8–13 μm). In this section, we present a large-area compatible and lithography-free nanoscale multilayer design of daytime passive radiative cooler.

7.2.1 Design and Simulation

Figure 7.8(a) depicts a two-dimensional (2D) graphical representation of a typical daytime passive radiative cooler. A 3D schematic view of our multilayered thin-film based passive radiative cooler is shown in Figure 7.8(b). Our design comprises four alternating dielectric layers of silicon dioxide (SiO_2;355 nm), aluminium nitride (AlN;850 nm), SiO_2 (1550 nm), and AlN (10 nm), followed by 125 nm thick silver (Ag) metallic layer placed on top of 750 nm thick silicon (Si) substrate. Note that the Si substrate is shown for demonstration only.

Figure 7.8(c) depicts a side view of the unit cell considered for 2D numerical simulation. For full-wave simulations, we use wave optics module of a commercial finite element method solver, COMSOL Multiphysics®, to simulate over 0.3–13 μm spectral range. To effectively capture all the structural details, we apply extra-fine mesh elements with the maximum and minimum sizes of 138 nm and 0.5 nm, respectively. We consider the period to be 1000 nm and apply Floquet boundary conditions along x and y directions to emulate a large-area thin-film. Perfectly matched layers (PMLs) are introduced to minimize scattering due to the confinement of the simulation domain. The thickness of each PML layer is taken as $\lambda_{max}/4$, where λ_{max} is the maximum wave-

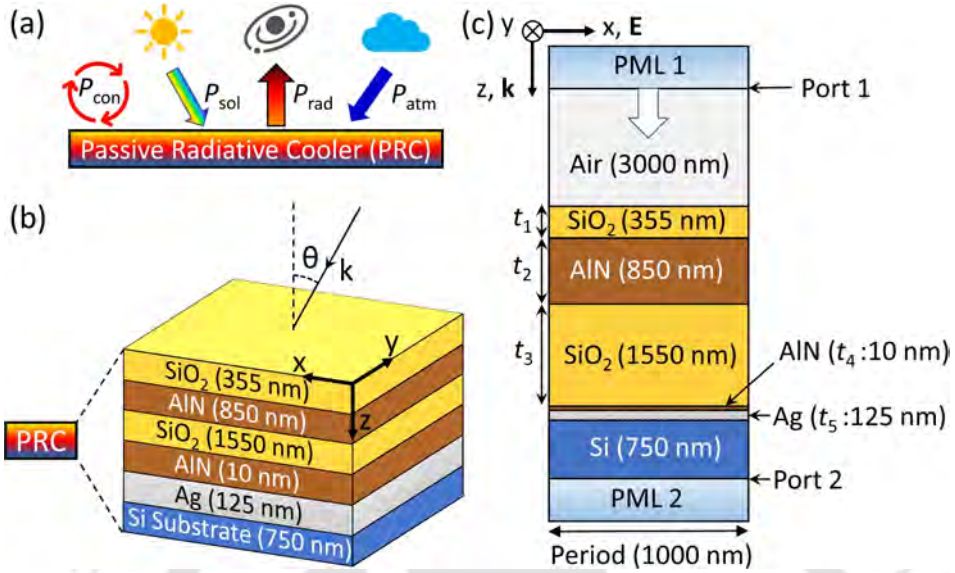

Figure 7.8: Our design of multilayered thin-film based passive radiative cooler in (a) a two-dimensional (2D) graphical representation, (b) 3D schematic view, and (c) side view of the unit cell considered for 2D numerical simulation. In (b) and (c), the incident radiation is a TM polarized plane wave traveling along the z-direction. Perfectly matched layers (PMLs) at the top and bottom of the unit cell minimize scattering due to the confinement of the simulation domain. Note that all the dimensions are specified within parenthesis.

length in the considered spectral range. The air cavity is considered 3000 nm thick. The frequency-dependent optical parameters of SiO_2 [145,245], AlN [245], and Ag [130] are obtained from the literature.

7.2.2 Spectral Characteristics Analysis

Ideal spectral characteristics of daytime passive radiative coolers require zero absorbance in the solar and atmospheric radiation spectral regimes and unity absorbance in the atmospheric transmittance window, as shown in Fig. 7.9(a). The spectral characteristics of our proposed design are shown in Figs. 7.9(b) and 7.9(c). We achieve an average absorbance of 2.7% over solar regime (0.3–2.5 μm), 2.3% over atmospheric radiation region (2.5–8 μm), and 80% in the atmospheric transparency window (8–13 μm). It is evident from the spectral characteristics that the optical response obtained from our passive radiative cooler is close to the ideal spectral characteristics.

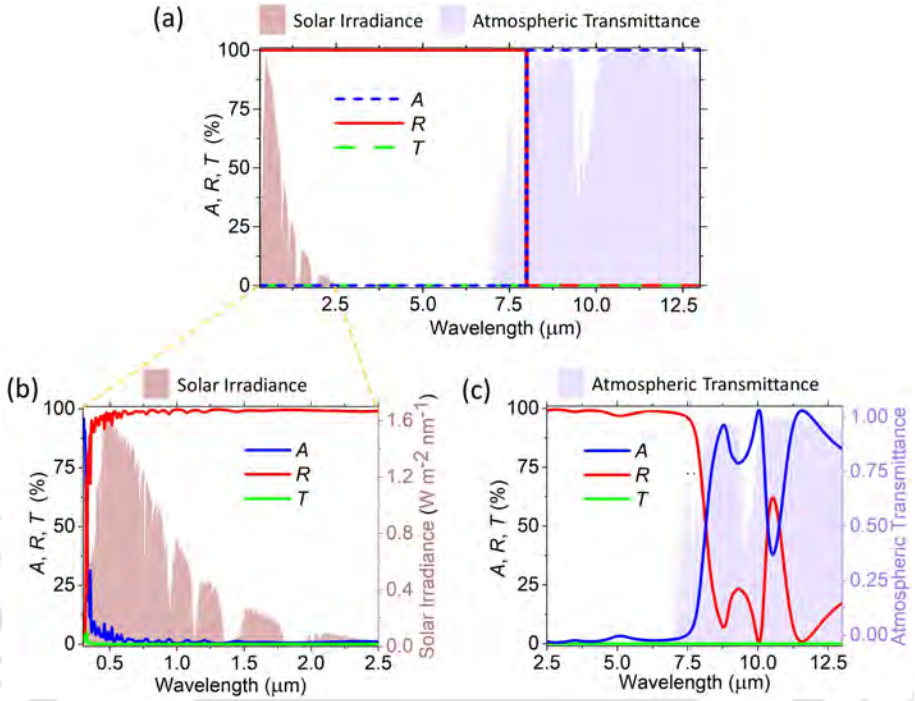

Figure 7.9: (a) Ideal spectral characteristics of passive radiative coolers over solar radiation spectral regime (0.3–2.5 μm), atmospheric radiation region (2.5–8 μm), and atmospheric transmittance window (8–13 μm). Numerically obtained spectral response for our proposed design in Fig. 7.8 showing absorbance (A), reflectance (R), and transmittance (T) spectra over (b) 0.3–2.5 μm and (c) 2.5–13 μm wavelength ranges.

7.2.3 Theoretical Verification

The numerical results are verified theoretically using transfer matrix method (TMM) implemented using MATLAB R2020b. While applying TMM, we assume the medium to be homogeneous, linear, and non-magnetic [132]. We consider a TM polarized plane wave incident normally on multilayered thin-film based passive radiative cooler. In Fig. 7.10(a), we approximate our design to consist of six interfaces and seven layers [air–SiO_2–AlN–SiO_2–AlN–Ag–Si]. Here, n, Y, and t are each layer's refractive index, admittance, and thickness, respectively. The incident radiation from air medium to IMI thin-film undergoes multiple reflection, transmission, and absorption, inside each layer. Note that **E** and **H** fields must be continuous across all the boundaries to satisfy the boundary conditions [131]. The numerically (FEM) and theoretically (TMM) cal-

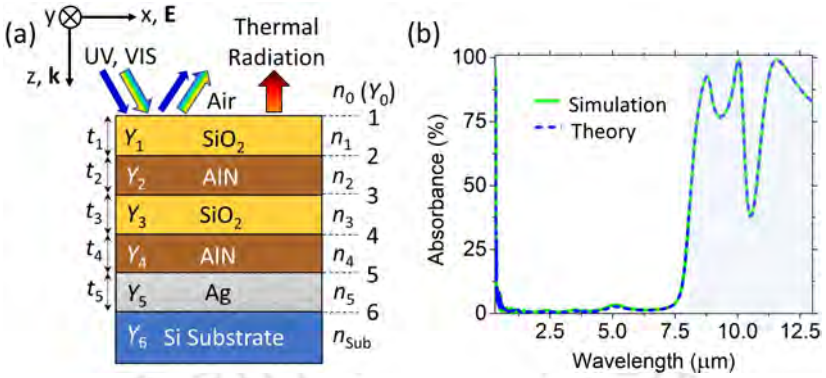

Figure 7.10: Analytical modeling of our passive radiative cooler design using transfer matrix method (TMM) showing (a) a 2D stack of our passive radiative cooler design for theoretical calculations and (b) comparison between numerically and theoretically obtained absorption spectra over 0.3–13 μm wavelength range. Note that n, t, and Y are refractive index, thickness, and admittance of each layer, respectively.

culated absorbance spectra are shown in Fig. 7.10(b). A perfect match over the entire 0.3–13 μm spectral range indeed validates our simulation findings.

7.2.4 Physical Mechanism

To design a passive radiative cooler with spectral characteristics close to an ideal cooler, the key idea is to select materials with high real and imaginary parts of refractive index (n and k). The electromagnetic waves travel slower through a medium when n is high. While a high k value ensures more loss as the wave propagates through a medium. Therefore, having high n and k values of wavelength-dependent refractive index is crucial for achieving high absorption within a medium [142]. The refractive indices of SiO_2 and AlN are shown in Figs. 7.11(a) and 7.11(b), respectively. It can be seen that both SiO_2 and AlN have negligible k values over solar (0.3–2.5 μm) and atmospheric radiation (2.5–8 μm) regimes. However, in the atmospheric transmittance window (8–13 μm), SiO_2 and AlN have relatively high values of n and k over 8–10 μm and 11–13 μm, respectively.

Figure 7.11(c) shows the normalized power loss density in each layer at three arbitrarily selected wavelengths: 8.8 μm, 10 μm, and 11.6 μm, in the atmospheric trans-

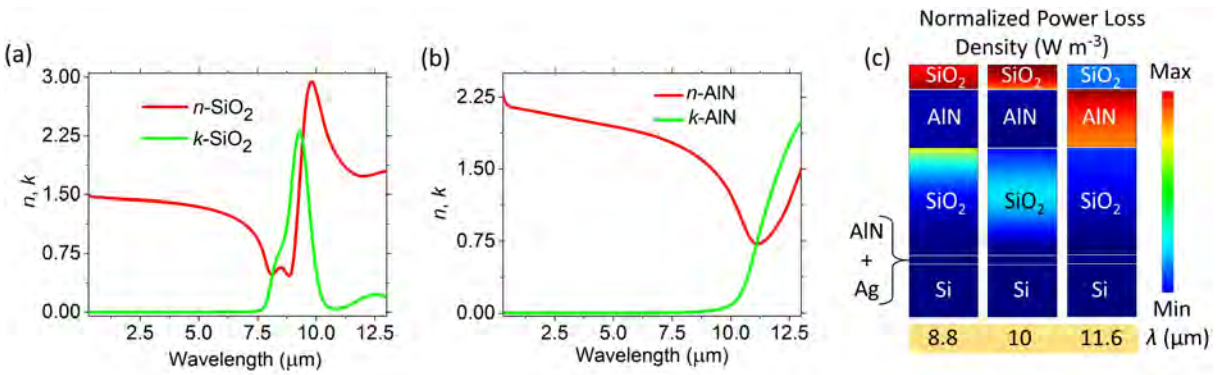

Figure 7.11: Wavelength-dependent real (n) and imaginary (k) parts of refractive indices of (a) SiO_2 and (b) AlN. Numerically obtained normalized power loss density at arbitrarily chosen wavelengths: 8.8 μm, 10 μm, and 11.6 μm in the atmospheric transmittance window.

mittance window where absorption peaks are seen in Fig. 7.9(c). It is evident from Fig. 7.11(c) that the maximum power loss or absorption happens inside SiO_2 layer below 10 μm wavelength. Whereas, above 11 μm wavelength, AlN is predominantly responsible for high absorption. Between 10 μm and 11 μm, relatively low n and k values of SiO_2 and AlN lead to a dip in the absorbance spectrum, shown in Fig. 7.9(c).

7.2.5 Parametric sweep of geometrical parameters

We manually optimized the thickness of each layer to maximize the cooling performance. Figure 7.12 shows the parametric analysis contour plots for varying thicknesses of each layer. The estimated optimal thickness of each layer is depicted using dotted horizontal white lines. In Figs. 7.12(a)–7.12(c), with an increase in the thickness of the top SiO_2 layer, top AlN layer, and bottom SiO_2 layer, we observe a significant variation of absorption in the atmospheric transmittance window. Therefore, for an ultra-compact design, we carefully chose the minimum possible thickness of the top SiO_2 layer as 355 nm, top AlN layer as 850 nm, and bottom SiO_2 layer as 1550 nm. As shown in Fig. 7.12(d), the bottom AlN layer does not play any role in absorption in the atmospheric window, but this 10 nm thick layer is crucial to reflect the UV and visible portions of solar radiation. In Fig. 7.12(e), a 125 nm 'optically thick' Ag metallic layer

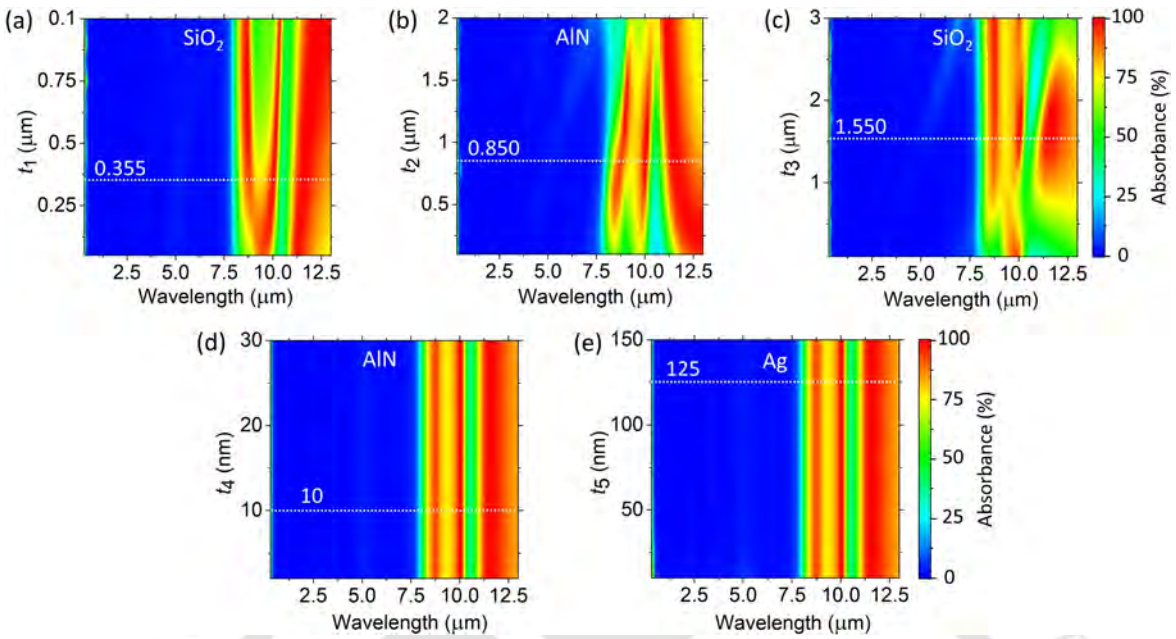

Figure 7.12: Simulated parametric analysis contour plots for varying thicknesses of each layer: (a) top SiO_2, (b) top AlN, (c) bottom SiO_2, (d) bottom AlN, and (e) Ag. Note that the optimal thickness of each layer is show using dotted horizontal white line.

is chosen as the back reflector to completely block the transmission of electromagnetic waves and enhance the absorption in the atmospheric transmittance window.

7.2.6 Physical Principles of Radiative Cooling

To achieve daytime radiative cooling, the thermal radiation from the object (P_{rad}) must exceed the cumulative sum of incoming thermal radiation of the atmosphere (P_{atm}), incident solar irradiation (P_{solar}), and the parasitic heat gain (P_{con}) due to convection and conductive heat transfer. Therefore, the net cooling power (P_{cool}) is defined as [254]:

$$P_{\text{cool}} = P_{\text{rad}} - P_{\text{sol}} - P_{\text{atm}} - P_{\text{con}} \tag{7.12}$$

where the radiated power emitted from the cooler is given by:

$$P_{\text{rad}} = A_{\text{prc}} \int d\Omega cos\theta \int_0^{\infty} I_{\text{BB}}(T_{\text{prc}}, \lambda)\epsilon(\lambda)d\lambda \tag{7.13}$$

where A_{prc} is the sky facing surface area of the cooler and it is assumed to be 1, $d\Omega = 2\pi \int_0^{\pi/2} d\theta \sin\theta$ represents the angular interval over a hemisphere with θ being the angle of incident radiation, λ is the wavelength, and $\epsilon(\lambda)$ is wavelength-dependent emissivity of the cooler. I_{BB} is defined as the wavelength-dependent spectral radiance of a blackbody at a temperature T_{prc}, expressed as:

$$I_{\mathrm{BB}}(T_{\mathrm{prc}}, \lambda) = \frac{2\pi \mathrm{hc}^2}{\lambda^5 (e^{\mathrm{hc}/\lambda \mathrm{K} T} - 1)} \tag{7.14}$$

where h is Planck's constant, K is Boltzmann's constant, c is the speed of light in free space, and T is temperature at the surface of the blackbody. As per Wien's displacement law equation: $\lambda_{\mathrm{p}} = 2900/T$ [3], the peak emission shifts towards shorter wavelengths when the blackbody temperature increases. For an ambient room temperature around 300K, the peak blackbody emission lies in long-wave infrared ($\sim$10 μm), located within the atmospheric transmittance window. Hence, through this atmospheric window, heat radiated by the cooler can exit to outer space. The solar power absorbed by the cooler can be mathematically expressed as:

$$P_{\mathrm{sol}} = A_{\mathrm{prc}} \int_0^{\infty} I_{\mathrm{AM1.5}}(\lambda) \epsilon(\lambda) d\lambda \tag{7.15}$$

where $I_{\mathrm{AM1.5}}(\lambda)$ is the standardized wavelength-dependent sun's solar irradiance at mid-altitude widely used in the photovoltaics industry [3]. As per AM 1.5 solar spectral irradiance, solar energy received on the earth's surface lies between 0.3 μm and 2.5 μm, comprising mostly ultraviolet, visible, near-infrared, and short-wave infrared radiations [255]. The power absorbed by the cooler from the surrounding atmosphere is given by:

$$P_{\mathrm{atm}} = A_{\mathrm{prc}} \int d\Omega cos\theta \int_0^{\infty} I_{\mathrm{BB}}(T_{\mathrm{amb}}, \lambda) \epsilon_{\mathrm{atm}}(\lambda, \theta) d\lambda \tag{7.16}$$

where T_{amb} is the ambient atmospheric temperature, ϵ_{atm} is the emissivity of the atmosphere. As per Kirchhoff's law of thermal radiation, under thermal equilibrium, the absorbance (A) is same as emissivity [$\epsilon(\lambda)$] for every wavelength [126]. Therefore, substituting absorbance with emissivity, the atmospheric emissivity can be written as: $\epsilon_{\mathrm{atm}}(\lambda,\theta) = 1 - t(\lambda)^{1/\cos\theta}$. Here $t(\lambda)$ denotes the atmospheric transmittance in the zenith direction and θ represents the zenith angle. Finally, the power loss caused due to parasitic thermal conduction and convection is given by [112]:

$$P_{\mathrm{con}} = A_{\mathrm{prc}} h_{\mathrm{c}} (T_{\mathrm{amb}} - T_{\mathrm{prc}}) \tag{7.17}$$

where h_{c} is parasitic heat load coefficient taking the combined effect of conduction and convection.

7.2.7 Cooling Power

For cooling power calculations, we consider the ambient temperature (T_{amb}) as 297K, surface temperature of the cooler (T_{PRC}) as 300K, and parasitic heat load coefficient (h_{c}) as 5. Substituting these values in Eqs. (7.12)–(7.17), the net cooling power of our proposed daytime passive radiative cooler comes out to be 115 Wm^{-2}. Note that our work essentially focuses on improving the optical performance of the daytime passive radiative cooler for near-ambient temperature. During cooling power calculations, we have taken simplifying assumptions. Under practical scenarios, the net cooling power is expected to vary depending upon several factors such as humidity, cloudiness, geographical location, and so on [251]. Although we have not primarily focused on the thermodynamic aspect, we have carefully chosen stack materials with matched thermal and mechanical properties. This will ensure reduced mechanical strain during expansion or cooling down. Moreover, to have longevity and practical value, the stack layers should also offer resistance to ultraviolet radiation, high humidity, exposure to

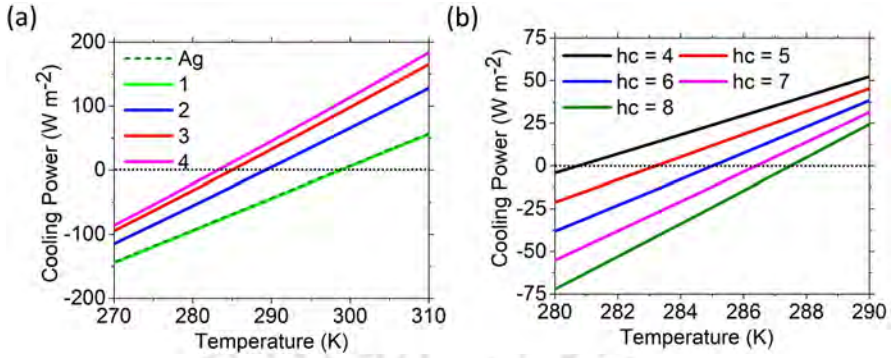

Figure 7.13: Net cooling power calculations for our passive radiative cooler with surface temperature (T_{PRC}) of the cooler for varying (a) number of layers and (b) parasitic heat load coefficient (h_{c}). In (a), 1: bottom AlN layer , 2: bottom SiO_2 layer, 3: top AlN layer, and 4: top SiO_2 layer.

direct sunlight, *etc*. In our multilayer design, we have chosen stable and chemically inert materials such as SiO_2 and AlN as the top alternating layers [252,253]. These materials are usually used as passivation layers in semiconductor fabrication processes. Therefore, the daytime passive radiative cooler proposed in this work could inherently exhibit superior mechanical robustness, thus assuring a long lifespan outdoors when exposed to exterior environment conditions [112].

Figure 7.13(a) shows the importance of each layer in enhancing the cooling power of our passive radiative cooler. With increase in the number of layers, the cooling power increases and reaches 115 Wm^{-2} for $h_{\mathrm{c}} = 5$. The equilibrium surface temperature (T_{PRC}) of the radiative cooler is calculated by equating the cooling power to zero. It can be inferred from Fig. 7.13(b) that the equilibrium surface temperature can decline up to 15K below the ambient temperature (T_{amb}) of 297K when h_{c} is set to 5. Moreover, the surface temperature of our passive radiative cooler can reach 60K below the ambient temperature when parasitic heat load coefficient is neglected. A comparison among recently reported daytime passive radiative cooler is shown in Table 7.3. It is evident that our proposed design offers the highest cooling power and temperature reduction below the ambient temperature, compared to some of the recently reported daytime

Table 7.3: Comparison between our proposed design and some of the recently reported daytime passive radiative coolers.[a,b]

Ref. (Year)	R_{avg} (0.3–2.5 μm)	A_{avg} (8–13 μm)	P_{cool} (Wm^{-2})	ΔT (K)
You *et al.* (2020) [256]	95	76	62	6.8
Mabchour *et al.* (2020) [257]	95	85	87	NA
Wang *et al.* (2021) [254]	98	70	110	7
Dai *et al.* (2021) [258]	NA	80–90	71	12
This Work	**97**	**80**	**115**	**15**

Note: [a] R_{avg} = average reflectance (in percentage) over solar spectral regime, A_{avg} = average absorbance (in percentage) over atmospheric transmittance window, P_{cool} = net cooling power, ΔT = temperature reduction below ambient temperature.
[b] Only simulation results are included in this table.

passive radiative coolers.

7.2.8 Effect of Different Polarizations and Incident Angles

It is important to understand that the incident solar radiation can be of any polarization and can fall at oblique angles due to the dynamically changing position of the sun with respect to the earth's surface. Therefore, to have practical utility, a passive radiative cooler design needs to be polarization- and angle-independent to some extent. Figure 7.14(a) shows absorbance spectra for both TM and TE polarization at a normal angle of incidence. The overlapping absorbance spectral response for both cases indicates that our passive radiative cooler design is polarization-insensitive. Further, in Figs. 7.14(b) and 7.14(c), we show colour contour plots for TM and TE case, respectively, for varying angle of incidence between 0 and 85 degrees. Fig. 7.14(d) shows radar plot for average absorbance (radial axes) in the atmospheric transmittance window (8–13 μm) for TM, TE, and unpolarized waves incident at different incident angles (circular axes). From Figs. 7.14(b)–7.14(d), it is clear that the absorption spectra show marginal variation with increase in the angle of incidence up to 70 degrees. The emis-

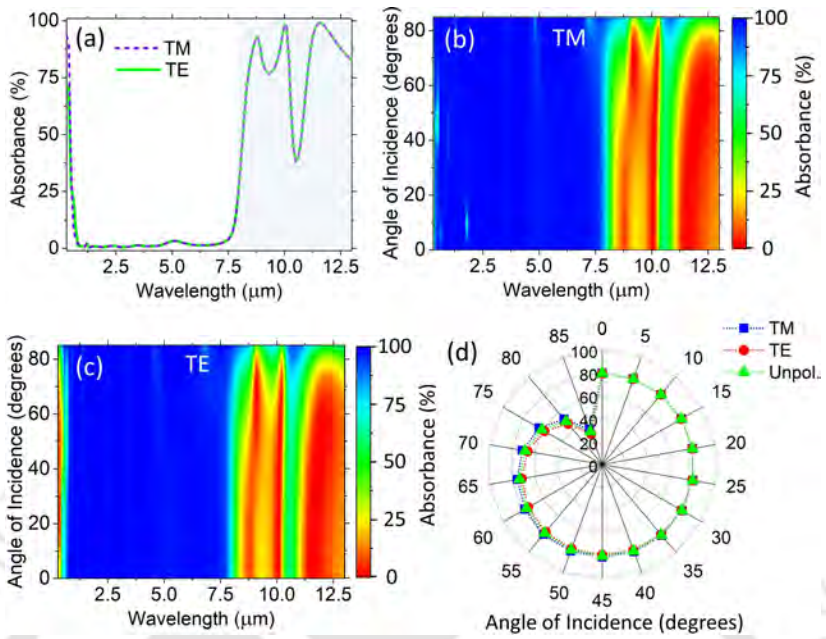

Figure 7.14: (a) Numerically calculated absorbance spectra for both TM and TE polarization at normal angle of incidence. Colour contour plots for (b) TM and (c) TE case, for the varying angle of incidence between 0 and 85 degrees. (d) Radar plot showing average absorbance (radially outward axes) in the atmospheric transmittance window (8–13 μm) for TM, TE, and unpolarized electromagnetic waves incident at different incident angles (clockwise circular axes).

sivity in the atmospheric transmittance window remains around 80% up to 60 degrees angle of incidence. However, at grazing angles (70 degrees and beyond), the absorption efficiency drops significantly. Hence, the above studies justify the practical utility of our choice of multilayer passive radiative cooler design which is polarization- and angle-independent up to 70 degrees of angle of incidence.

7.2.9 Prospective Fabrication Process and Tolerance Study

With the advancement in nanoscale fabrication technology, fabricating our thin-film multilayered passive radiative cooler should not be too difficult. First, a p-type (100) Si wafer of suitable thickness may be used as a substrate. Then an electron beam (e-beam) evaporation technique may be used depositing bottom Ag and AlN layers [118]. Next, the bottom SiO_2, top AlN, and top SiO_2 layers can be consecutively deposited *via* chemical vapour deposition (CVD) [112]. Here we emphasize that setting the right

Table 7.4: Fabrication tolerance study for our thin-film multilayered passive radiative cooler with ±5% change in the thickness of each layer.

PRC Layer (Thickness)	R_{avg} (0.3–2.5 μm)	A_{avg} (8–13 μm)	P_{cool} (Wm^{-2})
$t_1 + 5\%$	96.79	79.64	115.89
Top SiO_2 (t_1 = 355 nm)	96.52	79.60	115.68
$t_1 - 5\%$	94.77	79.53	115.13
$t_2 + 5\%$	94.61	79.49	111.09
Top AlN (t_2 = 850 nm)	96.52	79.60	115.68
$t_2 - 5\%$	96.47	79.63	108.52
$t_3 + 5\%$	95.96	79.49	106.82
Bottom SiO_2 (t_3 = 1550 nm)	96.52	79.60	115.68
$t_3 - 5\%$	96.65	79.48	112.18
$t_4 + 5\%$	96.46	79.60	114.63
Bottom AlN (t_1 = 10 nm)	96.52	79.60	115.68
$t_4 - 5\%$	96.08	79.60	114.28

Note: R_{avg} = average reflectance (in percentage) over solar spectral regime, A_{avg} = average absorbance (in percentage) over atmospheric transmittance window, P_{cool} = net cooling power.

temperature and deposition rate during the CVD deposition process is important to achieve smooth coating and avoid any damage to the underlying Ag layer. For optical characterization, UV-VIS-NIR spectrometer and Fourier-transform infrared spectroscopy (FT-IR) spectroscopy may be used to measure our passive radiative cooler's reflectivity over 0.3–2.5 μm and 2.5–13 μm spectral ranges, respectively [112, 115].

However, during fabrication, we believe that obtaining a smooth coating could be challenging, and minor surface roughness may arise, which could alter the estimated cooling power of our device. In Table 7.4, we show the tolerance study for our radiative cooler design with ±5% change in the thickness of each layer. The tolerance study unveils that the net cooling power of our radiative cooler shows marginal variation which is well within the acceptable limit, making our radiative cooler robust and less prone to fabrication imperfections.

7.2.10 Summary

We presented a design of daytime passive radiative cooler comprising four alternating dielectric layers of SiO_2, AlN, SiO_2, and AlN, on top of silver metallic layer placed on a silicon substrate. We could theoretically achieve **97.3% and 97.7% average reflection over solar regime (0.3–2.5 μm) and atmospheric radiation region (2.5–8 μm), respectively, while maintaining 80% emissivity in the atmospheric transparency window (8–13 μm)**. During the daytime under direct sunlight, **the net cooling power of our proposed daytime passive radiative cooler came out to be 115** Wm^{-2} with a temperature reduction up to 15K below the ambient temperature. When convective and conductive heat transfer contributions are neglected, we achieved **temperature reduction up 60K below ambient temperature**. Our design is polarization-insensitive and angle-independent up to 70 degrees of angle of incidence. Our theoretical results perfectly match with full-wave simulations, thus validating our findings. The fabrication tolerance study suggests that our design is robust and less prone to fabrication imperfections, indicating that cooling performance is unlikely to degrade much during practical realization. These passive radiative coolers may find potential application in energy-efficient buildings [122, 259], smart windows [141, 261], thermoelectric and thermophotovoltaic systems [260, 262], body thermal management textile [263], temperature-insensitive optoelectronic devices [264], and much more.

8

Conclusion and Future Scope

Contents

This chapter summarizes the thesis work, highlighting significant findings and contributions concerning modeling of nanophotonics and metamaterials based tunable optical devices for selectively filtering and harvesting solar radiation. Section 8.1 discusses a summary of the contributions. Section 8.2 concludes the chapter by jotting down the potential directions for future research.

8.1 Summary of Contributions

This thesis work aims to utilize nanophotonics and metamaterials based tunable optical devices for smart window design and solar energy harvesting. Chapter 1 introduced the outline of the thesis discussing the motivation, methodology, scope of this work, the major contributions of this thesis, and thesis organization. Chapter 2 presented a literature review relevant to the field of nanophotonics and metamaterials, followed by discussion on the theoretical background required for carrying out this work; and a couple of numerical techniques that would help to solve complex Maxwell equations and boundary conditions. Chapter 3 discussed the first objective of this thesis, *i.e.*, to design climate-specific passive windows capable of selectively filtering visible and infrared radiations. The designs were mainly based on metal–insulator–metal multilayer thin-films as these are lithography-free and hence, large-area compatible. However, passive windows once fabricated cannot be tuned to different weather-specific needs. To solve this problem, chapter 4 presented the second objective, *i.e.*, to design all-weather electrotunable windows. To begin with, a design of metal–insulator–metal multilayer thin-films based electrotunable window is discussed that can dynamically control the intensity of transmitted solar radiation, depending upon the weather condition. Then a low-power design of electrotunable, absorption- and transmission-mode color filters is presented for application as electrochromic windows.

Keeping in mind the current state-of-the-art nanofabrication technology, we ex-

plored alternative designs of passive and electrotunable windows presented in chapters 3 and 4, respectively, which would allow the use of a thicker metal film that would be easier to fabricate. Chapter 5 proposed designs of static and electrotunable 'smart' windows based on insulator–metal–insulator multilayer thin-films, followed by a comparative study between those. Chapter 6 presented the third objective, *i.e.*, to design broadband metamaterial absorbers for solar energy harvesting. This chapter investigated a plasmonics based broadband metamaterial absorber in a 400–1100 nm spectral window—a one-dimensional grating-based wide-angle and ultrabroadband metamaterial absorber in a 400–2500 nm spectral range and a two-dimensional grating based ultrabroadband 'perfect' metamaterial absorber over a wider spectral regime of 300–4500 nm. These absorbers have implications in solar cells and thermophotovoltaics. Finally, chapter 7 addressed the last objective of this thesis related to utilization of the waste solar heat, *i.e.*, to design spectrally-selective solar absorbers that can harness solar energy as heat and convert it into thermal energy, and to design passive radiative coolers which pump excess heat to cold exterior space *via* thermal radiation. The whole idea of this thesis revolves around designing transmission- and absorption-mode spectrally-selective filters for smart windows and solar energy harvesting.

This Ph.D. work is a small step towards fighting a bigger problem of global warming. The major contributions of this thesis have been accepted/published in prestigious international peer-reviewed journals and also were presented in renowned international conferences in the emerging field of nanophotonics and metamaterials. A summary outlining the major contributions towards fulfilling the research objectives is given below:

- **Nanoring Based 'Meta-glass' as Passive Windows:**

  In the first section of chapter 3, we presented a novel plasmonic 'meta-glass' as infrared-blocking nanophotonic windows that could block up to ∼87% infrared

radiation over 750–1800 nm spectral range while maintaining 60% average transmission in the visible regime. We achieved an infrared transmittance as low as 0.16 and a contrast ratio as high as 3.75, indicating that our proposed plasmonic glasses could outperform recently reported industry-standard window glasses. By virtue of surface plasmons excitation in the infrared regime, we could achieve selective suppression in the transmission spectrum, which is tailorable by adjusting the dimension of the nanorings. The simulation results obtained using finite element method and finite difference time domain solvers are in good agreement. Our designs are low-cost, easy to fabricate, polarization- and angle-insensitive to a large extent. These plasmonic meta-glasses based on relatively inexpensive material could be useful in places with warm climates. These findings were reported in '*Optics Letters*'.

- **Nanoparticles Based Passive Windows:**

  In the second section of chapter 3, we presented a design of meta-glasses capable of blocking ultraviolet and infrared radiations efficiently. By introducing different choices of metallic nanoparticles inside the dielectric layer of a metal–dielectric–metal cavity, we could achieve more than 90% UV and IR blocking while maintaining 60% visible transmittance. Our thin-film coatings may be applied on vehicle windows to provide ambient indoor temperature and brightness and improve the vehicle's performance. These findings are submitted to '*IEEE 9th International Conference on Photonics (ICP) 2022*'.

- **Multilayer Thin-film Based Nanophotonic Passive Windows:**

  In the third section of chapter 3, we theoretically demonstrated metal–insulator–metal thin-film based passive windows for controlling the amount of transmitted visible and infrared radiation, depending upon different specific climate conditions. We explored noble metals (Au, Ag, Cu) alongside alternative materials

(ITO, AZO, and ALON) to provide a cheaper alternative to commercially available windows. The figure of merit obtained for our passive glasses using relatively inexpensive materials (such as Ag, Cu, ITO, AZO, and ALON) outperform industry-standard commercial windows and previously reported infrared-blocking plasmonic glasses. The theoretical results obtained using transfer matrix method and Fabry–Perot interferometer technique perfectly match those of finite element method based full-wave numerical simulations. Our design is simple, lithography-free and hence large-area compatible, ultra-thin, polarization-independent, and angle insensitive (up to 83 degrees). These passive glasses can be integrated into security panels, privacy windows, advertising screens, room partitions, electronic curtains, and solar control skylight panels. Aluminium oxynitride based window glasses are suitable for high performance, portable, bulletproof, and blast-resistant windows that can be used in high security buildings, military vehicles, fighter aircrafts, and submarine applications. The findings were published in the journal '*Applied Optics*'.

- **Nanophotonic Passive Windows as Color Filters:**
  In the last section of chapter 3, we theoretically demonstrated designs of metal–dielectric–metal based blue and red transmission-mode color filters, which could be crucial for applications in greenhouses. The peak transmission of two passive filters A and B were optimized to perfectly match the wavelength of peak absorption spectra for chlorophyll A and B at 430 nm and 662 nm, respectively. Our theoretical results agree well with the simulation findings. Our design is ultra-thin, easy to fabricate, lithography-free, large-area compatible, polarization-independent, and angle-insensitive up to 80 degrees of angle of incidence. For practical application, designs of blue and red transmission-mode color filters can be individually coated on the exterior or interior surface of adjacent glasses in a greenhouse.

Greenhouses coated with these spectrally selective passive color filters could reduce the maturation period of plants by enhancing the rate of photosynthesis. Reduced maturation period will eventually bring sustainability by reducing the carbon footprint of heating and cooling systems used in greenhouses. The findings were presented in '*IEEE Photonics Conference (IPC) 2021*'.

- **All-weather Electrotunable Windows:**
  In the first section of chapter 4, we presented a theoretical design of metal–dielectric–metal based electrotunable smart glasses for dynamically controlling the amount of transmitted solar radiation depending on weather conditions. We explored noble metals as well as their relatively inexpensive alternatives as metallic layers. An electro-optic polymer is used as a dielectric layer to make the system tunable by using a bias voltage ranging from −15 V to +15 V. The figure-of-merit calculations show that our relatively inexpensive materials (Ag, Cu, ITO, AZO, and ALON) can outperform industry-standard commercial glasses and previously reported infrared-blocking plasmonic glasses. Our design is robust, low-cost, ultra-compact (60–100 nm thick), lithography-free, large-area compatible, polarization-independent, and angle-insensitive (up to 75 degrees). Our theoretical results obtained using transfer matrix method, transmission line method, and Fabry–Perot interferometer technique agree well with those of finite element method based full-wave simulations which validate our results. These ultra-thin smart glasses can be integrated into privacy windows, security panels, solar control skylight panels, *etc*. Aluminium oxynitride based glasses can be used in fighter aircraft, military vehicles, high security buildings, and submarine applications. The research was published in a top-ranked journal '*Solar Energy Materials and Solar Cells*'.

- **Tunable Colour Filters as Electrochromic Windows:**

  We presented a theoretical design of electrotunable absorption- and transmission-mode colour filter based on metal–dielectric–metal (MDM) structure. We illustrated the design of three colour filters (blue, green, and red) to show that only ± 10 V power supply should be sufficient to realize any intermittent colour filter in the visible regime. Our theoretical results obtained using transfer matrix method and transmission line method agree well with those of finite-element-method based full-wave simulations, which validates our results. For practical realization, our design is power-efficient, large-area compatible, lithography-free, angle-insensitive, polarization-independent, and has extremely narrow-bandwidth. The results were reported as an article in '*Journal of the Optical Society of America B*'.

- **Alternative designs of Static and Electrotunable Windows:**

  In chapter 5, we presented insulator–metal–insulator multilayer thin-films based designs of static and electrotunable 'smart' windows, followed by a comparative study between those. Our design is robust, lithography-free, large-area compatible, polarization-independent, and angle-insensitive up to 80 degrees of oblique incidence. Our theoretical results are in close agreement with simulation findings. The theoretically calculated figure of merit indicates that our static and electrotunable smart windows could be a better value proposition than industry-standard commercial windows. In addition, we obtained a better contrast ratio for diverse climatic conditions that could significantly improve the efficiency of smart windows. Our size-dependence analysis revealed that the performance of our smart windows is unlikely to degrade during practical realization. We found that the optical response remained unaltered when the insulator–metal–insulator thin-film was coated on the inside or outside the silica glass substrate. We have

also shown that a multilayer coating may be used to block the harmful ultraviolet radiation completely. Detail of the prospective fabrication technique is provided to show the experimental feasibility. These findings were reported in '*Journal of Optics*'.

- **Plasmonics Based Broadband Metamaterial Absorbers:**
  In the first section of chapter 6, we investigated the design of cross–ring based broadband plasmonic metamaterial absorber. An average absorption of 96.9% is achieved over 400–1100 nm wavelengths with a peak absorption of 99.9% at 750 nm wavelength—perfectly matching the wavelength of peak absorption by silicon solar cell [147]. A close agreement between absorption spectra obtained using finite difference time domain solver and finite element method solver validates our findings. Our design is polarization-independent and provides 90% average absorption up to 75 degrees of oblique incidence angle. Practically, these thin-film broadband absorbers can be integrated into photovoltaics modules for enhancing efficiency of silicon as well as organic solar cells [137,142]. These findings were presented in '*15th International Congress on Artificial Materials for Novel Wave Phenomena - Metamaterials 2021*'.
- **1D-Grating Based Ultrabroadband Metamaterial Absorbers:**
  In the second section of chapter 6, we designed and simulated an ultrabroadband absorber based on a one-dimensional periodic array of metallo-dielectric alternating multilayered tapered structure. It can absorb radiation over the whole visible and near-infrared spectrum, ranging from 400–2500 nm, *i.e.*, over entire solar spectrum. The average absorption of 98.2% was achieved by 20 pairs of alternating molybdenum–germanium based tapered structure. The absorbance was further enhanced to over 99% using more number of metallo-dielectric layers (64 pairs). The broadband absorption is attributed to multiple slow-wave

modes getting absorbed at different layers. The trapped rainbow effect and the anti-reflection effect together give broadband absorbance with high efficiency. Additionally, our simulation model shows angle insensitivity up to 60 degrees. Absorbance spectra, obtained from effective medium theory, agree well with our simulation results. Our presented work can be utilized in a wide range of applications such as solar energy harvesting, thermophotovoltaics, stealth technology, camouflage, and thermal emitters. The findings were presented in '*2019 Workshop on Recent Advances in Photonics (WRAP)*'.

- **2D-Grating Based Ultrabroadband Metamaterial Perfect Absorbers:** In the last section of chapter 6, we presented an ultra-broadband 'perfect' absorber consisting of a 2D array of hemi-ellipsoid shaped metallo-dielectric (MD) multilayered structure, due to lateral symmetry this design is polarization-insensitive, which was not achieved in the previous design using 1D array. An unprecedented average absorbance of $\sim$99% is achieved at normal incidence between 300 nm and 4500 nm spectral range. We used 20 pairs of molybdenum–germanium MD layer, with tungsten as ground metal. The ultra-broadband absorption is attributed to the anti-reflection effect (for $\lambda < 1500$ nm) and the trapped rainbow effect (for $\lambda > 1500$ nm). Our design is polarization-independent as well as angle-insensitive (up to 60 degrees). Our theoretical calculations agree well with those of full-wave simulation results. A perspective fabrication methodology and fabrication-imperfection tolerance study are also shown for the practical realization of our proposed design. The figure-of-merit calculations show that our 'perfect' absorber can outperform some of the broadband absorbers, recently reported in the literature. A potential application of our presented broadband metamaterial absorber includes integration into solar devices for solar energy harvesting using thermophotovoltaics. The research was published in '*Journal of*

the Optical Society of America B'.

- **Selective Solar Absorbers for Waste Heat Management:**

  In the first section of chapter 7, we theoretically presented a design of multilayer thin film based selective solar absorbers (SSAs) for solar thermal engineering applications. Our polarization- and angle-insensitive design offers 87% solar-to-thermal energy conversion efficiency with a total absorbed power of 889.4 $\mathrm{Wm^{-2}}$ when the temperature of the solar absorber is at 100°C. The absorption coefficient achieved is 0.90 and the emission coefficient is reported to be 0.04. Our proposed solar absorber manifests a stagnation temperature of 378°C. A perfect match between our theoretical and simulation results validates our findings. A detailed prospective fabrication technique is discussed to show the feasibility of the proposed design. Our proposed SSA could be useful in larger-scale engineering applications such as electricity generation, water desalination, air conditioning, industrial heating, just to name a few. The obtained results were published in '*IEEE Transactions on Nanotechnology*'.

- **Thermal Emitters for Passive Daytime Radiative Cooling:**

  In the second section of chapter 7, we presented a design of daytime passive radiative cooler (PRC) comprising four alternating dielectric layers of $\mathrm{SiO_2}$, AlN, $\mathrm{SiO_2}$, and AlN, on top of silver metallic layer placed on a silicon substrate. We could theoretically achieve 97.3% and 97.7% average reflection over solar regime (0.3–2.5 μm) and atmospheric radiation region (2.5–8 μm), respectively, while maintaining 80% emissivity in the atmospheric transparency window (8–13 μm). During the daytime under direct sunlight, the net cooling power of our proposed daytime PRC came out to be 115 $\mathrm{Wm^{-2}}$ with a temperature reduction up to 15 K below the ambient temperature. When convective and conductive heat transfer contributions are neglected, we achieved temperature reduction up 60K

below ambient temperature. Our design is polarization-insensitive and angle-independent up to 70 degrees of angle of incidence. Our theoretical results perfectly match with full-wave simulations, thus validating our findings. The fabrication tolerance study suggests that our design is robust and less prone to fabrication imperfections, indicating that cooling performance is unlikely to degrade much during practical realization. Our PRCs could be useful for applications in thermal power plants, smart windows, energy-efficient buildings, optoelectronic devices, to name a few. The results were reported as an article in '*Journal of Physics D: Applied Physics*'.

8.2 Suggestions for Future Work

So, the question remains: how will smart windows improve in the near future? Imagine a window that captures some portion of the solar energy falling on them during the day and store it in batteries that can power lights inside our home at night, as depicted in Fig. 8.1. With the help of this unique approach, we will now be able to control not only the amount of light and heat coming inside our homes and cars but also store the energy absorbed by the metamaterial absorbers which is otherwise wasted.

To accomplish this, we can integrate our broadband metamaterial absorbers with the thermoelectric generators. Using the Seebeck effect, we can utilize the absorbed heat from this highly efficient absorber and convert it into electrical energy. An artistic representation of the proposed design is shown in Fig. 8.2. Although the efficiency is relatively low considering the energy conversion using the Seebeck effect, imagine a bigger picture of a building and storage facility of food grains, where thousands of glass windows are installed. We may make a significant impact by saving a small amount of energy absorbed from each window. The harvested energy will be sufficient to serve our practical day-to-day applications such as lighting a bulb, charging a power

Figure 8.1: Artistic view of charging a smartphone by absorbing the heat through smart windows and converting heat into useful electrical energy [265, 266].

bank or a cell phone *etc*. Hence, we can take a small step towards a noble cause of promoting a greener tomorrow. Apart from these, there are many aspects of future works which are summarized below:

- Concerning passive window designs, there is a need for better optimization of thin-film structures using multiple metal–dielectric stacks. There is a possibility to explore some more unconventional alternative plasmonic materials that could bring down the overall cost while maintaining design aesthetics and durability. To address the UV part of the solar spectrum, TiO_2 or ZnO nanoparticles of a specific dimension may be introduced inside the transparent glass to block the UV spectrum completely. We may also look for electro– or thermo–optic materials that can provide real-time tunability *via* electrical or thermal energy supply, respectively.
- For electrotunable window designs, we have used 4-dimethyl-amino-N-methyl-

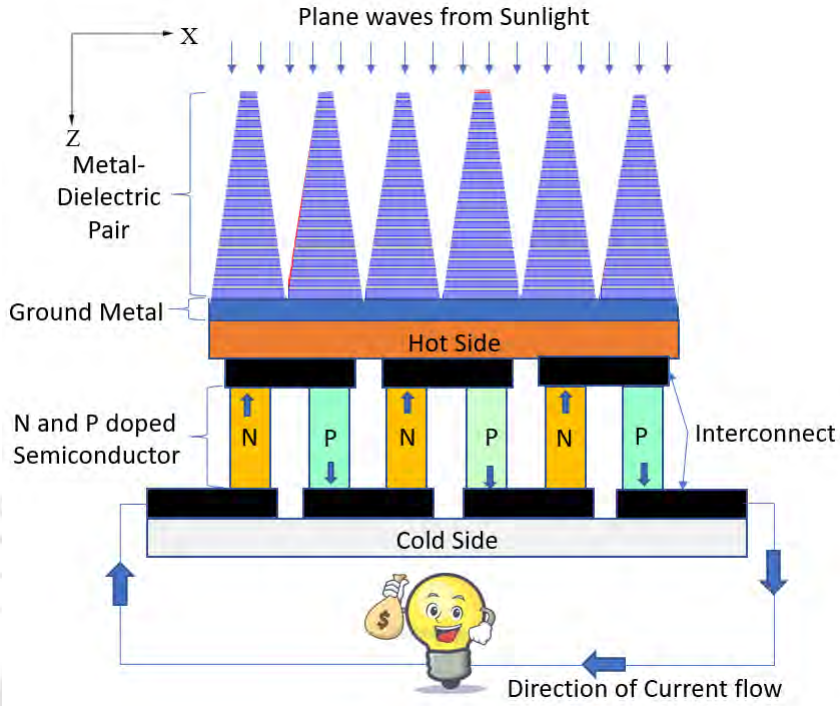

Figure 8.2: Pictorial demonstration of waste heat management by integrating broadband plasmonic absorber with thermoelectric generator.

4-stilbazoliumtosylate (DAST) polymer as an electro–optic (EO) material. This polymer possesses one of the largest EO coefficients among all those organic crystals available today. DAST also has a large melting point (259 °C), a large electrical bandwidth, and exhibits stability up to 250 °C. However, it is desirable to look for other alternative EO materials that have certain optical absorption in the non-powered state to achieve different modes as per the requirement of the geographical location. It is equally important that EO material exhibits matched mechanical as well as thermal properties. This will ensure that its thermal expansion coefficient closely matches the metals used in the metallo-dielectric multilayered glasses, therefore reducing the mechanical strain during expansion or cooling down. To have longevity and practical value, the EO material should also offer resistance to ultraviolet radiation, high humidity, exposure to direct sunlight, *etc*.

- For thermochromic smart window designs, there is a need to explore phase change materials (PCMs), such as GeSbTe (GST) and vanadium dioxide (VO_2), which could play an important role in dynamically tuning the optical devices [177]. For smart window applications, the typical transition temperature of VO_2 is too high (68°C). However, doping can bring the transition temperature down to room temperature.
- Apart from application in thermophotovoltaics, our broadband absorber may also be used for photodetection. This may help in detecting photons below the bandgap of the semiconductor. Besides, enhanced light absorption can be achieved due to the confinement of the electromagnetic waves inside the metamaterial absorber.

A

Appendix

A.1 Electrical Engineering of the Voltage Control for Electrotunable Windows

Figure A.1 depicts a scheme for electrical connections in MIM thin-film based smart windows. Using this circuit connection, the end-user can manually control smart window functionality by just switching between −15V, 0V, and +15V. For instance, when the switch is at +15 V, the window will block the light and allow the heat to pass through it *i.e.* dark and warm mode. Whereas when the switch is at −15 V, the window will allow light to pass through it but block the heat *i.e.* bright and cool mode. If we want our smart window to operate as an ordinary window, the switch should be at 0V to allow both light and heat to pass through the window, *i.e.* bright and warm mode.

For smart window design, the major challenge lies in the durability of such windows compared to ordinary windows. For long-term durability, the stack layers of MIM structure should be protected from exposure to direct sunlight, high humidity,

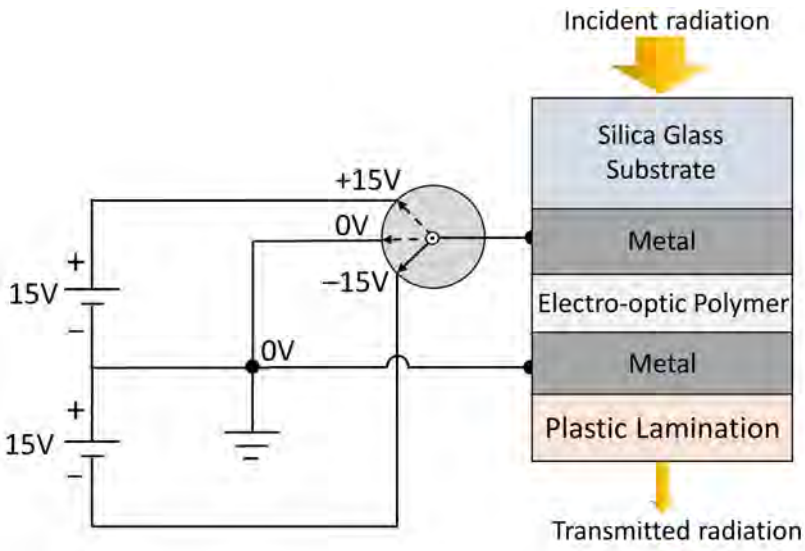

Figure A.1: A proposed scheme for electrical connections in MIM thin-film based smart windows. Two 15V batteries connected in series, with the common terminal grounded and connected to the switch and bottom metallic layer. The smart window can operate in three possible modes by changing the switch position between −15V, 0V, and +15V.

ultraviolet radiation, *etc*. To overcome this challenge, MIM thin-film can be coated on the inside of the window glass, as shown in Fig. A.1. Further, they need to be laminated with a plastic film to prevent liquid splashes, dust, scratches, electrical short-circuits and thus increasing the life span of these smart windows.

A.2 Detailed physics of the Electric Field Effects

The electric field distributions inside MIM thin-film based smart window corresponding to the resonance wavelength is shown below in Fig. A.2. One can clearly see that electric field is mainly concentrated inside the dielectric layer at the resonance wavelength. On applying the bias voltage, the magnitude of the electric field decreases inside the dielectric layer because of the shift in the resonance frequency due to a change in the refractive index of the electro-optic polymer, used as an insulator layer. Therefore, changing the bias voltage makes it possible to tune the peak transmission at the wavelength of interest.

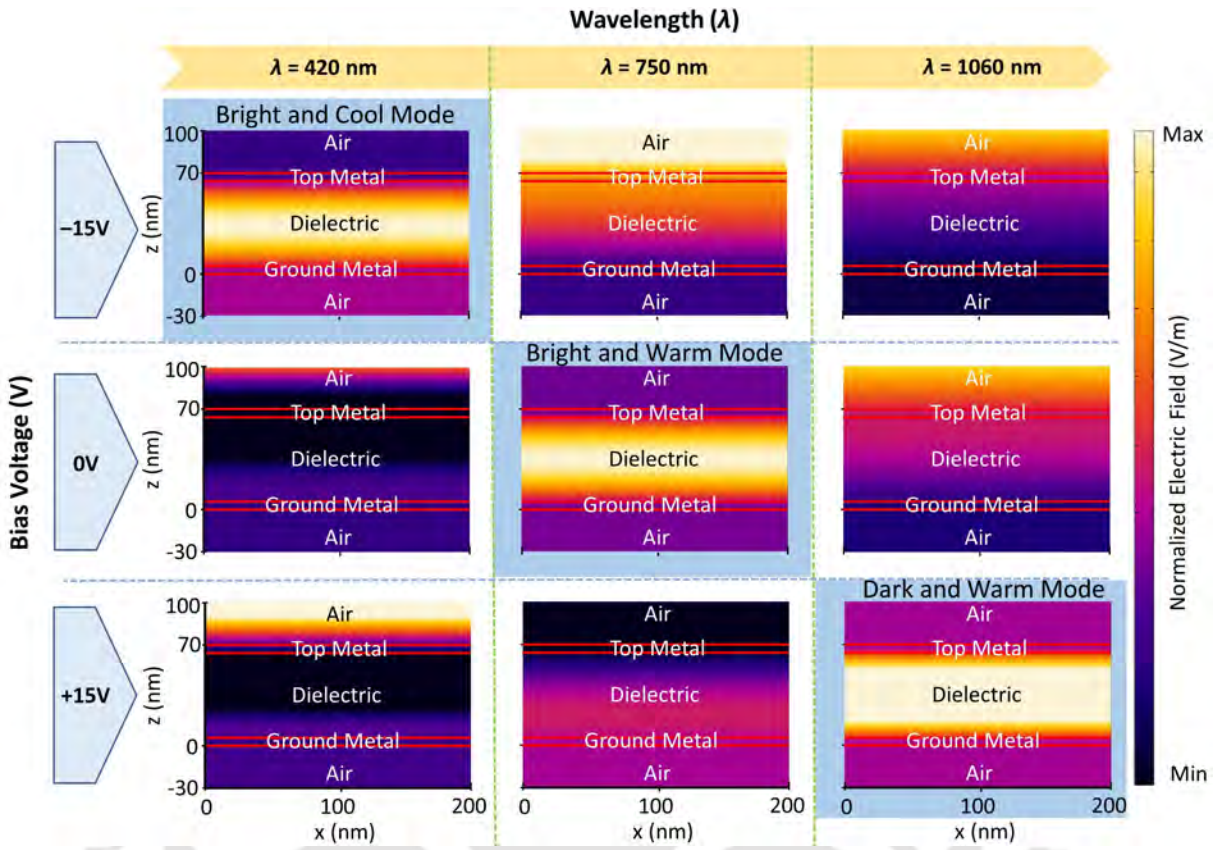

Figure A.2: Electric field distributions inside MIM thin-film based smart windows: normalized electric field (**E**) distributions corresponding to the resonance wavelength ($\lambda_0 = 420$ nm at -15V, $\lambda_0 = 750$ nm at 0V , and $\lambda_0 = 1060$ nm at $+15$V). Here the top and ground metallic layers are composed of silver of 5 nm thickness, and 60 nm thick electro-optic polymer (DAST) is used as the dielectric layer.

A.3 Experimental Realization of Passive Windows

For proof of the concept, we first started with fabrication of a passive window of 1 sq. inch area based on glass–metal–insulator–metal configuration. Figure A.3 shows three architecture designs selected to be fabricated. After successful realization of a lab scale prototype, we planned to scale up to 1 sq. foot, 1 sq. meter, and so on depending upon the outcome at each stage. After testing the durability and scalability, we have plans to go for industry scale production. Once the passive glasses are successfully realized and tested, we can go ahead to fabricate electrotunable windows depending upon the availability of the electro–optic polymer material.

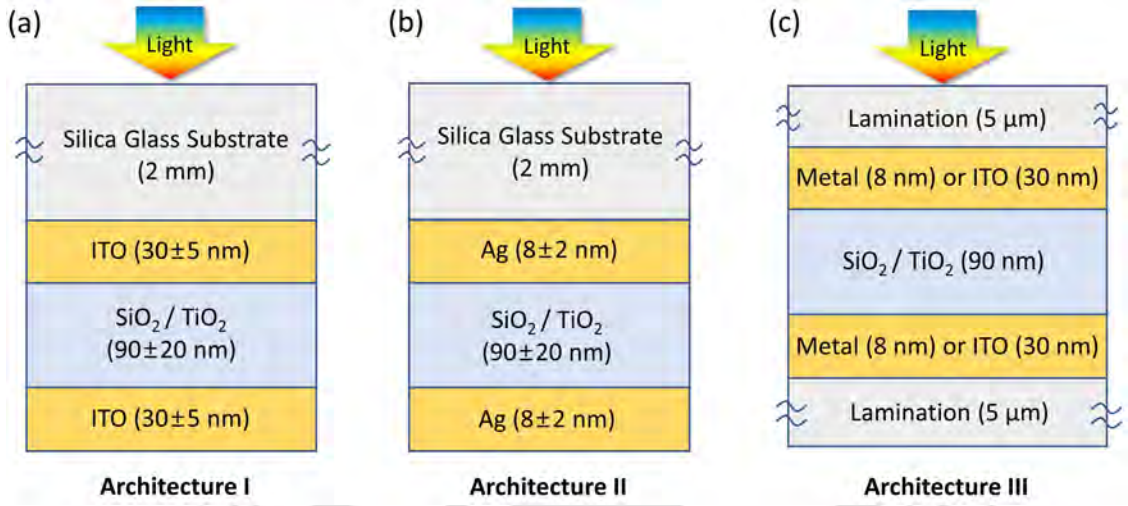

Figure A.3: Three architecture designs to be fabricated: (a) architecture I: passive windows glasses based on indum tin oxide (ITO), (b) architecture II: passive windows glasses based on silver (Ag), and (c) architecture III: rollable thin film coatings for ordinary windows. The dimensions with design tolerance are specified within parenthesis.

Currently, we are working towards depositing metal–insulator–metal thin-films over a glass substrate (architecture I) using RF magnetron sputtering at the Department of Physics, IIT Guwahati. In this direction, we performed some preliminary experiments, including UV-VIS spectroscopy, field-emission scanning electron microscopy (FESEM), profilometry for ITO coated glass. Different steps of the experimental work are presented in the following sections.

A.4 ITO Coated Glass Cleaning & UV-VIS Spectroscopy

A step-by-step procedure of ITO cleaning and UV-VIS spectroscopy measurement is depicted in Fig. A.4. We first took ITO coated glass (with ITO being 200 nm and silica glass being 1 mm thick) and cut them into pieces to get two glass slides, each of four sq. cm area. Then we cleaned those glass slides using detergent, followed by 15 minutes of sonification. The cleaning procedure was repeated using acetone and isopropanol, then sonification for 10 to 15 minutes. After that, the wet sample glass was dried using a standard hairdryer. Next, we performed UV–VIS spectroscopy by

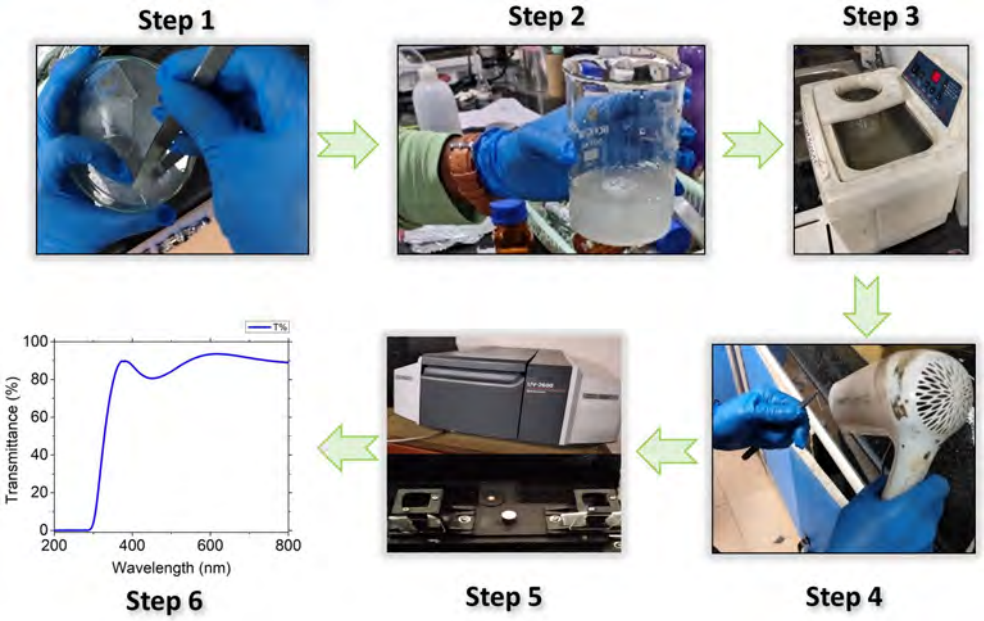

Figure A.4: Procedure for ITO cleaning steps and UV-VIS-Spectroscopy measurement procedure carried out at the Center for Nanotechnology and Department of Physics, IIT Guwahati.

placing the sample and slides in the holder, as shown in step 5 of Fig. A.4. Finally, we measured the transmittance over 200–800 nm spectral window. These measurements were carried out at the Center for Nanotechnology and the Department of Physics, IIT Guwahati.

A.5 Thickness measurement for Etched ITO coated Glass

A step-by-step procedure adopted for thickness measurement for etched ITO coated glass using Profilometer is shown in A.5. First, ITO coated glass was etched out using zinc dust and concentrated hydrocloric acid. Then, a similar cleaning and drying approach was adopted as mentioned in the previous section. For thickness measurement of the ITO coating, we used a profilometer at the Department of Physics, IIT Guwahati. This instrument helps to measure the thickness by moving the cantilever over the placed sample and generating a plot for its thickness profile. Then by finding the difference between the heights of the places with and witout the ITO coating, we found

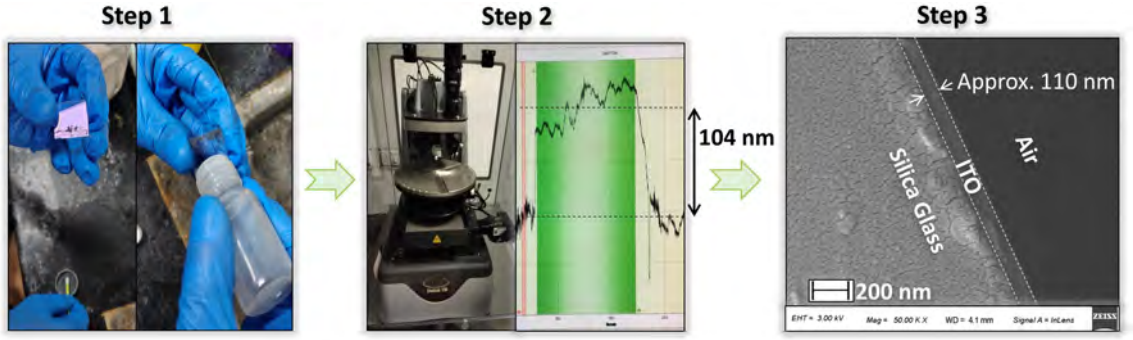

Figure A.5: Procedure for thickness measurement for etched ITO coated glass using profilometer at the Department of Physics and field-emission scanning electron microscopy (FESEM) at the Central Instrument Facility (CIF), IIT Guwahati.

the thickness to be approximately 104 nm. Further, to verify this thickness, we also used FESEM at the Central Instrument Facility (CIF), IIT Guwahati, to measure the thickness by taking cross-sectional images, as shown in Fig. A.5. The approximate thickness came out to be 110 nm, which is close to the thickness measured by the profilometer.

A.6 Validation of Preliminary Experimental Results using Theoretical Modeling

We now compare the experimental results obtained for ITO coated glass in section A2 of the appendix with our theoretical modeling to validate the experimental findings. For theoretical modeling we use transfer matrix method to obtain transmittance over 400–800 nm spectral window, as shown in Fig. A.6(a). Here, one may notice oscillations in the transmittance spectrum, which is due to wave interference when a thin-film of ITO is coated over a thick glass substrate [267]. However, during the experiment, the oscillations produced by interference in a thick substrate are liquidated, and only the curve close to that obtained using curve fitting will be observed experimentally. Hence, we took a polynomial fit for the theoretical data [see Fig. A.6(a)] and plotted it against the experimental data, as shown in Fig. A.6(b). The experimentally

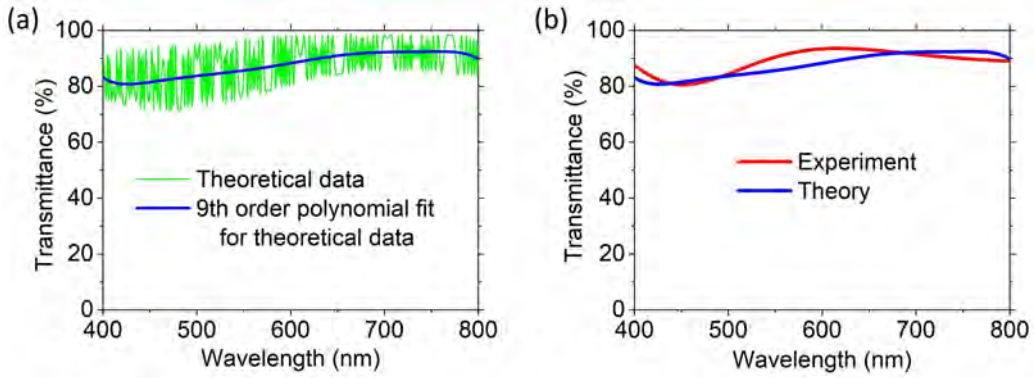

Figure A.6: Transmittance spectrum for ITO (200 nm thick) coated over a silica glass substrate (1 mm thick): (a) theoretical data with polynomial fit and (b) comparison between experimentally and theoretically obtained transmittance spectra.

and theoretically calculated average transmittance came out to be 88.8% and 87.6%, respectively. A close match between experimental and theoretical findings validates our initial findings. From these encouraging preliminary results, one may expect all experiments to closely follow our theoretical predictions made for smart window design.

Bibliography

[1] "Indian energy portal," http://www.indiaenergyportal.org/subthemes.php?text=solar (accessed: February 8, 2021).

[2] D. Sannigrahi, *Major Issues on Beneficial Utilization of Solar Energy in India*, In: Hussain C. (eds) Handbook of Environmental Materials Management, Springer, Cham (2019).

[3] "Solar irradiance A.M 1.5 spectrum," https://www.nrel.gov/grid/solar-resource/spectra-am1.5.html, (accessed: August 04, 2021).

[4] A. Cannavale, U. Ayr, F. Fiorito, F. Martellotta, "Smart electrochromic windows to enhance building energy efficiency and visual comfort," Energies **13**, 1449 (2020).

[5] H. Khandelwal, *Infrared regulating smart windows*, PhD thesis, Department of Chemical Engineering and Chemistry, 2017.

[6] A. K. Chowdhary, V. A. Reddy, and D. Sikdar, "Selective thermal emitters for high-performance all-day radiative cooling," J. Phys. D: Appl. Phys. **55**, 085504 (2022).

[7] "Seven Sun Windows - Insulating Glasses," http://www.sevensunwindows.com/windows/replacement/glass (accessed: March 08, 2021).

[8] "Double-glazed, High-solar-gain Low-E Glass," https://www.efficientwindows.org/gtypes_2lowe.php (accessed: February 23, 2021).

[9] N. Dean, "Colouring at the nanoscale," Nat. Nanotechnol. **10**, 15–16 (2015).

[10] Z. Yang, Y. Chen, Y. Zhou, Y. Wang, P. Dai, X. Zhu, and H. Duan, "Microscopic interference full-color printing using grayscale-patterned Fabry–Perot resonance cavities," Adv. Opt. Mater. **5**, 1700029 (2017).

[11] F. Liu, H. Shi, X. Zhu, P. Dai, Z. Lin, Y. Long, Z. Xie, Y. Zhou, and H. Duan, "Tunable reflective color filters based on asymmetric Fabry–Perot cavities employing ultrathin Ge2Sb2Te5 as a broadband absorber," Appl. Opt. **57**, 9040–9045 (2018).

[12] "Smart Glass and Windows 2018-2028: Electronic Shading and Semi-Transparent PV," https://www.idtechex.com/en/research-report/smart-glass-and-windows-2018-2028-electronic-shading-and-semi-transparent-pv/601 (accessed: July 2021)

[13] B. Zhao, M. Hu, X. Ao, N. Chen, and G. Pei, "Radiative cooling: A review of fundamentals, materials, applications, and prospects," Appl. Energy **236**, 489–513 (2019).

[14] X. Liu, S. Pian, R. Zhou, H. Shen, X. Liu, Q. Yang, and Y. Ma, "Tunable radiative cooling based on a stretchable selective optical filter," J. Opt. Soc. Am. B **37**, 2534–2537 (2020).

[15] B. E. A. Saleh and M. C. Teich, *Fundamentals of Photonics*, Wiley, New York, (1991).

[16] V. M. Shalaev (2013), "ECE 695S Lecture 10: The Exciting Science of Light with Metamaterials I," https://nanohub.org/resources/19581 (accessed: March 2019)

[17] Y. Cui, Y. He, Y. Jin, F. Ding, L. Yang, Y. Ye, S. Zhong, Y. Lin, and S. He, "Plasmonic and metamaterial structures as electromagnetic absorbers," Laser & Photonics Reviews **8**, 495–520 (2014).

[18] S. A. Maier, *Plasmonics Fundamentals and Applications*, Springer, 2007.

[19] L. Sun, P. Chen, and L. Lin, "Enhanced molecular spectroscopy via localized surface plasmon resonance, applications of molecular spectroscopy to current research in the chemical and biological sciences," 2016. (accessed: august 2019)

[20] G. V. Naik, V. M. Shalaev, and A. Boltasseva, "Alternative plasmonic materials: Beyond gold and silver," Advanced Materials **25**, 3264–3294 (2013).

[21] L. Escoubas, M. Carlberg, J. L. Rouzo, F. Pourcin, J. Ackermann, O. Margeat, C. Reynaud, D. Duche, J. J. Simon, R. M. Sauvage, and G. Berginc, "Design and realization of light absorbers using plasmonic nanoparticles," Prog. Quant. Electron. **63**, 1–22 (2019).

[22] S. Ogawa and M. Kimata, "Metal-insulator-metal-based plasmonic metamaterial absorbers at visible and infrared wavelengths: a review", Materials **11**, 1–18 (2018).

[23] W. Cai and V. Shalaev, *Optical Metamaterials*, Springer, (2010).

[24] F. Capolino, *Theory and Phenomena of Metamaterials*, Boca Raton, FL,USA: CRC Press, (2009).

[25] P. Yu, L. V. Besteiro, Y. Huang, J. Wu, L. Fu, H. H. Tan, C. Jagadish, G. P. Wiederrecht, A. O. Govorov, and Z. Wang, "Broadband metamaterial absorbers," Adv. Optical Mater. **7**, 1800995 (2019).

[26] H. Hajian, A. Ghobadi, B. Butun, and E. Ozbay, “Active metamaterial nearly perfect light absorbers: a review," J. Opt. Soc. Am. B **36**, F131–F143 (2019).

[27] J. Rhee, Y. Yoo, K. Kim, Y. Kim, and Y. Lee, “Metamaterial-based perfect absorbers," Journal of Electromagnetic Waves and Applications **28**, 1541–1580 (2014).

[28] C. M. Watts, X. Liu, and W. J. Padilla, “Metamaterial electromagnetic wave absorbers," Advanced Materials **24**, OP98–OP120 (2012).

[29] W. Li and S. Fan, “Nanophotonic control of thermal radiation for energy applications," Opt. Express **26**, 15995–16021 (2018).

[30] K. B. Alici, F. Bilotti, L. Vegni, and E. Ozbay “Metamaterial based microwave devices" in Proc. 3rd Int. Congress Adv. Electromagn. Mater. Microw. Opt, 363–365 (2009).

[31] Y. Ke, C. Zhou, Y. Zhou, S. Wang, S. H. Chan, Y. Long, “Emerging thermal-responsive materials and integrated techniques targeting the energy-efficient smart window application," Adv. Funct. Mater. **28**, 1800113 (2018).

[32] “2009 RECS Survey Data, Consumption & Expenditures (C&E) Tables." https://www.eia.gov/consumption/residential/data/2009/index.php?view=consumption (accessed January 29, 2021)

[33] S. C. Nunes, S. M. Saraiva, R. F. P. Pereira, S. Pereira, M. M. Silva, L. D. Carlos, E. Fortunato, R. A. S. Ferreira, R. Rego, and V. de Z. Bermudez, “Sustainable dual-mode smart windows for energy-efficient buildings," ACS Appl. Energy Mater. **2**, 3 (2019).

[34] E. Zhang, Y. Cao, C. Caloz, and M. Skorobogatiy, “Improving thermo-optic properties of smart windows via coupling to radiative coolers," Appl. Opt. **59**, D210–D220 (2020).

[35] R. S. Zakirullin, “Optical filter for smart windows with angle-selective light transmission," J. Opt. Technol. **86**, 278–283 (2019).

[36] M. J. Miller and J. Wang, “Multilayer ITO/VO2/TiO2 thin films for control of solar and thermal spectra," Sol. Energy Mater. Sol. Cells **154**, 88–93 (2016).

[37] L. V. Besteiro, X. T. Kong, Z. Wang, F. Rosei, and A. O. Govorov, “Plasmonic glasses and films based on alternative inexpensive materials for blocking infrared radiation," Nano Letters **18**, 3147–3156 (2018).

[38] Q. Gao, X. Wu, and L. Cai, “Dual functionality of K0.3WO3/Ag2O nanocomposites for smart window: Energy saving and visible photocatalytic self-cleaning performance," Sol. Energy Mater. Sol. Cells **196**, 111–118 (2019).

[39] G. Wei, D. Yang, T. Zhang, X. Yue, and F. Qiu, “Thermal-responsive PNIPAm-acrylic/Ag NRs hybrid hydrogel with atmospheric window full-wavelength thermal management for smart windows," Sol. Energy Mater. Sol. Cells **206**, 110336 (2020).

[40] W. J. Yoon, Y. J. Choi, S. I. Lim, J. Koo, S. Yang, D. Jung, S. W. Kang, and K. U. Jeong, “A single-step dual stabilization of smart window by the formation of liquid crystal physical gels and the construction of liquid crystal chambers," Adv. Funct. Mater. **30**, 1906780 (2020).

[41] S. Haghanifar, T. Gao, R. T. R. De Vecchis, B. Pafchek, T. D. B. Jacobs, and P. W. Leu, “Ultrahigh-transparency, Ultrahigh-haze Nanograss Glass with Fluid-induced Switchable Haze," Optica **4**, 1522 (2017).

[42] Y. Montelongo, D. Sikdar, Y. Ma, A. J. S. McIntosh, L. Velleman, A. R. Kucernak, J. B. Edel and A. A. Kornyshev, “Electrotunable Nanoplasmonic Liquid Mirror," Nature Materials **16**, 1127–1135 (2017).

[43] D. Sikdar, and A. A. Kornyshev, “An electro-tunable Fabry-Perot interferometer based on dual mirror-on-mirror nanoplasmonic metamaterials,” Nanophotonics 8, 2279–2290 (2019).

[44] Y. Ma, C. Zagar, D. J. Klemme, D. Sikdar, L. Velleman, Y. Montelongo, S. Oh, A. R. Kucernak, J. B. Edel, and A. A Kornyshev, “A Tunable Nanoplasmonic Mirror at an Electrochemical Interface," ACS Photonics **5**, 4604–4616 (2018).

[45] H. Weir, J. B. Edel, A. A. Kornyshev, and D. Sikdar, “Towards Electrotuneable Nanoplasmonic Fabry-Perot Interferometer," Sci. Rep. **8**, 565 (2018).

[46] Y. Ke, J. Chen, G. Lin, S. Wang, Y. Zhou, J. Yin, P. S. Lee, and Y. Long, “Smart windows: electro-, thermo-, mechano-, photochromics, and beyond," Adv. Energy Mater. **9**, 1970153 (2019).

[47] R. Basu, P. Magudapathy, M. Sardar, R. Pandian, and S. Dhara, “VO2 microcrystals as an advanced smart window material at semiconductor to metal transition," J. Phys. D: Appl. Phys. **50**, 465602 (2017).

[48] R. Tallberg, B. P. Jelle, R. Loonen, T. Gao, and M. Hamdy, “Comparison of the energy saving potential of adaptive and controllable smart windows: A state-of-the-art review and simulation studies of thermochromic, photochromic and electrochromic technologies," Sol. Energy Mater. Sol. Cells **200**, 109828 (2019).

[49] B. Ko, T. Badloe, S. J. Kim, S. H. Hong, and J. Rho "Employing vanadium dioxide nanoparticles for flexible metasurfaces with switchable absorption properties at near-infrared frequencies," J. Opt. **22**, 114002 (2020).

[50] S. Nundy and A. Ghosh, "Thermal and visual comfort analysis of adaptive vacuum integrated switchable suspended particle device window for temperate climate," Renewable Energy **156**, 1361–1372 (2020).

[51] A. Ghosh and B. Norton, "Durability of switching behaviour after outdoor exposure for a suspended particle device switchable glazing," Sol. Energy Mater. Sol. Cells **163**, 178–184 (2017).

[52] X. Q. Wang, A. M. W. Tam, S. Z. Jia, Q. Zhang, X. Y. Chen, Y. F. Xiong, Q. Zhang, Z. Liu, V. G. Chigrinov, H. S. Kwok, and D. Shen, "Low-voltage-driven smart glass based on micropatterned liquid crystal Fresnel lenses," Appl. Opt. **58**, 1146–1151 (2019).

[53] R. Baetens, B. P. Jelle, and A. Gustavsen, "Properties, requirements and possibilities of smart windows for dynamic daylight and solar energy control in buildings: A state-of-the-art review," Sol. Energy Mater. Sol. Cells **94**, 87–105 (2010).

[54] J. A. Dakheel and K. T. Aoul, "Building Applications, Opportunities and Challenges of Active Shading Systems: A State-of-the-Art Review," Energies **10**, 1672 (2017).

[55] C. Woodford, "Smart windows (electrochromic glass)," https://www.explainthatstuff.com/electrochromic-windows.html, (accessed November 12,2021).

[56] N. I. Landy, S. Sajuyigbe, J. J. Mock, D. R. Smith, and W. J. Padilla, "Perfect metamaterial absorber," Phys. Rev. Lett. **100**, 207402 (2008).

[57] T. V. Teperik, V. V. Popov, and F. J. G. de Abajo, "Total light absorption in plasmonic nanostructures," Journal of Optics A: Pure and Applied Optics **9**, S458–S462 (2007).

[58] A. Rastgordani and Z. G. Kashani, "Robust design method for metasurface high-sensitivity sensors and absorbers," J. Opt. Soc. Am. B **37**, 2006–2011 (2020).

[59] Y. Cheng, H. Zhao, and C. Li, "Broadband tunable terahertz metasurface absorber based on complementary-wheel-shaped graphene," Optical Materials **109**, 110369 (2020).

[60] Y. Wang, H. Liu, and J. Zhu, "Solar thermophotovoltaics: progress, challenges, and opportunities," APL Mater. **7**, 080906 (2019).

[61] W. Li and S. Fan, "Nanophotonic Control of Thermal Radiation for Energy Applications," Opt. Express **26**, 15995–16021 (2018).

[62] H. Noh, Y. Chong, A. D. Stone, and H. Cao, "Perfect coupling of light to surface plasmons by coherent absorption, Phys. Rev. Lett. **108**, 186805 (2012).

[63] Y. Q. Ye, Y. Jin, and S. He, "Omnidirectional, polarization-insensitive and broadband thin absorber in the terahertz regime," J. Opt. Soc. Am. B **27**, 498–504 (2010).

[64] G. Liu, X. Liu, J. Chen, Y. Li, L. Shi, G. Fu, and Z. Liu, "Near-unity, full-spectrum, nanoscale solar absorbers and near-perfect blackbody emitters," Sol. Energy Mater. and Sol. Cells **190**, 20–29 (2019).

[65] N. T. Q. Hoa, P. H. Lam, P. D. Tung, T. S. Tuan, and H. Nguyen, "Numerical study of a wide-angle and polarization-insensitive ultrabroadband metamaterial absorber in visible and near-infrared region", IEEE Photonics J. **11**, 1–9 (2019).

[66] M. C. Soydan, A. Ghobadi1, D. U. Yildirim1, V. B. Erturk, and E. Ozbay, "All ceramic-based metal-free ultra-broadband perfect absorber," Plasmonics **14**, 1801–1815 (2019).

[67] M. Aalizadeh, A. Khavasi, A.E. Serebryannikov, G. A. E. Vandenbosch, and E. Ozbay "A route to unusually broadband plasmonic absorption spanning from visible to mid-infrared," Plasmonics **14**, 1269–1281 (2019).

[68] H. Lin, B. C. P. Sturmberg, K. T. Lin, Y. Yang, X. Zheng, T. K. Chong, C. M. de Sterke, and B. Jia, "A 90-nm-thick graphene metamaterial for strong and extremely broadband absorption of unpolarized light," Nat. Photonics **13**, 270–276 (2019).

[69] H. Gao, W. Peng, W. Cui, S. Chu, L. Yu, and X. Yang, "Ultraviolet to near infrared titanium nitride broadband plasmonic absorber," Optical Materials **97**, 109377 (2019).

[70] Y. Cheng, H. Zhang, X. S. Mao, and R. Gong, "Dual-band plasmonic perfect absorber based on all-metal nanostructure for refractive index sensing application," Materials Letters **219**, 123–126 (2018).

[71] H. Zou and Y. Cheng, "Design of a six-band terahertz metamaterial absorber for temperature sensing application," Optical Materials **88**, 674–679 (2019).

[72] Y. Cheng, H. Luo, F. Chen, and R. Gong, "Triple narrow-band plasmonic perfect absorber for refractive index sensing applications of optical frequency," OSA Continuum **2**, 2113–2122 (2019).

[73] Y. Cheng, F. Chen, and H. Luo, "Multi-band giant circular dichroism based on conjugated bilayer twisted-semicircle nanostructure at optical frequency," Physics Letters A **384** (19), 126398 (2020).

[74] Y. Cheng, F. Chen, and H. Luo, "Triple-band perfect light absorber based on hybrid metasurface for sensing application," Nanoscale Research Letters **15**, 103 (2020).

[75] W. Li and Y. Cheng, "Dual-band tunable terahertz perfect metamaterial absorber based on strontium titanate (STO) resonator structure," Optics Communications **462**, 125265 (2020).

[76] Y. Cui, K. H. Fung, J. Xu, H. Ma, Y. Jin, S. He, and N. X. Fang, "Ultrabroadband light absorption by a sawtooth anisotropic metamaterial slab", Nano Lett. **12**, 1443–1447 (2012).

[77] K. Aydin , V. E. Ferry, R. M. Briggs, and H. A. Atwater, "Broadband polarization-independent resonant light absorption using ultrathin plasmonic super absorbers," Nat. Commun. **2**, 517 (2011).

[78] C. Liang, Z. Yi, X. Chen, Y. Tang, Y. Yi1, Z. Zhou1, X. Wu, Z. Huang, Y. Yi, and G. Zhang, "Dual-band infrared perfect absorber based on a Ag-dielectric-Ag multilayer films with nanoring grooves arrays," Plasmonics **15**, 93–100 (2020).

[79] B. Tang, Y. Zhu, X. Zhou, L. Huang, and X. Lang, "Wide-angle polarization independent broadband absorbers based on concentric multisplit ring arrays," IEEE Photonics Journal **9**, 1–7 (2017).

[80] H. Gao, D. Zhou, W. Cui, Z. Liu, Y. Liu, Z. Jing, and W. Peng, "Ultraviolet broadband plasmonic absorber with dual visible and near-infrared narrow bands," J. Opt. Soc. Am. A **36**, 264–269 (2019).

[81] H. Zhang, C. Guan, J. Luo, Y. Yuan, N. Song, Y. Zhang, J. Fang, and H. Liu, "Facile film-nanoctahedron assembly route to plasmonic metamaterial absorbers at visible frequencies," ACS Applied Materials & Interfaces **11**, 20241–20248 (2019).

[82] J. Liu, W. Chen, W. Z. Ma, G. X. Yu, J. C. Zheng, Y. S. Chen, and C. F. Yang, "Ultra-broadband infrared absorbers using iron thin layers," IEEE Access **8**, 43407–43412 (2020).

[83] W. Wang, Y. Qu, K. Du, S. Bai, J. Tian, M. Pan, H. Ye, M. Qiu, and Q. Li, "Broadband optical absorption based on single-sized metal-dielectricmetal plasmonic nanostructures with high- ϵ" metals," Applied Physics Lett. **110**, 101101 (2017).

[84] Y. Lin, Y. Cui, F. Ding, K. H. Fung, T. Ji, D. Li, and Y. Hao, "Tungsten based anisotropic metamaterial as an ultra-broadband absorber", Optical Mater. Exp. **7**, 1–12 (2017).

[85] S. K. Patel, J. Parmar, D. Katrodiya, T. K. Nguyen, E. Holdengreber, and V. Dhasarathan, "Broadband metamaterial-based near-infrared absorber using an array of uniformly placed gold resonators," J. Opt. Soc. Am. B **37**, 2163–2170 (2020).

[86] D. Kraemer, Q. Jie, K. McEnaney, F. Cao, W. Liu, L. A. Weinstein, J. Loomis, Z. Ren, and G. Chen, "Concentrating solar thermoelectric generators with a peak efficiency of 7.4%," *Nat. Energy* **1**, 16153 (2016).

[87] D. Narducci and B. Lorenzi, "Challenges and Perspectives in Tandem Thermoelectric–Photovoltaic Solar Energy Conversion," IEEE Trans. Nanotechnol. **15**, 348–355 (2016).

[88] X. Wang, H. Li, X. Yu, X. Shi, and J. Liu, "High-performance solution-processed plasmonic Ni nanochain-Al2O3 selective solar thermal absorbers," Appl. Phys. Lett., **101**, 203109 (2012).

[89] P. Tapsanit, "Theoretically comparative study of spectrally selective solar absorbers in concentrated solar-thermoelectric generators working at high temperature," Appl. Opt. **60**, 5291–5301 (2021).

[90] I.E. Khodasevych, L. Wang, A. Mitchell, and G. Rosengarten, "Micro- and Nanostructured Surfaces for Selective Solar Absorption," Adv. Optical Mater. **3**, 852–881 (2015).

[91] Y. Tian, X. Liu, A. Ghanekar, and Y. Zheng, "Scalable-manufactured metal-insulator-metal based selective solar absorbers with excellent high-temperature insensitivity," Appl. Energy **281**, 116055 (2021).

[92] G. Gong, X. Huang, J. Wang, and M. Hao, "An optimized model and test of the China's first high temperature parabolic trough solar receiver," Sol. Energy **84**, 2230–2245 (2010).

[93] D. Barlev, R. Vidu, and P. Stroeve, "Innovation in concentrated solar power," Sol. Energy Mater. Sol. Cells 95, 2703–2725 (2011).

[94] Z. Wu, F. Chen, Z. Xuan, Y. Chen, W. Shi, X. Liu, and S. Wang , "High energy efficient and thermally stable solar selective absorber constructed with TiNxOy based multilayers," *Opt. Mater. Express* **10**, 733–741 (2020).

[95] H. Wang, V. P. Sivan, A. Mitchell, G. Rosengarten, P. Phelan, and L. Wang, "Highly efficient selective metamaterial absorber for high-temperature solar thermal energy harvesting," Sol. Energy Mater. Sol. Cells **137**, 235–242 (2015).

[96] R. Pettit, R. Sowell, and I. Hall, "Black chrome solar selective coatings optimized for high temperature applications," Sol. Energy Mater. **7**, 153–170 (1982).

[97] C. K. Ho, A. R. Mahoney, A. Ambrosini, M. Bencomo, A. Hall, and T. N. Lambert, "Characterization of pyromark 2500 paint for high-temperature solar receivers," J. Sol. Energy Eng **136**, 014502 (2014).

[98] L. Gaouyata, Z. He, J. F. Colomer, Ph. Lambin, F. Mirabella, D. Schryvers, and O.Deparis, "Revealing the innermost nanostructure of sputtered NiCrOx solar absorber cermets," Sol. Energy Mater. Sol. Cells **122**, 303–308 (2014).

[99] C. M. Watts, X. Liu, and W. J. Padilla, "Metamaterial Electromagnetic Wave Absorbers," Adv. Mater. **24**, OP181 (2012).

[100] V. Stelmakh, W. R. Chan, M. Ghebrebrhan, J. Senkevich, J. D. Joannopoulos, M. Soljacic, I. Celanovic, "Sputtered Tantalum Photonic Crystal Coatings for High-Temperature Energy Conversion Applications," IEEE Trans. Nanotechnol. **15**, 303–309 (2016).

[101] A. Ghanekar, Y. Tian, S. Zhang, Y. Cui, and Y. Zheng, "Mie-metamaterials-based thermal emitter for near-field thermophotovoltaic systems," *Materials*, vol. 10, p. 885, 2017.

[102] A. Ghanekar, M. Sun, Z. Zhang, and Y. Zheng, "Optimal design of wavelength selective thermal emitter for thermophotovoltaic applications," J. Therm. Sci. Eng. Appl. **10**, 011004 (2018).

[103] A. Chen and Z. Song, "Tunable Isotropic Absorber With Phase Change Material VO2," IEEE Trans. Nanotechnol. **19**, 197–200 (2020).

[104] W. Chen, J. Liu, W. Z. Ma, G. X. Yu, J. Q. Chen, H. Y. Cai, and C. F. Yang, "Numerical Study of Multilayer Planar Film Structures for Ideal Absorption in the Entire Solar Spectrum," Appl. Sci. **10**, 3276 (2020).

[105] N. Khoza, Z. Y. Nuru, J. Sackey, L. Kotsedi, N. Matinise, C. Ndlangamandla, and M. Maaza, "Structural and optical properties of ZrOx/Zr/ZrOx/AlxOy multilayered coatings as selective solar absorbers," J. Alloys Compd. **773**, 975–979 (2019).

[106] S. A. Dereshgi, A. Ghobadi, H. Hajian, B. Butun, and E. Ozbay, "Ultrabroadband, lithography- free, and large-scale compatible perfect absorbers: the optimum choice of metal layers in metal-insulator multilayer stacks," Sci. Rep. **7**, 14872 (2017).

[107] "File: Atmospheric electromagnetic transmittance or opacity.jpg", https://commons.wikimedia.org/wiki/File:Atmospheric electromagnetic transmittance or opacity.jpg (accessed November 22,2021).

[108] M. Chen, D. Pang, X. Chen, and H. Yan, "Enhancing infrared emission behavior of polymer coatings for radiative cooling applications," J. Phys. D: Appl. Phys. **54**, 295501 (2021).

[109] C. G. Granqvist and A. Hjortsberg, "Surfaces for radiative cooling: silicon monoxide films on aluminum," Appl. Phys. Lett. **36**, 139–141 (1980).

[110] A. R. Gentle and G. B. Smith, "Radiative heat pumping from the earth using surface phonon resonant nanoparticles," Nano Lett. **10**, 373–379 (2010).

[111] M. Zeyghami, D. Y. Goswami, E. Stefanakos, "A Review of Clear Sky Radiative Cooling Developments and Applications in Renewable Power Systems and Passive Building Cooling," Sol. Energy Mater. Sol. Cells **178**, 115–128 (2018).

[112] D. Chae, M. Kim, P. H. Jung, S. Son, J. Seo, Y. Liu, B. J. Lee, and H. Lee, "Spectrally Selective Inorganic-Based Multilayer Emitter for Daytime Radiative Cooling," ACS Appl. Mater. Interfaces **12**, 8073–8081 (2020).

[113] Y. Yang and Y. Zhang, "Passive daytime radiative cooling: Principle, application, and economic analysis," MRS Energy & Sustainability **7**, 18 (2020).

[114] N. N. Shi, C.C. Tsai, F. Camino, G.D. Bernard, N. Yu, and R. Wehner, "Keeping cool: enhanced optical reflection and heat dissipation in silver ants," Science **349**, 298–301 (2015).

[115] M. M. Hossain, B. Jia, and M. Gu, "A metamaterial emitter for highly efficient radiative cooling," Adv. Opt. Mater. **3**, 1047–1051 (2015).

[116] E. Rephaeli, A. Raman, and S. Fan, "Ultrabroadband photonic structures to achieve high-performance daytime radiative cooling," Nano Lett. **13**, 1457–1461 (2013).

[117] Y. Zhai, Y. Ma, S. N. David, D. Zhao, R. Lou, G. Tan, R. Yang, and X. Yin, "Scalable-manufactured randomized glass-polymer hybrid metamaterial for daytime radiative cooling," Science **355**, 1062–1066 (2017).

[118] A. P. Raman, M. A. Anoma, L. Zhu, E. Rephaeli, and S. Fan, "Passive radiative cooling below ambient air temperature under direct sunlight," Nature **515**, 540–544 (2014).

[119] M. A. Kecebas, M. P. Menguc, A. Kosar, and K. Sendur, "Passive radiative cooling design with broadband optical thin-film filters," J. Quant. Spectrosc. Radiat. Transf. **198**, 179–186 (2017).

[120] A. R. Gentle and G. B. Smith, "A Subambient Open Roof Surface under the Mid-Summer Sun," Adv. Sci. **2**, 1500119 (2015).

[121] J. Chen and L. Lu, "Development of radiative cooling and its integration with buildings: A comprehensive review," Sol. Energy **212**, 125–151, (2020).

[122] H. Bao, C. Yan, B. Wang, X. Fang, C.Y. Zhao, X. Ruan, "Double-layer nanoparticlebased coatings for efficient terrestrial radiative cooling," Sol. Energy Mater. Sol. Cells **168**, 78–84 (2017).

[123] Y. Fu, J. Yang, Y.S. Su, W. Du, Y.G. Ma, "Daytime passive radiative cooler using porous alumina," Sol. Energy Mater. Sol. Cells **191**, 50–54 (2019).

[124] X. Liu, S. Pian, R. Zhou, H. Shen, X. Liu, Q. Yang, and Y. Ma, "Tunable radiative cooling based on a stretchable selective optical filter," J. Opt. Soc. Am. B **37**, 2534–2537 (2020).

[125] D. Wang, Y. Zhu, C. Fang, P. He, and Y. Ye, "Example of metal-multi-dielectric-metal cooling metamaterial use in engineering thermal radiation," Appl. Opt. **58**, 7035–7041 (2019).

[126] B. Ko, D. Lee, T. Badloe, and J. Rho, "Metamaterial-Based Radiative Cooling: Towards Energy-Free All-Day Cooling," Energies **12**, 89 (2019).

[127] T. A. Lyons, *A Treatise on Electromagnetic Phenomena and on the Compass and its Deviations Aboard Ship, Mathematical, Theoretical and Practical*, J. Wiley & Sons, 1901.

[128] J. C. Maxwell, "VIII. A dynamical theory of the electromagnetic field," Phil. Trans. R. Soc. **155**, 459–512 (1865).

[129] R. S. Kshetrimayum, *Electromagnetic Field Theory*, Cengage Learning India, 2012.

[130] P. B. Johnson and R. W. Christy, "Optical constants of transition metals: Ti, V, Cr, Mn, Fe, Co, Ni, and Pd," Phys. Rev. B **9**, 5056–5070 (1974).

[131] E. Hecht, *Optics*, 4th Edition. Addison-Wesley, New York, 2002.

[132] A. K. Chowdhary and D. Sikdar, "Low-power design of electrotunable color filters and optical switches," J. Opt. Soc. Am. B **37**, 3865–3873 (2020).

[133] D. M. Pozar, *Microwave Engineering*, Wiley, Hoboken, NJ, (2005).

[134] A. Ghatak and K. Thyagarajan, *Optical Electronics*, Cambridge University Press, (1989).

[135] H. Weir, J. B. Edel, A. A. Kornyshev, and D. Sikdar, "Towards electrotuneable nanoplasmonic Fabry–Perot interferometer, Sci. Rep. **8**, 565 (2018).

[136] T. C. Choy, Effective Medium Theory, Principles and Applications, Oxford University Press, (1999).

[137] A. K. Chowdhary and D. Sikdar, "Ultra-broadband wide-angle metallo-dielectric metamaterial absorber for solar energy harvesting," in 2019 Workshop on Recent Advances in Photonics (WRAP), 1–3 (2019).

[138] J. J. Wood, *Theory of surface modes in strucutred plasmonic arrays*, PhD Thesis, Imperial College London, UK, 2015.

[139] J. Parsons, C. Burrows, J. Sambles, and W. Barnes, "A comparison of techniques used to simulate the scattering of electromagnetic radiation by metallic nanostructures," Journal of Modern Optics **57**, 356–365 (2010).

[140] A. K. Chowdhary, T. Bhowmik, J. Gupta, and D. Sikdar, "Energy-saving all-weather window based on selective filtering of solar spectral radiation," Appl. Opt. **60**, 1315–1325 (2021).

[141] A. K. Chowdhary and D. Sikdar, "Design of electrotunable all-weather smart windows," Sol. Energy Mater. Sol. Cells **222**, 110921 (2021).

[142] A. K. Chowdhary, T. Bhowmik, and D. Sikdar, "Polarization-and angle-insensitive ultra-broadband perfect metamaterial absorber for thermophotovoltaics," J. Opt. Soc. Am. B **38**, 327–335 (2021).

[143] Lefebvre et al., "CMOS compatible metal-insulator-metal plasmonic perfect absorbers," Opt. Mater. Express **6**, 2389–2396 (2016).

[144] W. S. M. Werner, K. Glantschnig, and C. A. Draxl, "Optical constants and inelastic electron-scattering data for 17 elemental metals," J. Phys. Chem. Ref. Data **38**, 1013–1092 (2009).

[145] L. Gao, F. Lemarchand, and M. Lequime, "Exploitation of multiple incidences spectrometric measurements for thin film reverse engineering," Opt. Express **20**, 15734–15751 (2012).

[146] C. M. Wang et al., "Angle-Independent Infrared Filter Assisted by Localized Surface Plasmon Polariton," IEEE Photon. Technol. Lett. **20**, 1103–1105 (2008).

[147] V. Khoshdel, M. Joodaki, and M. S. Saremi, "UV and IR cut-off filters based on plasmonic crossed-shaped nano-antennas for solar cell applications," Opt. Commun. **433**, 275–282 (2019).

[148] G. Gu, L. Li, Y. Zhang, T. Kemsri, and X. Lu , "Analysis of mutual couplings in a concentric circular ring plasmonic optical antenna array," Sci. Rep. **7**, 10996 (2017).

[149] F. F. Mahani, A. Mokhtari, and M. Mehran, "Design and development of aluminum nanoring arrays for realization of dual-mode operation plasmonic color filters," J. Opt. Soc. Am. B **35**, 1764–1771 (2018).

[150] B. Sheng et al., "Tunable and Polarization-Independent Wedged Resonance Filter With 2D Crossed Grating," IEEE Photon. Technol. Lett. **28**, 2211–2214 (2016).

[151] N. I. Jaksic and C. Salahifar, “A feasibility study of electrochromic windows in vehicles," Sol. Energy Mater. Sol. Cells **79**, 409–423 (2003).

[152] L. Yao, Z. Qu, R. Sun, Z. Pang, Y. Wang, B. Jin, and J. He, “Long-Lived Multilayer Coatings for Smart Windows: Integration of Energy-Saving, Antifogging, and Self-Healing Functions," ACS Appl. Energy Mater. **2**, 7467–7473 (2019).

[153] A. K. Chowdhary and D. Sikdar, “Multilayer thin-film based nanophotonic windows: static versus electrotunable design," J. Opt. **24**, 024002 (2022).

[154] J. Carmody, S. Selkowitz, and L. Heschong, *Residential Windows: A Guide to New Technologies and Energy Performance*, New York, (1996).

[155] J. A. Duffie, W. A. Beckman, *Solar Engineering of Thermal Processes*, John Wiley, Hoboken, (2013).

[156] “Glass Knowledge Blog. Non-solar Heat Control Glasses," https://theglassblog.wordpress.com/2011/02/06/non-solar-heat-control-glasses, (accessed: Oct 23, 2019).

[157] M. Santamouris, *Buildings, Energy, Solar Technology*, Earthscan, London, (2007).

[158] F. Pacheco-Torgal, *Eco-efficient Materials for Mitigating Building Cooling Needs*, Elsevier, Boston, (2015).

[159] D. Wolfe and K. W. Goossen, “Evaluation of 3D printed optofluidic smart glass prototypes," Opt. Express **26**, A15 (2018).

[160] A. Llordes, G. Garcia, J. Gazquez, and D. J. Milliron, “Tunable near-infrared and visible-light transmittance in nanocrystal-in-glass composites," Nature **500**, 323–326 (2013).

[161] P. B. Johnson and R. W. Christy, “Optical constants of the noble metals," Phys. Rev. B **6**, 4370–4379 (1972).

[162] Z. Wang, P. Zhou, and G. Zheng, “Electrically switchable highly efficient epsilon-near-zero metasurfaces absorber with broadband response," Results in Physics **14**, 102376 (2019).

[163] H. Zheng, R. J. Zhang, D. H. Li, X. Chen, S. Y. Wang, Y. X. Zheng, M. J. Li, Z. G. Hu, N. Dai, and L. Y. Chen, “Optical properties of Al-doped ZnO films in the infrared region and their absorption applications," Nanoscale Res Lett. **13**, 149 (2018).

[164] T. M. Hartnett, S. D. Bernstein, E. A. Maguire, and R. W. Tustison, “Optical properties of ALON (aluminum oxynitride)," Proc. SPIE **3060**, 284–295 (1997).

[165] M. Aalizadeh, A. E. Serebryannikov, A. Khavasi, G. A. E.Vandenbosch, and E. Ozbay, "Toward electrically tunable, lithography-free, ultra-thin color filters covering the whole visible spectrum," Sci. Rep. **8**, 11316 (2018).

[166] S. O. Kasap, *Optoelectronics and Photonics: Principles and Practices*, (2013).

[167] M. Ramisetty, S. Sastri, U. Kashalikar, L. M. Goldman, and N. Nag, "Transparent polycrystalline spinels protect and defend," American Ceramic Society Bulletin **92**, 20–24 (2013).

[168] "Domes & Infrared Optics, Surmet," http://www.surmet.com/products-and-applications/Domes-and-IR-Optics (accessed: Mar 02, 2020).

[169] Z. Y. Li, S. Butun, and K. Aydin, "Large-area, lithography-free super absorbers and color filters at visible frequencies using ultrathin metallic films," ACS Photonics **2**, 183–188 (2015).

[170] J. Park, J. H. Kang, X. G. Liu, and M. L. Brongersma, "Electrically tunable epsilon-near-zero (ENZ) metafilm absorbers," Sci. Rep. **5**, 15754 (2015).

[171] K. Lee, S. Y. Han, Z. Li, H. W. Baac, and H. J. Park, "Flexible high-color-purity structural color filters based on a higher-order optical resonance suppression," Sci. Rep. **9**, 14917 (2019).

[172] R. J. Mortimer, D. R. Rosseinsky, and P. M. S. Monk, *Electrochromic Materials and Devices*, John Wiley & Sons, (2015).

[173] M. Akrami, A. H. Salah, A. A. Javadi, H. E.S. Fath, M. J. Hassanein, R. Farmani, M. Dibaj, and A. Negm, "Towards a Sustainable Greenhouse: Review of Trends and Emerging Practices in Analysing Greenhouse Ventilation Requirements to Sustain Maximum Agricultural Yield," Sustainability **12**, 2794 (2020).

[174] "LEDs - The Future of Horticultural Lighting," https://www.we-online.com/web/en/electronic_components/produkte_pb/application_notes/ano002_leds_thefutureofhorticulturallighting.php, (accessed: 15 March, 2021).

[175] N. Osterthun, N. Neugebohrn, K. Gehrke, M. Vehse, and C. Agert, "Spectral engineering of ultrathin germanium solar cells for combined photovoltaic and photosynthesis," Opt. Express **29**, 938–950 (2021).

[176] M. Cossu, A. Yano, S. Solinas, P. A. Deligios, M. T. Tiloca, A. Cossu, and L. Ledda, "Agricultural sustainability estimation of the European photovoltaic greenhouses," Eur. J. Agron. **118**, 126074 (2020).

[177] J.-N. Wang, B. Xiong, R.-W. Peng, C.-Y. Li, B.-Q. Hou, C.-W. Chen, Y. Liu, M. Wang, "Flexible Phase Change Materials for Electrically-Tuned Active Absorbers," Small **17**, 2101282 (2021).

[178] M. Nejat and N. Nozhat, "Design, theory, and circuit model of wideband, tunable and polarization-insensitive terahertz absorber based on graphene," IEEE Transactions on Nanotechnology **18**, 684–690 (2019).

[179] J. Kim, M. Remond, D. Kim, H. Jang, and E. Kim, "Electrochromic conjugated polymers for multifunctional smart windows with integrative functionalities," Adv. Mater. Technol. **5**, 1900890 (2020).

[180] A. Aoki, A. Ito, and S. Watanabe, "Reversible Ag electroplating onto ITO electrode for smart window," Sol. Energy Mater. Sol. Cells **200**, 109922 (2019).

[181] J. Pan, R. Zheng, Y. Wang, X. Ye, Z. Wan, C. Jia, X. Weng, J. Xie, and L. Deng, "A high-performance electrochromic device assembled with hexagonal WO3 and NiO/PB composite nanosheet electrodes towards energy storage smart window," Sol. Energy Mater. Sol. Cells **207**, 110337 (2020).

[182] W. Geis, R. Sinta, W. Mowers, S.J. Deneault, M.F. Marchant, K.E. Krohn, S.J. Spector, D.R. Calawa, and T.M. Lyszczarz, "Fabrication of crystalline organic waveguides with an exceptionally large electro-optic coefficient," Appl. Phys. Lett. **84**, 3729–3731 (2004).

[183] Z. Respondek, "Heat transfer through insulating glass units subjected to climatic loads," Materials **13**, 286 (2020).

[184] S. Yokogawa, S. P. Burgos, and H. A. Atwater, "Plasmonic color filters for CMOS image sensor applications," Nano Lett. **12**, 4349–4354 (2012).

[185] L. Cheng, J. Mao, K. Wang, J. Lu, K. Huang, Y. Zhang, and L. Zhang, "Rational design of colorimetric sensing for a customer-oriented index range using plasmonic substrates," J. Opt. Soc. Am. B **36**, 3168–3173 (2019).

[186] F. Cheng, J. Gao, L. Stan, D. Rosenmann, D. Czaplewski, and X. Yang, "Aluminum plasmonic metamaterials for structural color printing," Opt. Express **23**, 14552–14560 (2015).

[187] X. M. Goh, Y. Zheng, S. J. Tan, L. Zhang, K. Kumar, C. W. Qiu, and J. K. W. Yang, "Three-dimensional plasmonic stereoscopic prints in full colour," Nat. Commun. **5**, 5361 (2014).

[188] Y. Chen, X. Duan, M. Matuschek, Y. Zhou, F. Neubrech, H. Duan, and N. Liu, "Dynamic color displays using stepwise cavity resonators," Nano Lett. **17**, 5555–5560 (2017).

[189] Z. Wang, X.Wang, S. Cong, J. Chen, H. Sun, Z. Chen, G. Song, F. Geng, Q. Chen, and Z. Zhao, "Towards full-colour tunability of inorganic electrochromic devices using ultracompact Fabry–Perot nanocavities," Nat. Commun. **11**, 302 (2020).

[190] M. Srinivasarao, "Nano-optics in the biological world: Beetles, butterflies, birds, and moths," Chem. Rev. **99**, 1935–1961 (1999).

[191] F. P. Barrows, and M. H. Bart, "Photonic structures in biology: A possible blueprint for nanotechnology," Nanomat. Nanotech. **4**, 58289 (2014).

[192] C. Park, V. R. Shrestha, W. Yue, S. Gao, S. Lee, E. Kim, and D. Choi, "Structural Color Filters Enabled by a Dielectric Metasurface Incorporating Hydrogenated Amorphous Silicon Nanodisks," Sci. Rep. **7**, 2556 (2017).

[193] V. Vashistha, G. Vaidya, R. S. Hegde, A. E. Serebryannikov, N. Bonod, and M. Krawczyk, "All-Dielectric Metasurfaces Based on Cross-Shaped Resonators for Color Pixels with Extended Gamut," ACS Photonics **4**, 1076–1082 (2017).

[194] G. Si, Y. Zhao, J. Lv, M. Lu, F. Wang, H. Liu, N. Xiang, T. J. Huang, A. J. Danner, J. Teng, and Y. J. Liu, "Reflective plasmonic color filters based on lithographically patterned silver nanorod arrays," Nanoscale **5**, 6243–6248 (2013).

[195] C. Genet and T. W. Ebbesen, "Light in tiny holes," Nature **445**, 39–46 (2007)

[196] B. Zeng, Y. Gao, and F. J. Bartoli, "Ultrathin nanostructured metals for highly transmissive plasmonic subtractive color filters," CLEO, San Jose, CA, 1–2 (2014).

[197] Y. Yu, L. Wen, S. Song, and Q. Chen, "Transmissive/reflective structural color filters: theory and applications," J. Nanomater. **2014**, 212637 (2014).

[198] Y. T. Yoon and S. S. Lee, "Transmission type color filter incorporating a silver film based etalon," Opt. Express **18**, 5344–5349 (2010).

[199] C. Jiang, S. Liang, L. Wan, K. Du, W. Zhang, Z. Li, S. J. Chua, and T. Mei, "Plasmonic color filter based on a hetero-metal-insulator-metal grating," Appl. Opt. **59**, 4432–4436 (2020).

[200] S. S. Mirshafieyan, and D. A. Gregory, "Electrically tunable perfect light absorbers as color filters and modulators," Sci. Rep. **8**, 2635 (2018).

[201] J. Guo, Y. Tu, L. Yang, R. Zhang, L. Wang, and B. Wang, "Electrically tunable gap surface plasmon-based metasurface for visible light," Sci. Rep. **7**, 14078 (2017).

[202] A. Forouzmand and H. Mosallaei, "Electro-optical Amplitude and Phase Modulators Based on Tunable Guided-Mode Resonance Effect," ACS Photonics **6**, 2860–2869 (2019).

[203] A. Forouzmand and H. Mosallaei, "Tunable dual-band amplitude modulation with a double epsilon-near-zero metasurface," Journal of Optics **22**, 094001 (2020).

[204] M. J. Uddin, T. Khaleque, and R. Magnusson, "Guided-mode resonant polarization-controlled tunable color filters," Opt. Express **22**, 12307–12315 (2014).

[205] V. Vashistha, G. Vaidya, P. Gruszecki, A. E. Serebryannikov, and M. Krawczyk, "Polarization tunable all-dielectric color filters based on cross-shaped Si nanoantennas," Sci. Rep. **7**, 8092 (2017).

[206] L. Qian, D. Zhang, B. Dai, Q. Wang, Y. Huang, and S. Zhuang, "Optical notch filter with tunable bandwidth based on guided-mode resonant polarization-sensitive spectral feature," Opt. Express **23**, 18300–18309 (2015).

[207] L. Bibbo, K. Khan, Q. Liu, M. Lin, Q. Wang, and Z. Ouyang, "Tunable narrowband antireflection optical filter with a metasurface," Photon. Res. **5**, 500–506 (2017).

[208] F. Yi, E. Shim, A. Y. Zhu, H. Zhu, J. C. Reed, and E. Cubukcu, "Electrically tunable plasmonic absorber enabled by indium Tin Oxide", CLEO, San Jose, CA, 1-2 (2013).

[209] M. Salemizadeh, F. F. Mahani, and A. Mokhtari, "Tunable mid-infrared graphene-titanium nitride plasmonic absorber for chemical sensing applications", J. Opt. Soc. Am. B **36**, 2863–2870 (2019).

[210] S. Quader, J. Zhang, M. R. Akram, and W. Zhu, "Graphene-based high-efficiency broadband tunable linear-to-circular polarization converter for terahertz waves," IEEE Journal of Selected Topics in Quantum Electronics **26**, 1–8 (2020).

[211] K. J. Hornburg, R. K. Komanduri, and M. J. Escuti, "Highly chromatic retardation via multi-twist liquid crystal films," J. Opt. Soc. Am. B **36**, D28-D33 (2019).

[212] D. Marco, M. M. S. Lopez, P. G. Martinez, and I. Moreno, "Using birefringence colors to evaluate a tunable liquid-crystal q-plate," J. Opt. Soc. Am. B **36**, D34-D41 (2019).

[213] H. D. Jeong and S. Y. Lee, "Tunable plasmonic absorber using a nanoslit array patterned on a ge2sb2te5-inserted Fabry–Perot resonator," J. Lightwave Technol. **36**, 5857–5862 (2018).

[214] F. Hu, H. Wang, X. Zhang, X. Xu , W. Jiang, Q. Rong, S. Zhao, M. Jiang, W. Zhang, and J. Han, "Electrically triggered tunable terahertz band-pass filter based on VO2 hybrid metamaterial," IEEE Journal of Selected Topics in Quantum Electronics **25**, 1–7 (2019).

[215] D. Sikdar, J. B. Pendry, and A.A. Kornyshev, "Nanoparticle meta-grid for enhanced light extraction from light-emitting devices," Light Sci. Appl. **9**, 122 (2020).

[216] A. K. Chowdhary, T. Bhowmik and D. Sikdar, "Polarization-and angle-insensitive ultra-broadband perfect metamaterial absorber for thermophotovoltaics," J. Opt. Soc. Am. B **38**, (2021).

[217] Y. Liu, X. Weng, P. Zhang, W. Li, Y. Gong, L. Zhang, P. Zhou1, and L. Deng "Broadband absorption of infrared dielectric resonators for passive radiative cooling," J. Opt. **23**, 025102 (2021).

[218] H. Kim and A. Lenert "Optical and thermal filtering nanoporous materials for sub-ambient radiative cooling," J. Opt. **22**, 084002 (2018).

[219] T. Inagaki, L. C. Emerson, E. T. Arakawa, and M. W. Williams, "Optical properties of solid Na and Li between 0.6 and 3.8 eV," Phs. Rev. B **13**, 2305–2313 (1976).

[220] J. Pfluger, J. Fink, W. Weber, K. P. Bohnen, and G. Crecelius, "Dielectric properties of TiCx, TiNx, VCx, and VNx from 1.5 to 40 eV determined by electron-energy-loss spectroscopy," Phys. Rev. B **30**, 1155–1163 (1984).

[221] S. Yin, Y. J. Liu, D. Xiao, H. He, D. Luo, S. Jiang, H. Dai, W. Ji, and X. W. Sun, "Liquid-crystal-based tunable plasmonic waveguide filters," J. Phys. D: Appl. Phys. **51**, 235101 (2018).

[222] L. Chen, Q. Xu, M. G. Wood, and R. M. Reano, "Hybrid silicon and lithium niobate electro-optical ring modulator," Optica **1**, 112–118 (2014).

[223] M. Li, J. Ling, Y. He, U. A. Javid, S. Xue, and Q. Lin, "Lithium niobate photonic-crystal electro-optic modulator," Nat. Commun. **11**, 4123 (2020).

[224] R. Zheng, Y. Wang, J. Pan, H. A. Malik, H. Zhang, C. Jia, X. Weng, J. Xie, and L. Deng, "Toward Easy-to-Assemble, Large-Area Smart Windows: All-in-One Cross-Linked Electrochromic Material and Device," ACS Appl. Mater. Interfaces **12**, 27526–27536 (2020).

[225] J. Wu, "Polarization-insensitive broadband absorption enhancement with few-layer MoS2 film," Physics Letters A **408**, 127511 (2021).

[226] D. Sikdar, I. D. Rukhlenko, W. Cheng, and M. Premaratne, "Unveiling ultrasharp scattering–switching signatures of layered gold–dielectric–gold nanospheres," J. Opt. Soc. Am. B **30**, 2066–2074 (2013).

[227] S. G. Rodrigo, F. J. G. Vidal, and L. M. Moreno “Influence of material properties on extraordinary optical transmission through hole arrays," Phys. Rev. B **77**, 075401 (2008).

[228] D. Barchiesi and T. Grosges“Fitting the optical constants of gold, silver, chromium, titanium, and aluminum in the visible bandwidth," Journal of Nanophotonics **8**, 1–17 (2014).

[229] R. D. Averitt, S. L. Westcott, and N. J. Halas, “Linear optical properties of gold nanoshells," J. Opt. Soc. Am. B **16**, 1824–1832 (1999).

[230] W. E. S. W. A. Rashid, P. J. Ker, M. Z. B. Jamaludin, M. M. A. Gamel, H. J. Lee and N. B. A. Rahman, “Recent Development of Thermophotovoltaic System for Waste Heat Harvesting Application and Potential Implementation in Thermal Power Plant," IEEE Access **8**, 105156–105168, (2020).

[231] W. Li, U. Guler, N. Kinsey, G. V. Naik, A. Boltasseva, J. Guan, V. M. Shalaev, and A. V. Kildishev, “Refractory Plasmonics with Titanium Nitride: Broadband Metamaterial Absorber," Adv. Mater. **26**, 7959–7965 (2014).

[232] J. Emsley, “Nature’s Building Blocks", ISBN 978-0-19-850341-5, 262–266 (2001).

[233] M. A. Ordal, R. J. Bell, R. W. Alexander, L. A. Newquist, and M. R. Querry, “Optical properties of Al, Fe, Ti, Ta, W, and Mo at submillimeter wavelengths," Appl. Opt. **27**, 1203–1209 (1988).

[234] T. Amotchkina, M. Trubetskov, D. Hahner, and V. Pervak, “Characterization of e-beam evaporated Ge, YbF3, ZnS, and LaF3 thin films for laser-oriented coatings," Appl. Opt. **59**, A40–A47 (2020).

[235] D.E. Aspnes and A. A. Studna., “Dielectric functions and optical parameters of Si, Ge, GaP, GaAs, GaSb, InP, InAs, and InSb from 1.5 to 6.0 eV," Phys. Rev. B **27**, 985–1009 (1983).

[236] D. Ji, H. Song, X. Zeng, H. Hu, K. Liu, N. Zhang, and Q. Gan, “Broadband absorption engineering of hyperbolic metafilm patterns," Sci. Rep. **4**, 4498 (2014).

[237] K. Tsakmakidis, A. Boardman, and O. Hess, “Trapped rainbow storage of light in metamaterials," Nature **450**, 397–401 (2007).

[238] H. Hu, D. Ji, X. Zeng, K. Liu, and Q. Gan, “Rainbow trapping in hyperbolic metamaterial waveguide," Sci. Rep. **3**, 1249 (2013).

[239] Y. F. Huang, S. Chattopadhyay, Y. J. Jen, C. Y. Peng, T. A. Liu, Y. K. Hsu, C. L. Pan, H. C. Lo, C. H. Hsu, Y. H. Chang, C. S. Lee, K. H. Chen, and L. C. Chen “Improved broadband and

quasi-omnidirectional anti-reflection properties with biomimetic silicon nanostructures," Nature Nanotech. **2**, 770–774 (2007).

[240] S. He, F. Ding, L. Mo, and F. Bao, "Light absorber with an ultra-broad flat band based on multi-sized slow-wave hyperbolic metamaterial thin-films," Prog. Electromagnetics Res. **147**, 69–79 (2014).

[241] J. Zhou, A. F. Kaplan, L. Chen, and L. J. Guo, "Experiment and theory of the broadband absorption by a tapered hyperbolic metamaterial array," ACS Photonics **1**, 618–624 (2014).

[242] X. Chen, Y. Chen, M. Yan, and M. Qiu, "Nanosecond photothermal effects in plasmonic nanostructures," ACS Nano **6**, 2550–2557 (2012).

[243] G.V. Naik, J.L. Schroeder, X. Ni, A.V. Kildishev, T.D. Sands, and A. Boltasseva, "Titanium nitride as a plasmonic material for visible and near-infrared wavelengths," Opt. Mater. Express **2**, 478–489 (2012).

[244] J. Wang, M. Zhu, J. Sun, K. Yi, and J. Shao, "A broadband polarization-independent perfect absorber with tapered cylinder structures," Opt. Mater. **62**, 227–230 (2016).

[245] J. Kischkat, S. Peters, B. Gruska, M. Semtsiv, M. Chashnikova, M. Klinkmüller, O. Fedosenko, S. Machulik, A. Aleksandrova, G. Monastyrskyi, Y. Flores, and W. T. Masselink, "Mid-infrared optical properties of thin films of aluminum oxide, titanium dioxide, silicon dioxide, aluminum nitride, and silicon nitride," Appl. Opt. **51**, 6789–6798 (2012).

[246] A. D. Rakic, A. B. Djurisic, J. M. Elazar, and M. L. Majewski, "Optical properties of metallic films for vertical-cavity optoelectronic devices," Appl. Opt. **37**, 5271–5283 (1998).

[247] P. Yang, C. Chen, and Z. M. Zhang, "A dual-layer structure with record-high solar reflectance for daytime radiative cooling," Sol. Energy **169**, 316–324 (2018).

[248] M. Langlais, P. P. homme, H. Bru, and P. B. Abdallah, "High temperature layered absorber for thermo-solar systems," J. Quant. Spectrosc. Radiat. Transf. **149**, 8–15 (2014).

[249] K. Yao, H. Ma, M. Huang, H. Zhao, J. Zhao, Y. Li, S. Dou, and Y. Zhan, "Near-Perfect Selective Photonic Crystal Emitter with Nanoscale Layers for Daytime Radiative Cooling," ACS Appl. Nano Mater. **2**, 5512–5519 (2019).

[250] J. M. Gordon, *Solar energy - the state of the art ISES position papers*, United Kingdom: N. p., 2001.

[251] X. Yu and C. Chen, "A simulation study for comparing the cooling performance of different daytime radiative cooling materials," Sol. Energy Mater. Sol. Cells **209**, 110459 (2020).

[252] H. S. Nalwa, *Silicon-based material and devices, two-volume set: materials and processing, Properties and Devices*, **1**, Academic Press, 2001.

[253] H. S. Nalwa, *Handbook of thin film materials*, Academic Press, 2002.

[254] L. Wang, Z. Zheng, Y. Gou, W. Liang, and W. Yu "Fabry–Perot resonance assisted dual-layer coating with enhanced wavelength-selective refection and emission for daytime radiative cooling," Opt. Commun. **483**, 126673 (2021).

[255] "Atmospheric transmittance," https://webarchive.gemini.edu/20210519-sciops–instruments–mid-ir-resources–spectroscopic-calibrations/atmospheric-transmission-data.html (accessed: August 23, 2021).

[256] P. You, X. Li, Y. Huang, X. Ma, M. Pu, Y. Guo, and X. Luo, "High-Performance Multilayer Radiative Cooling Films Designed with Flexible Hybrid Optimization Strategy," Materials **13**, 2885 (2020).

[257] G. Mabchour, M. Benlattar, K. Saadouni, and M. Mazroui, "Daytime radiative cooling purposes with selective multilayer design based on Ta2O5," Optik **214**, 164811 (2020).

[258] Y. Dai, Z. Zhang, and C. Ma, "Radiative cooling with multilayered periodic grating under sunlight," Opt. Comm. **475**, 126231 (2020).

[259] G. Smith, A. Gentle, M. Arnold, and M. Cortie, "Nanophotonics-enabled smart windows, buildings and wearables," Nanophotonics **5**, 55–73 (2016).

[260] I. A. O. Tedah, F. Maculewicz, D. E. Wolf, and R. Schmechel, "Thermoelectrics versus thermophotovoltaics: two approaches to convert heat fluxes into electricity," J. Phys. D: Appl. Phys. **52**, 275501 (2019).

[261] A. K. Chowdhary and D. Sikdar, "Nanophotonic All-weather Windows for Energy-efficient Smart Buildings," 2021 Conference on Lasers and Electro-Optics (CLEO), 1–2 (2021).

[262] A. K. Chowdhary, A. Kumar, and D. Sikdar, "Cross–Ring Based Broadband Plasmonic Metamaterial Absorbers for Boosting Silicon Solar Cell Efficiency," 2021 Fifteenth International Congress on Artificial Materials for Novel Wave Phenomena (Metamaterials), 102–104 (2021).

[263] P. C. Hsu, A. Y. Song, P. B. Catrysse, C. Liu, Y. Peng, J. Xie, S. Fan, and Y. Cui, "Radiative human body cooling by nanoporous polyethylene textile," Science **353**, 1019–1023 (2016).

[264] B. Zhao, M. Hu, X. Ao, and G. Pei, "Performance analysis of enhanced radiative cooling of solar cells based on a commercial silicon photovoltaic module," Sol. Energy **176**, 248–255 (2018).

[265] J. Lin, M. Lai, L. Dou, C. S. Kley, H. Chen, F. Peng, J. Sun, D. Lu, S. A. H, C. Xie, F. Cui, A. P. Alivisatos, D. T. Limmer, and P. Yang, "Thermochromic halide perovskite solar cells," Nature Mater. **17**, 261–267 (2018).

[266] "New smart windows darken in the sun—and generate electricity at the same time," https://www.science.org/content/article/new-smart-windows-darken-sun-and-generate-electricity-same-time (accessed: January 3, 2022).

[267] A. Barybin and V. Shapovalov, "Substrate Effect on the Optical Reflectance and Transmittance of Thin-Film Structures," International Journal of Optics **2010**, (2010).